



UNIVERSIDAD NACIONAL AUTÓNOMA DE MÉXICO
PROGRAMA DE POSGRADO EN ASTROFÍSICA

INSTITUTO DE RADIOASTRONOMÍA Y ASTROFÍSICA

MÁSERES DE METANOL CLASE I EN OBJETOS PROTOESTELARES
DE ALTA MASA / CLASS I METHANOL MASERS IN
HIGH-MASS PROTOSTELLAR OBJECTS

TESIS
QUE PARA OPTAR POR EL GRADO DE
DOCTORA EN CIENCIAS (ASTROFÍSICA)

PRESENTA
CAROLINA BERENICE RODRÍGUEZ GARZA

TUTOR
DR. STANLEY E. KURTZ SMITH
Instituto de Radioastronomía y Astrofísica

MORELIA, MICHOACÁN, JUNIO DE 2019



Universidad Nacional
Autónoma de México



UNAM – Dirección General de Bibliotecas
Tesis Digitales
Restricciones de uso

DERECHOS RESERVADOS ©
PROHIBIDA SU REPRODUCCIÓN TOTAL O PARCIAL

Todo el material contenido en esta tesis esta protegido por la Ley Federal del Derecho de Autor (LFDA) de los Estados Unidos Mexicanos (México).

El uso de imágenes, fragmentos de videos, y demás material que sea objeto de protección de los derechos de autor, será exclusivamente para fines educativos e informativos y deberá citar la fuente donde la obtuvo mencionando el autor o autores. Cualquier uso distinto como el lucro, reproducción, edición o modificación, será perseguido y sancionado por el respectivo titular de los Derechos de Autor.

*A la memoria de mis queridos abuelos:
Don Leandro, Don Pedrito y Doña Lola*

Agradecimientos

Le quiero agradecer a cada una de las personas que fueron apareciendo a lo largo de este proceso, algunas pasajeras, otras llegaron para quedarse, pero sin duda, todas tuvieron el impacto de que debían tener en cada momento de mi estancia en Morelia. Muy especialmente y con todo mi cariño le quiero agradecer a cinco personas fundamentales durante la realización de esta Tesis: mi querido asesor, mi amado novio y mis pilares de toda la vida, mi papá, mi mamá y mi hermana.

No creo poder poner en palabras el profundo agradecimiento y especial cariño que le he tomado a lo largo de estos diez años a mi querido asesor, el Dr. Stan Kurtz. Muchas pero muchas gracias por haber compartido conmigo su conocimiento y su tiempo, por enseñarme a desarrollar un pensamiento crítico y por haber sido un excelente guía durante estos años. Muchas gracias por todos sus consejos, por su paciencia y por haberme apoyado cuando más lo necesité de una manera que no creo que otro investigador hubiera hecho. Espero haber hecho el trabajo que usted esperaba.

A mi novio Antonio, muchas gracias por el amor y gran apoyo que me has brindado durante estos cinco años. Tu compañía y tus palabras de aliento fueron muy importantes para mantenerme firme durante la realización de esta meta. Muchas gracias por hacer que todo parezca naturalmente más fácil cuando estamos juntos.

Le agradezco a mis padres, Mario y Jesusita, por permitirme llegar a esta meta a partir del esfuerzo de toda una vida de trabajo, de trabajo de verdad, del que es duro y pesa con los años. Muchas gracias por enseñarme a resolver con entereza los problemas más difíciles, los de la vida misma. Gracias a esas enseñanzas he logrado enfrentar y superar el reto que representa una tesis de doctorado. Agradezco también a mi hermana, Mara Papicha, por estar ahí siempre para escucharme, cuidarme la espalda y para compartirlo todo juntas.

Agradezco al resto de mi familia, especialmente a mi wely Eudelia Castillo, a mis tíos Inocencio Garza, Margarita Garza, Gustavo Rodríguez, Clemente Rodríguez y Pedro Rodríguez, a mis primos José Luis, Claudia y Pedro Rodríguez. A todos ellos, y a sus respectivas familias, muchas gracias por su invaluable apoyo durante momentos adversos.

Le agradezco a mis amigos de posgrado con quienes compartí horas de estudio, desveladas, intercambio de ideas, pachangas, risas y momentos estresantes. Muy especialmente quiero agradecer a mis roomies de casi toda mi estancia en Morelia, Gisela Ortiz y Mariana Ramos, y a mis amigos Sergio Dzib y Raúl Naranjo.

Todo mi agradecimiento para los investigadores del IRyA que de alguna u otra manera me apoyaron durante el posgrado: Dr. Javier Ballesteros, Dr. Gilberto Gómez, Dr. Luis F. Rodríguez, Dra. Susana Lizano, Dr. Laurent Loinard y Dra. Adriana Gazol. Muchas gracias.

Tengo mucho que agradecer a mi gran amiga Sandra Eguía y a sus padres, Don Juan y Doña Irene, por su invaluable amistad y apoyo.

Le agradezco mucho a mi querida amiga Avith Mendoza y a su familia por su cálido recibimiento en mi

llegada a Morelia hace diez años y por estar, desde entonces, siempre presente. Agradezco también a mi querida amiga Iselita Maravilla y a sus padres, Don Chava y Doña Rosa, por abrirme las puertas de su casa y por poner en mí su confianza. Agradezco a mi querida amiga Ariadna Quintana y a su familia por su cariño, su apoyo y por compartirme el pan de platano de su mamá. A mi amiga Shaindel Ruiz y su familia por sacarme de la rutina e integrarme en su grupo. A los Mau's y a Fatima por los días de cine y boliche. A mi amiga Heidi Ruiz por seguirme la corriente en cada locura y por su compañía en el radiolab. A mi amigui Diana García y a mi compi Sergio Mata y su familia, muchas gracias por las risas terapéuticas, las pláticas, los bailongos y los tacos de Pátzcuaro. A Karin Hollenberg por los apapachos y su cariño y a la futura Dra. Iveth Adaena por contagiarme su entusiasmo y alegría. A todos ustedes muchas gracias por enseñarme la riqueza de la cultura michoacana y por darme un sentido de pertenencia.

Finalmente, agradezco mucho a CONACyT por otorgarme la beca de doctorado, sin la cual probablemente nada de esto hubiera sido posible. También agradezco a la UNAM y a la DGAPA por el financiamiento recibido a través del proyecto IN114514.

Resumen

En esta Tesis se presenta un estudio observacional de máseres de metanol Clase I alrededor de un total de 88 regiones de formación de estrellas masivas mediante observaciones tomadas con el radio interferómetro Karl G. Jansky Very Large Array (VLA) y el Gran Telescopio Milimétrico Alfonso Serrano (GTM).

En la primera parte de este trabajo estudiamos 56 regiones de formación estelar masiva con el VLA usando una alta resolución espacial ($\sim 1''.5$) y espectral (0.17 km s^{-1}) con el objetivo de buscar emisión en la transición máser de metanol $7_0 \rightarrow 6_1 A^+$ a la frecuencia de 44 GHz. Encontramos emisión máser en 24 de las 56 regiones (una tasa de detección del 43%). Hallamos un total de 83 componentes máser con anchos de línea entre 0.17 y 3.3 km s^{-1} , con un valor de la mediana igual a 1.1 km s^{-1} . Cada una de las líneas máser mostraron velocidades muy cercanas a la velocidad LSR de su nube anfitriona, lo cual también ha sido reportado para otras fuentes similares en la literatura. Dado que los máseres de metanol y los EGOs (Extended Green Objects) están asociados con gas chocado en flujos moleculares, buscamos correlaciones en las posiciones proyectadas de ambos en imágenes de la banda IRAC del Telescopio Espacial Spitzer. Observamos un número considerable de regiones que sugieren la existencia de tal correlación, lo que apoyaría la idea de que los máseres de metanol son trazadores de flujos moleculares. También encontramos una componente máser proyectada sobre una protoestrella que ha sido propuesta como un objeto de baja masa. Si llegara a comprobarse su naturaleza, entonces se trataría de la quinta protoestrella de baja masa asociada con máseres de metanol Clase I. Además encontramos posible evidencia de variabilidad en la densidad de flujo de los máseres de una de las regiones estudiadas.

Para completar nuestro estudio, hicimos observaciones con el VLA hacia otras 13 regiones de formación de estrellas masivas. El objetivo de las observaciones era buscar emisión de continuo a 7 mm con una resolución espacial de $\sim 0''.5$ y una resolución espectral de 13.6 km s^{-1} . A pesar de la baja resolución espectral, la buena sensibilidad y alta resolución espacial de estas observaciones nos permitieron detectar la línea de metanol a 44 GHz, y también, obtener la posición de los máseres con buena precisión. Detectamos emisión de continuo en 5 de las 13 regiones observadas y emisión de la línea máser de metanol en 4 de las 13 regiones. De éstas, 4 corresponden a nuevas detecciones de continuo a 7 mm.

Aprovechando la capacidad del Redshift Search Receiver (RSR) —instalado en el GTM— para obtener un espectro instantáneo de 38 GHz de ancho de banda, llevamos a cabo las primeras observaciones de máseres de metanol en 38 regiones de formación de estrellas de alta masa durante la fase de ciencia temprana del telescopio. Estas regiones fueron seleccionadas por tener emisión de la línea de 44 GHz con el VLA y fueron observadas en la banda de 3 mm del RSR (desde 73 hasta 111 GHz). A pesar de que la resolución espectral del RSR es de 100 km s^{-1} , pudimos identificar algunas de las transiciones de metanol, aunque no fue posible derivar parámetros físicos a partir de las líneas, y por lo tanto, no pudimos comprobar su naturaleza máser o térmica. Estas observaciones representan el tercer estudio sistemático reportado hasta la fecha de la transición máser de metanol a 84.5 GHz, la cual mostró una alta tasa de detección de 84%. También detectamos muchas otras líneas moleculares de especies tales como HCN, HCO^+ , HNC, N_2H^+ , ^{13}CO , HC_3N , CS y SO. Finalmente, encontramos una correlación moderada entre las densidades de flujo de los máseres de metanol y algunos de estos trazadores de gas denso. En particular, encontramos una buena correlación de los máseres con la línea de SiO (2–1), la cual es un buen trazador de flujos moleculares.

Summary

In this Thesis we present an observational study of Class I methanol masers towards 88 high-mass star-forming regions based on interferometric observations taken with the Karl G. Jansky Very Large Array (VLA) and the Large Millimeter Telescope Alfonso Serrano (LMT).

In the first part of this work we studied 56 high-mass star-forming regions with the VLA at high spatial ($1''.5$) and spectral resolution (0.17 km s^{-1}) in order to detect emission from the $7_0 \rightarrow 6_1 A^+$ methanol maser transition at 44 GHz. We found maser emission in 24 of the 56 regions (detection rate of 43%). We found a total of 83 maser components with line widths between 0.17 and 3.3 km s^{-1} with a median value of 1.1 km s^{-1} . Each of the maser lines showed velocities close to the LSR velocity of their parent clouds. This effect has been reported previously in the literature for similar sources. Since Class I methanol masers and EGOS (Extended Green Objects) are associated with shocked gas in molecular outflows, we searched for correlations in the projected positions of the masers against the infrared sources seen in three-color images taken with the Spitzer Space Telescope. We observed a number of regions suggesting the existence of such correlation, supporting the idea that this type of methanol masers are good tracers of molecular outflows. We also found a maser component projected toward a protostar that is thought to be a low-mass object. If its nature is corroborated, this protostar would be the fifth low-mass protostar associated with Class I methanol masers. Moreover, we found evidence of variability of the maser flux densities in one of the studied regions.

To improve the completeness of our study, we made additional observations toward 13 high-mass star-forming regions with the VLA at high spatial resolution ($0''.5$) but with low spectral resolution (13.6 km s^{-1}) in order to detect continuum emission at 7 mm. Despite the low spectral resolution, the good sensitivity and high angular resolution of the observations allowed us to detect the methanol line at 44 GHz and also to obtain the maser positions with good accuracy. We detected continuum emission in 5 out of the 13 observed regions and methanol maser emission in 4 of the 13 regions. From these, 4 of them correspond to new continuum detections at 7 mm.

Taking advantage of the capabilities of the Redshift Search Receiver (RSR) —installed at the LMT— to obtain an instantaneous spectrum over a bandwidth of 38 GHz (from 73 to 111 GHz), we observed 38 class I 44 GHz maser sites during the Early Science Phase of the LMT using RSR. Although the spectral resolution of the RSR is about 100 km s^{-1} , we were able to detect emission in a number of methanol transitions, including the transitions that are usually known as class I methanol masers in the literature. We could not derive physical parameters from the lines, and therefore, we were not able to probe their maser or thermal nature. These observations represent the third systematic study to date of the maser transition at 84.5 GHz which showed a high detection rate of 84%. In addition, we detected many other molecular lines from species such as HCN, HCO^+ , HNC, N_2H^+ , ^{13}CO , HC_3N , CS and SO. Finally, we found a moderate correlation between the flux density of the methanol masers and some of these dense gas tracers. In particular, we found a good correlation with the methanol masers and the SiO (2–1) transition, which is known to be a good tracer of molecular outflows.

Contents

1	Introduction	11
1.1	Historical Overview	11
1.2	Basic Concepts	12
1.2.1	Radiative transfer	13
1.2.2	Saturation	17
1.2.3	Line Narrowing	20
1.2.4	Usefulness of Masers	21
1.2.5	Pump Models	22
1.3	Outline of this Thesis	22
2	Methanol Masers and Star Formation	25
2.1	Massive Star Formation	25
2.2	Structure of Methanol	26
2.2.1	A-type Methanol	27
2.2.2	E-type Methanol	28
2.3	Methanol Masers in Star-Forming Regions	29
2.3.1	Class I CH ₃ OH Masers	30
2.3.2	Class II CH ₃ OH Masers	33
3	A catalog of 44 GHz Methanol Masers in MSFRs	37
3.1	Introduction	37
3.2	The sample	38
3.3	Observations and Data Reduction	39
3.4	Results	42
3.4.1	Line properties	45
3.4.2	Comments on individual sources	47
3.5	Discussion	51
3.5.1	Comparison with previous surveys	51
3.5.2	Relation with molecular outflows	53
3.5.3	On the classification between HMPOs and UCHII regions	54
3.6	Summary and conclusions	55
4	Continuum emission and methanol masers toward HMPOs	61
4.1	Introduction	61
4.2	Observations and data reduction	62
4.3	Results	63

4.3.1	Continuum emission	63
4.3.2	Class I methanol masers	66
4.4	Discussion	72
4.5	Summary	75
5	LMT 3 mm molecular line survey	77
5.1	Introduction	77
5.2	Observations and Data Reduction	78
5.3	Results	82
5.3.1	Class I methanol maser detections	83
5.3.2	Class II methanol masers detections	88
5.3.3	Thermal methanol detections	90
5.3.4	Molecular line detections	90
5.4	Discussion	94
5.4.1	Line Identification	94
5.4.2	Spectral Dilution	94
5.4.3	Double pointing observations	96
5.4.4	Comparison between 44, 84, and 95 GHz flux densities	99
5.4.5	Comparison between methanol lines and other molecular emission	100
5.5	Summary	105
6	Conclusions and Future Work	117
6.1	Future Work	118
	Bibliography	123
	Appendices	133
A	Three-color images with DS9	135
A.1	Download Spitzer images	135
A.2	Managing images with DS9	137

Chapter 1

Introduction

The word maser is an acronym for **M**icrowave **A**mplification by **S**timulated **E**mission of **R**adiation. Maser emission is a non-thermal process that was first produced in the laboratory in 1954, six years before lasers. Both, masers and lasers, describe the same phenomenon of amplification of radiation —visible light for lasers, radio waves for masers— at a particular frequency, phase and direction (so-called coherent radiation) based on population inversion of the atomic or molecular energy levels.

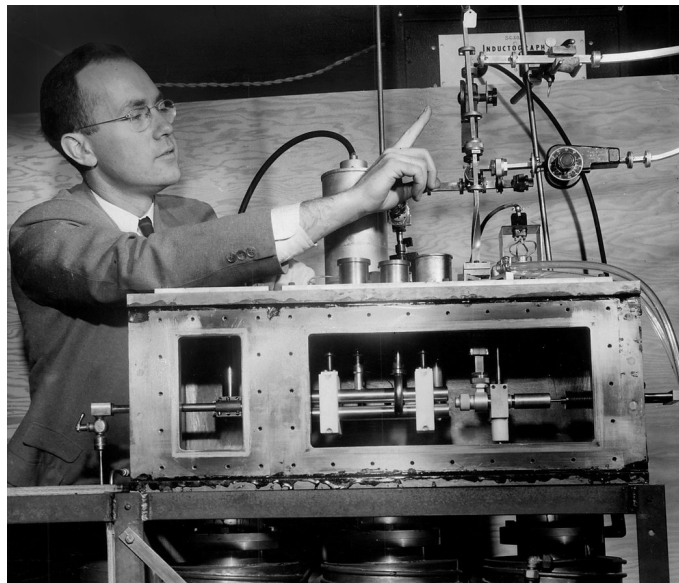


Figure 1.1: The molecular spectroscopist Charles Townes developed a basic design for a maser, using ammonia as the active molecule, at Columbia University. For his creation of the maser, Townes received the Nobel Prize in Physics in 1964.

1.1 Historical Overview

The discovery of maser emission from space did not occur until 1965, a decade after its discovery in the laboratory. Initially it was considered unlikely that a maser could arise in interstellar space. However,

the physical conditions in certain molecular gas clouds are such that population inversion in the rotational states of molecules can occur naturally.

The first molecule detected in the interstellar medium at radio wavelengths was hydroxyl (OH); it was detected in absorption by Weinreb et al. (1963) towards Cassiopeia A. The first signs that there was something different in the characteristics of OH came from observations of the Galactic Center. Weaver et al. (1965) were searching for OH absorption, but instead detected strong and narrow emission—which they labeled “mysterium”—toward several HII regions. As this new type of source was observed with progressively higher angular resolution it became clear that the observed emission could not have a thermal origin. The OH masers appeared to be confined close to the radio continuum emission and the velocity range of the maser spectrum rarely exceeded $\sim 15 \text{ km s}^{-1}$. Elitzur and de Jong (1978) suggested that these masers originated in the compressed shell between the shock and the ionization fronts around HII regions.

Water (H_2O) was the second maser molecule discovered, by Cheung et al. (1969). It was detected in the $6_{16} \rightarrow 5_{23}$ transition toward the star-forming regions Orion A and W49. Unlike OH masers, H_2O masers are found at greater separations from the exciting source and their spectra cover a wide range of velocity; hundreds of kilometers per second in some cases (Reid and Moran 1981). Although it was not obvious at the time, the existence of high velocity features was early evidence for the now well-accepted model, that H_2O masers form in the outflows from newly formed stars (Strel'nitskii and Sunyaev 1973).

Methanol (CH_3OH) was discovered in interstellar space by Ball et al. (1970) and the first methanol masers were detected towards Orion-KL by Barrett et al. (1971). They detected five CH_3OH lines with frequencies close to 25 GHz and from the relative line intensities, they concluded that the molecular populations were inconsistent with local thermodynamic equilibrium (LTE). This was confirmed four years later by Barrett et al. (1975). These transitions near 25 GHz were the only known methanol maser transitions until Wilson et al. (1984) discovered two new transitions, near 23 and 19 GHz, toward the star-forming region W3(OH). Shortly after, new maser lines were discovered at 6.6 GHz (Menten 1991b), 12 GHz (Batra et al. 1987), 36 and 44 GHz (Morimoto et al. 1985).

1.2 Basic Concepts

The basic principle involved in the operation of a maser is *population inversion*, a mechanism in which the population of some excited state is maintained higher than that of a lower energy state. This situation is only possible out of thermodynamic equilibrium. Figure 1.2 shows a simplified three-level energy diagram. In this system, the molecules are excited to a short-lived high-energy state. From this level, the molecules quickly decay by spontaneous emission to a *metastable* level, i.e. a state with a long lifetime which facilitates the population inversion. Raising the molecules to the short-lived excited state requires energy; the process that accomplishes this task is known as the *pump* and can be either *radiative* or *collisional* in nature.

Stimulated emission results from the fact that more molecules are available in the upper excited (metastable) state than in the lower state. Photons emitted due to a transition from the metastable level to the lower level, stimulate further emission from nearby molecules resulting in a cascade of photons at the same frequency and with identical phase and direction (coherent photons), a process known as *amplification*.

Masers are compact sites of molecular emission where certain transitions can be amplified by the process of population inversion, giving rise to intense and narrow spectral lines. Physically, the maser regions must be dense ($10^6 - 10^{11} \text{ cm}^{-3}$), be near to some powerful energy source, and the molecular energy structure must contain a metastable level to facilitate population inversion. Maser emission can be identified when at least one of the following properties is observed:

Large T_B : as will be explained in the next section, the maser mechanism can produce an exponential

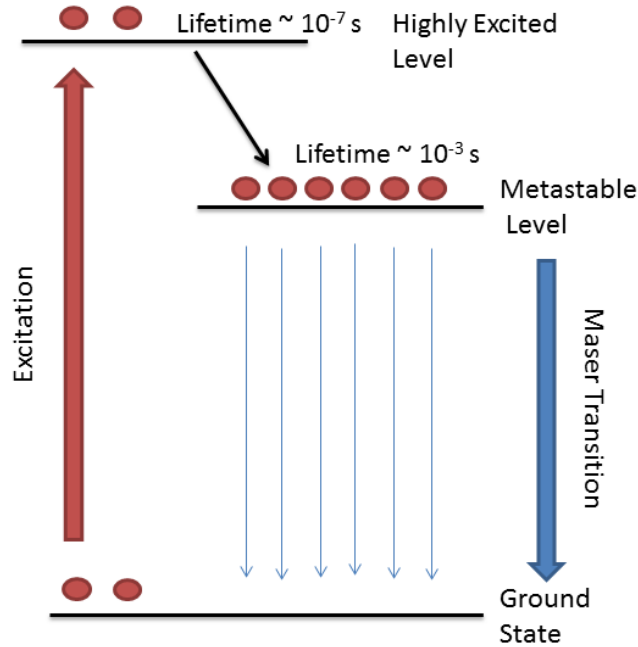


Figure 1.2: Simplified tree-level energy diagram to show the population inversion mechanism.

amplification of the line brightness temperature.

Point-like source: the exponential amplification depends on the “gain” factor τ , which is related to the length (s) traversed by the rays along the maser region. The larger the length traveled by the maser photons, the larger τ will be and hence T_B will be much brighter than along adjacent lines of sight corresponding to slightly smaller values of τ . This makes the apparent angular size of the maser sources extremely small —basically unresolved in many cases.

Narrow line width: for the same reason causing small source sizes, the width of a maser line is also quite small, as the brightness of the central part of the line (where τ is maximum) is enhanced with respect to the line wings.

Line ratios: incompatible with LTE. For example, LTE predicts intensity ratios for 1665, 1667, 1720 and 1612 MHz of 5: 9: 1: 1 (in this order), while the relative intensities found for the W3 region were 50: 2: 1: not detected (Weinreb et al. 1965).

In the following sections these points will be discussed in more detail.

1.2.1 Radiative transfer

To understand the concept of population inversion, it is instructive to present first the radiative transfer equation and its solution in the simple case of a homogeneous and isothermal region.

The specific intensity of the radiation, I_ν , that is propagated through empty space is constant along the path it follows. If radiation interacts with matter in some region of space, the matter will absorb a fraction of the radiation and will emit at the same time its own radiation. The intensity variation through the path

s can be described with the absorption coefficient κ_ν (the attenuation per length unit at the frequency ν), and with the emission coefficient j_ν (intensity produced per length unit). The equation that provides the variation of the intensity per unit of length, taking into account these two coefficients, is the radiative transfer equation

$$\frac{dI_\nu}{ds} = -\kappa_\nu I_\nu + j_\nu. \quad (1.1)$$

The emission coefficient j_ν has dimensions of $\text{erg s}^{-1} \text{cm}^{-3} \text{sr}^{-1} \text{Hz}^{-1}$, while the absorption coefficient κ_ν has dimensions of cm^{-1} . The propagation in empty space corresponds to the particular case where $\kappa_\nu = j_\nu = 0$, i.e., without any radiation-matter interaction. The absorption and emission coefficients can be expressed in terms of the Einstein coefficients:

$$\kappa_\nu = \frac{h\nu_{ul}}{4\pi} (n_l B_{lu} - n_u B_{ul}) \phi(\nu), \quad (1.2)$$

$$j_\nu = \frac{h\nu_{ul}}{4\pi} n_u A_{ul} \phi(\nu), \quad (1.3)$$

where subindices u and l refers to the upper and the lower levels, n_u and n_l are the number density of particles in the upper and lower levels, respectively, ν_{ul} is the frequency of the transition, h is the Planck constant, and $\phi(\nu)$ is the normalized line profile, usually taken to be Gaussian. A_{ul} , B_{lu} and B_{ul} are the Einstein coefficients of spontaneous emission, absorption, and stimulated emission, respectively.

Equation 1.1 may be also expressed in terms of the optical depth along the line of sight, defined as

$$d\tau_\nu = \kappa_\nu ds \quad (1.4)$$

giving

$$\frac{dI_\nu}{d\tau_\nu} = -I_\nu + \frac{j_\nu}{\kappa_\nu} = -I_\nu + S_\nu, \quad (1.5)$$

where $\frac{j_\nu}{\kappa_\nu}$ describes the properties of the medium and is known as the source function, S_ν which has dimensions of intensity.

The formal solution of the radiative transfer equation is

$$I_\nu = I_{\nu_0} e^{-\tau_\nu} + \int_0^{\tau_\nu} S_\nu e^{-(\tau_\nu - \tau'_\nu)} d\tau'_\nu. \quad (1.6)$$

Assuming a constant source function, the radiative transfer equation may be solved to obtain an expression for the observed intensity, I_ν :

$$I_\nu = I_{\nu_0} e^{-\tau_\nu} + S_\nu (1 - e^{-\tau_\nu}), \quad (1.7)$$

where I_{ν_0} is the intensity of radiation entering the gas at $\tau_\nu = 0$. This is the form of the radiative transfer equation most commonly used.

We can define the excitation temperature T_{ex} as the temperature associated with the source function, i.e., the excitation temperature is the temperature at which the value of the source function is equal to the value of the Planck function for a given frequency ν ,

$$S_\nu = B_\nu(T_{\text{ex}}) = \frac{2h\nu^3}{c^2} \frac{1}{e^{\frac{h\nu}{kT_{\text{ex}}}} - 1}. \quad (1.8)$$

It is also convenient to define the excitation temperature through the Boltzmann distribution:

$$\frac{n_u}{n_l} = \frac{g_u}{g_l} e^{-h\nu/kT_{\text{ex}}}, \quad (1.9)$$

where g_u and g_l are the statistical weights of the corresponding levels.

Similarly, we can define the brightness temperature T_B as the temperature for which the intensity I_ν is equal to the value of the Planck function for a given frequency ν ,

$$I_\nu = B_\nu(T_B) = \frac{2h\nu^3}{c^2} \frac{1}{e^{\frac{h\nu}{kT_B}} - 1}. \quad (1.10)$$

At low frequencies or high temperatures ($h\nu \ll kT_B$), the Planck function is approximated by the Rayleigh-Jeans formula:

$$I_\nu \simeq \frac{2k\nu^2}{c^2} T_B. \quad (1.11)$$

We can define the radiation temperature T_R , that in the Rayleigh-Jeans approximation is equal to the brightness temperature,

$$I_\nu \simeq \frac{2k\nu^2}{c^2} T_R. \quad (1.12)$$

The solution to the radiative transfer equation (Equation 1.7) can be written in terms of temperatures (taking into account Equations 1.8 and 1.10) by

$$T_R = T_{\text{bg}} e^{-\tau_\nu} + T_{\text{ex}} (1 - e^{-\tau_\nu}). \quad (1.13)$$

T_R is the brightness temperature, T_{ex} is the excitation temperature and T_{bg} is the background temperature assumed to be 2.73 K which corresponds to the background intensity I_{ν_0} .

Line Temperature

When a spectral line is observed, the detected intensity, I_ν^{ON} , has two contributions; one from the line emission itself and another from the background continuum emission

$$I_\nu^{\text{ON}} = I_{\nu_0} e^{-\tau_\nu} + S_\nu (1 - e^{-\tau_\nu}). \quad (1.14)$$

In order to obtain the pure line intensity, we need to subtract the background emission, $I_\nu^{\text{OFF}} = I_{\nu_0}$ (i.e., the intensity where $\tau_\nu = 0$), from the total emission. Therefore, the line intensity is of the form:

$$I_\nu^L = I_\nu^{\text{ON}} - I_\nu^{\text{OFF}} = [S_\nu - I_{\nu_0}] (1 - e^{-\tau_\nu}). \quad (1.15)$$

Similar to Equation 1.13, the line intensity can be expressed in terms of temperature as:

$$T_L = [T_{\text{ex}} - T_{\text{bg}}] (1 - e^{-\tau_\nu}). \quad (1.16)$$

Here, T_L is the line temperature defined in a similar way to T_R .

Population Inversion

From Equation 1.16, we can see three cases:

1. $T_{\text{ex}} > T_{\text{bg}}$: the line is in emission
2. $0 < T_{\text{ex}} < T_{\text{bg}}$: the line is in absorption
3. $T_{\text{ex}} < 0$: population inversion occurs

The interesting case for maser emission is that of $T_{\text{ex}} < 0$. According to Eq. 1.9 this occurs when the upper level of the transition is statistically overpopulated with respect to the lower level: $\frac{n_u/g_u}{n_l/g_l} > 1$. Consequently, the optical depth, τ_ν , defined as:

$$\tau_\nu = \frac{c^3}{8\pi\nu_{ul}\Delta\nu} A_{ul} N_u (e^{h\nu_{ul}/kT_{\text{ex}}} - 1) < 0, \quad (1.17)$$

is also negative. Here, $\Delta\nu$ is the linewidth and N_u is the column density of the upper level along the line of sight.

Therefore, the expression for the line brightness temperature can be written as

$$T_L = |T_{\text{ex}} + T_{\text{bg}}| (e^{|\tau_\nu|} - 1) \simeq |T_{\text{ex}}| e^{|\tau_\nu|}. \quad (1.18)$$

A negative excitation temperature and optical depth correspond to population inversion between the upper and lower levels and cause an exponential amplification, rather than absorption, on the line brightness temperature, which is said to be *masing*. The absolute value of the optical depth ($|\tau_\nu|$), is therefore referred to as a *gain*. For example, many astrophysical masers show τ of the order of -25 , leading to gain factors of order $e^{|-25|} \simeq 10^{10}$.

1.2.2 Saturation

There are limitations on the exponential growth of the maser line intensity, known as *saturation*. Maser saturation occurs when the photons produced by the stimulated emission start to reduce the population inversion and hence the maser gain. When this happens, the maser is said to be *saturated*. In contrast, when the pumping processes are able to maintain the population inversion against the growing losses by stimulated emission, such a maser is said to be *unsaturated* (Elitzur 1992). In the following, we will show in a quantitatively simplified way, the expressions for the maser intensity in these two cases: saturated and unsaturated.

If we substitute the expressions for the absorption and emission coefficients (Equations 1.2 and 1.3) into the radiative transfer Equation 1.1, we can see its dependence on the population difference $n_u - n_l$,

$$\frac{dI_\nu}{ds} = \frac{h\nu_{ul}}{4\pi} \phi(\nu) [(n_u B_{ul} - n_l B_{lu}) I_\nu - n_u A_{ul}]. \quad (1.19)$$

Therefore, in order to obtain a solution for the line intensity, we first need to derive an expression for the level populations. Considering two energy levels denoted 1 and 2 for the lower and upper levels (see Figure 1.3), respectively, the level populations can be calculated from the steady-state rate equations

$$\frac{dn_2}{dt} = -n_2 A_{21} - (n_2 - n_1) B_{21} J_\nu - (n_2 C_{21} - n_1 C_{12}) + P_2(n - n_{12}) - \Gamma_2 n_2 = 0 \quad (1.20a)$$

$$\frac{dn_1}{dt} = n_2 A_{21} + (n_2 - n_1) B_{21} J_\nu + (n_2 C_{21} - n_1 C_{12}) + P_1(n - n_{12}) - \Gamma_1 n_1 = 0. \quad (1.20b)$$

where the population in the maser levels is defined as

$$n_{12} = n_1 + n_2 \quad (1.21)$$

and n is the total population density, P_1 and P_2 are the pump rates into levels 1 and 2, respectively, from all other states, Γ_1 and Γ_2 are the loss rates. There is only one Einstein B_{21} coefficient because from the Einstein relation

$$g_1 B_{12} = g_2 B_{21}, \quad (1.22)$$

we assume equal statistical weights $g_1 = g_2$. C_{12} and C_{21} are the collisional coefficients across the masing levels which obey the detailed balance relation

$$g_1 C_{12} = g_2 C_{21} \exp(-h\nu/kT_k) \quad (1.23)$$

T_k is the kinetic temperature. For microwave lines, and typical kinetic temperatures of several hundred degrees, the exponential can be neglected and therefore,

$$C_{12} \simeq C_{21}. \quad (1.24)$$

With this approximation, Equations 1.20a and 1.20b can be re-written as

$$\frac{dn_2}{dt} = -n_2 A_{21} - (n_2 - n_1) B_{21} J_\nu - (n_2 - n_1) C_{21} + P_2 (n - n_{12}) - \Gamma_2 n_2 = 0 \quad (1.25a)$$

$$\frac{dn_1}{dt} = n_2 A_{21} + (n_2 - n_1) B_{21} J_\nu + (n_2 - n_1) C_{21} + P_1 (n - n_{12}) - \Gamma_1 n_1 = 0. \quad (1.25b)$$

The radiation can propagate in all directions, so, instead of $B_{21} I_\nu$, the stimulated transition term in the rate equations is actually $B_{21} J_\nu$, where

$$J_\nu = \frac{1}{4\pi} \int I_\nu d\Omega \simeq I_\nu \frac{\Delta\Omega}{4\pi}. \quad (1.26)$$

When the radiation is isotropic ($\Delta\Omega = 4\pi$), then the two expressions are equal ($J_\nu = I_\nu$), but when radiation is beamed into a small solid angle $\Delta\Omega$ —as is the case for masers which show small spot sizes—it is more appropriate to use the angle-averaged intensity, J_ν .

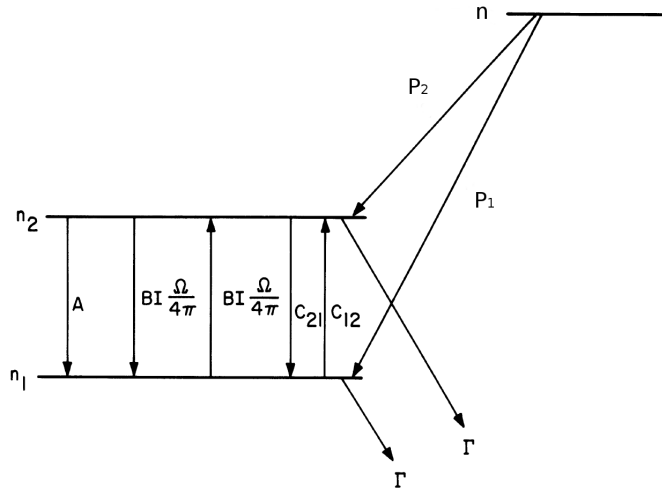


Figure 1.3: Schematic energy level diagram. The masing levels 1 and 2 have population densities n_1 and n_2 . The molecules move from one energy state to another by radiative and collisional mechanisms. A and B are the Einstein coefficients of spontaneous emission ($A_{21} = A$), absorption ($B_{12} = B$) and stimulated emission of photons ($B_{21} = B$). C_{12}, C_{21} represent the coefficients for collisions. P_1, P_2 are the pump rates into levels 1 and 2, respectively, from all other states, Γ is the rate at which molecules are transferred from the masing levels to others (assumed equal for the two levels $\Gamma_1 = \Gamma_2 \equiv \Gamma$). Figure from Kellermann and Verschuur (1988, Chapter 6).

To simplify Equations 1.25a and 1.25b, we assume that spontaneous emission and collisional transitions are negligible. With these simplifications, for a steady state:

$$(n_2 - n_1)(2B_{21} J_\nu + \Gamma_2) = (P_2 - P_1)(n - n_{12}) + n_1(\Gamma_1 - \Gamma_2). \quad (1.27)$$

Thus the population inversion depends on the differences between the pump and loss rates, shown on the right-hand side of the equation, and on the losses by stimulated emission and other processes (the term

$2B_{21}J_\nu + \Gamma_2$). Then, we will assume that the two loss rates are equal $\Gamma_1 = \Gamma_2 = \Gamma$. Taking into account the separate rates is not difficult, but only complicates the algebra without changing the physical meaning. Solving for the population difference

$$\Delta n = n_2 - n_1 \quad (1.28)$$

therefore

$$\Delta n = \frac{P_2 - P_1}{\Gamma + 2BJ_\nu} = \frac{\Delta P/\Gamma}{1 + 2BJ_\nu/\Gamma}. \quad (1.29)$$

Defining

$$\Delta n_0 = \Delta P/\Gamma \quad (1.30)$$

and the intensity of saturation J_s as

$$J_s = \Gamma/2B_{21}, \quad (1.31)$$

equation 1.29 is then

$$\Delta n = \frac{\Delta n_0}{1 + J_\nu/J_s} \phi(\nu) \quad (1.32)$$

From this equation, we can see that for $J_\nu < J_s$, the radiation hardly affects the population levels, Δn . On the other hand, if J_ν is amplified so much that it exceeds J_s , then the population difference will be reduced significantly.

Thus, ignoring the spontaneous emission factor and replacing Δn , we can approximate the radiative transfer Equation 1.19 as

$$\frac{dI_\nu}{ds} \simeq \frac{h\nu_{21}}{4\pi} \phi(\nu) B_{21} \Delta n I_\nu = \frac{h\nu_{21}}{4\pi} \phi(\nu) B_{21} \frac{\Delta n_0}{1 + J_\nu/J_s} I_\nu \phi(\nu). \quad (1.33)$$

We need to integrate Equation 1.33 over frequency

$$I = \int I_\nu \phi(\nu) d\nu \quad (1.34)$$

and define

$$\kappa_{\nu_0} = \frac{h\nu}{4\pi} \phi(\nu) \Delta n_0 B_{21} \quad (1.35)$$

for the line center frequency. We also need to integrate J_ν over frequency in a similar way as was done for I_ν (Equation 1.34). The definition of J_ν (Equation 1.26) tells us that $J = I\Delta\Omega/4\pi$, thus we can write

$$\frac{J}{J_s} = \frac{I}{I_s} \quad (1.36)$$

where $I_s = 4\pi J_s/\Delta\Omega$ determines the radiation intensity at which the stimulated transitions begin to affect the level populations. Now, the radiative transfer equation becomes

$$\frac{dI}{ds} = -\frac{\kappa_0 I}{1 + I/I_s}, \quad (1.37)$$

from this equation, we can finally derive an expression for the maser intensity in the limits where $I \ll I_s$ and $I \gg I_s$.

For $I \ll I_s$, then $\Delta n = \Delta n_0$, and the level populations are essentially independent of the radiation field. In this limit the radiative transfer equation is of the form

$$\frac{dI}{I} = -\kappa_0 ds, \quad (1.38)$$

whose solution is

$$I(s) = I_0 e^{\kappa_0 s}. \quad (1.39)$$

In this case there is an exponential amplification of the intensity and the maser is said to be *unsaturated*. For the case of $I \gg I_s$, Equation 1.37 becomes

$$dI = -\kappa_0 I_s ds \quad (1.40)$$

whose solution is of the form

$$I(s) = I_0 + \kappa_0 s. \quad (1.41)$$

In this case the intensity increases linearly with the distance, and the maser is said to be *saturated*.

1.2.3 Line Narrowing

Most astronomical masers have line widths that are smaller by factors of up to 10 than those expected from thermal motions in the masing regions. During unsaturated amplification, where exponential growth is achieved, the intensity at the center of the line will grow much faster than the intensity in the wings. The unsaturated absorption coefficient κ_{ν_0} is peaked at the line-center frequency, and the unsaturated exponential amplification $\exp(\kappa_{\nu_0} s)$ will therefore enhance the center of the line much more than its wings. The amplified line will be narrower than the input line.

1.2.4 Usefulness of Masers

Maser emission is observed from a variety of species and in many astronomical environments. Very useful information can be obtained from their observations given its widespread presence and unique properties. Applications range from estimations of magnetic fields to measuring the Hubble constant, and attempts to detect the variation of what we usually know as physical constants over a cosmological time. Here, we discuss a few of the many applications of maser studies, mainly focused on star-forming regions.

As we noted in previous sections, in maser lines, the excitation temperature T_{ex} has nothing to do with the gas kinetic temperature, this makes it difficult to derive the gas physical parameters. However, maser emission has two advantages which make it ideal for high-angular resolution measurements: it can be very bright and point-like. These properties make astronomical masers an excellent target for Very Long Baseline Interferometry (VLBI) observations, which allow us to derive a number of important quantities:

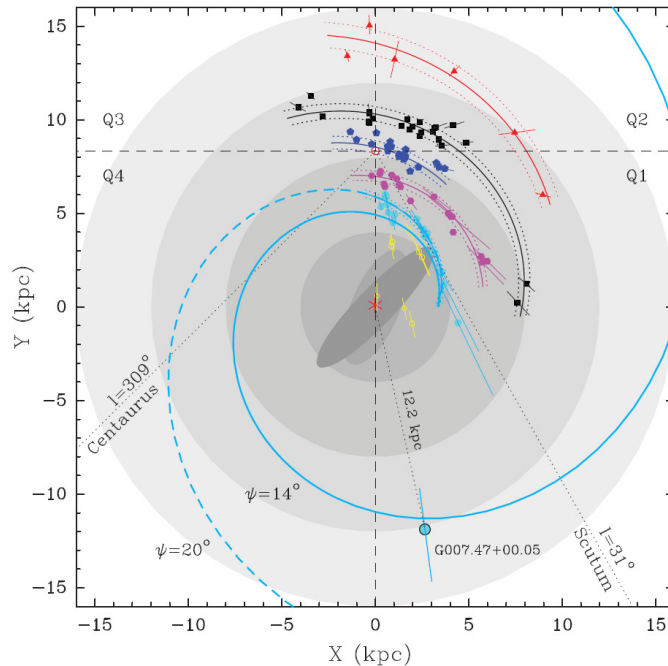


Figure 1.4: Location of different maser sources in our Galaxy determined via trigonometric parallaxes using the VLBI technique. Figure from Sanna et al. (2017).

3D Velocity: Since maser spots are basically unresolved even with VLBI observations achieving angular resolutions of 1 milli-arcsec, they can be used as “target particles” to study the gas dynamics from which the maser emission originates. Multi-epoch imaging allows to derive the spot proper motion and thus obtain the velocity in the plane of the sky. This, combined with the velocity along the line of sight obtained from the Doppler shift of the line, makes it possible to derive the 3D velocity of the gas, and study its kinematics.

Distance: VLBI proper motions of maser spots (parallax) are used to estimate the distance to the associated source up to several kiloparsecs. Two major projects to map the spiral structure of the Milky Way are providing parallaxes and proper motions for water and methanol masers associated with

high-mass star forming regions across large portions of the Milky Way (see Figure 1.4). The Bar and Spiral Structure Legacy (BeSSeL) Survey and the Japanese VLBI Exploration of Radio Astrometry (VERA) have yielded over 100 parallax measurements (Reid et al. 2014; Sanna et al. 2017).

Magnetic Field: Zeeman splitting of the maser lines has been used for some species (OH, H₂O and CH₃OH) to estimate the magnetic field in the maser regions on scales as small as a few AU. Sarma and Momjian (2009, 2011) report the discovery of circular polarization in the 36 and 44 GHz methanol maser lines, which they interpret as a result of the Zeeman effect.

1.2.5 Pump Models

The large velocity gradient (LVG) or Sobolev approximation (Sobolev 1960) allows to decouple the population level calculation from the radiative transfer equation. In LVG, the integrations that appear in the formal solution of the radiative transfer equation (Eq. 1.19) can be carried out, so the line mean intensity can be expressed explicitly as a function of the energy level populations from the same transition (Eqs. 1.20a and 1.20b). Elimination of the mean intensities in favour of the population expressions leads to a set of master equations which are non-linear algebraic equations in the populations. The LVG approximation is therefore not really a numerical method, but a clever approximation that allows much simpler numerical methods to be used than suggested by the original problem. LVG is a widely used method that is rarely strictly appropriate in maser studies, and it should be applied with care.

Model Requirements

The requirements for the construction of a maser model (as listed by Kylafis 1991) are:

- The energy levels of the molecule that exhibits maser emission. These are generally well-known.
- The Einstein coefficients A_{ul} for the transitions from any upper level u to any lower level l . These are also well-known, at least for the most common molecules.
- The collision rates C_{ul} for transitions from any level u to any level l of the maser molecules. The colliding particles are the other molecules in the region (e.g., H₂). These rates are only approximately known. Therefore, when maser models are constructed, it should always be kept in mind that the currently published collision rates may be revised.
- The velocity field in the maser region. This is unknown and it is only guessed in maser models. Two types of velocity field have generally been assumed. In one, the medium is static and the molecules obey a distribution of velocities —typically Gaussian. In the other, the medium exhibits a large velocity gradient, i.e., the macroscopic velocity differences are significantly larger than the thermal velocities.
- The geometry of the maser regions is also unknown and in maser models a simple (typically spherical or cylindrical) geometry is assumed.

1.3 Outline of this Thesis

This Thesis is focused in the study of some of the millimeter transitions of Class I methanol masers toward regions of massive star formation.

Chapter 2: We present a brief overview on the structure of the methanol molecule which is the focus species for this Thesis. We discuss the methanol asymmetry (A-type and E-type) that give rise to its rich spectrum of thermal and maser transitions in the microwave range. We give a summary on the empirical classification of methanol masers, Class I and Class II, and the current state of knowledge in star-forming regions.

Chapter 3: We present a systematic study of Class I methanol masers in its transition $7_0 \rightarrow 6_1A^+$ at the frequency of 44 GHz toward 56 well-known high-mass star-forming regions. The observations were made with the Karl G. Jansky Very Large Array at a spectral resolution of 0.17 km s^{-1} .

Chapter 4: We present 7 mm continuum emission and Class I methanol maser emission in the transition $7_0 \rightarrow 6_1A^+$ at the frequency of 44 GHz toward 13 well-known massive star-forming regions. The observations were also made with the Very Large Array at a spectral resolution of 13.6 km s^{-1} .

Chapter 5: We present spectral line observations in the 3 mm band toward 38 high-mass protostars with Class I 44 GHz methanol masers previously detected (half of these objects belong to the sample presented in Chapter 3). The observations were taken during the Early Science Program of the Large Millimeter Telescope Alfonso Serrano using the Redshift Search Receiver at a spectral resolution of 100 km s^{-1} . The Class I methanol masers detected are at the frequencies of 84.5 and 95.1 GHz. We also included the Class II methanol masers at 107.0 and 108.8 GHz as well as the thermal methanol emission near 96.7 GHz.

Chapter 6: We give the conclusions and future work.

The work presented in this Thesis has originated the following publications:

- “*A Catalog of 44 GHz Methanol Masers in Massive Star-forming Regions. IV. The High-mass Protostellar Object Sample*”
Rodríguez-Garza, C. B.; Kurtz, S. E.; Gómez-Ruiz, A. I.; Hofner, P.; Araya, E. D.; Kalenskii, S. V., 2017, *The Astrophysical Journal Supplement Series*, 233, 4
- “*Interferometric and single-dish observations of 44, 84 and 95 GHz Class I methanol masers*”
Rodríguez-Garza, Carolina B.; Kurtz, Stanley E.; Gómez-Ruiz, Arturo I.; Hofner, Peter; Araya, Esteban D.; Kalenskii, Sergei V., 2018, *Astrophysical Masers: Unlocking the Mysteries of the Universe*, 336, 239
- “*Continuum emission and methanol masers toward high-mass star-forming regions*”
Rodríguez-Garza, C. B.; Kurtz, S. E. et al., in preparation
- “*Millimeter line survey toward high-mass protostars with the Large Millimeter Telescope*”
Rodríguez-Garza, C. B.; Kurtz, S. E., Gómez-Ruiz, A. I. et al., in preparation

Chapter 2

Methanol Masers and Star Formation

Maser emission is a very useful tool in the study of star formation. This Chapter describes interstellar methanol masers, in particular, those in massive star-forming regions.

2.1 Massive Star Formation

Massive stars are characterized for having more than 8 times the mass of the Sun. They play a central role in the evolution of the Universe. High-mass stars are the principal source of heavy elements and ultraviolet (UV) radiation. They can trigger the formation of new stars and possibly planetary systems through powerful outflows, winds, regions of ionized Hydrogen (HII regions), and supernova explosions. At large scales they dominate the physical, chemical, and morphological structure of their host galaxies. Understanding the formation of massive stars is essential to address fundamental questions in modern astrophysics, such as: When did the first stars in the Universe form and how did they influence their environments? What are the cosmic origins of chemical elements, particularly those fundamental to life? How does the exchange of mass and momentum between massive stars and the environment shape the origin and evolution of galaxies?

Despite decades of intensive research, the processes that produce massive stars are still under debate for a number of reasons. First, massive stars form in clusters at large distances (typically 30 times further than the nearest regions of low-mass star formation), which makes difficult to distinguish between individual protostars. Massive stars are less common than their lower-mass counterparts, and their formation timescales are so short that it is less likely to observe them in early evolutionary phases. Additionally, these stars form deep within giant molecular clouds of high density gas and dust, which obscures all visible radiation emitted. High-mass star formation is a much more complex problem to tackle than isolated low-mass star formation, whose formation via accretion is well-established.

Due to this obscuration, the best tracers of the earliest phases of formation are at centimeter, millimeter and (sub)millimeter wavelengths, through observations of ionized gas, dust continuum emission and molecular emission. Although at present there is no clear evolutionary sequence for the formation of massive stars, several stages have been identified observationally. Figure 2.1 shows an illustration with the proposed evolutionary scenario of a cluster of massive stars¹. The main stages can be summarized as follows:

1. Massive stars form in sub-structures known as clumps of cold gas and dust embedded in giant molecular clouds.

¹Figure taken from Cormac Purcell's web page: <http://web.science.mq.edu.au/~cpurcell/>

2. These clumps collapse into cores through gravitational instabilities and increase in mass, via mergers or accretion.
3. Heat and molecular outflows from the central object(s) evaporate the ice on the dust grains, enriching the chemistry in the immediate vicinity and leading to the production of organic molecules in the so-called hot molecular core. CH_3OH masers appear in this phase.
4. The young embedded stars produce large amounts of UV photons which ionize the surrounding environment, forming an ultracompact HII (UCHII) region. As the ionization increases, it destroys the complex molecules and the methanol masers.
5. The continuing expansion of the hot ionized gas forms a giant HII region. Eventually, the gas is dissipated by the ionized winds, exposing the young cluster of stars.

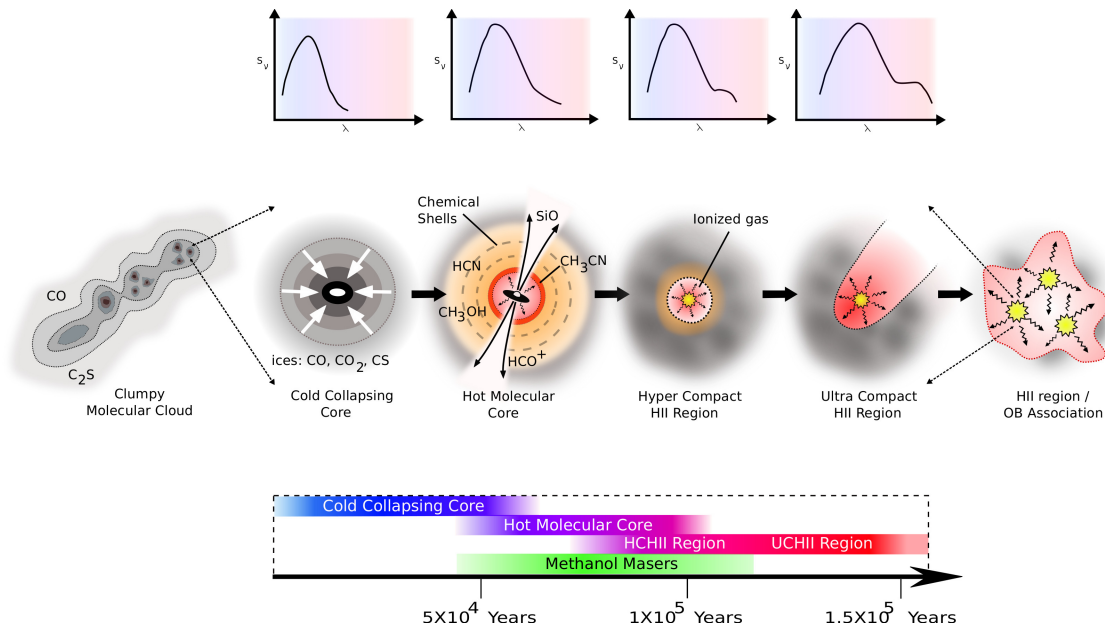


Figure 2.1: Illustration of the evolutionary scenario of massive stars. Cartoon taken from Cormac Purcell's web page.

The timescales for each phase are uncertain, as are the times at which the CH_3OH masers turn on and off.

2.2 Structure of Methanol

The methanol molecule is an asymmetric top because the hydroxyl axis is slightly inclined relative to the three-fold symmetry axis of the methyl (CH_3) group (see Figure 2.2). Methanol consists of six atoms ($N=6$) which corresponds to a $3N - 6 = 12$ vibrational modes. However, for maser studies, only one of these twelve vibrational modes will be considered, the lowest energy mode, i.e., the torsion of the OH bond around the axis of the tetrahedron defined by the CH_3 group, which is excited at an energy of 300 K above the ground state (Cragg et al. 2005). This torsional motion is a form of rotation and is also known as hindered internal rotation because as the hydrogen of the hydroxyl group rotates around the symmetry axis of the

methyl group, it will encounter potential barriers that “hinder” its motion when it passes over the hydrogen atoms of the methyl group. However, the hydrogen may overcome these potential barriers through the quantum-mechanical tunneling effect (Lin and Swalen 1959).

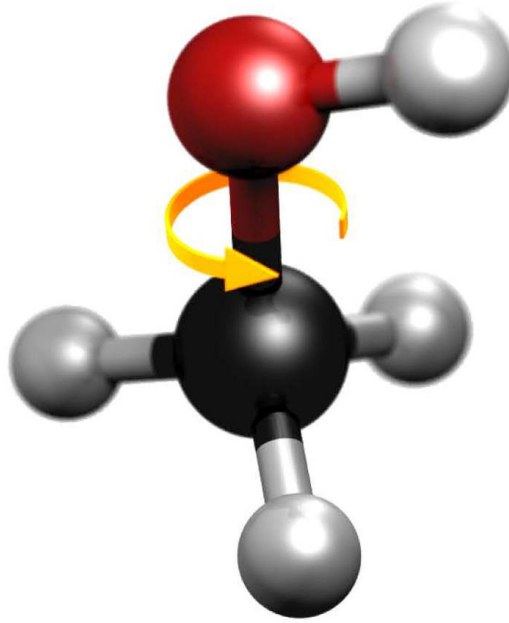


Figure 2.2: Methanol molecule structure. The gray spheres represent the hydrogen atoms, the red and the black spheres indicate oxygen and carbon atoms, respectively. The yellow arrow symbolizes the internal rotation of the OH group around the CH₃ group.

The tunnelling splits each torsional level into two sublevels of different symmetry, the non-degenerate A-type and the doubly degenerate E-type, which differ in the alignment of the nuclear spins in the hydrogen atoms of the CH₃ group. In A-type methanol, the proton spins are parallel (total nuclear spin quantum number $I = \frac{3}{2}$) while in the E-type, one of the proton spins is anti-parallel ($I = \frac{1}{2}$). The A and E species are often referred to by the quantum number σ : 0 corresponds to A, and ± 1 to E. The energy levels are labeled by the notation J_K . J is the angular momentum and K is the projection of J onto the axis of the tetrahedron.

2.2.1 A-type Methanol

The A species has a non-negative K between $0 \leq K \leq J$ and for $K > 0$, the levels are split into K-doublets due to the molecular asymmetry and are labeled as A^+ and A^- (Lees and Baker 1968). There is no K -doubling for $K = 0$; this can be seen in the energy level diagram presented in Figure 2.3 and more clearly in Figure 2.8, the ladder with $K = 0$ is always of the form A^+ . The selection rules for A-methanol are,

$$\begin{aligned} \Delta J = 0 \quad \Delta K = 0, \pm 1 \quad \pm \leftrightarrow \mp \\ \Delta J = \pm 1 \quad \Delta K = 0, \pm 1 \quad \mp \leftrightarrow \pm, \end{aligned} \tag{2.1}$$

given in Kalenskii and Kurtz (2016). Figure 2.3 shows the energy levels of A methanol with $J \leq 10$. The ladders with ground levels $J = 0$ and $K = 0$ are called the backbone ladders, and other ladders are called

side ladders. The backbone ladder is always of the form A^+ while the side ladders can have either, A^+ or A^- .

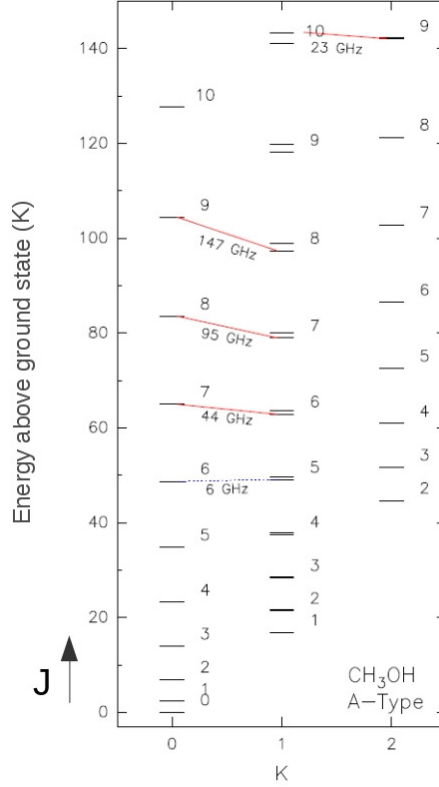


Figure 2.3: Energy level scheme for the A torsional species of methanol. Class I maser transitions are connected by red lines with frequencies indicated; blue dotted lines represent anti-inverted transitions. Figure from Leurini et al. (2016).

2.2.2 E-type Methanol

E-type methanol has two exactly degenerate forms, E_1 and E_2 , corresponding to the direction of rotation of the methyl group (Lees and Baker 1968). In this case the quantum number K can take negative values, usually denoted by a k that can take values between $-J \leq k \leq J$. The E_1 $k \geq 0$ is degenerate with E_2 $k \leq 0$. The selection rules for E-methanol are

$$\begin{aligned} \Delta J &= 0 & \Delta K &= \pm 1 \\ \Delta J &= \pm 1 & \Delta K &= 0, \pm 1, \end{aligned} \tag{2.2}$$

given in Kalenskii and Kurtz (2016) as well. Figure 2.4 shows the energy levels of E methanol with $J \leq 15$. In this case, the ladder with the ground level $J = 1$ and $k = -1$ is the backbone ladder.

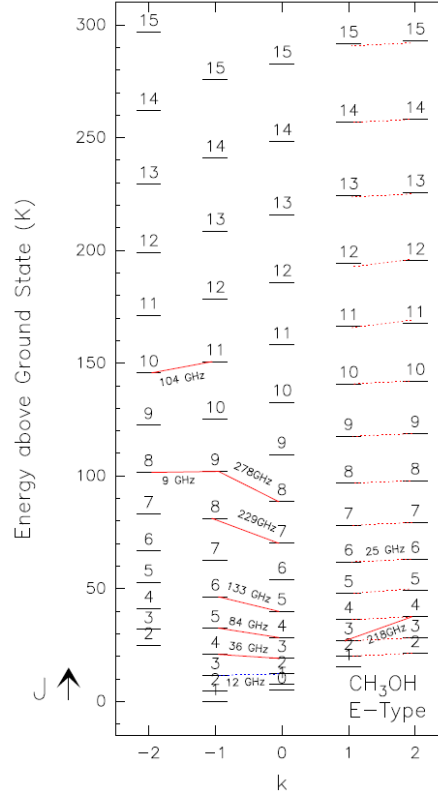


Figure 2.4: Energy level diagram for the E torsional species of methanol. Class I maser transitions are connected by red lines with frequencies indicated; blue dotted lines represent anti-inverted transitions. The $J_2 \rightarrow J_1$ E series near 25 GHz are indicated by the dotted red lines. Figure from Leurini et al. (2016).

2.3 Methanol Masers in Star-Forming Regions

As mentioned in Section 1.1, the first detection of strong maser emission from interstellar methanol was reported by Barrett et al. (1971) toward the Orion-KL region in the line series of $J_{k=2} \rightarrow J_{k=1}$ with $J = 4$ to 8 of the E species at a frequency of approximately 25 GHz. It took 14 years before Wilson et al. (1984, 1985) discovered methanol maser emission in other transitions. They observed several Galactic star-forming regions in the 23.1 and 19.9 GHz lines corresponding to the transitions $9_2 \rightarrow 10_1 A^+$ and $2_1 \rightarrow 3_0 E$, respectively. Two further transitions were discovered shortly afterwards in the 36 GHz $4_{-1} \rightarrow 3_0 E$ and the 44 GHz $7_0 \rightarrow 6_1 A^+$ transitions by Morimoto et al. (1985) toward four Galactic sources, all of them regions hosting high-mass star formation. Later, Batrla et al. (1987) discovered methanol masers in the 12 GHz $2_0 \rightarrow 3_{-1} E$ transition toward several Galactic HII regions.

Based on the results from observations of various methanol maser lines, Batrla et al. (1987) classified methanol masers in two categories that were initially labelled Class A and B. This nomenclature was later replaced by Menten (1991a) as Class I and II to avoid confusion with the A and E symmetry species of CH_3OH . The classification was based on several factors, including the association with other astronomical sources, which transitions were present or absent (or seen in emission or absorption), and the complexity of the spectral features and their similarity to spectra of other maser species (Haschick et al. 1989; Plambeck and Menten 1990). In the following sections we will discuss in more detail the Class I and Class II methanol

maser classification.

Interstellar methanol masers are one of the best signpost of young high-mass star-forming regions. In particular, the 6.6 GHz transition of methanol has been found to be a useful signpost as it appears only associated to massive star formation regions. At present remains somewhat uncertain the position of the different maser species in an evolutionary sequence of star formation. Ellingsen et al. (2007) presented masers and UCHII regions as an evolutionary clock that was later refined by Breen et al. (2010). They suggested (see Figure 2.5) an evolutionary scheme in which during process of high-mass star formation, the Class I CH₃OH masers may be the first maser species to turn on (pumped by collisions from protostellar outflows), then Class II CH₃OH masers (radiatively pumped by photons emitted by warm dust), then H₂O masers (associated with outflows), and finally OH masers (pumped by far infrared photons), and UCHII regions. Some stages can be overlapped. Ellingsen et al. (2007) note that there are sources known to be inconsistent with this sequence.

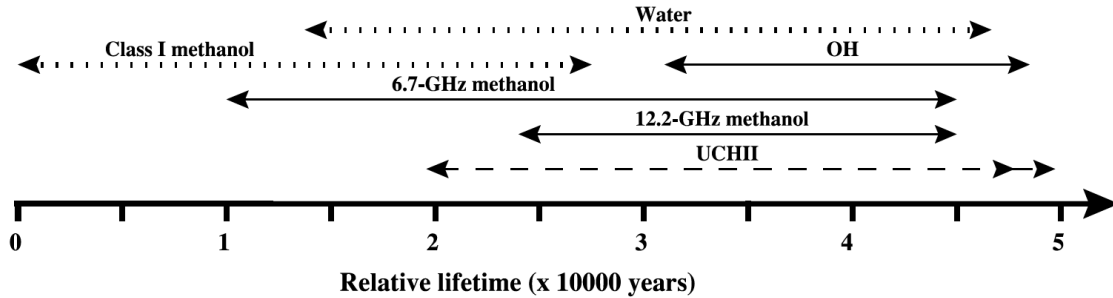


Figure 2.5: Evolutionary sequence for masers associated with massive star-forming regions. The double arrow indicated UCHII exist beyond the boundary of the plot. From Breen et al. (2010) using data from references therein.

2.3.1 Class I CH₃OH Masers

Transitions

Thirty years ago, only three Class I methanol maser transitions have been reported in the literature, the ones at 25, 36 and 44 GHz presented above. Thereafter, the number of methanol transitions detected in maser emission increased rapidly. The transitions list continued with the $5_{-1} \rightarrow 4_0 E$ at 84.5 GHz discovered towards DR21(OH) by Batrla and Menten (1988), and the 95.1 GHz line in the $8_0 \rightarrow 7_1 A^+$ transition, found in Orion KL by Plambeck and Wright (1988). Table 2.1 shows all the Class I transitions reported to date and their corresponding frequencies and references as presented by Leurini et al. (2016).

Table 2.1: Class I methanol maser lines detected in star-forming regions to date.

Transition	Frequency (MHz)	Discovery Reference
$9_{-1} \rightarrow 8_{-2} E$	9 936	Slysh et al. (1993)
$10_1 \rightarrow 9_2 A^-$	23 445	Voronkov et al. (2011)
$3_2 \rightarrow 3_1 E$	24 929	Menten et al. (1986)
$4_2 \rightarrow 4_1 E$	24 933	Barrett et al. (1971)

$2_2 \rightarrow 2_1E$	24 934	Buxton et al. (1977)
$5_2 \rightarrow 5_1E$	24 959	Barrett et al. (1971)
$6_2 \rightarrow 6_1E$	25 018	Barrett et al. (1971)
$7_2 \rightarrow 7_1E$	25 125	Barrett et al. (1971)
$8_2 \rightarrow 8_1E$	25 294	Barrett et al. (1971)
$9_2 \rightarrow 9_1E$	25 541	Menten et al. (1986)
$12_2 \rightarrow 12_1E$	26 847	Wilson et al. (1996)
$13_2 \rightarrow 13_1E$	27 473	Wilson et al. (1996)
$14_2 \rightarrow 14_1E$	28 169	Wilson et al. (1996)
$15_2 \rightarrow 15_1E$	28 906	Wilson et al. (1996)
$16_2 \rightarrow 16_1E$	29 637	Wilson et al. (1996)
$17_2 \rightarrow 17_1E$	30 308	Wilson et al. (1996)
$4_{-1} \rightarrow 3_0E$	36 169	Morimoto et al. (1985)
$7_0 \rightarrow 6_1A^+$	44 069	Morimoto et al. (1985)
$5_{-1} \rightarrow 4_0E$	84 521	Batrla and Menten (1988)
$8_0 \rightarrow 7_1A^+$	95 169	Nakano and Yoshida (1986)
$11_{-1} \rightarrow 10_{-2}E$	104 300	Slysh et al. (2002)
$6_{-1} \rightarrow 5_0E$	132 891	Slysh et al. (1997)
$9_0 \rightarrow 8_1A^+$	146 618	Cragg et al. (1992)
$4_2 \rightarrow 3_1E$	218 440	Hunter et al. (2014)
$8_{-1} \rightarrow 7_0E$	229 758	Slysh et al. (2002)
$9_{-1} \rightarrow 8_0E$	278 305	Yanagida et al. (2014)

The transition $7_0 \rightarrow 6_1$ at 44 GHz is typically the strongest of all known Class I transitions.

Locations

The original classification established that Class I masers were frequently offset by one or two parsec from other star formation signposts such as HII regions, strong infrared sources and OH and H₂O masers. These arguments were based predominantly on the low spatial resolution observations that were available at that time (Haschick et al. 1989, Menten and Batrla 1989, Bachiller et al. 1990). Plambeck and Menten (1990) proposed that Class I masers arise in molecular gas shocked by outflows (see Figure 2.6). This hypothesis has been supported by recent interferometric observations that found spatial coincidence between Class I methanol masers and emission at 4.5 μm (Cyganowski et al. 2009) which is dominated by indicators of shocked gas such as the H₂ lines and the CO fundamental bands (De Buizer & Vacca 2010). Sources with extended emission at 4.5 μm were denominated as extended green objects (EGOs) by Cyganowski et al. (2009) since they appear in color green according to the standard coding of three-color images (3.6 μm = blue; 4.5 μm = green; 8 μm = red). Although the exact nature of EGOs is still uncertain, it is likely that they arise in shocks where protostellar outflows collide with the ambient gas.

Class I methanol masers does not seem to be exclusive to massive stars since weak masers have been detected toward four star-forming regions associated with low-mass protostars (Kalenskii et al. 2006). They are probably associated with the red and blue-shifted wings of the bipolar outflows from the low-mass objects.

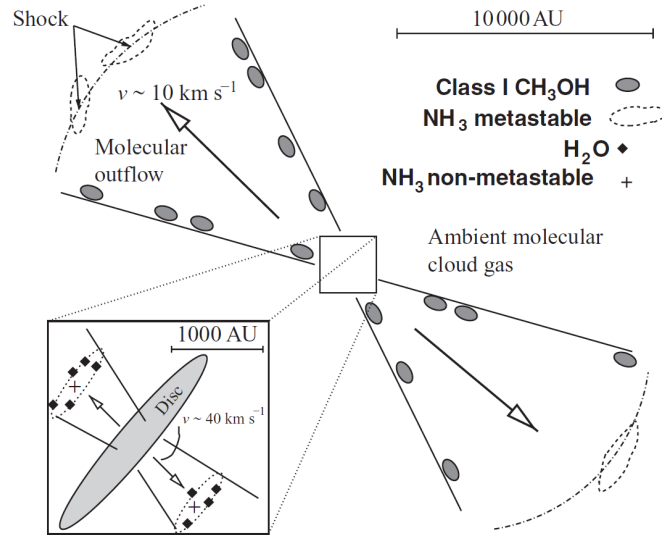


Figure 2.6: Sketch of a molecular outflow and the positions of various maser species. The Class I methanol masers are located at the interface where the outflow interacts with the molecular gas in its vicinity. Figure from Gray (2012).

Spectral Aspect

Class I methanol masers show simple spectra compared to other species such as water masers, which have numerous velocity components spread over several km s^{-1} (Genzel and Downes 1977). Instead, all Class I masers are confined to velocity intervals less than 1 km s^{-1} with line widths of a few tenths of km s^{-1} and centered close to the systemic velocity of the region in question. Figure 2.7 shows various Class I maser transitions toward several star-forming regions, taken with different velocity resolutions and a number of telescopes.

Excitation of Class I Methanol Masers

The pumping scheme for Class I masers is that methanol molecules are excited by collisions with H_2 to high energy states followed by fast spontaneous radiative decay that tends to overpopulate the backbone ladders corresponding to each methanol species (Lees 1973). For example, in A-type methanol:

1. CH_3OH molecules are collisionally excited to high J_K states, the molecules will rapidly decay from all other K levels to the $K = 0$ ladder (the backbone ladder). This is shown in Figure 2.8, where the arrows denote that the fastest spontaneous transitions are directed to the backbone ladder.
2. Therefore, an excited molecule after one or several spontaneous transitions, arrives at the backbone ladder, resulting in an overpopulation of the lower energy levels of the backbone ladder with respect to those in adjacent ladders. This is possible because $\Delta K = 0$ collisions are strongly preferred and radiative transitions out of the $K = 0$ ladder are slower than those down the backbone ladder ($J_0 \rightarrow (J - 1)_0$).

This property of methanol excitation is responsible for inversion in most of the A-type Class I methanol masers (e.g. $7_0 \rightarrow 6_1A^+$, $8_0 \rightarrow 7_1A^+$, and $9_0 \rightarrow 8_1A^+$ transitions at 44, 95, and 146 GHz). The same

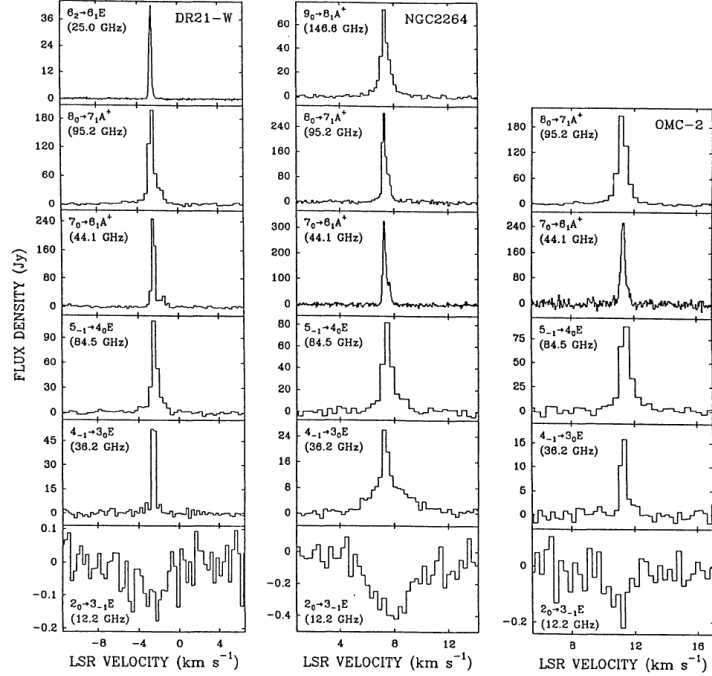


Figure 2.7: Various Class I maser transitions toward the star-forming regions: DR21-W, NGC2264 and OMC-2. The data were taken with different spectral resolutions and a number of telescopes. The lowest spectrum in all sources shows absorption in the $\text{CH}_3\text{OH } 2_0 \rightarrow 3_{-1} E$ line. Figure from Menten (1991a).

mechanism explains the E-type masers with the difference that the overpopulation occurs in the $k = -1$ ladder (except for the $J_2 \rightarrow J_1$ line series near 25 GHz).

2.3.2 Class II CH_3OH Masers

Transitions

The discovery of the strong and widespread Class II methanol maser transition $2_0 \rightarrow 3_1 E$ was made by Batrla et al. (1987). A few years after, Menten (1991b) reported even stronger emission from the methanol transition $5_1 \rightarrow 6_0 A^+$ at 6.6 GHz. Menten (1991b) noted that all of the detected 6.6 GHz sources had 12.1 GHz counterparts and therefore suggested that this new transition belonged to the Class II maser group. The 6.6 and 12.1 GHz transitions are the most common and strong transitions detected at early evolutionary stages of high-mass star formation (Ellingsen 2006). Table 2.2 shows a list of the Class II methanol maser transitions reported to date.

Table 2.2: Class II methanol maser lines detected in star-forming regions to date.

Transition	Frequency (MHz)	Discovery Reference
$5_1 \rightarrow 6_0 A^+$	6 668	Menten (1991b)
$2_0 \rightarrow 3_{-1} E$	12 178	Batrla et al. (1987)
$2_1 \rightarrow 3_0 E$	19 967	Wilson et al. (1985)

$9_2 \rightarrow 10_1 A^+$	23 121	Wilson et al. (1984)
$8_2 \rightarrow 9_1 A^-$	28 970	Wilson et al. (1993)
$7_{-2} \rightarrow 8_{-1} E$	37 703	Haschick et al. (1989)
$6_2 \rightarrow 5_3 A^-$	38 293	Haschick et al. (1989)
$6_2 \rightarrow 5_3 A^+$	38 452	Haschick et al. (1989)
$6_{-2} \rightarrow 7_{-1} E$	85 568	Cragg et al. (2001)
$7_2 \rightarrow 6_3 A^-$	86 615	Cragg et al. (2001)
$7_2 \rightarrow 6_3 A^+$	86 902	Cragg et al. (2001)
$3_1 \rightarrow 4_0 A^+$	107 013	Val'tts et al. (1995)
$0_0 \rightarrow 1_{-1} E$	108 893	Val'tts et al. (1999)
$15_0 \rightarrow 15_{-1} E$	148 100	Salii and Sobolev (2006)
$8_0 \rightarrow 8_{-1} E$	156 488	Slysh et al. (1995)
$2_1 \rightarrow 3_0 A^+$	156 602	Slysh et al. (1995)
$7_0 \rightarrow 7_{-1} E$	156 828	Slysh et al. (1995)
$6_0 \rightarrow 6_{-1} E$	157 048	Slysh et al. (1995)
$5_0 \rightarrow 5_{-1} E$	157 178	Slysh et al. (1995)
$4_0 \rightarrow 4_{-1} E$	157 246	Slysh et al. (1995)
$1_0 \rightarrow 1_{-1} E$	157 270	Slysh et al. (1995)
$3_0 \rightarrow 3_{-1} E$	157 272	Slysh et al. (1995)
$2_0 \rightarrow 2_{-1} E$	157 276	Slysh et al. (1995)
$10_2 \rightarrow 9_3 A^-$	231 281	Salii and Sobolev (2006)
$10_2 \rightarrow 9_3 A^+$	232 418	Salii and Sobolev (2006)

Locations

Class II methanol masers are closely associated with young high-mass (proto)stellar objects and arise from the same regions of hot molecular cores as hydroxyl masers and are pumped by far-infrared radiation in dense ($n \sim 10^7 \text{ cm}^{-3}$), warm ($T \sim 150 \text{ K}$) gas. Unlike Class I masers, Class II masers are exclusively associated with high-mass star formation regions since observations for 6.6 GHz methanol masers towards low-mass stars have failed to discover any luminous emission (Minier et al. 2003; Xu et al. 2008).

Spectral Aspect

The Class II CH_3OH masers often have quite complex spectral morphology, with many components covering a wide velocity range, similar to H_2O and OH masers (see Figure 2.9). Although the Class II CH_3OH masers observed in the same location typically cover the same velocity range, they are not as similar as the Class I masers.

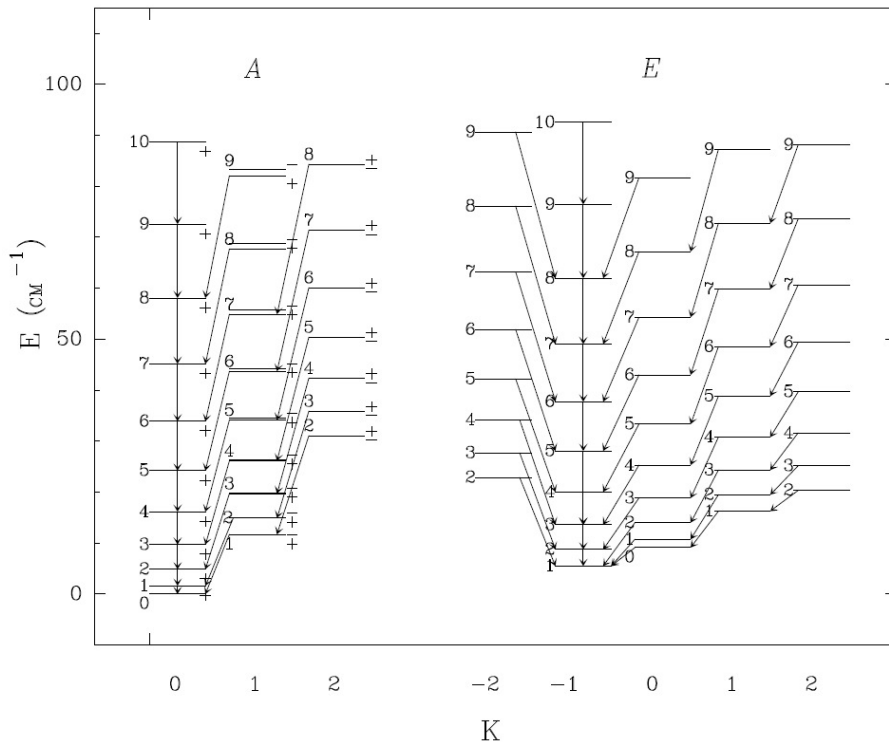


Figure 2.8: Energy levels of A and E methanol. The arrows show the fastest spontaneous transitions that tend to overpopulate the lower levels of the backbone ladder corresponding to each methanol species. Figure from Kalenskii and Kurtz (2016).

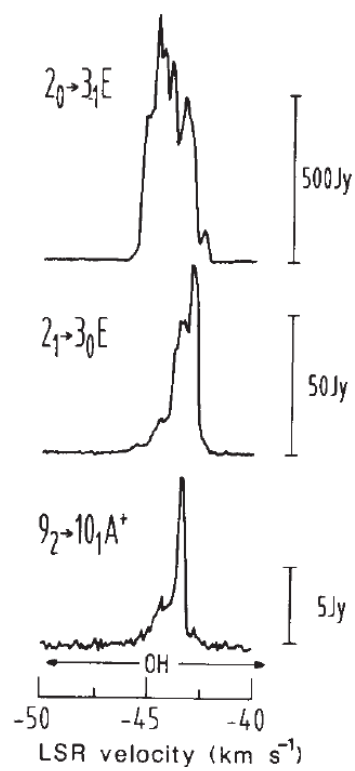


Figure 2.9: Various Class II maser transitions observed toward the star-forming region W3(OH). The emission covers the same velocity interval and it is comparable to the velocity range covered by the OH masers. Figure from Batrla et al. (1987).

Chapter 3

A Catalog of 44 GHz Methanol Masers in Massive Star-Forming Regions. IV. The High-mass Protostellar Object Sample

We present a survey of 56 massive star-forming regions in the 44 GHz methanol maser transition made with the Karl G. Jansky Very Large Array (VLA); 24 of the 56 fields showed maser emission. The data allow us to demonstrate associations, at arcsecond precision, of the Class I maser emission with outflows, HII regions, and shocks traced by 4.5 micron emission. We find a total of 83 maser components with linewidths ranging from 0.17 to 3.3 km s⁻¹ with a nearly flat distribution and a median value of 1.1 km s⁻¹. The relative velocities of the masers with respect to the systemic velocity of the host clouds range from -2.5 to 3.1 km s⁻¹ with a distribution peaking near zero. We also study the correlation between the masers and the so-called extended green objects (EGOs) from the GLIMPSE survey. Multiple sources in each field are revealed from IR images as well as from centimeter continuum emission from VLA archival data; in the majority of cases the 44 GHz masers are positionally correlated with EGOs which seem to trace the younger sources in the fields. We report a possible instance of a 44 GHz maser associated with a low-mass protostar. If confirmed, this region will be the fifth known star-forming region that hosts Class I masers associated with low-mass protostars. We discuss three plausible cases of maser variability.

3.1 Introduction

A number of surveys have been made to search for Class I methanol masers. The majority of these were made with single-dish telescopes and mainly at the 44 and 95 GHz transitions (northern hemisphere: Morimoto et al. 1985; Bachiller et al. 1990; Haschick et al. 1990; Kalenskii et al. 1992; Fontani et al. 2010; Gan et al. 2013; Yang et al. 2017; southern hemisphere: Slysh et al. 1994; Val'tts et al. 2000; Ellingsen et al. 2005; Chen et al. 2011). To establish the environments where these masers are excited and their relation to other star formation tracers on arcsecond scales, higher resolution, interferometric surveys are required, but only a few have been carried out to date (northern hemisphere: Kurtz et al. 2004; Cyganowski et al. 2009; Gómez-Ruiz et al. 2016; McEwen et al. 2016; southern hemisphere: Voronkov et al. 2014; Jordan et al. 2015).

A series of papers has been devoted to VLA studies of 44 GHz Class I masers in high-mass star-forming regions: Kurtz et al. (2004; Survey I), Gómez et al. (2010; Survey II) and Gómez-Ruiz et al. (2016; Survey III). Survey I reports the observations of a heterogenous sample of 44 massive star-forming regions

spanning from young protostars to compact and ultracompact HII (UCHII) regions. Three of the sources in Survey I could not be imaged and so were re-observed in Survey II to complete the previous survey and provide accurate positions and line parameters. Survey III studied a sub-sample of 69 YSOs selected from the catalog of Molinari et al. (1996). The Survey III contains candidates of high-mass protostellar objects along with more-evolved sources that have already formed UCHII regions; approximately half of these sources show outflow activity (Zhang et al 2001; 2005).

The present survey (Survey IV) covers the sample of high-mass protostellar objects (HMPOs) reported by Sridharan et al. (2002; hereafter S02). In this chapter, we present the data of a 44 GHz VLA survey of Class I methanol masers toward 56 sources of the S02 sample.

In Section 3.2, we describe the sample selection criteria. In Section 3.3, we describe the observational program and data reduction. In Section 3.4, we present the results of the survey in tabular form and provide mid-IR and centimeter continuum images. In Section 3.5, we give a brief discussion and in Section 3.6 we give the conclusions.

3.2 The sample

The sources observed in the present survey were taken from the sample of 69 HMPOs developed by S02. S02 selected sources north of -20° declination from the IRAS Point Source Catalog (PSC) using four selection criteria: 1) they satisfy the Wood & Churchwell (1989) infrared color-color criteria for UCHII regions, 2) they are bright at FIR wavelengths ($S_{60} > 90$ Jy, $S_{100} > 500$ Jy), 3) undetected in single-dish radio continuum surveys at 5 GHz to a limit of 25 mJy and 4) detected in the single-dish CS(2–1) survey of Bronfman, Nyman, & May (1996). The first two criteria favor the selection of massive embedded objects. The third criterion favors young isolated HMPO; i.e., either objects prior to the formation of UCHII regions (which have not yet ionized their surroundings) and/or without more-evolved objects (UCHII regions) in the immediate vicinity. The presence of CS emission indicates that the objects are likely to be embedded within molecular cores.

In a series of papers, Sridharan, Beuther and collaborators (S02, Beuther et al. 2002a, 2002b, 2002c) systematically studied these 69 HMPOs. They characterize the whole sample from mid-IR to centimeter wavelengths; searching for molecular outflows, massive dust cores, ionized gas and maser emission with the aid of single-dish and interferometric observations.

Multiple dust cores with a variety of morphologies were detected in essentially all of the 69 sources through single-dish observations at 1.2 mm (S02, Beuther et al. 2002a). These millimeter peaks are typically offset by several arcseconds from the IRAS position. The brightest core in each field typically has a mass on the order of $10^2 - 10^3 M_\odot$; the H_2 column densities are typically a few times 10^{23} cm^{-2} , which corresponds to a few hundred magnitudes of visual extinction; average gas densities are around 10^5 cm^{-3} .

Dense gas in these regions was detected toward 40 of the 69 sources by single-dish and interferometric observations of the NH_3 (1,1) and (2,2) inversion lines (S02; Lu et al. 2014). The average rotation temperature and deconvolved linewidth are 18 K and 1.1 km s^{-1} , respectively (Lu et al. 2014). Three morphology types were identified: filamentary, centrally-peaked and diffuse. The ammonia emission coincides with the dust continuum emission peaks at 1.2 mm reported by Beuther et al. (2002a).

Eighty-five percent of the sample shows evidence of massive and energetic bipolar outflows with parsec-scale sizes based on single-dish observations of the CO (2–1) line (S02, Beuther et al. 2002b). In most cases, the outflows are centered on the mm peaks, which likely harbor the most massive and youngest proto-stars.

In spite of the non-detection in single-dish centimeter continuum surveys at a level of 25 mJy (Gregory & Condon 1991; Griffith et al. 1994; Wright et al. 1994), more sensitive interferometric studies revealed such emission in 40 of the 69 sources at a detection limit of 1 mJy (S02). No free-free emission above 1

mJy was found in the remaining 29 sources (S02). However, deeper VLA observations toward 20 of the 29 non-detections found thermal free-free emission at the μJy level ($\sim 3 - 50 \mu\text{Jy}$) in all sources (Zapata et al. 2006; Rosero et al. 2016). Thus, 60 of the 69 sources have centimeter continuum emission.

Maser emission is also associated with these objects. The single-dish studies of S02 revealed 26 fields with 6.6 GHz Class II CH_3OH masers and 29 fields with H_2O masers; Beuther et al. (2002c) report interferometric positions for some of these. OH masers are also associated with only three sources of the sample (Forster et al. 1999; Argon et al. 2000).

A summary of these various star-formation indicators is given in Table 3.1 for those sources with 44 GHz maser detections.

Table 3.1: Characteristic parameters of the 24 HMPOs associated with 44 GHz methanol masers.

IRAS	CH_3OH	H_2O	OH	CO	Radio (3.6 cm; Figure 3.5) ^a		$T_{\text{rot}}(\text{NH}_3)$
					σ ($\mu\text{Jy beam}^{-1}$)	Contours	
Name	6.6 GHz	22 GHz	1665 MHz	Outflow/Wings			(K)
05358+3543	162	45	1.72 ^b	+	18
18089-1732	54	75	4.16 ^b	+	40 ^c	-4, 4, 6, 8, 10	38
18102-1800	8.8	+	77 ^d	-3, 3, 6, 9	15
18151-1208	50	0.8	...	+	6 ^e	-2, 3, 9, 15, 25	17
18182-1433	24	18	2.2 ^f	+	40 ^c	-4, 4, 6, 8, 10	20
18247-1147	1.6	+	500 ^g	-3, 3, 15, 30, 60	...
18264-1152	3.8	50	...	+	40 ^c	-4, 4, 6, 8	18
18290-0924	15.1	4	...	+	70 ^g	-3, 3, 4, 5, 6	20
18306-0835	...	0.7	...	+	520 ^g	-3, 3, 9, 15, 30, 45	...
18308-0841	...	1.5	...	+	45 ^c	-5, 5, 10, 20, 30, 60, 90	18
18310-0825	12 ^h	+	70	-4, 4, 8, 12, 16	18
18337-0743	-	7 ^e	-2, 3, 5, 9, 12	17
18345-0641	5.4	3	...	+	7 ^e	-1.2, 3, 5, 6.5	16
18488+0000	16.9	1	...	+	170 ^d	-4, 4, 8, 12	20
18517+0437	279	45.3	...	+	4.5 ^e	-2, 3, 5, 7, 11	8-31 ⁱ
18521+0134	1.3	-	5 ^e	-2, 3, 7, 9, 12	8-37 ⁱ
18530+0215	+	330	-4, 4, 12, 20, 30, 40, 50	16
18553+0414	...	50	...	+	4.5 ^e	-1.5, 3, 9, 21, 31	8-27 ⁱ
18566+0408	7.2	3	...	+	4 ^e	-2, 3, 5, 7, 9, 13, 20, 29	15
20126+4104	36	15	...	+	16 ^j	-3, 3, 5, 6, 7	23
20293+3952	...	100	...	+	70	-3, 3, 4, 5, 6	15
23033+5951	...	4	...	+	60	-4, 5, 6, 7, 8, 9	20
23139+5939	2.6	400	...	+	60	-4, 5, 6, 7, 8, 9, 10	8-31 ⁱ
23151+5912	...	60	...	+

Notes.

The numbers in columns 2, 3, and 4 are the maser peak flux densities in units of Jansky. Except when indicated, the maser fluxes, outflow detections, 3.6 cm emission and rotational temperatures are taken from S02. The plus and minus signs are detections and nondetections, respectively.

^aThe parameters reported here correspond to the rms and contour levels (in multiples of the rms) from Figure 3.5.

^bArgon et al. (2000).

^cC-configuration VLA archival observations from Zapata et al. (2006).

^dWe applied the UVTAPER parameter with a value of 100 k λ .

^eA-configuration VLA archival observations made at 6 cm from Rosero et al. (2016).

^fForster et al. (1999).

^gWe applied the UVTAPER parameter with a value of 80 k λ .

^hSzymczak et al. (2000).

ⁱLu et al. (2014).

^jB-configuration VLA archival data from Hofner et al. (1999).

3.3 Observations and Data Reduction

The observations were made with the NRAO¹ VLA in D configuration (project code AK0699) during seven observing runs on 2008 August 26 and 31, and 2008 September 05, 07, 08, 12 and 14. A summary of the flux and phase calibrators used in each observing period is given in Table 3.2. The observations on September 12 were divided in time ranges separated by about an hour. The first time range suffered from poor weather conditions; this is reflected in the large channel map rms reported in Table 3.3. Ten sources were observed in this group and no masers were detected in any of them.

¹The National Radio Astronomy Observatory (NRAO) is operated by Associated Universities, Inc., under a cooperative agreement with National Science Foundation.

The data were observed in Q band (0.7 cm) using the dual IF mode and the fast-switching method. One IF was centered on the methanol maser transition ($7_0 \rightarrow 6_1 A^+$) with a rest frequency of 44069.43 MHz. A 3.125 MHz bandwidth was used, divided in 127 channels of 24.4 kHz each, providing a spectral resolution of 0.16 km s^{-1} and a velocity coverage of 21 km s^{-1} .

Table 3.2: Observational Programm Summary

Observation Date	Phase Calibrator	Flux Density (Jy)	Calibrator ^a Code	Sources Calibrated
2008 Aug 26	J0555+398	2.06 ± 0.06	A	05358+3543, 05490+2658
	J0539+145	0.34 ± 0.01	A	05553+1631
2008 Aug 31	J1733-130	4.42 ± 0.15	B	18089-1732, 18090-1832, 18102-1800, 18151-1208, 18159-1550, 18182-1433 18223-1243
2008 Sep 05	J2015+371	3.10 ± 0.08	C	20051+3435, 20126+4104, 20205+3948
	J2023+318	1.04 ± 0.02	A	20081+2720
	J2007+404	1.74 ± 0.04	B	20216+4107, 20293+3952, 20319+3958, 20332+4124, 20343+4129
2008 Sep 07	J1832-105	0.57 ± 0.01	C	18247-1147, 18264-1152, 18272-1217, 18290-0924, 18306-0835, 18308-0841
2008 Sep 08	J1832-105	0.59 ± 0.01	C	18310-0825, 18337-0743, 18345-0641, 18348-0616, 18372-0541
2008 Sep 12	J2022+616	1.02 ± 0.04	B	22134+5834
	J0014+612	0.52 ± 0.02	C	22551+6221, 22570+5912, 23033+5951, 23139+5939, 23151+5912, 23545+6508
2008 Sep 12 ^b	J1851+005	0.90 ± 0.05	C	18385-0512, 18426-0204, 18431-0312, 18437-0216, 18440-0148, 18445-0222, 18447-0229, 18454-0158, 18454-0136, 18460-0307
2008 Sep 14	J1851+005	0.81 ± 0.01	C	18470-0044, 18472-0022, 18488+0000, 18517+0437, 18521+0134, 18530+0215, 18540+0220, 18553+0414, 18566+0408

Notes.

^aThe codes A, B, y C correspond to the positional accuracy of $< 0''.002$, $0''.002-0''.01$, y $0''.01-0''.15$, respectively.

^bObserving run with a large channel map rms and no maser detection (see Table 3.3).

We performed a standard calibration with the AIPS software package. We used channel-0 data (comprised of the central 75% of the bandpass) to calibrate the complex instrumental gain of each antenna and the results were copied to the line data set. The flag and calibration tables were applied to the line data and then individual sources were imaged. No bandpass calibration was performed. At the time of the observations, Doppler tracking was not supported owing to the VLA to EVLA conversion; Doppler corrections were made with the CVEL task.

For each field we made a dirty data cube to identify the channel of the brightest maser component. We made a clean image of this peak channel, setting a clean box around the maser emission. If the signal-to-noise ratio was high enough, the cleaned channel was used as a model to self-calibrate the data. A first iteration was performed in phase with short solution intervals. When appropriate, we did a second iteration in amplitude and phase with longer solution intervals. Finally, we made a clean data cube setting boxes around all the maser components identified. In this step we fixed the parameter FLUX to clean to a 5σ level, where σ is the theoretical noise for each field.

Table 3.3 shows the general information of each field. We list the associated IRAS source name, the

pointing center in J2000 coordinates, the central velocity of the bandpass (set to the systemic velocity reported by S02), and the synthesized beam size of the image. The 1σ rms noise is given in column 7; it was obtained from the central portion of the final data cube, but excluding channels with maser emission. In the last column, we report the number of maser components detected.

Table 3.3: Observed Source List

Source IRAS Name	J 2000 Pointing Center		Central Velocity km s ⁻¹	Synthesized Beam		Channle Map rms mJy beam ⁻¹	Maser Detection
	α (h m s)	δ ($^{\circ}$ ' ")		(arcsec)	(deg)		
05358+3543	05 39 10.4	+35 45 19	-17.6	1.69×1.48	-57.0	39	3
05490+2658	05 52 12.9	+26 59 33	+0.8	1.57×1.43	-83.5	51	0
05553+1631	05 58 13.9	+16 32 00	+5.7	1.67×1.48	-49.9	51	0
18089-1732	18 11 51.3	-17 31 29	+33.8	2.16×1.35	-4.1	76	7
18090-1832	18 12 01.9	-18 31 56	+109.8	2.21×1.33	-0.3	79	0
18102-1800	18 13 12.2	-17 59 35	+21.1	2.27×1.35	+2.1	85	6
18151-1208	18 17 57.1	-12 07 22	+32.8	2.05×1.42	+1.9	66	4 ^a
18159-1550	18 18 47.3	-15 48 58	+59.9	2.25×1.43	+3.9	66	0
18182-1433	18 21 07.9	-14 31 53	+59.1	2.18×1.47	+2.2	69	4
18223-1243	18 25 10.9	-12 42 17	+45.5	2.12×1.45	+7.9	78	0
18247-1147	18 27 31.1	-11 45 56	+121.7	2.14×1.47	-4.9	43	1
18264-1152	18 29 14.3	-11 50 26	+43.6	2.13×1.47	-0.1	41	10
18272-1217	18 30 02.7	-12 15 27	+34.0	2.13×1.47	+3.9	44	0
18290-0924	18 31 44.8	-09 22 09	+84.3	2.08×1.56	-6.5	72	3
18306-0835	18 33 21.8	-08 33 38	+76.8	2.13×1.48	+14.2	36	3
18308-0841	18 33 31.9	-08 39 17	+77.1	2.05×1.51	+12.8	44	5
18310-0825	18 33 47.2	-08 23 35	+84.4	1.99×1.52	-10.8	45	1
18337-0743	18 36 29.0	-07 40 33	+57.9	1.95×1.53	-12.4	44	2
18345-0641	18 37 16.8	-06 38 32	+95.9	1.89×1.54	-10.4	41	8
18348-0616	18 37 29.0	-06 14 15	+109.5	1.87×1.52	-3.5	42	0
18372-0541	18 39 56.0	-05 38 49	+23.6	1.90×1.53	+1.0	50	0
18385-0512	18 41 12.0	-05 09 06	+26.0 ^{b,c}
18426-0204	18 45 12.8	-02 01 12	+15.0 ^{b,c}
18431-0312	18 45 46.9	-03 09 24	+105.2	1.77×1.34	+20.9	404	0 ^c
18437-0216	18 46 22.7	-02 13 24	+110.8	1.84×1.45	+29.6	191	0 ^c
18440-0148	18 46 36.3	-01 45 23	+97.6	1.87×1.52	+20.9	134	0 ^c
18445-0222	18 47 10.8	-02 19 06	+86.8	1.94×1.51	+29.2	113	0 ^c
18447-0229	18 47 23.7	-02 25 55	+102.6	1.97×1.51	+29.3	110	0 ^c
18454-0158	18 48 01.3	-01 54 49	+52.6	2.03×1.49	+35.4	112	0 ^c
18454-0136	18 48 03.7	-01 33 23	+38.9	1.98×1.52	+36.5	110	0 ^c
18460-0307	18 48 39.2	-03 03 53	+83.7	2.10×1.50	+36.9	105	0 ^c
18470-0044	18 49 36.7	-00 41 05	+96.5	1.75×1.49	+14.1	50	0
18472-0022	18 49 50.7	-00 19 09	+49.0	1.75×1.50	+19.0	48	0
18488+0000	18 51 24.8	+00 04 19	+82.7	1.76×1.50	+18.3	46	1
18517+0437	18 54 13.8	+04 41 32	+43.9	1.71×1.52	+17.6	48	2 ^d
18521+0134	18 54 40.8	+01 38 02	+76.0	1.76×1.52	+33.0	45	2
18530+0215	18 55 34.2	+02 19 08	+77.7	1.81×1.55	+21.7	46	2
18540+0220	18 56 35.6	+02 24 54	+49.6	1.83×1.55	+29.1	48	0
18553+0414	18 57 52.9	+04 18 06	+10.0	1.77×1.54	+37.5	50	1
18566+0408	18 59 09.9	+04 12 14	+85.2	1.70×1.53	+45.6	46	5
20051+3435	20 07 03.8	+34 44 35	+11.6	1.69×1.47	-72.3	43	0
20081+2720	20 10 11.5	+27 29 06	+5.7	1.83×1.54	-89.1	47	0
20126+4104	20 14 26.0	+41 13 32	-3.8	1.72×1.44	-67.4	77	5 ^{d,e}
20205+3948	20 22 21.9	+39 58 05	-1.7	1.73×1.42	-66.5	42	0
20216+4107	20 23 23.8	+41 17 40	-2.0	1.79×1.43	-72.3	43	0
20293+3952	20 31 10.7	+40 03 10	+6.3	1.80×1.43	-78.2	42	3

Table 3.3 – continue

Source IRAS Name	J 2000 Pointing Center α (h m s)	δ ($^{\circ}$ ' ")	Central Velocity km s $^{-1}$	Synthesized Beam (arcsec)	(deg)	Channel Map rms mJy beam $^{-1}$	Maser Detection
20319+3958	20 33 49.3	+40 08 45	+8.8	1.82 \times 1.42	−72.9	46	0
20332+4124	20 35 00.5	+41 34 48	−2.0	1.86 \times 1.42	−79.2	43	0
20343+4129	20 36 07.1	+41 40 01	+11.5	1.88 \times 1.43	−79.5	46	0
22134+5834	22 15 09.1	+58 49 09	−18.3	1.65 \times 1.28	−15.8	62	0
22551+6221	22 57 05.2	+62 37 44	−13.4	1.80 \times 1.26	−11.6	78	0
22570+5912	22 59 06.5	+59 28 28	−46.7	1.70 \times 1.29	−15.6	76	0
23033+5951	23 05 25.7	+60 08 08	−53.1	1.74 \times 1.28	−19.3	78	2
23139+5939	23 16 09.3	+59 55 23	−44.7	1.73 \times 1.30	−17.4	85	1
23151+5912	23 17 21.0	+59 28 49	−54.4	1.62 \times 1.27	−19.4	83	2
23545+6508	23 57 05.2	+65 25 11	−18.4	1.78 \times 1.34	−10.4	85	0

Notes.

^a The channels in the velocity range of 29.4–31.6 km s $^{-1}$ presented an rms noise about six times larger than that in the rest of the data cube. Our detection limit in this velocity range is ~ 2 Jy.

^b This source was not calibrated because of the low SNR of the phase calibrator.

^c Observations made under bad weather conditions on 2008 September 12 in the time range from 03:15:00 to 05:14:20. The null maser detection is inconclusive.

^d This source was also observed in Survey II.

^e This source was also observed in Survey I.

For the pointing center of each field we used the position given by S02. We caution that these positions (given in their Table 1 and also our Table 3.3) in general are not the same as the IRAS PSC positions. The offsets from the IRAS positions range from 0''10 to 33''; the biggest separation is for IRAS 18306–0835. In some cases, this positional difference may be due to a truncation in the coordinate values (T.K. Sridharan, private communication). In Figure 3.5 we show the IRAS error ellipses centered on the PSC position given by the SIMBAD astronomical database². We also show the primary beam of these observations ($\sim 1'$) centered on the positions reported by S02. Except for 18306–0835, the IRAS error ellipses fall almost entirely within the VLA primary beam.

For the source 18151–1208, the channels in the velocity range of 29.4 km s $^{-1}$ to 31.6 km s $^{-1}$ presented an rms noise about six times larger than in the rest of the data cube. Our detection limit for masers in this velocity range is about 2 Jy.

3.4 Results

We detected 44 GHz methanol masers in 24 out of 56 fields (a 43% detection rate). A total of 83 maser components were detected; for these masers we report the line parameters in Table 3.4. Column 1 shows the IRAS name of the source. Column 2 lists a number associated to the maser component assigned by increasing Right Ascension. Columns 3 and 4 give the J2000 position of the peak emission obtained from a two-dimensional Gaussian fit to the peak maser channel. Column 5 is the LSR velocity of the peak emission channel. Column 6 is the flux density obtained from the 2D gaussian fit. Column 7 gives the full width of the line at zero intensity (FWZI) at a 4σ level; in this case σ is the channel-to-channel rms noise from the spectra. Column 8 shows the flux density integrated over velocity for channels above the 4σ level of the spectra. Of the 83 maser components, there are 10 that overlap with a stronger maser component, causing a larger uncertainty in the reported parameters. We indicate these ten cases in Column 9. An example of

²This research has made use of the SIMBAD database, operated at CDS, Strasbourg, France.

an overlapping feature is shown in Figure 3.1. The strongest maser in our sample showed a flux density of 62.73 Jy and was detected toward IRAS 18290–0924 (see Figure 3.1).

To estimate the uncertainty in the flux density, we consider two contributing factors. First, the Q-band flux density calibration is limited to about 3% accuracy due to pointing errors. The second is the statistical uncertainty of the flux bootstrapping for the phase calibrators reported by the task GETJY. The highest uncertainty reported is $\sim 6\%$. Considering other sources of uncertainty in the VLA flux scale, we conservatively adopt an uncertainty of 15%. We note that the flux densities reported in Table 3.4 were corrected for primary beam attenuation via the task PBCOR. We indicate correction factors greater than 2 in Column 9 of Table 3.4. The uncertainty of the flux density is larger for these masers, and increases with the primary beam correction factor applied (i.e., the further the maser is outside the beam half-power point, the larger is the uncertainty). We used 3C147 and 3C286 as flux calibrators for the observing runs made during August and 3C48 and 3C286 for the observations taken in September. To set the flux density scales, we used the coefficients defined by Perley-Butler 2010 (Perley & Butler 2013).

To estimate the positional accuracy we consider three sources of uncertainty. The first uncertainty is given by the VLA calibrator code; these range from $0''.002$ to $0''.15$ for calibrator codes A, B and C (see Table 3.2). The second uncertainty depends on the image quality and was calculated using the expression reported by Condon et al. (1998): $\theta = \frac{1}{2}\theta_{\text{syn}}\frac{\sigma_{\text{rms}}}{I_{\text{peak}}}$. We use the largest synthesized beam size and the weakest maser from each observing run to obtain an upper limit to the uncertainty; this contribution ranges from $0''.004$ to $0''.095$. An additional source of positional error is the phase transfer between calibrator and source. We estimated this positional uncertainty from the phase noise of the calibrators which ranged from 9° to 65° . We use the expression $\theta = \frac{\sigma_\phi\theta_{\text{syn}}}{2\pi\sqrt{n_p}}$ where σ_ϕ is the phase rms, θ_{syn} is the synthesized beam and n_p is the number of visibilities for each phase calibrator. This contribution ranges from $0''.0002$ to $0''.0009$. As the positional uncertainty from the phase noise was derived from observations of phase calibrators, then, for the maser sources, the positional error should be taken as a lower limit. We add in quadrature these three sources of uncertainty to obtain a conservative estimate of the positional error. For the observations made during August we estimate an uncertainty of $0''.1$ and for the observing runs taken in September, we estimate a positional uncertainty of $0''.2$.

Table 3.4: Class I Methanol Masers Detected

Source IRAS Name	Maser Number	J2000 Peak Coordinates		Peak Velocity ^a km s ⁻¹	S _{max} Jy	Δv km s ⁻¹	$\int S_\nu dv$ Jy km s ⁻¹	Note ^b
		α (h m s)	δ ($^\circ$ ' ")					
05358+3543	1	05 39 11.37	+35 45 08.4	-18.4	0.84	0.49	0.20	
	2	05 39 13.20	+35 45 36.0	-18.0	5.01	1.16	2.65	3.4
	3	05 39 13.48	+35 45 43.0	-16.6	24.72	0.99	14.91	5.8
18089-1732	1	18 11 51.29	-17 31 23.8	+31.5	17.70	3.31	10.82	^c
	2	18 11 51.39	-17 31 24.6	+32.5	1.87	-	-	^c
	3	18 11 51.70	-17 31 23.8	+32.4	4.39	1.49	2.09	
	4	18 11 52.18	-17 31 21.7	+31.8	1.20	0.33	0.22	
	5	18 11 51.51	-17 31 21.6	+33.6	1.55	2.32	1.51	
	6	18 11 51.41	-17 31 22.2	+33.8	1.52	1.66	0.37	
	7	18 11 51.64	-17 31 22.0	+33.1	1.00	0.33	0.06	
18102-1800	1	18 13 10.29	-18 00 03.8	+22.5	7.64	0.49	2.52	3.7
	2	18 13 11.01	-18 00 02.4	+21.4	5.87	0.33	1.55	2.3
	3	18 13 11.10	-18 00 01.4	+21.4	3.45	0.49	0.80	2.1
	4	18 13 11.17	-18 00 04.2	+22.9	3.63	1.32	2.90	2.3
	5	18 13 11.24	-18 00 03.1	+22.0	2.39	1.32	0.65	2.2
	6	18 13 11.82	-18 00 01.8	+19.6	7.36	1.66	6.40	
18151-1208	1	18 17 57.12	-12 07 34.7	+33.2	1.34	1.32	0.98	

Table 3.4 – continue

Source IRAS Name	Maser Number	J2000 Peak α (h m s)	Coordinates δ (o' ")	Peak Velocity ^a km s ⁻¹	S _{max} Jy	Δv km s ⁻¹	$\int S_\nu dv$ Jy km s ⁻¹	Note ^b
	2	18 17 58.20	-12 07 29.4	+33.7	2.94	0.66	1.12	
	3	18 17 58.56	-12 07 17.0	+32.1	13.83	0.99	7.08	
	4	18 17 58.58	-12 07 18.8	+33.6	5.71	0.49	1.91	
18182–1433	1	18 21 08.78	-14 31 46.7	+60.7	2.31	1.32	1.19	
	2	18 21 08.90	-14 31 46.8	+60.4	1.33	1.32	0.69	
	3	18 21 09.14	-14 31 49.7	+61.2	33.63	2.32	24.85	
	4	18 21 09.85	-14 31 46.7	+60.2	13.90	1.16	7.77	
18247–1147	1	18 27 31.80	-11 46 00.5	+120.7	6.53	1.66	2.66	
18264–1152	1	18 29 14.18	-11 50 27.4	+43.6	3.82	1.82	1.82	
	2	18 29 14.33	-11 50 27.4	+45.2	1.12	0.49	0.33	
	3	18 29 14.28	-11 50 18.9	+44.4	7.40	2.32	4.13	
	4	18 29 14.38	-11 50 24.8	+43.6	14.80	–	–	c
	5	18 29 14.39	-11 50 24.7	+43.1	19.73	1.66	12.47	c
	6	18 29 14.49	-11 50 17.4	+43.9	12.19	1.49	6.41	
	7	18 29 14.57	-11 50 23.8	+41.1	1.09	0.49	0.37	
	8	18 29 14.66	-11 50 26.4	+42.9	2.04	0.99	0.71	
	9	18 29 14.77	-11 50 22.3	+42.7	2.01	2.15	1.36	
	10	18 29 15.42	-11 50 11.1	+42.7	1.20	0.82	0.55	
18290–0924	1	18 31 43.18	-09 22 31.7	+85.8	1.23	0.16	0.16	2.4
	2	18 31 43.40	-09 22 22.5	+83.9	62.73	2.32	29.41	
	3	18 31 44.20	-09 22 12.6	+82.8	1.17	0.49	0.40	
18306–0835	1	18 33 22.95	-08 33 35.3	+76.4	2.86	0.99	1.31	
	2	18 33 23.96	-08 33 30.2	+79.9	5.45	1.32	4.97	2.4
	3	18 33 24.07	-08 33 34.5	+77.6	18.23	2.98	20.10	2.5
18308–0841	1	18 33 32.49	-08 39 08.5	+76.6	0.82	0.66	0.27	
	2	18 33 33.08	-08 39 17.5	+76.4	0.75	0.33	0.08	
	3	18 33 33.21	-08 39 14.7	+76.4	14.93	2.49	10.42	c
	4	18 33 33.16	-08 39 13.6	+75.8	6.20	–	–	c
	5	18 33 33.24	-08 39 15.7	+76.9	6.49	–	–	c
18310–0825	1	18 33 47.31	-08 23 43.1	+84.2	1.10	0.49	0.24	
18337–0743	1	18 36 27.98	-07 40 22.7	+60.7	6.53	1.99	4.01	c
	2	18 36 28.00	-07 40 24.0	+58.5	2.45	–	–	c
18345–0641	1	18 37 16.53	-06 38 34.4	+95.9	1.30	1.32	0.89	
	2	18 37 16.56	-06 38 25.6	+94.9	0.57	0.16	0.07	
	3	18 37 16.89	-06 38 29.7	+95.4	7.74	2.98	6.58	
	4	18 37 16.94	-06 38 30.7	+97.0	1.66	–	–	c
	5	18 37 17.30	-06 38 31.5	+96.2	1.98	2.49	2.24	c
	6	18 37 17.21	-06 38 30.5	+94.5	0.45	–	–	c
	7	18 37 17.33	-06 38 34.4	+97.2	0.66	0.66	0.18	
	8	18 37 17.92	-06 38 47.0	+95.7	6.39	0.33	1.44	
18488+0000	1	18 51 25.42	+00 04 06.1	+83.1	11.65	1.66	7.97	
18517+0437	1	18 54 14.74	+04 41 42.7	+43.4	4.19	1.16	2.70	
	2	18 54 14.46	+04 41 44.3	+44.0	1.09	1.16	0.73	
18521+0134	1	18 54 40.90	+01 38 04.8	+78.1	0.66	0.82	0.36	
	2	18 54 40.79	+01 38 05.5	+77.8	0.36	0.16	0.02	
18530+0215	1	18 55 34.76	+02 19 00.5	+80.1	1.14	2.15	1.32	
	2	18 55 34.90	+02 18 58.6	+79.1	0.94	0.66	0.24	
18553+0414	1	18 57 53.34	+04 18 16.9	+12.5	1.47	0.99	0.70	
18566+0408	1	18 59 09.23	+04 12 22.3	+86.8	1.04	0.33	0.26	
	2	18 59 09.30	+04 12 25.7	+86.3	3.75	1.49	2.90	c
	3	18 59 09.20	+04 12 25.4	+86.8	1.73	–	–	c
	4	18 59 09.97	+04 12 14.8	+83.8	1.28	1.82	0.92	
	5	18 59 10.17	+04 12 16.3	+87.0	1.09	0.66	0.40	

Table 3.4 – continue

Source IRAS Name	Maser Number	J2000 Peak α (h m s)	Coordinates δ ($^{\circ}$ ' ")	Peak Velocity ^a km s ⁻¹	S _{max} Jy	Δv km s ⁻¹	$\int S_{\nu} dv$ Jy km s ⁻¹	Note ^b
20126+4104	1	20 14 25.17	+41 13 36.2	-2.3	5.07	2.32	3.92	^c
	2	20 14 25.22	+41 13 35.1	-2.3	3.88	–	–	^c
	3	20 14 25.30	+41 13 40.6	-3.1	2.55	0.49	0.53	
	4	20 14 25.41	+41 13 37.9	-3.3	7.87	2.15	5.59	
	5	20 14 26.71	+41 13 29.8	-4.4	2.81	0.82	1.33	
20293+3952	1	20 31 12.80	+40 03 20.8	+6.9	10.17	2.15	6.58	
	2	20 31 11.97	+40 03 12.1	+6.1	9.58	1.66	4.95	
	3	20 31 12.80	+40 03 24.0	+4.8	14.58	1.32	8.06	
23033+5951	1	23 05 24.56	+60 08 09.4	-54.4	17.81	1.16	8.30	^c
	2	23 05 24.72	+60 08 09.3	-52.9	2.14	–	–	^c
23139+5939	1	23 16 10.83	+59 55 20.7	-44.5	0.91	0.66	0.28	
23151+5912	1	23 17 21.86	+59 28 45.6	-52.7	4.02	0.99	2.18	
	2	23 17 21.30	+59 28 50.6	-54.7	3.67	0.33	0.84	

Notes.

^aWe report the channel velocity of the peak emission.

^bAll flux densities were corrected for primary beam attenuation. We show the primary beam correction factors that were larger than 2 to indicate sources for which this correction may result in larger flux density uncertainties.

^cThis maser component is blended with another feature at a nearby velocity. We were not able to determine the line width and integrated flux density precisely. We report the values for the strongest component.

3.4.1 Line properties

Linewidths

In Figure 3.2 we show a histogram of the maser linewidths measured in our survey. The linewidths range from 0.16 km s⁻¹ (the channel width) to 3.31 km s⁻¹. We caution that components with linewidths greater than ~ 1 km s⁻¹ may occur because of overlapping weak maser features (as reported in Table 3.4) or because of a thermal (i.e., non-maser) contribution to the emission.

The observations reported here were made in a similar manner to those of Survey III, using the VLA D-configuration with a spectral resolution of 0.16 km s⁻¹ and a velocity coverage of 21 km s⁻¹. Therefore, it is reasonable to make a direct comparison between the linewidth distributions obtained in the two surveys. We find very similar linewidth ranges with the difference that this work does not show a clear peak of the distribution whereas Survey III found a peak at 0.35 km s⁻¹. The median linewidth of the present data is 1.16 km s⁻¹, similar to the 1.0 km s⁻¹ found in Survey III.

Relative velocity distribution

In Figure 3.3 we show a histogram of the maser velocities relative to the ambient molecular cloud. We use the systemic cloud velocities reported by S02 from CS(2–1) observations and plot the difference between the maser velocity and the cloud velocity. The relative velocities range from -2.5 to +3.1 km s⁻¹; the mean value of the distribution is 0.22 km s⁻¹ with a standard deviation of 1.22 km s⁻¹. The total range of velocities is less than 5.6 km s⁻¹. The statistics from Survey III are similar to ours: their relative velocities range from -2.7 to +3.8 km s⁻¹ with a mean of 0.09 km s⁻¹ and a standard deviation of 1.27 km s⁻¹. The median value of both distributions is 0.2 km s⁻¹. Similar results were obtained by Jordan et al. (2015). Their distribution shows a total velocity range less than 9 km s⁻¹ with a mean value of 0.0 \pm 0.2 km s⁻¹ and a standard deviation of 1.5 \pm 0.1 km s⁻¹.

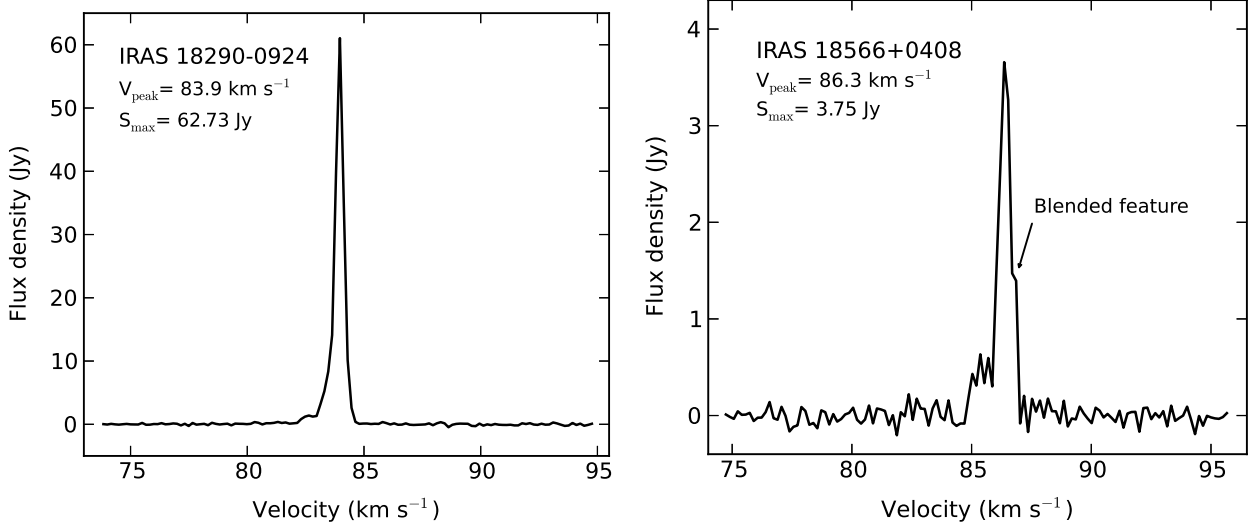


Figure 3.1: Left: Spectrum of the strongest maser component found in our sample toward IRAS 18290–0924. Right: Example of a typical blended feature. We show the strongest maser component in source IRAS 18566+0408 which is blended with another feature at a nearby velocity (see Table 3.4).

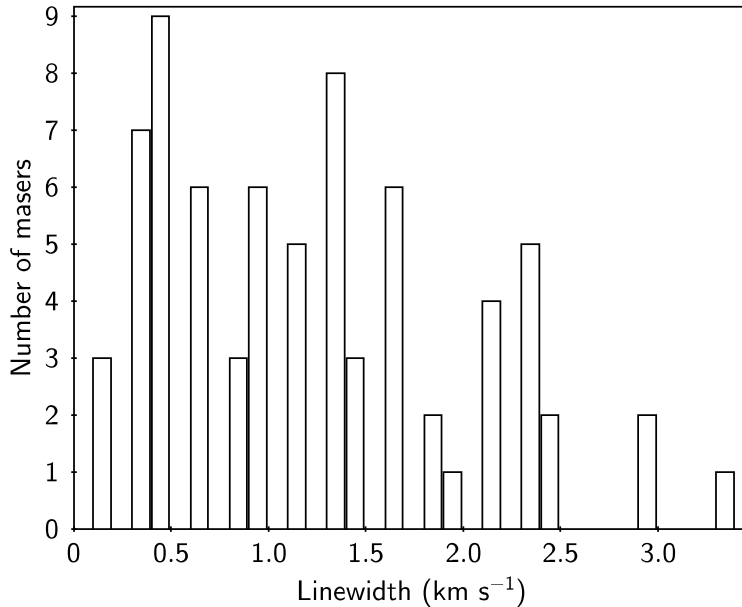


Figure 3.2: Histogram of the maser linewidths in our sample. The first bin (with 3 masers) corresponds to components with linewidth equal to the spectral resolution.

Although our histogram peaks near zero, there is a small but discernible redshifted asymmetry (see Figure 3.3). This tendency was also noted in the velocity histogram of Survey III.

To determine if the redshifted trend is real, as suggested by inspection of the velocity distributions from this survey and Survey III (see our Figure 3.3 and their Figure 2), we performed the D’Agostino-Pearson

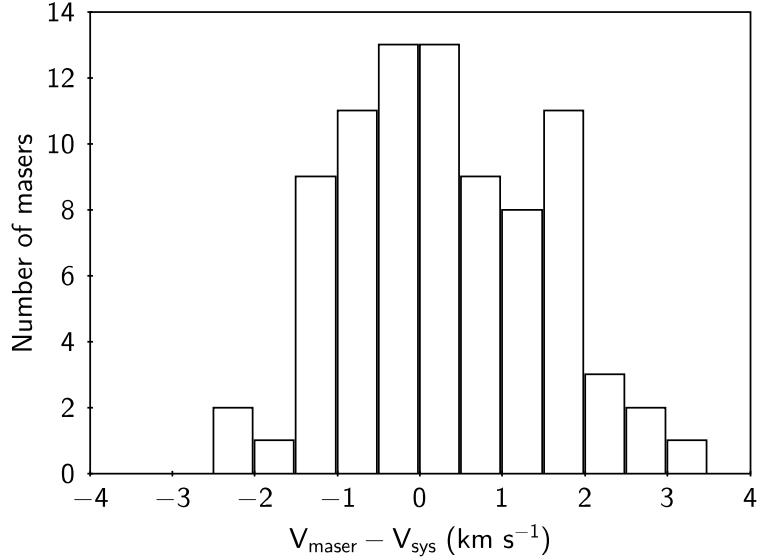


Figure 3.3: Histogram of the maser–cloud relative velocity distribution.

test for normality on both samples to check for deviations from a normal distribution based on the skewness and kurtosis. The null hypothesis to test is that the relative velocity distribution comes from a normally distributed population. The normality test reports a p-value which is a measure of the significance level of the test. A p-value higher than 0.05 would be the criterion to accept the null hypothesis that the data have a normal distribution. We obtained a p-value of 0.44 and 0.61 for the velocity distributions of this survey and Survey III, respectively. Thus, the normality test suggests a 44% and 61% probability that both datasets are consistent with a normal distribution. Although we cannot confirm the redshifted tendency in our data, we consider this point to be an open question.

Kirsanova et al. (2017) compared 6.6 GHz maser velocities with systemic cloud velocities traced by CS(2–1) toward 24 high-mass star-forming regions in the Perseus spiral arm. They find a predominance of redshifted masers and suggest this is related to large-scale galactic motions.

3.4.2 Comments on individual sources

In Table 3.1, we summarize single-dish and interferometric observations of some common star formation sign posts made toward the 24 sources with 44 GHz maser detections. We consider seven sources for special comments because they have additional information available in the literature to understand their nature in relation to the 44 GHz masers. Three-color images from Spitzer/IRAC of all regions with 44 GHz masers are shown in Figure 3.5³.

IRAS 05358+3543

This source is part of the star-forming complex S233IR located at a distance of 1.8 kpc (Snell et al. 1990). S233IR contains two young embedded clusters in different evolutionary states separated by 0.5 pc. They are labeled as the NE and SW clusters with estimated ages $\lesssim 2$ Myr and 3 Myr, respectively (Porrás et al. 2000). Several star formation tracers are present in the NE cluster: H₂O and OH masers (Tofani et

³This research has made use of SAOImage DS9, developed by the Smithsonian Astrophysical Observatory.

al. 1995; Argon et al. 2000; Beuther et al. 2002c), intense Class II 6.6 GHz methanol masers (256 Jy; Menten et al. 1991; Szymczak et al. 2000) and at least three highly-collimated jets revealed from shocked H₂ emission (Qiu et al. 2008; Porras et al. 2000). Three millimeter sources and possibly four molecular outflows are found in this cluster (mm1, mm2 and mm3; outflows A, B, C and D: Beuther et al. 2002d). Outflow A is a large-scale (~ 1 pc) highly-collimated CO outflow possibly powered by mm1; outflow B is a high-velocity CO outflow and outflow C is observed mainly in SiO emission. In marked contrast, the SW cluster — which harbors the IRAS source — does not show any of the star formation activity described above. No radio continuum emission at 3.6 cm was detected toward either cluster (S02).

Our observations were centered on the IRAS source in the SW cluster where one maser spot was detected; the NE cluster is outside our primary beam although two maser spots were detected here (see Figure 3.5). The largest primary beam correction factors reported in Table 3.4 were applied to this source. In total, three methanol maser spots were detected; the one detected toward the SW cluster is coincident with SiO emission from the southern lobe of outflow C and also with an extended green object that appears emanating from the SW cluster in a NW-SE direction. The other two in the NE cluster are either coincident with the inner knots of outflow A or with the tip of the south-eastern lobe of outflow B. One of these two masers is also coincident with H₂ emission (knot N4A: Porras et al. 2000; bow shock 1: Varricatt et al. 2010; Beuther et al. 2002d). In contrast to the Class II, H₂O and OH masers which are projected near the center of the NE cluster (Porras et al. 2000), the Class I masers are located at the borders of the star formation regions.

Litovchenko et al. (2011) made single-dish observations of 44 GHz masers in this source. Their pointing was centered toward the NE cluster and did not detect emission. Their primary beam covers the complete area where we detect two bright masers of 24.72 Jy and 5.01 Jy. Their nondetection suggests variability.

IRAS 18089–1732

This source is common to the S02 sample and the “High” sub-sample of Molinari et al. (1996). Beuther et al. (2004a) favor the near kinematic distance of 3.6 kpc corresponding to a luminosity of $\sim 32,000 L_{\odot}$ (S02). A compact core oriented in the north-south direction was found through interferometric continuum observations at 1.3 mm and 3.6 cm (Beuther et al. 2004a; Zapata et al. 2006). Emission from SiO(5–4) reveals a molecular outflow with both the red and blue lobes oriented to the north of the core (Beuther 2004a). Sensitive VLA observations at 7 mm resolve the core into two components: sources “a” and “b” (Zapata et al. 2006). Zapata et al. interpret source “a” as a thermal jet that is driving the SiO(5–4) outflow and, source “b” as an optically thick HII region. H₂O, OH and Class II 6.6 GHz methanol masers are projected inside the 3.6 cm continuum source (Argon et al. 2000; Beuther et al. 2002c).

Six of the seven 44 GHz masers are distributed in an arc-like feature about 8'' (0.1 pc) to the north of the compact core and the star formation indicators mentioned above (see Figure 3.5). We speculate that this arc feature could be tracing the shocked gas from the SiO(5–4) outflow lobes. The lobes extend northward about 5'' from the millimeter peak with a 20° position angle; the 44 GHz masers are located at the northern edge of the outflow. The 44 GHz maser velocities are within a few km s⁻¹ of the systemic velocity (+33.8 km s⁻¹ from S02), while the SiO outflow has a velocity range from +26 to +41 km s⁻¹. These masers appear at the interface between the outflowing gas and the ambient material. Fontani et al. (2010) report single-dish detections of both 44 and 95 GHz Class I maser emission that closely matches the velocities of the 44 GHz masers that we detect. The isolated CH₃OH maser to the east of the arc-like feature is close to (but not coincident with) a weak green excess in the Spitzer image.

IRAS 18102–1800

The near and far distances reported by S02 for this source are 2.6 kpc and 14.0 kpc corresponding to $10^{3.8}$ and $10^{5.3} L_{\odot}$, respectively. The Spitzer image shows an extended source with an $8 \mu\text{m}$ excess — which hosts the IRAS source — and a compact infrared source $\sim 20''$ to the SW of the IRAS position. IRAS 18102–1800 has a bright 3.6 cm continuum source (44 mJy) detected with the VLA. Class II methanol masers are located at the peak position of the SW compact source (Beuther et al. 2002c). An extended millimeter core is located $5'' - 7''$ south of the Class II masers (see Fig. 1 in Beuther et al. 2002c). No water masers were detected (S02).

Our observations were centered on the IRAS position but the majority of the 44 GHz methanol masers are distributed along the SW compact source which is at the edge of the VLA primary beam (see Figure 3.5). Large primary beam correction factors were applied to this source (see Table 3.4). The 44 GHz masers lie roughly along an east-west line of length ~ 0.3 pc (1.6 pc) for a distance of 2.6 kpc (14.0 kpc). The absence of centimeter continuum emission — but the presence of Class II methanol masers — suggests that the compact SW object is in a younger evolutionary state than the IRAS source. If so, the indication is that 44 GHz methanol masers appear preferentially toward the younger source. Alternatively, the masers at 44 GHz may trace an outflow powered by a protostar near the millimeter core.

IRAS 18182–1433

A distance of 3.6 kpc has been adopted for this source (Moscadelli et al. 2013). The IRAS source is formed by two mid-IR objects separated by $10''$ along the NW-SE direction (De Buizer et al. 2005). VLA observations at 7 mm, 1.3 cm and 3.6 cm detected one millimeter source (source “a”) and two centimeter sources (sources “b” and “c”; Zapata et al. 2006). Sources “a” and “b” are coincident with the NW mid-IR object while source “c” coincides with the stronger SE object. Class II CH_3OH , H_2O and OH masers are located toward the region of sources “a” and “b” (Walsh et al. 1998; Forster & Caswell 1999; Beuther et al. 2002c; Sanna et al. 2010). Multiple CO and SiO outflows seem to emanate from the location of sources “a” and “b” (Beuther et al. 2002b; 2006). None of these star formation tracers are seen toward source “c”. All these data suggest that the NW source is younger and more embedded than the SE source (De Buizer et al. 2005).

Our observations were pointed toward the position reported by S02 which is offset from the IRAS position by $19''.5$ (see Figure 3.5). We detect 4 Class I methanol masers which are distributed in the region around the NW sources “a” and “b” but no masers were found toward the SE source “c”. The 44 GHz masers are located at the edges of the green excess seen in the $4.5 \mu\text{m}$ band. The suggestion in this case, is that 44 GHz masers tend to favor the younger objects in the region.

IRAS 18264–1152

S02 report near and far kinematic distances of 3.5 and 12.5 kpc, respectively, with luminosities of $10^4 L_{\odot}$ and $10^{5.1} L_{\odot}$. Class II CH_3OH , H_2O and Class I 95 GHz masers are reported in the region (S02; Beuther et al. 2002c; Chen et al. 2011). Multiple molecular outflows were revealed from interferometric and single-dish observations: a high-velocity SiO outflow ($\Delta v \sim 60 \text{ km s}^{-1}$) and a CO outflow oriented in an east-west direction (Beuther et al. 2002b; Qiu et al. 2007) also traced by H_2 emission (Varricatt et al. 2010). Although undetected at 3.6 cm by S02, more sensitive observations detected emission at the 1 mJy level (Zapata et al. 2006; Rosero et al. 2016). This source is resolved into three components at 1.3 cm and 7 mm: called sources “a”, “b” and “c”. Zapata et al. suggest an optically thick HII region or dust emission

from a core and disk for source “a”, a thermal jet or a partially optically thick HII region for source “b”; and an optically thick HII region or dust emission from a core and disk for source “c”.

This source shows the highest level of 44 GHz maser activity in our survey. We report 10 maser components; 9 of them are located in the general vicinity of the YSO and other star formation indicators. The remaining maser spot is isolated, some $10''$ to the NE. Two of the 9 masers are projected against the 3.6 cm emission and near the peak position of H₂O and Class II methanol masers. IRAS 18264–1152 has been classified as an EGO by Cyganowski et al. (2008), indicating the presence of shocked gas.

None of these maser components with flux densities ranging from 1.09 to 19.73 Jy (see Table 3.4) were detected by the single-dish observations of Litovchenko et al. (2011) which suggests maser variability.

IRAS 18517+0437

This source is located at a distance of 2.9 kpc and has a luminosity of $\sim 13000 L_{\odot}$ (S02). Two mid-IR objects located with a NE-SW orientation contribute to the IRAS source. A third object with a bipolar structure seen in the $4.5 \mu\text{m}$ band (green) consistent with an EGO is located some $10''$ east of the NE source. Intense Class II 6.6 GHz methanol masers were found by single-dish observations (279 Jy; Schutte 1993; Szymczak 2000) as well as H₂O 22 GHz masers (Brand et al. 1994; Codella et al. 1996; S02) but their precise positions are unknown, making it difficult to compare their positions with those of the other objects in the field. Thermal free-free emission at 3.6 cm was not detected by S02 but recent VLA observations detected three weak sources at 6 cm (Rosero et al. 2016; see Figure 3.5). Source “A” as labeled by Rosero et al. appears to power the EGO. Although CO line wings were detected by S02, no molecular outflows were found by the CO observations of Zhang et al. (2005). This source was also observed in the Survey III; the line parameters reported are consistent with our findings within the uncertainties.

We find two 44 GHz methanol maser spots located at the borders of the green emission, consistent with the idea that EGOs trace shocked gas where methanol masers are excited.

IRAS 20293+3952

This region is a typical source from our sample which hosts multiple star formation sites (see Figure 3.4). It is located at a distance of 2 kpc (Beuther et al. 2004b). The IRAS source is associated to an UCHII region which dominates the luminosity of the region $\sim 6300 L_{\odot}$ and has an estimated ionizing photon rate corresponding to a B1 zero-age main-sequence star (Beuther 2004b; Palau et al. 2007). IR studies have reveal two regions, IRS 1 and IRS 2. IRS 1 is a possible binary system (Palau et al. 2007), in which the northern and fainter source is associated with the UCHII region and the whole system is surrounded by a ring of H₂ emission (Kumar et al. 2002; Varricatt et al. 2010). Approximately $20''$ north-east of the UCHII region there is a dense cloud of $\sim 250 M_{\odot}$ and ~ 0.5 pc of size that hosts a number of YSOs in different evolutionary stages from starless cores to (proto)stars (mm1, mm2, mm3, BIMA 3, BIMA 4, etc; Beuther et al. 2004b; Palau et al. 2007). The millimeter source mm1 is an intermediate-mass protostar of $4 M_{\odot}$ while mm2 and mm3 are low-mass protostars with estimated masses around $1 M_{\odot}$. All of these millimeter sources are associated with four highly-collimated outflows identified from CO(2–1) and SiO(2–1) interferometric observations (Beuther et al. 2002b; 2004b; outflows A, B, C and D). Outflows A and B emanate from mm1; outflow C from mm3, and outflow D from mm2 (see Figure 3.4). Weak radio continuum sources were detected by very sensitive VLA observations at 6 cm and 1.3 cm, see Figure 3.4 (sources A, B, C, D and E; Rosero et al. 2016). Particularly, source B is a weak and compact object projected inside the UCHII region which is similar to that found in other UCHII regions such as W3(OH) and M8 (Dzib et al. 2013; Masqué et al. 2014). The peak position of source E is coincident with the position reported for the millimeter source mm1 and also with a water maser reported by Beuther et al. (2002c).

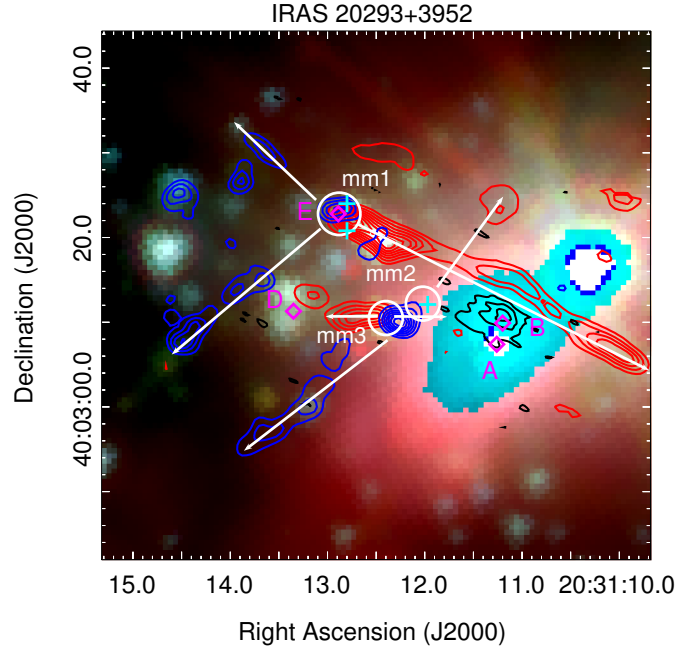


Figure 3.4: Three-color image from Spitzer (blue = $3.6 \mu\text{m}$, green = $4.5 \mu\text{m}$; red = $8 \mu\text{m}$). The red and blue contours represent the CO molecular outflows detected by Beuther et al. (2004b). The white arrows indicate the direction of the molecular outflows. The black contours trace the UCHII region from Beuther et al. (2004b). The white circles symbolize the three millimeter sources (mm1, mm2, mm3) reported by Beuther et al. (2004b). The magenta diamonds indicate the peak position of the four compact centimeter sources (A, B, D, E) detected by Rosero et al. (2016). The cyan crosses represent the three 44 GHz maser spots reported in this work.

Figure 3.4 shows contours of CO emission tracing the molecular outflows and the UCHII region overlaid with the three 44 GHz masers detected. Two of the three 44 GHz masers overlap with mm1 and radio source E while the other maser is very close to the peak position of mm2. The methanol masers toward mm1 arise near the base of outflows A and B rather than at the interaction region of the outflow lobes with the ambient medium. A green feature seems to extend in the same direction as outflow B but no masers were found along the outflowing gas. The excitation of the maser close to mm2 is not clear; it is possible that the excitation may be related to the outflows from the low-mass protostars mm1 and mm2. Only a few cases of Class I masers in low-mass sources have been reported (Kalenskii et al. 2010); this maser may be a similar case. Because this maser is close to an H_2 knot from the expanding ring-like structure, an alternative explanation is that this maser traces shocked gas from the interaction between the expanding UCHII region and the ambient molecular environment.

3.5 Discussion

3.5.1 Comparison with previous surveys

Several sources appear multiple times in Surveys I-IV. Survey I observed 44 massive star-forming regions in different evolutionary states, taken from the catalogs of Bachiller et al. (1990), Haschick et al. (1990),

Slysh et al. (1994) and Molinari et al. (1996). Three of the sources in Survey I could not be imaged and so were re-observed in Survey II to complete the previous survey and provide accurate positions and line parameters. Survey III presented a study of 69 YSOs taken from the catalog of high-mass protostellar candidates of Molinari et al. (1996). Thirteen of these 69 YSOs were previously studied in Survey I. The criteria used to select the sample of Survey I were different from those used for the subsequent surveys. Survey I consists of a heterogeneous collection of sources while the sample of Survey III satisfies specific selection criteria and so was selected systematically. The overlap of 13 YSOs between Surveys I and III is merely a consequence of the different goals of each project.

The present survey (Survey IV) consists of 56 HMPOs taken from the S02 catalog. One source, IRAS 20126+4104, is common to the samples of Surveys I and III. Another source, IRAS 18517+0437, is common to Survey III. These two sources were observed in a similar manner in each survey, using the VLA D-configuration with a spectral resolution of 0.16 km s^{-1} and a velocity coverage of 21 km s^{-1} . Thus, it is reasonable to make comparisons between the maser line properties obtained in the different surveys to check the consistency of the observations and as a test of variability.

For 20126+4104, we detect five maser components. Components 1–4 (see Table 3.4) are clustered $\sim 10''$ to the northwest of the IRAS source while component 5 is located $\sim 10''$ to the southeast of the IRAS source (see Figure 3.5). For all 5 maser components, the coordinates and velocities coincide within the uncertainties for all three observations. The maser fluxes are similar between Surveys I and III; in this work, however, we find somewhat higher fluxes. The peak flux densities of components 1 to 4 are almost a factor of 2 larger than those reported in Surveys I and III. For example, component 4 has the largest peak flux density of 7.87 Jy while Surveys I and III measured peak fluxes of 3.91 Jy and 4.24 Jy, respectively. In contrast, the peak flux density and linewidth of the isolated component 5 is consistent with the two previous observations, i.e., it remained nearly the same. The data were treated in a similar manner in each of the three surveys with the exception that we apply primary beam correction. Nevertheless, the maser locations are near the pointing center, consequently the correction factors are small (less than 8%) which is insufficient to explain the difference in measured fluxes. A common amplification factor to the maser peak fluxes of the NW group and the absence of this amplification in the isolated maser in the SE suggest that some physical event occurred between March 2007 and August 2008, affecting only the NW masers.

Class I masers are known to be collisionally pumped, so it is plausible to suppose a shock front emerging from the HMPO as the cause of the NW maser group brightening. We consider maser components 3 and 4 to define the width of a spherical shell surrounding the IRAS source which is located at a distance of 1.64 kpc (Moscadelli et al. 2011). The radial separation between IRAS 20126+4104 and maser components 3 and 4 is $12.98''$ and $10.10''$, respectively. This corresponds to a shell width of about $2.9''$ (0.023 pc). We use the 15 month time separation between the observations as an upper limit to the travel time for such a shock moving along the shell. This implies a lower limit to the shock velocity of about $18,300 \text{ km s}^{-1}$ which is unrealistically high. An alternative possibility is that the putative shock originated from a different location.

For 18517+0437, we detect two maser components. The positions, flux densities and linewidths are consistent with the parameters reported in Survey III within the uncertainties. The brightest maser we measured has a peak flux density of 4.19 Jy (component 2) while Survey III reported a maser peak flux of 3.32 Jy. The other maser we detect has a flux density of 1.09 Jy (component 1) while Survey III reported a flux of 1.28 Jy. A weak third component was reported in Survey III but we did not detect it. The flux density variation between both Surveys is because we apply primary beam correction and Survey III did not. Components 1 and 2 are near the edges of the VLA primary beam (see Figure 3.5), so the correction factors here become significant. In fact, for component 2, we measured exactly the same flux density than Survey III (3.32 Jy) but the 4.19 Jy reported is the result of applying a correction factor of 26% of the

measured flux. This source is discussed in detail in Section 3.4.2.

A single-dish survey of 59 sources was made by Litovchenko et al. (2011) to search for 44 GHz methanol masers; 22 of the 59 sources were among our sample. They used a broad-bandwidth spectrometer with a spectral resolution of 0.18 km s^{-1} , similar to our resolution. They did not report the detection limit of their observations but their spectra indicate a 1σ noise level of about 1 Jy. They detect maser emission in 6 of the 22 sources; the line parameters reported are similar to our results. However, they report 4 sources as nondetections while we detect maser activity in all of them (05358+3543, 18264–1152, 18566+0408, 23139+5939). Their single-dish pointing centers are the same as our VLA pointings, except for source 05358+3543. Despite this pointing difference, for IRAS 05358+3543 we detect 2 masers of 24.72 Jy and 5.01 Jy in a region well-covered by their single-dish primary beam. Their nondetection suggests variability. For IRAS 18264–1152, we detect 10 maser components with flux densities ranging from 1.09 to 19.73 Jy but none of them were detected by Litovchenko et al., again suggesting variability. These two sources are discussed in detail in Sections 3.4.2 and 3.4.2. For IRAS 18566+0408, we detect five maser features with fluxes from 1.04 to 3.75 Jy but were not detected by Litovchenko et al., however, these may have been below their detection limit. For IRAS 23139+5939, we detect one maser with a flux density of 0.91 Jy which was not detected by their single-dish observations. As in the previous case, the maser we detect is below their sensitivity limit.

3.5.2 Relation with molecular outflows

The GLIMPSE survey, performed with the Spitzer Space telescope⁴, is a powerful tool to identify high-mass YSO with outflow activity (Benjamin et al. 2003; Churchwell et al. 2009). Extended and enhanced emission at $4.5 \mu\text{m}$ is commonly known as “extended green objects” (EGOs; Cyganowski et al. 2008; 2009) or “green fuzzies” (Chambers et al. 2009) as they appear green in the three-color composite images ($3.6 \mu\text{m}$ in blue, $4.5 \mu\text{m}$ in green and $8 \mu\text{m}$ in red; Fazio et al. 2004). The $4.5 \mu\text{m}$ band contains H_2 lines and the CO fundamental band (De Buizer & Vacca 2010) and hence strong emission in this band is an indicator of shocked gas. Although the exact nature of EGOs is still uncertain, it is likely that they arise in shocks where protostellar outflows collide with the ambient gas.

Nearly all of the sources in our sample were observed by the GLIMPSE survey and the majority of them are associated with CO line emission related to molecular outflows (Beuther et al. 2002b). Class I methanol masers are collisionally pumped and it has been suggested that they are excited at the interface where outflows encounter the molecular ambient medium (Plambeck & Menten 1990). To investigate this assertion, we used the GLIMPSE survey to search for correlations between 44 GHz masers and EGOs.

We present three-color images in Figure 3.5 along with the peak positions of our 44 GHz methanol maser detections for the 24 fields. Three of the 24 fields were catalogued as EGOs by Cyganowski et al. (2008; 18182–1433, 18264–1152, and 18566+0408). The images reveal nine more fields with extended green emission with morphology similar to EGOs (05358+3543, 18151–1208, 18247–1147, 18290–0924, 18345–0641, 18488+0000, 18517+0437, 20126+4104 and 20293+3952). Except for 18517+0437, the other three sources are well-correlated with CO emission which traces the molecular outflows (Beuther et al. 2002b; 2002d; Zhang et al. 2005). The masers appear in some cases at the base of the outflows while in others they appear at the outflow lobes.

Two more sources with 44 GHz masers (18102–1800 and 18488+0000) and bright centimeter emission have a special behavior. In these two cases each field is dominated by an extended red feature which is also traced by bright centimeter emission with a morphology typical of a cometary UCHII region. Next to the

⁴This work is based [in part] on observations made with the Spitzer Space Telescope, which is operated by the Jet Propulsion Laboratory, California Institute of Technology under a contract with NASA.

dominant feature, both fields show a compact green object. The masers are preferentially located toward the compact green feature, and not toward the centimeter sources.

For sources 23033+5951 and 23139+5939 Spitzer images are not available; instead, we use images from the Wide-field Infrared Survey Explorer (WISE; Wright et al. 2010)⁵. IRAS 23033+5951 also presents extended green emission in the 4.6 μm band but, due to the lower angular resolution of WISE compared to IRAC, no relationship with the masers can be established.

3.5.3 On the classification between HMPOs and UCHII regions

We discuss here the distinction made in Survey III between HMPOs and UCHII regions. In that survey, the objects were classified based on whether centimeter continuum emission from ionized gas (at a detection limit of ~ 1 mJy) was found near the IRAS source (less than $40''$). Regions with no centimeter emission were referred to as HMPOs and those with centimeter emission as UCHII regions. Given this classification, the conclusion in Survey III was that methanol masers are more common toward the more-evolved sources of their sample, i.e., toward the UCHII regions.

In this Survey, we avoid the HMPO/UCHII classification for three reasons: 1) it is ambiguous, since the free-free thermal emission may have other explanations besides a UCHII region. Different phenomena can give rise to such emission, for example, shocks produced by the interaction of thermal jets with surrounding material (Rodríguez et al. 2012), stellar winds (Carrasco-Gonzalez et al. 2015), etc. 2) As more sensitive continuum observations become available, weaker continuum emission will be detected and therefore, almost all sources will be classified as UCHII regions, regardless of the nature of the emission, and 3) because massive stars form in cluster environments, HMPO and UCHII regions may co-exist within a single star formation region. To classify the entire region as “more-evolved” owing to the presence of UCHII region could be misleading — especially if the masers are clearly associated with a HMPO and not with the UCHII region.

S02 defined their HMPOs candidates as isolated young objects in evolutionary stages prior to the formation of UCHII regions and/or without more-evolved objects (with photo-ionized gas) in their near vicinity. They based this definition on the fact that the objects were undetected in 5 GHz single-dish surveys of free-free thermal emission at a level of ~ 25 mJy (Gregory & Condon 1991; Griffith et al. 1994; Wright et al. 1994). Once they selected a sample of 69 HMPOs, they made follow-up VLA 3.6 cm observations at a level of 0.1 mJy and found that 40 of the previously undetected 69 sources show continuum emission above their detection limit of 1 mJy. Recently, with the improved VLA continuum sensitivity, deeper 1.3 cm and 6 cm observations with $\sim 10\mu\text{Jy}$ sensitivity have revealed multiple and even weaker and more compact radio sources in 23 of the 29 non-detections from S02 (Rosero et al. 2016).

In this survey, we observed 56 of 69 sources from S02. At the time when S02 selected their sources and following the Survey III classification, we would have had 0 UCHII regions and 56 HMPOs. Our detection rate would have been 43% toward the younger sources and 0% toward more-evolved sources. After their follow-up VLA observations, S02 detected centimeter continuum emission (≥ 1 mJy) in 34 of the 56 fields while 22 were undetected (< 1 mJy). The more sensitive images at the μJy level ($\sim 3 - 50 \mu\text{Jy}$) toward 15 of the 22 non-detections revealed weak and compact centimeter emission (Zapata et al. 2006; Rosero et al. 2016). Following the Survey III classification we would have a total of 49 UCHII regions and 7 HMPOs. We detect maser emission in 22 of the 49 UCHII regions and in 2 of the 7 HMPOs. In this case, our conclusion would be a 45% (22/49) detection rate of methanol masers toward the more evolved objects (UCHII regions) and a 29% (2/7) detection rate toward the younger sources (HMPOs) of our sample, i.e.;

⁵This publication makes use of data products from the Wide-field Infrared Survey Explorer, which is a joint project of the University of California, Los Angeles, and the Jet Propulsion Laboratory/California Institute of Technology, funded by the National Aeronautics and Space Administration.

masers would appear more common toward the UCHII regions. As pointed out before, as more sensitive observations become available, more centimeter sources will appear, further increasing the fraction of sources classified as UCHII regions regardless of the nature of the ionized gas. Moreover, a spectral index analysis of the 15 weak sources indicates that in almost all cases the emission comes from thermal jets, suggesting that these compact and weak sources are in a pre-UCHII region phase, so, they should not be counted as UCHII regions (Rosero et al. 2016).

A final factor to consider is that many of the 56 fields observed have multiple objects in different evolutionary stages, as discussed in Section 3.4.2. This was revealed from IR, millimeter and centimeter observations (S02; Beuther et al. 2002a; Zapata et al. 2006; Rosero et al. 2016). In some cases (18102–1800, 18290–0924, 18488+0000, 20293+3952), the dominant source in the field is a bright, extended centimeter source which also dominates the mid-IR emission and appears as an extended red feature in the Spitzer images. Close to these extended red sources, there are compact green objects. In these four cases, the masers are projected against the compact objects — not the more-extended (and presumably more-evolved) centimeter sources. Clearly it would be misleading to associate these masers with the HII regions, even though the latter are present in the field.

3.6 Summary and conclusions

This survey (Survey IV) presents VLA observations of the 44 GHz Class I methanol maser transition toward a sample of 56 high-mass protostellar objects selected from the catalog of Sridharan et al. (2002). Our main conclusions can be summarized as follows:

1. We detect the 44 GHz transition of Class I methanol maser emission in 24 of the 56 fields observed (a 43% detection rate).
2. We find a total of 83 maser components with linewidths ranging from 0.17 km s^{-1} to 3.3 km s^{-1} . A histogram of the linewidths shows a flat distribution without a clear peak; the median linewidth is 1.1 km s^{-1} .
3. The maser velocities relative to the host molecular clouds range from -2.5 to $+3.1 \text{ km s}^{-1}$. The distribution of these relative velocities peaks near zero but we note a possible small redshift asymmetry.
4. The Spitzer/IRAC images together with VLA centimeter continuum emission reveal multiple sources in different evolutionary stages in each field. The majority of the 44 GHz masers appear to favor the younger sources in each region. The more notorious cases are 18102–1800, 18290–0924, 18488+0000 and 20293+3952 where the 44 GHz masers are preferentially located toward the more compact and presumably younger object in the field.
5. We report a possible instance of a 44 GHz maser associated with a low-mass protostar in the region IRAS 20293+3952. If confirmed, this region will be the fifth known star-forming region that hosts Class I masers associated with low-mass protostars.
6. Three of the 24 fields with maser emission were catalogued as EGOs by Cyganowski et al. (2008; 18182–1433, 18264–1152 and 18566+0408). We suggest that at least nine more fields host objects with green excess and morphology similar to EGOs (05358+3543, 18151–1208, 18247–1147, 18290–0924, 18345–0641, 18488+0000, 18517+0437, 20126+4104 and 20293+3952). The spatial coincidence of the 44 GHz masers and the shocked molecular gas traced by the green excess supports the idea that these masers may arise from molecular outflows.

7. A comparison of our results with previous VLA surveys suggests that IRAS 20126+4104 is a plausible case of maser variability. We detect bright masers (about 20 Jy) in sources 05358+3543 and 18264–1152 which were not detected by single-dish observations, suggesting variability.

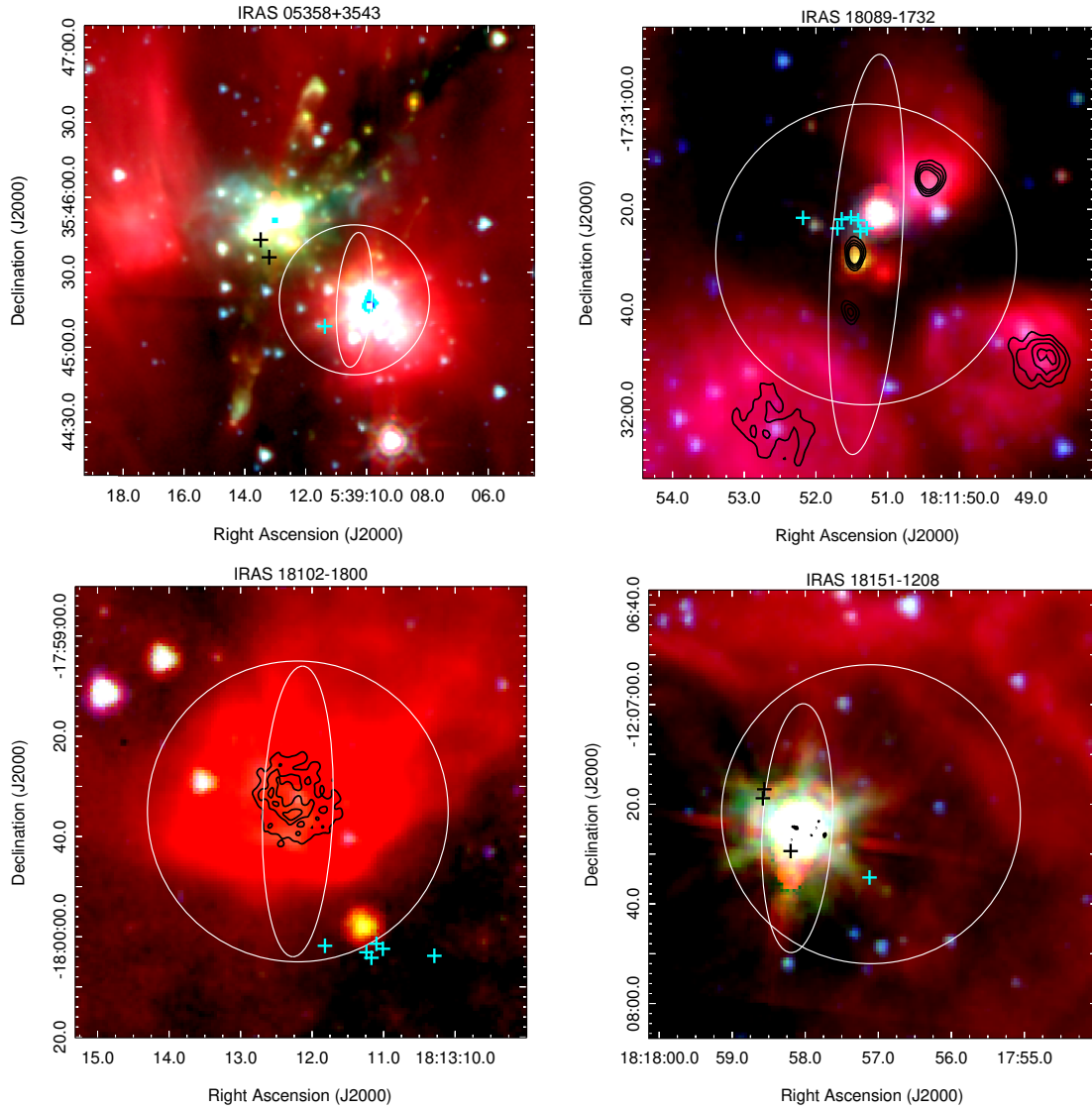


Figure 3.5: Three-color images taken from the GLIMPSE catalog obtained with the Spitzer Space Telescope (IRAC bands: blue = $3.6 \mu\text{m}$; green = $4.5 \mu\text{m}$; red = $8.0 \mu\text{m}$). Black/white contours show observations of centimeter continuum emission from VLA archival data (see Table 3.1 for contour levels and references). Cyan/black crosses mark the peak position of 44 GHz methanol masers from Table 3.4. For sources 23033+5951 and 23139+5939 Spitzer images are not available, instead, we use mid-IR images from WISE (WISE bands: blue = $3.4 \mu\text{m}$; green = $4.6 \mu\text{m}$; red = $12 \mu\text{m}$). The white circles represent the VLA primary beam of our observations ($\sim 1'$). The white ellipses are centered at the IRAS position which in some cases is offset by several arcseconds from the positions reported by S02.

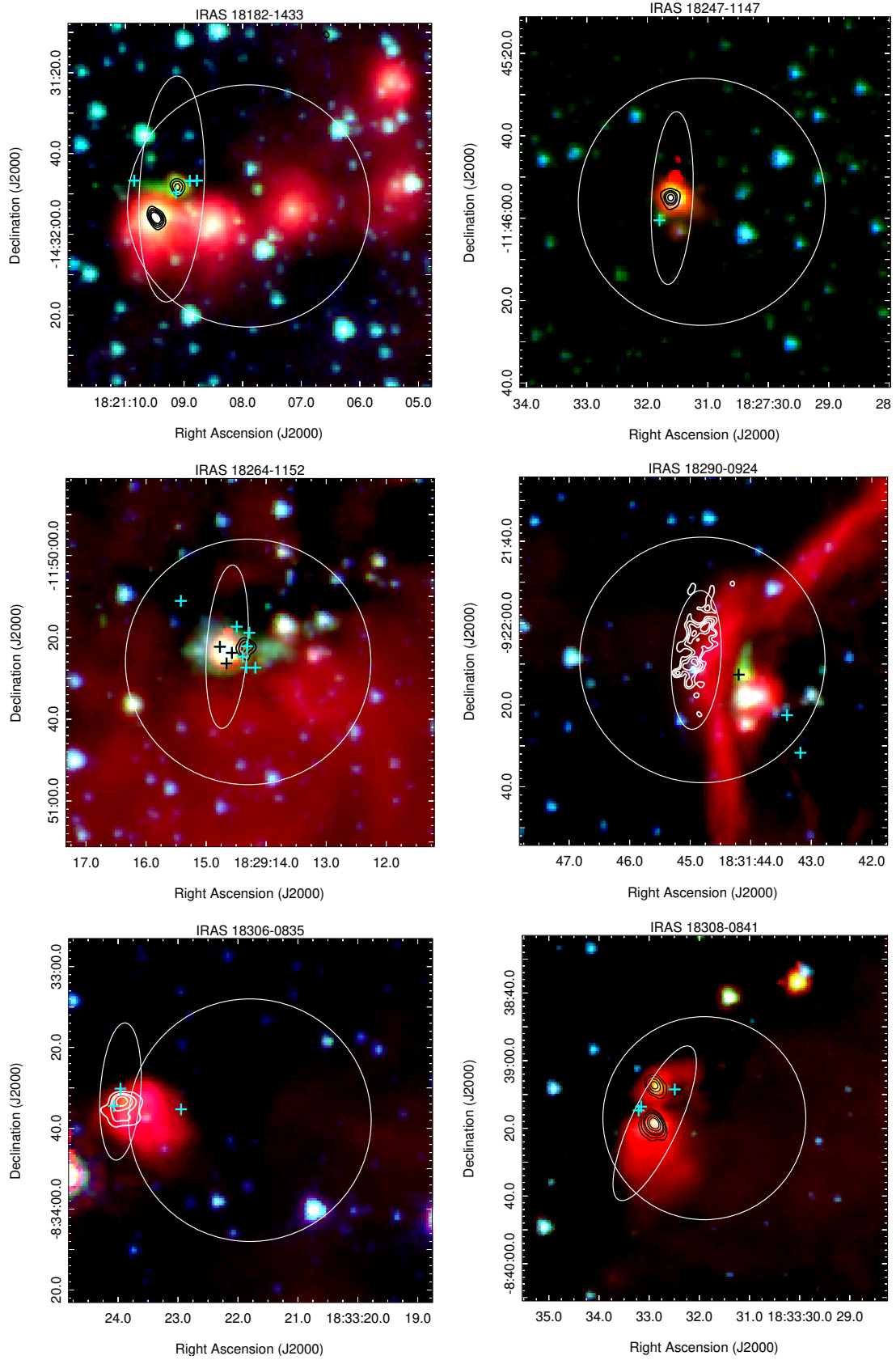


Figure 3.5: Continued

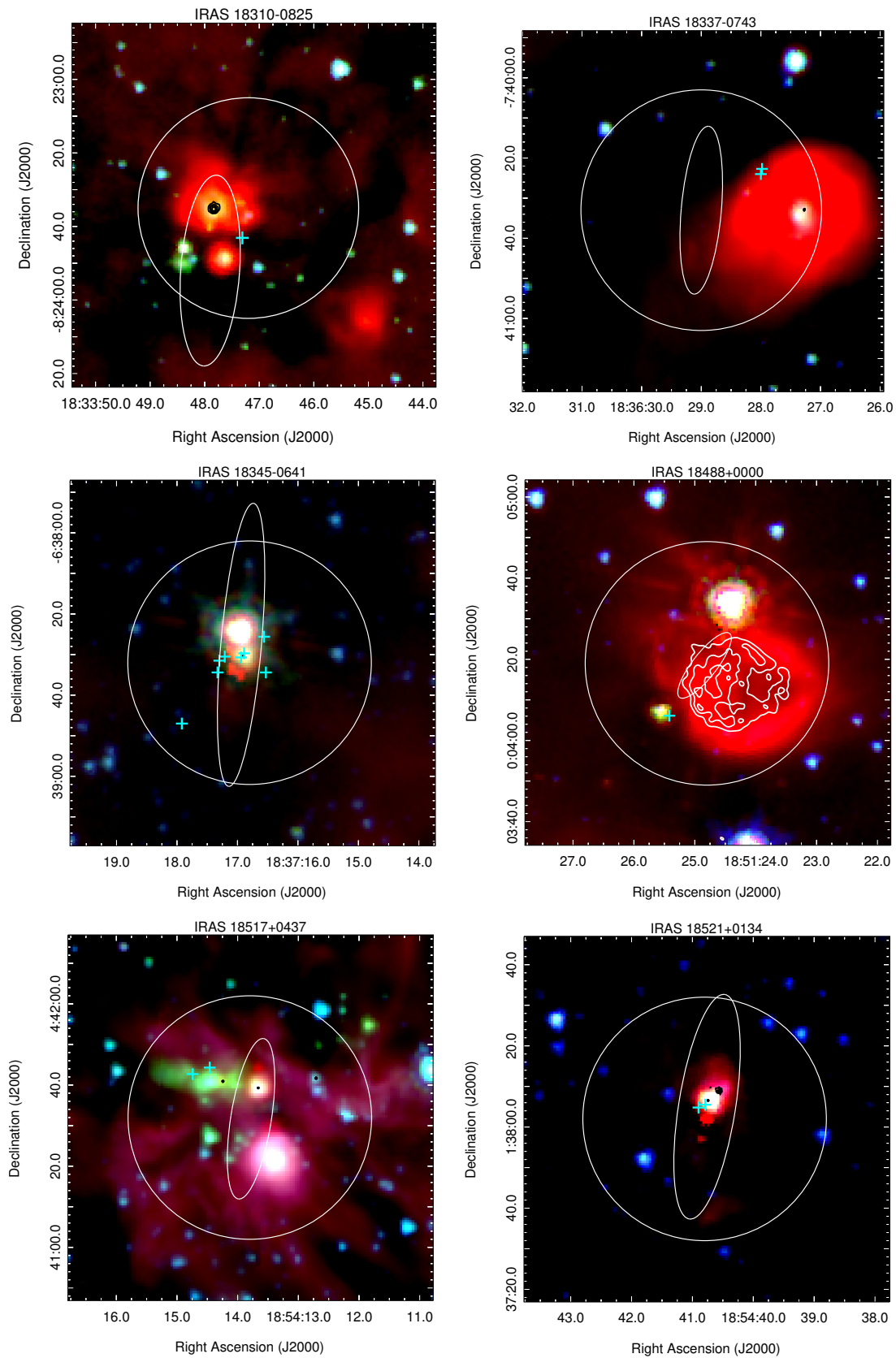


Figure 3.5: Continued

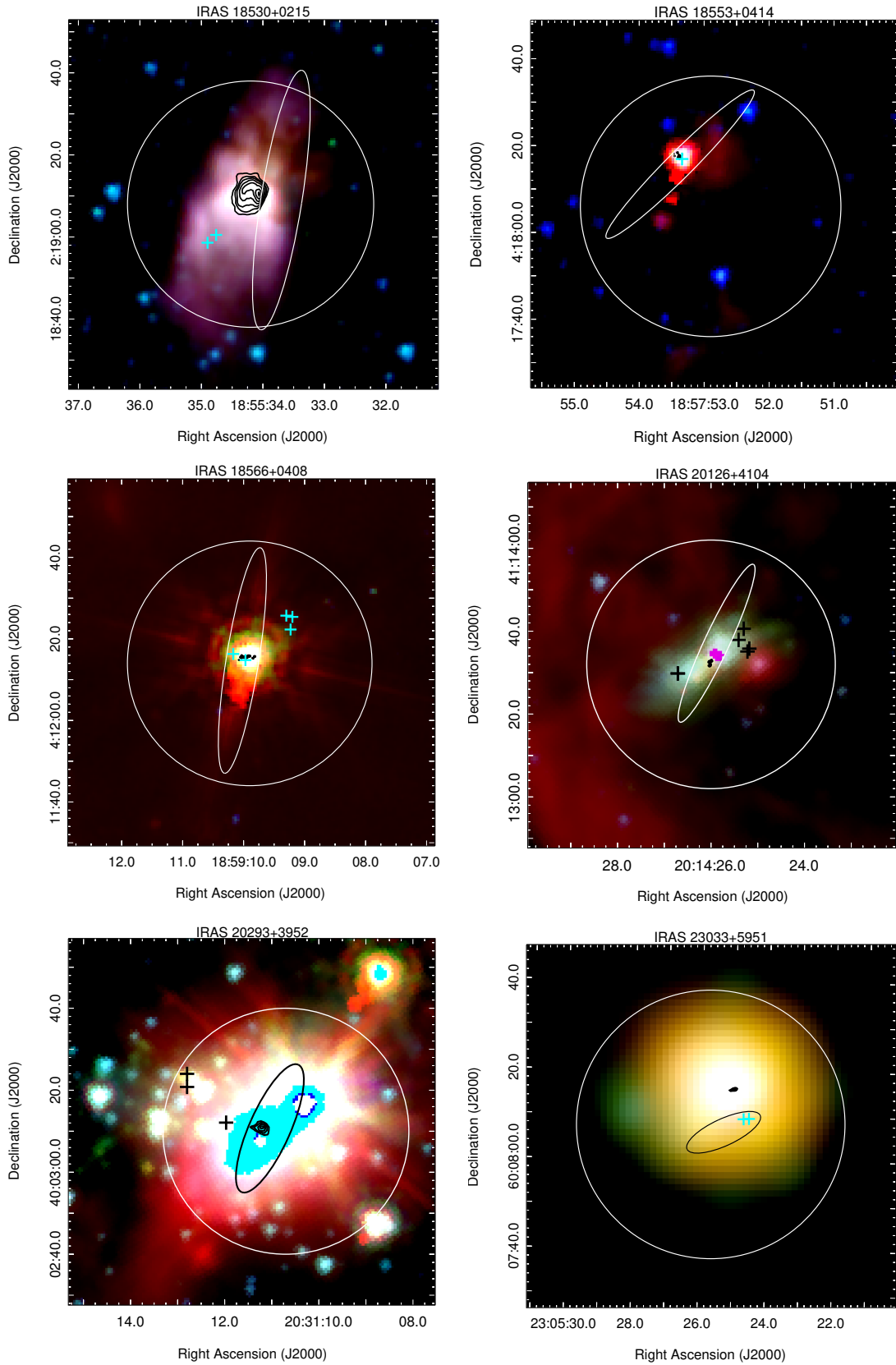


Figure 3.5: Continued

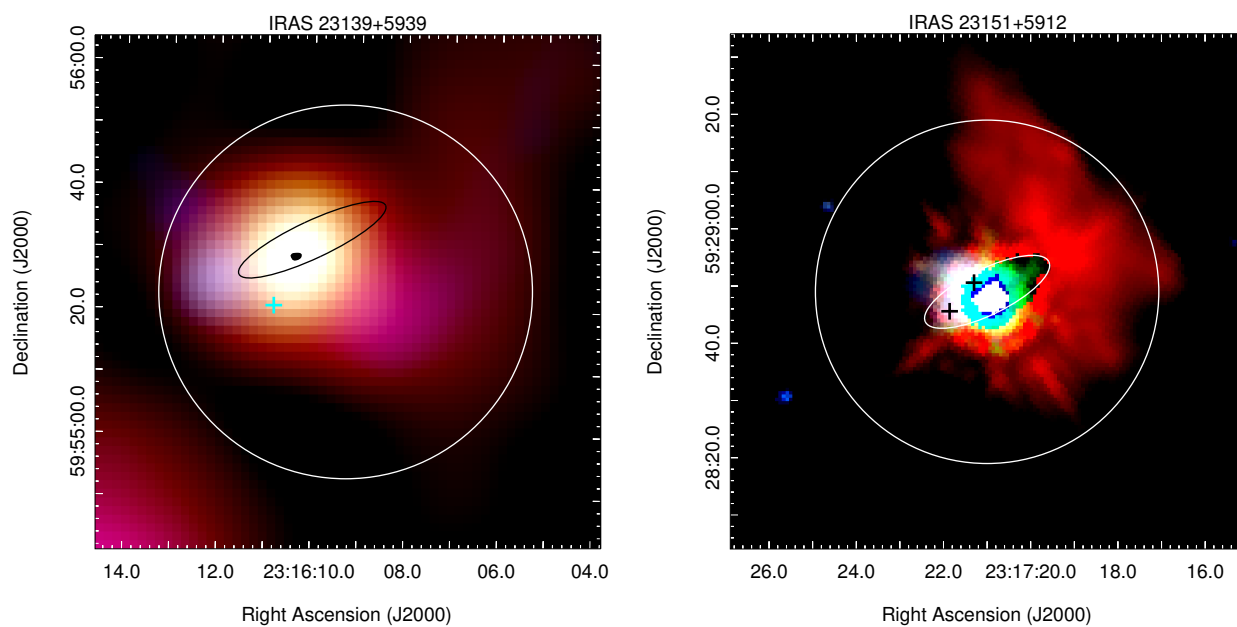


Figure 3.5: Continued

Chapter 4

Continuum emission and methanol masers toward high-mass star-forming regions

We present 7 mm continuum observations toward 13 well-known high-mass protostellar objects. The observations were taken with the Karl G. Jansky Very Large Array in the C-configuration at an angular resolution of about $0''.4$. We detect radio continuum emission in 5 of the 13 regions observed. Our observations were also sensitive to the Class I methanol maser transition $7_0 \rightarrow 6_1 A^+$ at 44 GHz; we detect masers toward 4 of the 13 regions. The observations had a spectral resolution of 13.6 km s^{-1} ; because of this low spectral resolution, we are unable to precisely characterize the line parameters, but the positions provided have sub-arcsecond accuracy, and thus precisely locate the masers with respect to the continuum emission.

4.1 Introduction

The Sridharan et al. (2002, hereafter S02) sample consists of 69 high-mass protostellar objects that have been extensively studied in different star formation tracers. Such tracers include maser emission of different molecules, including methanol. Rodríguez-Garza et al. (2017, defined as Survey IV in Chapter 3) presented a catalog of Class I 44 GHz methanol masers toward 56 of these 69 HMPOs. At the time of those observations in 2008, due to the dynamical scheduling of the Very Large Array (VLA), observations of the remaining 13 HMPOs were not completed. After the VLA was upgraded in 2012, its new capabilities facilitated the observation of continuum emission for large samples of weak sources.

Here we report Q-band VLA observations toward the remaining 13 HMPOs of the S02 sample. We detect continuum emission at 7 mm in 5 HMPOs. The continuum emission is reported here for the first time, and provides useful data points in the spectral energy distributions for modelling of these regions. We find methanol emission toward 4 HMPOs in the transition $7_0 \rightarrow 6_1 A^+$ at 44 GHz. This is a well-known Class I maser transition that is generally correlated with outflows in star-forming sites (Cyganowski et al. 2009). Typically, Class I 44 GHz methanol masers show narrow line widths of $\lesssim 1 \text{ km s}^{-1}$, so, we will refer to our detections as “maser candidates”, considering that they were observed at the low spectral resolution of 13.6 km s^{-1} . Nevertheless, the emission is almost certainly maser because only bright masers are likely to overcome the spectral dilution and permit detection. Similar low resolution studies of Class I methanol “maser candidates” at 36 GHz (Yusef-Zadeh et al. 2013) have been confirmed to be masers at higher spectral resolution (Cotton and Yusef-Zadeh 2016). Even though we cannot obtain the maser line parameters, the

high angular resolution observations give accurate positions of the masers.

The chapter is organized as follows: Section 4.2 describe the observational program and data reduction, Section 4.3 presents the results in tabular form and provides mid-IR images overlaid with the continuum emission and the positions of the masers detected, and Section 4.4 gives a brief discussion of the results obtained. In the rest of the chapter, we use the abbreviated names of the regions, e.g., I19012 for IRAS 19012+0536.

4.2 Observations and data reduction

The observations were made with the Karl G. Jansky Very Large Array of the NRAO¹ during two observing sessions on 2012 April 05 and 07 under project code 12A-334. Each source was observed for 7 minutes, under excellent weather conditions (with rms phase variations $\leq 2^\circ$), in the Q (7 mm) band. The array was in C-configuration, resulting in uv distances from 10 to 480 k λ , which yield $0''.4$ angular resolution and about $20''$ maximum detectable angular scales. The observations covered a total bandwidth of 2024 MHz distributed in two subbands of 8 spectral windows each. Each spectral window had a bandwidth of 128 MHz divided into 64 channels of 2 MHz each, providing a spectral resolution of about 13.6 km s^{-1} . The total bandwidth ranges from 42987 MHz to 45011 MHz which includes the Class I methanol maser transition $7_0 \rightarrow 6_1 A^+$ at a rest frequency of 44069.430 MHz. This methanol line falls in a single spectral window which we will refer to as the “maser window”.

The data were edited, calibrated and imaged in a standard fashion using the Common Astronomy Software Applications package (CASA). The images were formed with $0''.06$ pixels and using a Briggs weighting with a robustness of 0.5. No self-calibration was performed. The quasar 3C286 was used as the flux density calibrator for all sources. A summary of the observed sources and phase calibrators is given in Table 4.1.

Table 4.1: Observational program summary

Observation Date	Phase Calibrator	Flux Density mJy	Calibrator* Code	Sources calibrated
2012 Apr 05	J1850+2825	432.9	A	19266+1745, 19282+1814
	J1902+3159	681.7	A	19403+2258, 19410+2336, 19411+2306, 19413+2332, 19471+2641
2012 Apr 07	J1856+0610	164.2	B	19012+0536, 19035+0641, 19074+0752, 19175+1357, 19217+1651, 19220+1432

Notes.

*The codes A and B correspond to positional accuracies of $< 0''.002$ and $0''.002-0''.01$, respectively.

Table 4.2 shows general information of the continuum and line observations. Column (1) shows the IRAS source name, columns (2) and (3) list the pointing center in J2000 coordinates, columns (4) through (9) present the 1σ rms noise, synthesized beam size and position angle of the continuum image and spectral line cube, respectively.

For the continuum emission, we imaged the complete passband excluding the edge channels of each spectral window, and when detected, we exclude the channels with methanol maser emission to avoid contamination. The images were cleaned until the residuals were noise-like. The mean 1σ rms noise of the

¹The National Radio Astronomy Observatory (NRAO) is operated by Associated Universities, Inc., under a cooperative agreement with the National Science Foundation.

continuum images is $0.23 \text{ mJy beam}^{-1}$ (see Table 4.2).

For the methanol line, we made an image cube from the central channels of the maser window. The cubes were cleaned interactively by setting boxes around the maser components and we stopped cleaning when the residuals were noise-like. The 1σ rms noise reported in column (7) of Table 4.2 was obtained from the image cube excluding channels with maser emission, the band edges and the image borders. The mean 1σ rms noise of the continuum images is $5.2 \text{ mJy beam}^{-1}$.

Table 4.2: Summary of continuum and line observational parameters

Source IRAS Name	J2000 Pointing Center		Continuum Images			Line Images		
	$\alpha(\text{h m s})$	$\delta(^{\circ} ' ")$	rms (mJy beam^{-1})	Synthesized Beam (arcsec)	(deg)	rms (mJy beam^{-1})	Synthesized Beam (arcsec)	(deg)
19012+0536	19 03 45.1	+05 40 40	0.20	0.54×0.41	-19.6	4.8	0.57×0.47	-18.3
19035+0641	19 06 01.1	+06 46 35	0.22	0.53×0.42	-19.3	4.9	0.56×0.48	-16.6
19074+0752	19 09 53.3	+07 57 22	0.20	0.53×0.42	-18.2	5.0	0.56×0.48	-20.9
19175+1357	19 19 49.1	+14 02 46	0.20	0.50×0.42	-18.8	4.7	0.54×0.48	-30.3
19217+1651	19 23 58.8	+16 57 37	0.52	0.49×0.43	-18.6	4.9	0.53×0.48	-25.0
19220+1432	19 24 19.7	+14 38 03	0.22	0.49×0.42	-19.1	5.0	0.52×0.48	-23.1
19266+1745	19 28 54.0	+17 51 56	0.23	0.52×0.43	-54.5	5.8	0.67×0.46	-52.0
19282+1814	19 30 28.1	+18 20 53	0.22	0.51×0.43	-52.3	6.1	0.66×0.46	-50.6
19403+2258	19 42 27.2	+23 05 12	0.20	0.51×0.44	-66.5	5.3	0.65×0.47	-54.9
19410+2336	19 43 11.4	+23 44 06	0.20	0.55×0.43	-56.1	5.3	0.64×0.47	-53.9
19411+2306	19 43 18.1	+23 13 59	0.20	0.50×0.44	-62.8	5.3	0.63×0.47	-52.8
19413+2332	19 43 28.9	+23 40 04	0.20	0.49×0.44	-63.9	5.3	0.63×0.47	-54.1
19471+2641	19 49 09.9	+26 48 52	0.21	0.49×0.44	-70.0	5.2	0.63×0.47	-52.8

4.3 Results

We considered a detection when the peak flux density was above the 5σ rms noise level of the image. Following this criterion, we detected continuum emission toward 5 of the 13 regions while class I 44 GHz methanol masers were detected in 4 regions. Toward I19035 we detected two continuum sources, therefore, a total of 6 different continuum sources were detected. Three sources, I19012, I19217 and I19410, showed both continuum emission and 44 GHz maser emission.

4.3.1 Continuum emission

The parameters obtained from the continuum maps for the 5 regions detected are reported in Table 4.3. The IRAS name of each region is listed in column (1); in some cases, two sources were detected in a single region, we add a letter to the source name to distinguish between them. The peak positions of the detected continuum emission are given in columns (2) and (3). The deconvolved source size was obtained by fitting a 2D Gaussian and is given in column (4); when the source is unresolved, we give upper limits to the source size. The peak and integrated flux densities from the 2D Gaussian fits are given in columns (5) and (6). Column (7) indicates the multiples of the rms noise that were used to build the contour maps shown in Figure 4.1.

Table 4.3: Parameters obtained for the 7 mm continuum sources detected.

Source IRAS Name	J2000 Peak Position		Source Size (arcsec)	Peak Intensity (mJy beam ⁻¹)	Integrated Intensity (mJy)	Contour ^a levels
	α (h m s)	δ (° ' ")				
19012+0536 A	19 03 45.27	+05 40 42.7	< 0.5 ^b	1.45 ± 0.06	1.74 ± 0.13	-4, 4, 5, 6, 7
19035+0641 A	19 06 01.60	+06 46 36.0	< 0.5 ^b	1.13 ± 0.03	1.17 ± 0.06	-4, 4, 6, 8, 10
19035+0641 B	19 06 01.48	+06 46 35.4	< 0.5 ^b	2.30 ± 0.09	2.08 ± 0.15	-4, 4, 6, 8, 10
19074+0752	19 09 53.55	+07 57 15.1	1.08 × 0.81	2.61 ± 0.25	12.9 ± 1.50	-4, 4, 6, 8, 10, 12
19217+1651 A	19 23 58.81	+16 57 41.1	0.26 × 0.10	34.9 ± 1.30	42.1 ± 2.50	-6, 6, 10, 20, 30, 40, 50, 60
19410+2336	19 43 11.19	+23 44 03.0	0.29 × 0.19	1.73 ± 0.13	2.15 ± 0.26	-4, 4, 6, 8

Notes.

The errors for the peak intensities and integrated flux densities were obtained from the 2D gaussian fit.

^a The contour levels are multiples of the rms noise reported in Table 4.2. The contour maps are shown in Figure 4.1.

^b Component is a point source. We give the geometric mean of the synthesized beam size reported in Table 4.2 as an upper limit to the source size.

Assuming that the detected continuum emission arises from homogeneous optically thin HII regions, we estimate physical parameters and list them in Table 4.4. The distance ambiguity has not been resolved for some sources, therefore, we calculate the parameters for both the near and far distance (D , col. 2). The linear diameter of the sources (d , col. 3) was obtained using the geometric mean of the deconvolved source sizes given in Table 4.3. We calculated the source brightness temperature (T_b , col. 4) using

$$T_b = \frac{S_\nu c^2}{2 k_b \nu^2 \Omega_s}, \quad (4.1)$$

where S_ν is the integrated flux density, c the speed of light, k_b the Boltzmann constant, ν the frequency of the observations and Ω_s is the solid angle of the source. We consider a solid angle of the form $\Omega_s = \frac{\pi}{4 \ln(2)} \theta_s^2$, where θ_s is the geometrical mean of the major and minor axes of the source, $\theta_s = \sqrt{\theta_{maj} \theta_{min}}$. Substituting this expression and normalizing to convenient units, we obtained equation 4.2 for the brightness temperature,

$$T_b = 1224.4 \left[\frac{S_\nu}{\text{mJy}} \right] \left[\frac{\nu}{\text{GHz}} \right]^{-2} \left[\frac{\theta_s}{''} \right]^{-2}. \quad (4.2)$$

For unresolved sources (I19012, I19035), we give a lower limit to T_b .

At the observing frequency of 44 GHz all but the highest density HII regions will be optically thin ($\tau \ll 1$). Under this assumption, the brightness temperature can be expressed as $T_b \simeq T_e \tau_\nu$. T_e is the electron temperature and the optical depth of free-free emission (Altenhoff et al. 1960) can be approximated as

$$\tau_\nu \simeq 0.08235 \left[\frac{EM}{\text{cm}^{-6} \text{ pc}} \right] \left[\frac{T_e}{\text{K}} \right]^{-1.35} \left[\frac{\nu}{\text{GHz}} \right]^{-2.1}, \quad (4.3)$$

where EM (col. 5) is the emission measure along the line of sight, $EM = \int n_e n_i dl$, and n_e and n_i are the electron and ion density, respectively. Using Equations 4.2, 4.3 and the approximation $T_b \simeq T_e \tau_\nu$, the emission measure can be written as

$$\left[\frac{EM}{\text{cm}^{-6} \text{ pc}} \right] = 1.5 \times 10^4 \left[\frac{S_\nu}{\text{mJy}} \right] \left[\frac{\nu}{\text{GHz}} \right]^{0.1} \left[\frac{T_e}{\text{K}} \right]^{0.35} \left[\frac{\theta_s}{''} \right]^{-2}. \quad (4.4)$$

We note that this equation is 1.13 times smaller than that reported by Sánchez-Monge et al. (2013); the difference comes from the factor $\frac{\pi}{4 \ln(2)}$ which appears in equation 4.1, which assumes a Gaussian shape for the source solid angle.

For ionized hydrogen in a homogeneous medium of depth L , the emission measure is $EM = n_e^2 L$. In our case, considering spherical geometry, L corresponds to the source linear diameter given by $d = \theta_s D$. From this, we can obtain an expression for the electron density (n_e , col. 6),

$$\left[\frac{n_e}{\text{cm}^{-3}} \right] = 1751.2 \left[\frac{S_\nu}{\text{mJy}} \right]^{0.5} \left[\frac{\nu}{\text{GHz}} \right]^{0.05} \left[\frac{T_e}{\text{K}} \right]^{0.175} \left[\frac{\theta_s}{''} \right]^{-1.5} \left[\frac{D}{\text{kpc}} \right]^{-0.5}. \quad (4.5)$$

The mass of ionized gas (M_i , col. 7) is defined as $M_i = \int n_e m_H dV$; m_H is the hydrogen mass and the integral is over the volume of a sphere of radius $d/2$. Using equation 4.5 and $V = \frac{4\pi}{3} \left(\frac{\theta_s D}{2}\right)^3$, the mass of an HII region is

$$\left[\frac{M_i}{M_\odot} \right] = 2.6 \times 10^{-6} \left[\frac{S_\nu}{\text{mJy}} \right]^{0.5} \left[\frac{\nu}{\text{GHz}} \right]^{0.05} \left[\frac{T_e}{\text{K}} \right]^{0.175} \left[\frac{\theta_s}{''} \right]^{1.5} \left[\frac{D}{\text{kpc}} \right]^{2.5}. \quad (4.6)$$

The emission rate of Lyman continuum photons with $\lambda < 912 \text{ \AA}$ and capable of ionizing hydrogen (\dot{N}_i , col. 8), necessary to maintain the ionization of an HII region can be estimated by considering the equation between the number of recombinations and the number of photoionizations. Therefore, the number of ionizing photons is

$$\dot{N}_i = \frac{4\pi}{3} R_s^3 n_e^2 \alpha^{(2)}, \quad (4.7)$$

where R_s is the Strömgen radius and $\alpha^{(2)}$ is the sum of recombination coefficients to level 2 or higher. For $T_e \simeq 10^4 \text{ K}$, $\alpha^{(2)}$ is equal to $3 \times 10^{-13} \text{ cm}^3 \text{ s}^{-1}$. In practical units, \dot{N}_i is

$$\left[\frac{\dot{N}_i}{\text{s}^{-1}} \right] = 1.6 \times 10^{42} \left[\frac{S_\nu}{\text{mJy}} \right] \left[\frac{\nu}{\text{GHz}} \right]^{0.1} \left[\frac{T_e}{\text{K}} \right]^{0.35} \left[\frac{D}{\text{kpc}} \right]^2. \quad (4.8)$$

With the flux of ionizing photons and assuming the HII region is produced by a single star, we estimate the spectral type (col. 9) of the ionizing star using the table of Panagia (1973).

We estimate the spectral index of the 6 continuum sources by a linear fitting of data points between 6 cm and 7 mm. The results of the fitting are summarized in Table 4.4 (col. 10) and shown in Figure 4.2. We searched in the literature for flux densities at various wavelengths from 6 cm to 1.3 cm (see Table 4.5). We used VLA observations at 6 cm from the surveys of Rosero et al. (2016) and the Co-Ordinated Radio 'N' Infrared Survey for High-mass star formation (CORNISH; Purcell et al. 2013), respectively. For the 3.6 cm observations we used the results given by S02 and the unpublished data presented in Sánchez-Monge (2011). The 2 cm and 1.3 cm flux densities were taken from observations reported by Rosero et al. (2016) and Garay et al. (2007). When a source was not detected, we give the detection limit of the corresponding observations as an upper limit for the source flux density. Our 7 mm observations have roughly similar resolutions and sensitivities as the observations found in the literature. CORNISH was conducted in B-configuration at $1.''5$ resolution with a 1σ rms sensitivity of $0.4 \text{ mJy beam}^{-1}$. S02 observations were taken in B-configuration as well, with an angular resolution of $0.''7$ and an 1σ rms noise of $0.1 \text{ mJy beam}^{-1}$. A detailed discussion on each of the flux density distributions will be given in Section 4.4.

Table 4.4: Physical parameters of detected continuum sources, assuming optically thin free-free emission.

Source Name	D (kpc)	Diameter (pc)	T_b (K)	EM (cm^{-6}pc)	n_e (cm^{-3})	M_i (M_\odot)	N_i (s^{-1})	Spectral Type	Spectral Index
19012+0536 A*	4.6	<0.0104	> 4.9	> 4.3×10^6	> 2.0×10^4	< 3.0×10^{-4}	2.1×10^{45}	B1	+0.9 ± 0.1
	8.6	<0.0196	> 4.9	> 4.2×10^6	> 1.4×10^4	< 1.4×10^{-3}	7.6×10^{45}	B1	+0.9 ± 0.1
19035+0641 A*	2.3	< 0.0052	> 3.3	> 2.8×10^6	> 2.3×10^4	< 4.3×10^{-5}	3.6×10^{44}	B2	+0.9 ± 0.1
	12.9	< 0.0295	> 3.3	> 2.8×10^6	> 9.8×10^3	< 3.2×10^{-3}	7.3×10^{44}	B2	+0.9 ± 0.1
19035+0641 B*	2.3	< 0.0052	> 5.9	> 5.1×10^6	> 3.1×10^4	< 5.8×10^{-5}	6.4×10^{44}	B2	-0.1 ± 0.1
	12.9	< 0.0295	> 5.9	> 5.1×10^6	> 1.3×10^4	< 4.3×10^{-3}	2.0×10^{46}	B0.5	-0.1 ± 0.1
19074+0752	8.7	0.0394	9.3	8.0×10^6	1.4×10^4	1.1×10^{-2}	5.7×10^{46}	B0.5	-0.1 ± 0.1
19217+1651 A	10.5	0.0082	1020	8.8×10^8	3.3×10^5	2.3×10^{-3}	2.7×10^{47}	B0	+0.3 ± 0.1
19410+2336	2.1	0.0023	24.6	2.1×10^7	9.4×10^4	1.6×10^{-5}	5.6×10^{44}	B2	> +0.8

Notes.

* This source is unresolved; we use the synthesized beam size to calculate its parameters.

Table 4.5: Flux densities at various wavelengths taken from different VLA observations.

IRAS Name	6 cm	3.6 cm	2 cm	1.3 cm	7 mm [†]
19012+0536 A	0.22 ^a	<1.0 ^c	...	0.91 ^a	1.74
19035+0641 A	0.18 ^a	0.2 ^e	...	0.75 ^a	1.17
19035+0641 B	2.81 ^a	2.8 ^e	...	2.27 ^a	2.08
19074+0752	14.80 ^b	14.8 ^c	12.90
19217+1651 A	22.55 ^b	24.8 ^d	29.8 ^f	32.0 ^d	42.10
19410+2336	<0.4 ^b	0.77 ^g	2.15

Notes. The flux density units are mJy.^aRosero et al. (2016). ^bCORNISH survey Purcell et al. (2013).^cSridharan et al. (2002). ^dRodríguez-Esnard et al. (2012).^eUnpublished data of Sánchez-Monge (2011)^fGaray et al. (2007). ^gXu et al. (2009).[†] This work. ... No data available.

4.3.2 Class I methanol masers

We detected methanol emission toward four of the 13 HMPOs, the emission parameters are reported in Table 4.6. Column (1) gives the IRAS name of the field, Columns (2) and (3) show the peak position of the emission, Column (4) gives the angular size of the emitting region as determined by a 2D gaussian fit. Column (5) lists the LSR velocity of the channel where the emission was found. Columns (6) and (7) give the peak intensity and the integrated flux density calculated from a gaussian fit using the task IMFIT. Column (8) shows the maser brightness temperature, calculated using equation 4.2. The velocity uncertainty is about $\pm 7 \text{ km s}^{-1}$, given by the channel width (13.6 km s^{-1}). The size of some emission regions could not be obtained, in those cases, we use the synthesized beam size reported in Column (8) of Table 4.2 to estimate the brightness temperature.

The emission line we detected is a known Class I methanol maser transition. Because the observations were taken with a low spectral resolution of 13.6 km s^{-1} we are unable to confirm the linewidth and precise velocity of the emission. In spite of the low spectral resolution, we are confident that the methanol emission detected is maser emission. Arguments that support this premise are that methanol masers are bright, often

with tens to hundreds of Jy, and show linewidths of tenths of km s^{-1} . In contrast, (quasi)thermal methanol emission typically shows intensities of tenths of Jy and linewidths from a few to tens of km s^{-1} (Mehringer and Menten 1997; Araya et al. 2008). Thus, only maser emission can overcome the spectral dilution of our observations and be detected in a single channel.

Table 4.6: Parameters of Class I 44 GHz methanol masers detected

Source IRAS name	J2000 Peak Position		Size ($''$)	Channel Velocity (km s^{-1})	Peak Intensity (mJy beam^{-1})	Integrated Intensity (mJy)	T_b^\dagger (K)
	$\alpha(\text{h m s})$	$\delta(\text{° ' ''})$					
19012+0536	19 03 45.38	+05 40 41.4	a	+67	94.0	149.1 ^c	350
	19 03 44.94	+05 40 41.9	a	+67	47.6	54.5	128
19175+1357	19 19 48.76	+14 02 48.2	0.45×0.37	+11	48.2	79.7	300
19217+1651	19 23 58.66	+16 57 42.8	0.24×0.22	-3	156.4	189.0	2256
	19 23 58.79	+16 57 38.2	0.45×0.12	-3	60.4	82.3	960
19410+2336	19 43 12.21	+23 44 08.7	$\lesssim 0.36 \times 0.14$	+21	297.0	332.0	4152
	19 43 12.10	+23 44 07.2	^b	+21	224.4	238.0	500
	19 43 12.06	+23 44 05.3	$\lesssim 0.48 \times 0.06$	+21	100.6	124.1	2725
	19 43 11.92	+23 44 05.4	0.36×0.22	+21	100.2	129.0	1030

Notes.

We remind the reader that the maser velocity is within $\pm 7 \text{ km s}^{-1}$ of the reported channel velocity.

^a Component is a point source. An upper limit on its size cannot be determined.

^b Could not deconvolve source from beam. Source may be (only marginally) resolved in only one direction.

^c There are at least two masers very close in position that were spectrally unresolved (see discussion in Section 4.4).

[†] The brightness temperature was calculated using the near distance for sources with distance ambiguity.

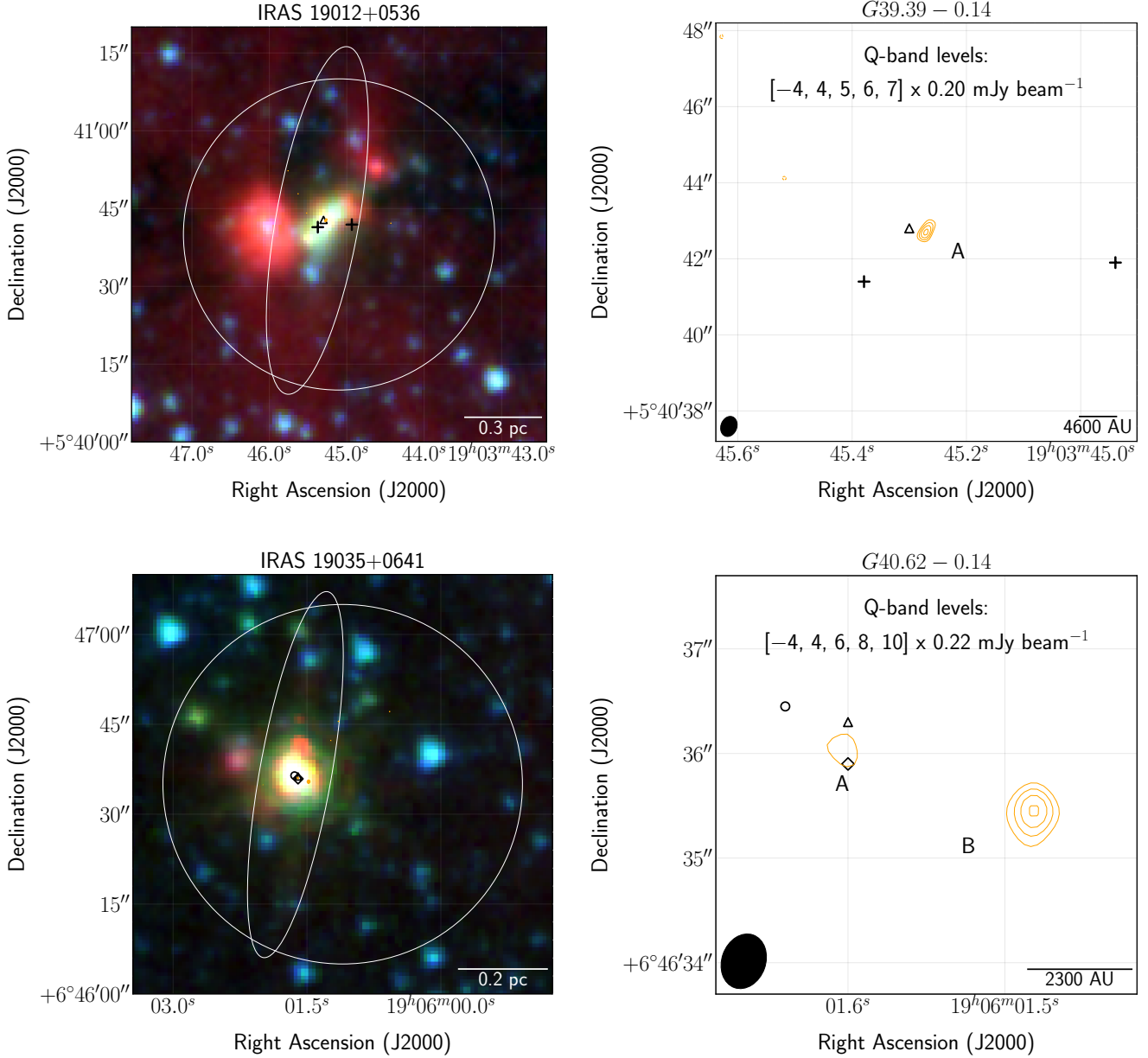


Figure 4.1: Left: Three-color images taken from the GLIMPSE catalog obtained with the Spitzer Space Telescope (IRAC bands: blue = 3.6 μm , green = 4.5 μm ; red = 8 μm). The crosses represent the peak position of the 44 GHz methanol masers reported in Table 4.6. The diamonds represent Class II methanol masers. The triangles represent the peak position of water masers. The black circles represent the OH masers. The stars indicate millimeter cores detected at 1.3 mm toward I19074 (Lu et al. 2018) and at 2.6 mm toward I19410 (Beuther et al. 2003). The white ellipses are centered at the IRAS position and symbolize the positional accuracy. The black contours trace the 7 mm continuum emission. For all sources except IRAS 19175+1357, the contour levels are shown in Table 4.3. The contour levels for IRAS 19175+1357 are $[-2, 2]$ times the rms noise of 0.20 mJy reported in Table 4.2. The synthesized beam is shown in the bottom left corner. Right: Zoomed version of the 7 mm continuum emission shown in the left.

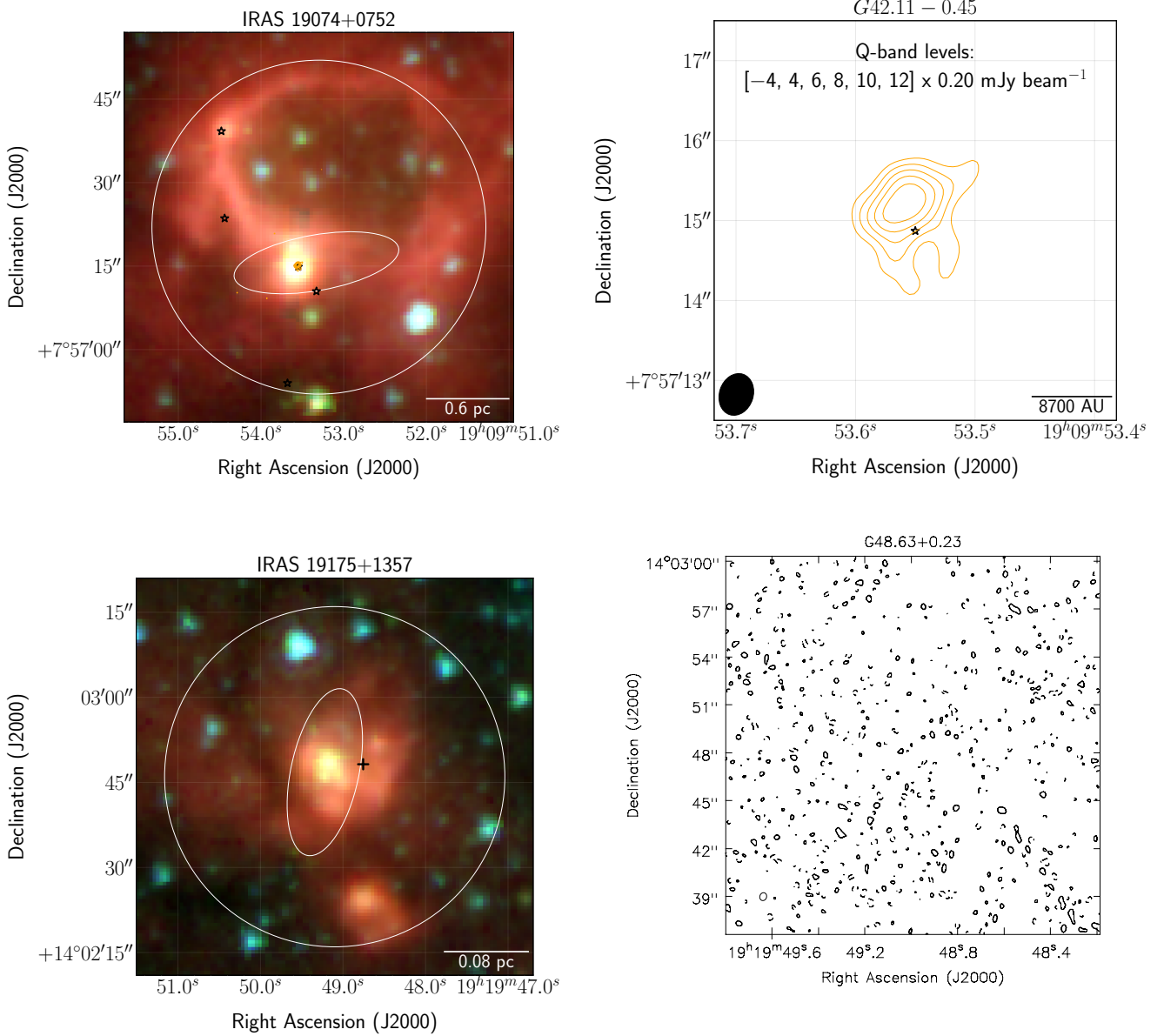


Figure 4.1: Continued

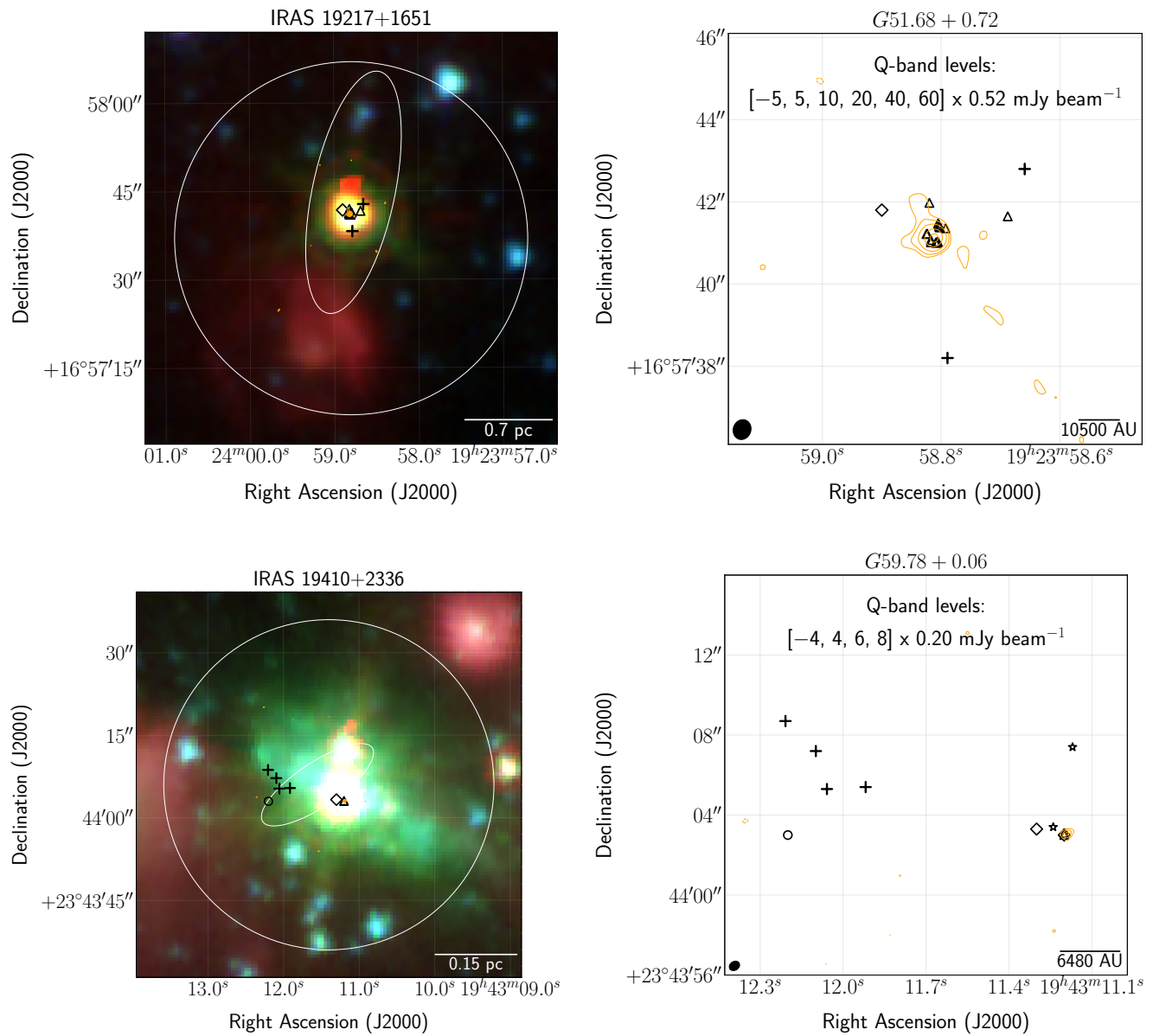


Figure 4.1: Continued

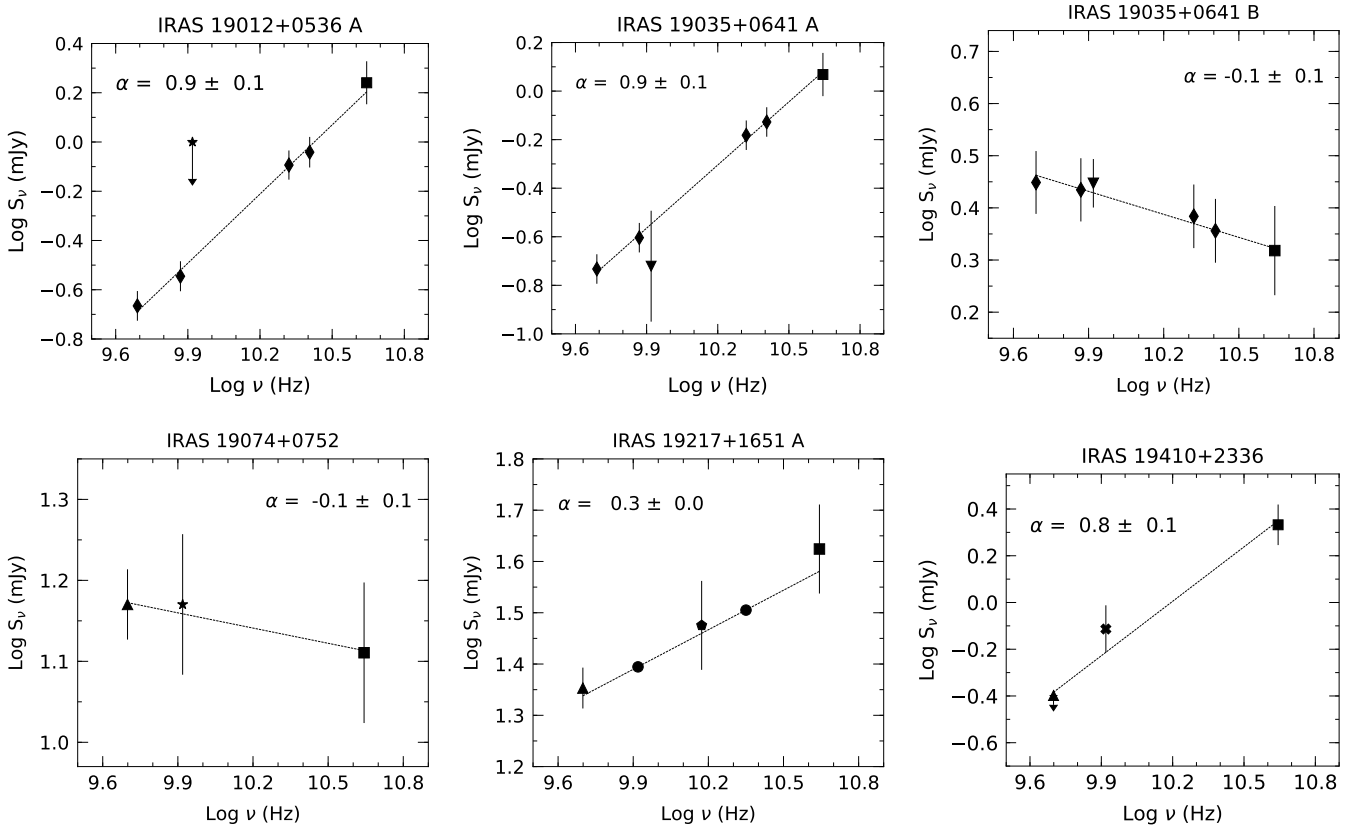


Figure 4.2: Flux density distribution of the six continuum sources detected at 7 mm (squares). Other data points were taken from the literature; the flux densities and the corresponding references are reported in Table 4.5. The vertical lines represent the error bars. The diamonds represent 5 to 25 GHz continuum emission from Rosero et al. (2016). The triangles show 5 GHz continuum emission from CORNISH survey (Purcell et al. 2013). The stars indicate 8 GHz continuum emission from Sridharan et al. (2002). The inverted triangles represent 8 GHz continuum emission taken from unpublished data of Sánchez-Monge (2011). The circles represent 5 and 22 GHz emission from Rodríguez-Esnard et al. (2012); the error bars are smaller than the circles. The pentagon symbolizes 15 GHz emission from Garay et al. (2007). The cross indicates the 8 GHz flux density reported by Xu et al. (2009). The downward arrows represent upper limits for the source flux density given by the 1σ rms noise reported by the authors. The lines are the best fit to the data assuming a power law of the form $S_\nu \propto \nu^\alpha$.

4.4 Discussion

Here we will discuss each of the 6 IRAS regions where continuum or maser emission, or both, were detected: I19012, I19035, I19074, I19175, I19217 and I19410.

IRAS 19012+0536

This region suffers the distance ambiguity; S02 reported both the near and far kinematic distances, which are 4.6 and 8.6 kpc, respectively. The corresponding luminosities are about 16,000 and 50,000 L_{\odot} (S02). It hosts a single dense core associated with a massive molecular outflow (Beuther et al. 2002a; 2002b). Two sources with different morphologies were detected by sensitive VLA observations between 5 and 25.5 GHz (Rosero et al. 2016). Rosero et al. reported a compact source, I19012-A, with flux densities of 0.22 and 0.91 mJy at 6 and 1.3 cm (see Table 4.5), respectively, while an extended source, G39.389–0.143 (G39.389 hereafter), was detected with 2.66 and 2.56 mJy at 6 and 1.3 cm. They measured a spectral index of +0.9 for I19012-A, whereas G39.389 showed a flatter spectral index of +0.2. We detect I19012-A with a 7 mm flux density of 1.74 mJy; we did not detect G39.389 since it is an extended source with a peak intensity at 1.3 cm around 0.05 mJy beam⁻¹ which lies below our 1σ rms noise of 0.2 mJy beam⁻¹.

I19012-A is a known EGO named as G39.39–0.14 by Cyganowski et al. (2008). I19012-A does not show H₂ outflows although two knots along the EGO's axis were found through K-band infrared images (Lee et al. 2013). Class I 44 GHz CH₃OH masers were not detected by Litovchenko et al. (2011) at a 1σ rms noise of about 1 Jy. Class I 95 GHz and Class II 6.7 GHz methanol masers were found in the region but their precise positions were not reported (S02; Beuther et al. 2002c; Chen et al. 2011). A water maser appears projected toward I19012-A (Beuther et al. 2002c).

The 7 mm continuum emission appears well-centered toward the green bipolar structure seen in the 4.5 μ m band suggesting that it is the powering source of the EGO (see Figure 4.1). The radio continuum spectrum of component A, in the range from 5 to 44 GHz, is shown in Figure 4.2. We note a rising spectral index of +0.9 consistent with that reported by Rosero et al., which could be explained by either an ionized jet or an optically thick non-uniform HII region. Naively assuming a homogeneous region of ionized gas located at 4.6 kpc with an angular size less than 0''5, we estimate an emission measure of 4.3×10^6 pc cm⁻⁶ (see Table 4.4). The total number of ionizing photons per second required to excite this region is 2×10^{45} s⁻¹, which could be supplied by a B1 Zero Age Main Sequence (ZAMS) star (Panagia 1973).

We detect two methanol masers at 44 GHz, although there is an indication of a third maser component. The brighter maser is marginally resolved, suggesting that it consists of at least two maser components closeby in position at nearby velocities. We report a single feature but we strongly suspect that at least 2 maser components are present with an angular separation of $\lesssim 0''3$. The brighter maser is projected against the EGO while the other appears at the EGO edge (see Figure 4.1). Both masers are at an LSR velocity of $+67 \pm 7$ km s⁻¹, consistent with that reported for the Class I 95 GHz and H₂O masers.

The 44 GHz masers are separated by 2''1 and 5''0 from the peak of the 7 mm emission. Taking 8.6 kpc as the source distance, this corresponds to a physical separation of 0.09 and 0.2 pc, respectively. Even at the far distance, the Class I masers are closer to the ionized region and the H₂O maser than the 1 pc distance suggested by the original classification of Class I methanol masers proposed by Menten and Batrla (1989).

IRAS 19035+0641

Caswell and Haynes (1983) reported near and far kinematic distances for this region of 2.2 and 12.9 kpc, respectively. The distance ambiguity has not been resolved although several authors have adopted the near value of 2.2 kpc (Forster and Caswell 1999; Hughes and MacLeod 1993; S02). At 2.2 kpc its luminosity is

about $8,000 L_{\odot}$ (S02). The region contains a single dust core related to a molecular outflow (Beuther et al. 2002a; 2002b). Two sources (A and B) were detected by VLA observations at 1.3 and 6 cm (Rosero et al. 2016). I19035-A is a faint compact source with an increasing flux density with frequency ($\alpha = +0.9$) and coincides with the peak position of an infrared source seen in the Spitzer/IRAC bands (see Figure 4.1). On the other hand, I19035-B is brighter and shows a flat spectral index ($\alpha = -0.1$) and appears displaced by $1''$ from the peak position of the infrared source shown in Figure 4.1. Class II 6.7 GHz CH₃OH and intense OH and H₂O masers are seen in projection against I19035-A (Forster and Caswell 1999; Argon et al. 2000; S02; Beuther et al. 2002c).

We detect I19035-A and B with 7 mm flux densities of 1.17 and 2.08 mJy, respectively (see Table 4.3). The flux density distribution of both sources from 5 to 44 GHz is shown in Figure 4.2. Both spectral indices agree with those reported by Rosero et al. We find a spectral index of +0.9 for I19035-A which could result from an ionized jet or an optically thick HII region. The spectral index of I19035-B is flat with a value of -0.1 , typical of optically thin free-free emission. This SED can be produced by an HII region with a size of 0.005 pc (at 2.2 kpc), an emission measure of $5.1 \times 10^6 \text{ cm}^{-6}\text{pc}$, an electron density of $3.1 \times 10^4 \text{ cm}^{-3}$, an ionized gas mass of $5.8 \times 10^{-5} M_{\odot}$ and flux of ionizing photons of $6.4 \times 10^{44} \text{ s}^{-1}$ which corresponds to a B2 ZAMS star (Panagia 1973; see Table 4.4).

No Class I 44 GHz methanol masers were detected toward this region; if masers are present, they have fluxes of less than a few Jy.

IRAS 19074+0752

For this region, Watson et al. (2003) and Anderson and Bania (2009) resolved the kinematic distance ambiguity through the H₂CO absorption and HI emission/absorption methods, respectively. Both of them favored the 8.7 kpc far distance with a corresponding luminosity of $60,000 L_{\odot}$ (S02). Churchwell et al. (2006) identified an infrared ring (N83) in this region and proposed that it is the projection of a three-dimensional shell or bubble. Five dense cores were identified by interferometric observations at 1.3 mm by Lu et al. (2018); four of them appear projected at the borders of the bubble (see Figure 4.1). The core I19074-c1 has VLA centimeter counterparts at 3.6 and 6 cm (S02; Purcell et al. 2013) and has been classified as an UCHII region in the CORNISH catalog (G042.1090 – 00.4469). We detect I19074-c1 at 7 mm with a flux density of 12.9 mJy (see Figure 4.1). The flux density distribution of this source shows a flat distribution between 5 and 44 GHz with a spectral index of -0.1 suggesting optically thin free-free emission (see Figure 4.2). Assuming a homogeneous HII region, we estimate a source size of 0.04 pc, an emission measure of $8 \times 10^6 \text{ cm}^{-6}\text{pc}$, an electron density of $1.4 \times 10^4 \text{ cm}^{-3}$, a mass of ionized gas of $1.1 \times 10^{-2} M_{\odot}$ and a flux of ionizing photons of $5.7 \times 10^{46} \text{ s}^{-1}$ which corresponds to a B0.5 ZAMS star (Panagia 1973; see Table 4.4). According to Panagia, the luminosity that corresponds to a B0.5 ZAMS star is about $10,000 L_{\odot}$ which is 6 times lower than the luminosity inferred by the IRAS observations (O8 ZAMS star; S02). Possible explanations for the difference in luminosities are that a substantial fraction of the ionizing stellar UV photons is absorbed by dust within the UCHII region or that nonionizing stars are present in the region (or a combination of both).

CO emission permeates the region around the millimeter cores but a clear outflow structure cannot be established (Lu et al. 2018). Neither Class II methanol nor water masers were detected in this region (S02; Szymczak et al. 2000; Slysh et al. 1999). We did not detect Class I 44 GHz methanol masers as well.

IRAS 19175+1357

I19175 is part of a large filamentary star-forming region located at a distance of 1.1 kpc (Sridharan et al. 2005) with a luminosity of $1000 L_{\odot}$ (Beuther and Henning 2009). I19175 consists of two millimeter cores (Beuther et al. 2002a) where neither class II methanol masers (Szymczak et al. 2000; Slysh et al. 1999)

nor water masers were detected (S02). We do not detect 7 mm continuum emission although the S02 observations reported 3.6 cm continuum emission of 5.1 mJy indicative of ionized gas in the vicinity of the IRAS source. We find one Class I methanol maser of 79.7 mJy projected toward the edge of I19175 (see Figure 4.1).

IRAS 19217+1651

I19217 is located at a distance of 10.5 kpc and has a luminosity of 79,400 L_{\odot} (S02). It is dominated by a single massive core (S02; Beuther et al. 2002a) and associated with a CO molecular outflow (Beuther et al. 2004). Class I 95 GHz and Class II 6.7 GHz CH_3OH masers (Gan et al. 2013; Beuther et al. 2002c) as well as H_2O and OH masers (Rodríguez-Esnard et al. 2012; Edris et al. 2007) were detected in the region by single-dish observations. Two sources, I19217-A and I19217-B, were resolved by high angular resolution observations at 3.6 and 1.3 cm (Rodríguez-Esnard et al. 2012). Source A is the stronger component at both wavelengths and shows a cometary morphology and a spectral index of +0.3 which led Rodríguez-Esnard et al. to classify it as an UC HII region. Source B shows extended emission with three continuum peaks (Rodríguez-Esnard et al. 2012). We detect 7 mm continuum emission with an integrated flux density of 42.1 mJy; its peak corresponds in position to I19217-A (see Figure 4.1). This 7 mm continuum source was previously detected with 50.4 mJy by Garay et al. (2007). The flux density difference could be explained by the smaller (four times) synthesized beam used in our observations which may be filtering out some of the emission. We did not detect I19217-B. Source B showed a peak flux density of 0.8 mJy beam^{-1} at 1.3 cm (Rodríguez-Esnard et al. 2012) which is near to our 1σ rms noise. Nonetheless, we detect a protuberance toward the north of source A which may have a contribution from source B.

Assuming that I19217-A is a homogeneous optically thin HII region with spherical symmetry and diameter of 0.008 pc, we estimate a brightness temperature of 1020 K, an EM of $8.8 \times 10^8 \text{ cm}^{-6} \text{ pc}$ and an electron density of $3.3 \times 10^5 \text{ cm}^{-3}$ (see Table 4.4). These parameters are consistent with a UC HII region according to Kurtz (2005). We also calculated an ionized hydrogen mass of $2.3 \times 10^{-3} M_{\odot}$ which requires $2.7 \times 10^{47} \text{ photons s}^{-1}$ to be excited and can be provided by a B0 ZAMS star (Panagia 1973). Our estimation is consistent with the parameters obtained by Garay et al. (2007) from modelling the radio continuum spectrum of source A in the range from 8.4 to 43.4 GHz. We estimate a spectral index of +0.3 for source A by fitting a power law to the flux density distribution between 5 to 44 GHz using recent and more sensitive data (see Figure 4.2).

We detect two Class I 44 GHz methanol masers at an LSR velocity of $-3 \pm 7 \text{ km s}^{-1}$ which is consistent with the velocities reported for the Class I 95 GHz methanol masers by Gan et al. (2013). The 44 GHz masers are isolated, with no obvious connection to the 7 mm continuum source. They appear offset by $\lesssim 0.2 \text{ pc}$ from the continuum source and the water masers.

IRAS 19410+2336

I19410 is a young massive star-forming region located at 2.16 kpc (Xu et al. 2009) with a luminosity of 10,000 L_{\odot} (S02). Two massive dust cores were detected by single-dish observations at 1.2 mm oriented in a north-south direction. The northern core was resolved into 2 sub-cores whereas the southern core was split into at least 4 sub-cores by higher angular resolution observations at 2.6 mm (Beuther et al. 2003). Multiple CO molecular outflows, H_2 emission (Beuther et al. 2003) and strong and variable Class II 6.7 GHz CH_3OH masers (Menten 1991b; Szymczak et al. 2000; Beuther et al. 2002c) and H_2O masers (Beuther et al. 2002c) as well as Class I 44 (Litovchenko et al. 2011) and 95 GHz methanol masers (Val'tts et al. 1995; Gan et al. 2013) were detected toward the southern core.

We detect a 7 mm continuum source with a flux density of 2.15 mJy which was also detected at 3.6 cm with 0.77 mJy by Xu et al. (2009). We estimate a spectral index of +0.8 from 5 to 44 GHz, using the non detection from the CORNISH survey as an upper limit for the source flux density (see Figure 4.2). Assuming that the emission arises from a homogeneous optically thin HII region, we estimate an $EM = 2.1 \times 10^7 \text{ cm}^{-6} \text{ pc}$, an electron density of $9.4 \times 10^4 \text{ cm}^{-3}$ and a mass of ionized gas of $1.6 \times 10^{-5} M_{\odot}$ which can be produced by an ionizing photon rate of $5.6 \times 10^{44} \text{ s}^{-1}$, corresponding to a B2 ZAMS star (Panagia 1973).

We detect four Class I CH_3OH masers at an LSR velocity of $21 \pm 7 \text{ km s}^{-1}$ which is consistent with the velocities of the three 44 GHz masers (22.2, 22.9 and 23.6 km s^{-1}) reported by the higher spectral resolution observations made by Litovchenko et al. with a single-dish telescope. The corresponding separation between the positions of our 44 GHz masers and the position of the H_2O masers given by Beuther et al. is less than 0.15 pc. The four methanol masers appear aligned in a northeast-southwest direction at the border of the green emission seen in the $4.5 \mu\text{m}$ band (see Figure 4.1). This alignment also coincides with the elongated H_2 emission feature labeled as (2) by Beuther et al. (2003) which in turn correlates well with the molecular gas. This scenario supports the relation between class I methanol masers and shocked gas traced by EGOs and H_2 emission. High spectral resolution observations are needed to confirm the maser nature of the emission and to search for a possible velocity gradient along the maser alignment.

4.5 Summary

We observed 13 HMPOs that form part of the sample of 69 HMPOs of Sridharan et al. (2002). We searched for 7 mm continuum emission although our observations were also sensitive to the Class I methanol transition $7_0 \rightarrow 6_1 A^+$ at 44 GHz. We use the VLA at Q-band and C-configuration which give us an angular resolution of $0''.5$ and a spectral resolution of 13.6 km s^{-1} . The low spectral resolution precludes obtaining the line parameters, and therefore, the actual nature of the emission: maser or thermal. We suspect that only bright methanol masers are able to overcome the spectral dilution, thus we refer to the line emission as methanol masers although further high spectral resolution observations are needed for confirmation. For both, continuum and maser emission, we consider a detection when the source peak flux density was above the 5σ rms noise level. The average 1σ detection limit for the continuum emission was $0.23 \text{ mJy beam}^{-1}$ and for the masers was $5.2 \text{ mJy beam}^{-1}$. We estimate the spectral index of the continuum emission using flux densities reported in the literature from 5 to 22 GHz and our data point at 44 GHz.

We summarize our results as follows:

- We detect 7 mm continuum emission toward 5 of the 13 IRAS regions observed. These regions are: 19012+0536, 19035+0641, 19074+0752, 19217+1651 and 19410+2336. Except for I19217, all of them are new detections. We detect continuum emission from 2 sources toward I19035, therefore, we report the parameters of 6 sources.
- We detect emission in the class I methanol transition at 44 GHz toward 4 of the 13 regions. These regions are: 19012+0536, 19175+1357, 19217+1651 and 19410+2336. The 44 GHz methanol masers of I19012 and I19410 were previously detected at higher spectral resolution but with a single-dish telescope. Therefore, we complement the maser parameters providing their positions at a sub-arcsecond accuracy.
- A correlation between the masers and the EGOs is not obvious but we find two examples where the masers appear projected toward the green emission seen in the $4.5 \mu\text{m}$ band. For I19012, the 7 mm continuum emission appears well-centered toward the EGO suggesting that it is the powering source of the EGO and one methanol maser appears projected toward the southern lobe of the EGO. More

intriguing are the 44 GHz methanol masers found toward I19410 which are aligned at the EGO edge. This alignment also coincides with the position and orientation of an elongated H₂ feature seen in the 2.12 μm band which correlates as well with CO molecular gas. This spatial correlation supports the idea that methanol masers are tracers of shocked-gas phenomena in star-forming regions.

- We measure the projected separation between the 44 GHz masers and the water masers reported in the literature for three regions, except for I19175 where water masers were not detected. In the three cases the projected separation was $\lesssim 0.2$ pc which is 5 times smaller than the typical 1 pc suggested by the original classification of Menten and Batrla (1989) based mainly on single-dish observations.

Chapter 5

Millimeter line survey toward high-mass protostars with the Large Millimeter Telescope

We present the results of a millimeter search for methanol maser and thermal lines in 12 transitions toward a sample of 38 well-known class I 44 GHz maser sites. The observations were part of the Early Science Program of the Large Millimeter Telescope in 2016, when the telescope had a usable surface 32-m in diameter. We used the Redshift Search Receiver which is a broad-band (73–111 GHz) and low-spectral resolution (100 km s^{-1}) spectrometer. Our primary goal was to search for maser candidates in the class I methanol transitions at 84.5 and 95.1 GHz and the class II transitions at 107.0 and 108.8 GHz. We found detection rates of 84%, 76%, 5% and 39%, respectively. We also searched for the thermal methanol line series around 96.7 GHz and we interestingly found a 100% detection rate. Nevertheless, the RSR bandpass covers many other spectral lines that are common in star-forming regions. Although the spectral resolution of the RSR is quite low, we were able to unambiguously identify many spectral lines. We show an overview of the molecular lines detected. Confirmation of maser emission will require follow-up observations, but our survey found numerous regions with rich molecular emission, and suggests a number of possible correlations.

5.1 Introduction

As mentioned in previous chapters, the class I methanol masers are less-studied and understood compared to the class II masers partly because the brighter transitions occur at relatively high frequencies, e.g., 44 and 95 GHz. Observations of masers at these frequencies with interferometers are limited by the frequency coverage of the receivers and by the atmospheric effects that make the data calibration more complicated. The difficulty of searching new maser sites is compounded by the lack of a large sample of sources that are expected to be associated with class I methanol masers. Nevertheless, searches for class I methanol masers have advanced significantly due to new single-dish telescopes at millimeter wavelengths and the availability of data at infrared and longer wavelengths from surveys of the Galactic plane with high sensitivity and angular resolution.

There are several methanol maser lines in the 3 mm band but only a few systematic single-dish searches have been made to date. The majority of them have searched for class I masers at 95 GHz which belong to the same transition family as the 44 GHz line ($J_0 \rightarrow (J-1)_1A^+$). Almost 1500 sources have been targeted to search for 95 GHz masers by several authors (Val'tts et al. 2000; Fontani et al. 2010; Chen et al. 2011,

2012, 2013; Yang et al. 2017) and emission has been detected toward about 200 sources. In contrast, for the class I methanol maser transition at 84.5 GHz, only one extensive search has been conducted to date, by Kalenskii et al. (2001). Kalenskii et al. observed 48 objects and detected maser emission toward 14 sources and quasi-thermal emission toward the remaining 34 objects. The class I methanol transition at 104.3 GHz is known as a rare maser line since it has been detected toward only two sources (2 of 69 observed) in the southern hemisphere (Voronkov et al. 2007).

The class II methanol transitions at 85.5, 86.6 and 86.9 are also known as rare masers because they usually show low detection rates and weak emission (Cragg et al. 2001; Minier and Booth 2002; Ellingsen et al. 2003). For the maser lines at 107.0 and 108.8 GHz, several searches have been made (Val'tts et al. 1995; Val'tts et al. 1999; Caswell et al. 2000). In summary, except for the 95 GHz line, the high frequency methanol maser transitions have been poorly investigated. This motivated us to conduct a multitransition search for methanol maser emission toward a relatively large sample of known class I 44 GHz maser sites.

The Large Millimeter Telescope (LMT) is an excellent tool to study class I methanol masers and their environments. This radio telescope is equipped with a broad-band spectrometer that can observe simultaneously twelve methanol transitions of thermal and maser nature. It covers 3 class I and 5 class II methanol maser transitions of different types (A and E) along with a series of four thermal lines near 96.7 GHz. This is very useful because the detection of multiple frequency transitions provides important information about the physical and chemical conditions of star-forming regions (Purcell et al. 2009).

Taking advantage of the relatively large samples of high-mass protostellar objects with 44 GHz methanol masers detected in the VLA surveys made by Gómez-Ruiz et al. (2016, defined as Survey III in Chap. 3) and Rodríguez-Garza et al. (2017, hereafter Survey IV), we performed LMT observations toward 38 HMPOs to search for methanol emission in the millimeter range. We selected 19 HMPOs from Survey III which correspond to the Molinari sample and 19 more from Survey IV that belong to the Sridharan catalog. As discussed in previous chapters, both samples were taken from the IRAS Point Source Catalog and satisfy criteria that favor embedded massive protostars.

In this chapter, we present the results of a 3 mm spectral line survey made with the LMT. In section 5.2 we introduce the observational details and data reduction. Section 5.3 presents the results separately for different sets of lines detected. In section 5.4 we give a brief discussion of the main challenges we faced such as the line identification and spectral dilution. In section 5.5 we present a summary of the more salient findings of our observations.

5.2 Observations and Data Reduction

The observations (project ID: 2015ARODC168) were made in 12 epochs between 2016 February and April during the early science phase of the Large Millimeter Telescope (LMT) located on the Sierra Negra, Mexico at an altitude of 4600 m. We used the Redshift Search Receiver (RSR) which uses an analog autocorrelation spectrometer to cover a frequency range from 73 to 111 GHz (38 GHz bandwidth) with a spectral resolution of 31 MHz ($\sim 100 \text{ km s}^{-1}$ at 93 GHz). The RSR is configured to observe simultaneously two points on the sky, the **ON-SOURCE** and **OFF-SOURCE** positions, separated by $39''$ or $147''$ depending on the required configuration, called the narrow or wide configuration, respectively. In this experiment we used the wide configuration. At the time of these observations the LMT had a usable surface 32-m in diameter, providing a beam size of $26''$ at 73 GHz and $18''$ at 111 GHz.

The pointing was corrected by observing nearby quasars at the beginning of each observing session and then once per hour, resulting in pointing uncertainties in the range 1 – 11 arcseconds which changed with the observing day. We made calibration scans every 15 – 20 minutes to calibrate the antenna temperature. The values of sky opacity, $\tau_{225\text{GHz}}$, range between 0.06 – 0.32 and were only used to give an idea of the weather

conditions at the time of the observations. Each program source was observed during a total ON-SOURCE time of 20 minutes that was obtained by averaging four different scans of 5 minutes each. A summary of the observational log is given in Table 5.1.

Table 5.1: LMT observing log for the data taken during the Early Science Phase in 2016.

Date 2016	Opacities $\tau_{225\text{GHz}}$	T_{sys} K	Elevation ($^{\circ}$)	Pointing Calibrators	Pointing Error ($''$)
Feb 11	0.14 – 0.15	102 – 111	30.5 – 46.2	J0533+483	4
Feb 12	0.06 – 0.07	97	34.3 – 46.0	3C111	1
Feb 14	0.07 – 0.08	94	49.8 – 64.7	3C111	2
Mar 18	0.16 – 0.18	100 – 116	27.8 – 55.6	NRAO530, J1743–038	5
Apr 10	0.20 – 0.25	102 – 115	36.2 – 63.0	J1743–038, J1911–201	5
Apr 11	0.14	100 – 102	46.1 – 58.0	NRAO530	4
Apr 12	0.24 – 0.26	102 – 111	41.0 – 80.5	J1751+096	1 – 3
Apr 13	0.20	99 – 100	48.2 – 56.4	NRAO530	3
Apr 14	0.23 – 0.28	100 – 148	31.2 – 80.3	NRAO530, J1743–038, J1751+096	4 – 11
Apr 15	0.24 – 0.32	101 – 115	40.6 – 80.8	J1751+096	1 – 5
Apr 16	0.20 – 0.22	–	63.1 – 72.9	J2023+318	1
Apr 17	0.26 – 0.29	102 – 105	61.2 – 78.0	J1751+096, J2015+371	3

The RSR passband covers twelve methanol transitions and many other thermal molecular lines. The typical 1σ rms noise for some of the targeted lines is given in Table 5.2.

Table 5.2: Molecular lines in the passband of RSR.

Transition	Frequency MHz	E_u K	Maser class or thermal	1σ rms mJy
Methanol transitions				
$5_{-1} \rightarrow 4_0\text{E}$	84521.169	40.1	Class I	3
$6_{-2} \rightarrow 7_{-1}\text{E}$	85568.084	74.7	Class II	
$7_2 \rightarrow 6_3\text{A}^-$	86615.602	102.7	Class II	
$7_2 \rightarrow 6_3\text{A}^-$	86902.949	102.7	Class II	
$8_0 \rightarrow 7_1\text{A}^+$	95169.440	83.6	Class I	3
$2_{-1} \rightarrow 1_{-1}\text{E}$	96739.39	12.6	Thermal	3
$2_0 \rightarrow 1_0\text{A}^+$	96741.42	7.0	Thermal	3
$2_0 \rightarrow 1_0\text{E}$	96744.58	20.1	Thermal	3
$2_1 \rightarrow 1_1\text{E}$	96755.51	28.0	Thermal	3
$11_{-1} \rightarrow 10_{-2}\text{E}$	104300.414		Class I	
$3_1 \rightarrow 4_0\text{A}^+$	107013.812	28.3	Class II	10
$0_0 \rightarrow 1_{-1}\text{E}$	108893.948	13.1	Class II	10
Other molecular lines				
$\text{CH}_3\text{CN} (4_3 - 3_3)$	73577.451	73.13	Thermal	
$\text{CH}_3\text{CN} (4_2 - 3_2)$	73584.543	37.41	Thermal	
$\text{CH}_3\text{CN} (4_1 - 3_1)$	73588.799	15.98	Thermal	
$\text{CH}_3\text{CN} (4_0 - 3_0)$	73590.218	8.83	Thermal	
$\text{HC}_3\text{N} (9 - 8)$	81881.467	19.6	Thermal	
$\text{SiO} (2_0 - 1_0)$	86846.985	6.25	Thermal	8

Table 5.2 – Continued

Transition	Frequency MHz	E_u K	Maser class or thermal	1σ rms mJy
HCN(1 – 0)	88631.602	4.2	Thermal	10
HCO ⁺ (1-0)	89188.525	4.3	Thermal	20
HNC(1 – 0)	90663.568	4.3	Thermal	7
HC ₃ N (10 – 9)	90979.023	24.0	Thermal	7
CH ₃ CN (5 ₄ – 4 ₄)	91958.726	127.5	Thermal	
CH ₃ CN (5 ₃ – 4 ₃)	91971.130	77.5	Thermal	
CH ₃ CN (5 ₂ – 4 ₂)	91979.994	41.8	Thermal	
CH ₃ CN (5 ₁ – 4 ₁)	91985.314	20.4	Thermal	
CH ₃ CN (5 ₀ – 4 ₀)	91987.087	13.2	Thermal	
N ₂ H ⁺ (1 – 0)	93173.398	4.4	Thermal	10
CS(2 ₀ – 1 ₀)	97980.953	7.0	Thermal	8
SO(2 ₃ – 1 ₂)	99299.870	9.2	Thermal	6
HC ₃ N (11 – 10)	100076.392	28.8	Thermal	
HC ₃ N (12 – 11)	109173.634	34.0	Thermal	
¹³ CO (1 – 0)	110201.354	5.2	Thermal	40

We found in the previous VLA Surveys III and IV several cases where the 44 GHz methanol masers were located offset from the IRAS source position by several arcseconds, lying at the edge or outside the 1' VLA primary beam. Since the LMT has a smaller field of view ($\sim 20 - 28''$), we use the accurate interferometric positions of the brightest 44 GHz masers for the LMT pointing centers thus assuming that the 44 GHz masers are more likely tracers of 3 mm emission than is the IR emission. The IRAS regions 05358+3543 and 05274+3345 are both associated with two clusters, apparently in different evolutionary stages and separated by about $30''$ (Porras et al. 2000). For this reason, we made two pointings toward the same IRAS region to cover both clusters (see Figure 5.1). We made one pointing toward the brightest 44 GHz maser and one toward the IRAS position to compare their chemical richness. A dual pointing was also made toward another four IRAS regions (18144–1723, 18264–1152, 18345–0641 and 18507+0121). The 44 GHz masers detected in these regions showed an intriguing behavior: the majority of the masers were clustered around the IRAS position with the exception of a single isolated feature several arcseconds apart. In these four cases we made one pointing toward the brightest 44 GHz maser and another centered on the isolated maser. We made a total of 44 different pointings which are listed in Table 5.3.

The data were reduced and calibrated using *Data Reduction and Analysis Methods in Python* (DREAMPY), which is a software package developed by G. Narayanan for the RSR data reduction. The RSR produces one spectrum for each of the four 5-min scans ON-SOURCE. The four spectra were calibrated individually and visually inspected for flat baselines. We made linear fits in DREAMPY to subtract the baseline from each 5-min spectrum. The final spectrum was obtained by averaging the four 5-min spectra. The intensity scale of all spectra are in antenna temperature units, T_A^* (corrected only for atmospheric opacity). These scales are converted to flux density units using the conversion factor 6.4 Jy K^{-1} for $\nu \leq 92 \text{ GHz}$ and 7.6 Jy K^{-1} for $\nu > 92 \text{ GHz}$, which are based on observations of Uranus and MWC 349A.

Table 5.3: Observed Source List.

ID	Source IRAS Name	Pointing Center (J2000)		Detected methanol transition frequency (GHz)									
		α (h m s)	δ ($^\circ$ ' ")	84.5	85.5	86.6	86.9	95.1	96.7	104.3	107.0	108.8	
M	05274+3345	05 30 47.62	+33 47 52.2	Y	N	N	N	Y	Y	N	N	Y	
S	05358+3543	05 39 13.48	+35 45 43.0	Y	N	N	N	Y	Y	N	N	Y	
M	18018–2426	18 04 53.01	–24 26 40.5	Y	N	N	N	Y	Y	N	N	N	

Table 5.3 – continued

ID	Source IRAS Name	Pointing Center (J2000)		Detected methanol transition frequency (GHz)								
		α (h m s)	δ ($^{\circ}$ ' ")	84.5	85.5	86.6	86.9	95.1	96.7	104.3	107.0	108.8
M	18024–2119	18 05 25.39	–21 19 16.9	Y	N	N	N	Y	Y	N	Y	Y
S	18089–1732	18 11 51.29	–17 31 23.8	Y	N	N	N	Y	Y	N	N	N
S	18102–1800	18 13 10.29	–18 00 03.8	Y	N	N	N	Y	Y	N	N	Y
M	18144–1723	18 17 24.07	–17 22 13.8	Y	N	N	N	Y	Y	N	N	Y
S	18151–1208	18 17 58.20	–12 07 29.4	Y	N	N	N	Y	Y	N	N	N
M	18162–1612	18 19 07.63	–16 11 25.4	Y	N	N	N	Y	Y	N	N	N
S	18182–1433	18 21 09.14	–14 31 49.7	Y	N	N	N	Y	Y	N	Y	N
S	18247–1147	18 27 31.80	–11 46 00.5	N	N	N	N	N	Y	N	N	N
S	18264–1152	18 29 14.39	–11 50 24.7	Y	N	N	N	Y	Y	N	N	Y
S	18290–0924	18 31 43.40	–09 22 22.5	Y	N	N	N	Y	Y	N	N	N
S	18306–0835	18 33 24.07	–08 33 34.5	Y	N	N	N	Y	Y	N	N	Y
S	18308–0841	18 33 33.21	–08 39 14.7	Y	N	N	N	Y	Y	N	N	Y
S	18310–0825	18 33 47.31	–08 23 43.1	N	N	N	N	N	Y	N	N	N
S	18337–0743	18 36 27.98	–07 40 22.7	Y	N	N	N	Y	Y	N	N	N
S	18345–0641	18 37 16.89	–06 38 29.7	Y	N	N	N	Y	Y	N	N	Y
M	18396–0431	18 42 17.91	–04 28 56.5	Y	N	N	N	Y	Y	N	N	N
S	18488+0000	18 51 25.42	+00 04 06.1	Y	N	N	N	Y	Y	N	N	Y
M	18507+0121	18 53 18.68	+01 24 41.2	Y	N	N	N	Y	Y	N	N	Y
M	18511+0146	18 53 37.71	+01 50 25.5	Y	N	N	N	N	Y	N	N	N
S	18517+0437	18 54 14.74	+04 41 42.7	Y	N	N	N	Y	Y	N	N	Y
S	18521+0134	18 54 40.90	+01 38 04.8	Y	N	N	N	N	Y	N	N	N
M	18527+0301	18 55 16.77	+03 05 06.9	N	N	N	N	Y	Y	N	N	N
S	18530+0215	18 55 34.76	+02 19 00.5	Y	N	N	N	Y	Y	N	N	N
M	18532+0047	18 55 51.34	+00 51 26.4	N	N	N	N	Y	Y	N	N	N
M	18551+0302	18 57 41.81	+03 06 02.7	Y	N	N	N	N	Y	N	N	Y
S	18553+0414	18 57 53.34	+04 18 16.9	Y	N	N	N	Y	Y	N	N	N
M	18565+0349	18 59 03.73	+03 53 42.8	Y	N	N	N	N	Y	N	N	N
S	18566+0408	18 59 09.30	+04 12 25.7	Y	N	N	N	Y	Y	N	N	Y
M	19043+0726	19 06 47.84	+07 31 41.9	Y	N	N	N	Y	Y	N	N	N
M	19088+0902	19 11 17.34	+09 07 33.1	Y	N	N	N	Y	Y	N	N	Y
M	19092+0841	19 11 38.76	+08 46 37.9	Y	N	N	N	Y	Y	N	N	N
M	19094+0944	19 11 51.47	+09 49 41.7	N	N	N	N	N	Y	N	N	N
M	19198+1423	19 22 08.10	+14 29 17.2	N	N	N	N	N	Y	N	N	N
M	20050+2720	20 07 06.20	+27 28 58.5	Y	N	N	N	Y	Y	N	N	N
M	20056+3350	20 07 31.51	+33 59 46.9	Y	N	N	N	N	Y	N	N	N
Total detection rate				84%	0%	0%	0%	76%	100%	0%	5%	39%
Additional pointings toward IRAS positions												
M	05274+3345	05 30 45.6	+33 47 52	N	N	N	N	N	Y	N	N	N
S	05358+3543	05 39 10.4	+35 45 19	Y	N	N	N	N	Y	N	N	N
M	18144–1723	18 17 24.5	–17 22 13	Y	N	N	N	Y	Y	N	N	Y
S	18264–1152	18 29 14.3	–11 50 26	Y	N	N	N	Y	Y	N	N	N
S	18345–0641	18 37 16.8	–06 38 32	Y	N	N	N	Y	Y	N	N	N
M	18507+0121	18 53 17.4	+01 24 55	Y	N	N	N	Y	Y	N	N	Y

Notes.

Letters indication are as follows:

S = Sridharan et al. (2002), M = Molinari et al. (1996), Y = Detected, N = Not Detected.

The first 38 pointing centers correspond to the positions of brightest class I 44 GHz masers detected in previous VLA surveys of Gómez-Ruiz et al. (2016) and Rodríguez-Garza et al. (2017). The six additional pointings were centered on the IRAS source position reported by the catalogs of Molinari et al. (1996) and Sridharan et al. (2002).

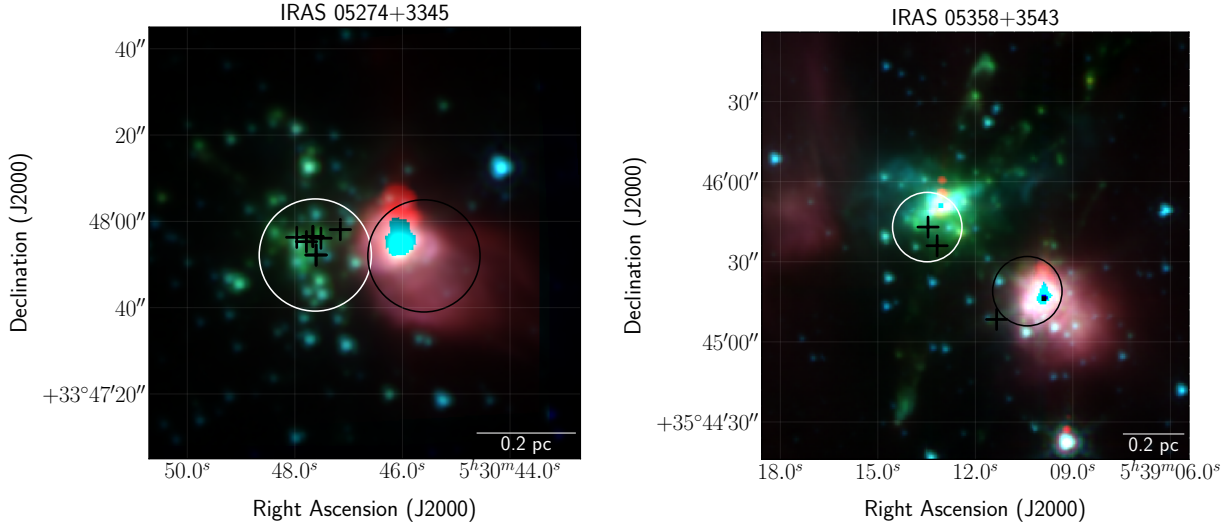


Figure 5.1: Left panel: IRAS 05274+3345 from Survey III. Right panel: IRAS 05358+3543 from Survey IV. The color scales show Spitzer images of the IRAC bands at 3.6, 4.5, and 8 μm . The crosses indicate the 44 GHz methanol masers detected in the VLA surveys. The white circles represent the LMT primary beam (26'' at 73 GHz) pointed toward the position of the brightest 44 GHz maser (related to shocked gas traced by EGOs) and the black circles represent the LMT primary beam toward the IRAS source.

5.3 Results

We detect emission from nine of the twelve methanol transitions observed alongside many other thermal molecular lines that are common in star-forming regions. We will describe our results in subsections for different sets of detected lines. For simplicity, we will refer to the methanol lines at 84.5, 95.1 and 104.3 GHz as class I methanol masers and to the 85.5, 86.6, 86.9, 107.0 and 108.8 GHz lines as class II methanol masers since they are usually associated with these classes of masers in the literature (see Sections 2.3.1 and 2.3.2 of Chapter 2). Similarly, the quartet of lines near 96.7 GHz will be referred to as thermal methanol lines. However, we caution that this is just a label since we can not confirm the true nature of the emission given the low spectral resolution of our observations.

A general overview of our observations is given in Table 5.3. It shows in column 1 the corresponding sample from which the IRAS sources were taken, “M” or “S” to indicate whether the source was taken from the Molinari sample observed in Survey III or from the Sridharan sample of Survey IV. In columns 2 and 3, we list the pointing centers used; we remind the reader that these positions are not the positions reported in the IRAS catalog except when indicated as additional pointings. Thirty eight pointings were made toward the peak position of the brightest 44 GHz methanol masers detected in the VLA Surveys III and IV and six additional pointings were made toward the IRAS source position. The last columns indicate with a letter “Y” or “N” when emission was detected or not detected, respectively.

The measured parameters of all methanol and other thermal lines will be given in tabular form in the following subsections. For all targets, we give the rms noise level (mJy), the channel peak flux density (Jy) and the integrated flux density (Jy km s^{-1}). We consider a detection when the peak flux density was above the 5σ rms level. These parameters were obtained following a simple procedure within CASSIS¹, a software

¹CASSIS has been developed by IRAP-UPS/CNRS (<http://cassis.irap.omp.eu>).

package developed for spectral analysis. For each line, we selected a spectral window 6000 km s^{-1} wide centered on the line of interest. We note that the baselines were not completely corrected by DREAMPY, therefore, we made another polynomial fit—within CASSIS—in the adjacent line-free channels to subtract the continuum level. From this fit, we obtain the rms noise. Due to the low spectral resolution of our observations ($\Delta v \sim 100 \text{ km s}^{-1}$), we can not perform Gaussian fits to obtain the line parameters, but instead, CASSIS computes the area covered by the channels selected ($\sum_i S_i \Delta v$).

We notice that almost all the brightest lines showed emission above the 5σ level in two—and sometimes in three—adjacent channels. This was unexpected since masers typically have line widths less than 1 km s^{-1} and such narrow lines were expected to be within one single RSR channel. We suspect that this phenomenon can have at least three explanations:

1. Gibbs effect: this phenomenon consists of strong oscillations resulting from the convolution of the correlator response with the signal of the spectral line. In general, the brighter the line, the stronger the oscillations are. These ripples are commonly found in single-dish autocorrelator spectrometers and can be clearly seen at the band edges of our spectra and other parts since the observed bandwidth consist of six adjacent frequency windows. This ringing is more notable in the most intense lines of the spectrum which also coincide with the borders of the spectrum (e.g. HCN, HCO⁺, ¹³CO, etc). Therefore, the strong line emission detected in two channels could arise from this ringing.
2. Doppler shifting: none of the detected methanol nor other thermal lines have rest frequencies centered on the 31 MHz width RSR channels. For example, the four thermal methanol lines near 96.7 GHz span 16 MHz in frequency (see Figure 5.2). Emission at this frequency was detected toward source 18566+0408 which has the largest LSR velocity of all sources observed ($+85.2 \text{ km s}^{-1}$). Thus, the Doppler shift in this case would be 28 MHz, which is almost the channel width. Consequently, there could be cases where these Doppler shifted lines could cross the channel boundary, adding a contribution to an adjacent channel.
3. Contamination of other species: another explanation may be the fact that dozens of molecules are contributing to the emission in the channel of interest and its immediate neighbors. In addition to the thermal methanol lines mentioned above, there are other molecules within the channels near 96.7 GHz, for example, ³⁴SO which has a rest frequency of 96781.76 MHz (see Figure 5.2). This molecule is abundant in star-forming regions compared to other more complex molecules in this frequency range, e.g., CH₃OCHO. The full range of lines spans 42 MHz—more than a channel width. If the Doppler shift of the region were to move all the lines toward an adjacent channel, the result could be strong emission in both channels.

Therefore, we caution that two-channel emission probably does not arise from extremely broad line emission.

5.3.1 Class I methanol maser detections

We detect emission in the class I methanol transitions at 84.5 and 95.1 GHz but no emission was detected at 104.3 GHz. The properties of the detected lines are listed in Table 5.4. For each line, we report the rms noise, the channel peak flux density (S_p) and the integrated flux density (S_{int}). The 84.5 GHz line was detected toward 32 of the 38 targets observed (84% detection rate), all of them are new detections. The peak flux densities range from 0.01 to 0.44 Jy (mean and median are 0.09 and 0.05 Jy) and the integrated flux densities range from 1.1 to 83.0 Jy (mean and median are 17.6 and 11.0 Jy). The strongest 84.5 GHz source is 18018–2426 and the weakest is 18521+0134.

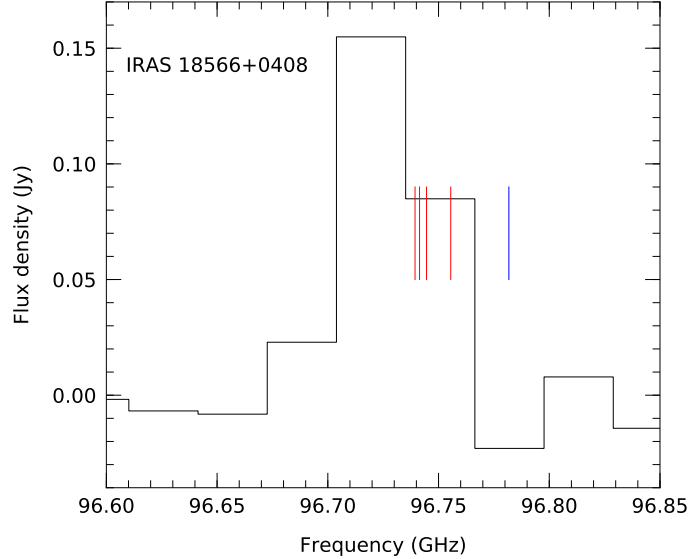


Figure 5.2: Emission detected toward source 18566+0408. The four red lines indicate the rest frequencies of the thermal methanol transitions $2_{-1} \rightarrow 1_{-1}E$, $2_0 \rightarrow 1_0A^+$, $2_0 \rightarrow 1_0E$, $2_1 \rightarrow 1_1E$ at 96739.39, 96741.42, 96744.58 and 96755.51 MHz, respectively. The blue line indicate the rest frequency of ^{34}SO which is 96781.76 MHz.

The 95.1 GHz methanol line was detected toward 29 of the 38 targets observed (76% detection rate). The peak flux densities range from 0.01 to 0.16 Jy (mean and median of 0.05 and 0.03 Jy) and the integrated flux densities range from 0.9 to 26.3 Jy (mean and median of 7.6 and 4.8 Jy). The strongest 95.1 GHz source is 18264–1152 and the weakest are several sources that were detected very close to the detection limit of the observations, e.g., 18527+0301, 18530+0215, 18532+0047, 18553+0414 and 19043+0726. A similar detection rate (87%) was found for this transition toward a sample of 23 star-forming regions by Minier and Booth (2002).

We found a marginally higher detection rate for the 84.5 GHz line (84%) compared to the 95.1 GHz line (76%). We also noted that the integrated flux density of the 84.5 GHz line is on average 2.3 times larger than the 95.1 GHz line. This was somewhat unexpected since it is usually mentioned in the literature that the 44 GHz $7_0 \rightarrow 6_1A^+$ and 95 GHz $8_0 \rightarrow 7_1A^+$ lines are the most widespread and the strongest class I methanol lines while the 84.5 GHz $5_{-1} \rightarrow 4_0E$ transition is to some extent ignored. This is in part due to the results of the few observations that have compared these three transitions simultaneously toward a handful of sources, showing that the 84.5 GHz line shows the less intense emission (Menten 1991b; Voronkov et al. 2006). There are systematic searches presenting comparisons, but again, only between the 44 and 95 GHz lines leaving the 84.5 GHz line excluded. This is in part as well, due to the closer relationship between the 44 and 95 GHz lines since they are consecutive transitions of the same backbone ladder ($J_0 \rightarrow (J-1)_1A^+$) while the 84.5 GHz line is an E species originated in the $K = -1$ side ladder. However, statistical equilibrium calculations have predicted that the 84.5 GHz line intensity is slightly larger than the 95.1 GHz line (Cragg et al. 1992). The only systematic observations made to date that included simultaneously the 84.5 and 95.1 GHz lines is the work presented by Kalenskii et al. (2001). Their findings are in agreement with the model predictions since they found higher flux densities for the 84.5 GHz line compared to the 95.1 GHz line and also suggest a correlation between them. Our observations are the second in observing both transitions simultaneously

toward a considerable number of sources, suggesting that the 84.5 GHz line is more widespread and stronger than the 95.1 GHz line. The most notable case is for 18018–2426 which has the brightest class I 44 GHz methanol maser of all the sources observed. It was detected in Survey III with an integrated flux density of $329.5 \text{ Jy km s}^{-1}$. We found an integrated flux density for the 84.5 GHz line of $82.6 \text{ Jy km s}^{-1}$ which is about four times brighter than the 95.1 GHz methanol line (see Table 5.4). We also suggest a correlation between the integrated flux densities of both transitions that will be discussed in Section 5.4.4.

The 95.1 GHz methanol line was previously observed toward 32 of our 38 targets with higher spectral resolution by several authors (Gan et al. 2013; Chen et al. 2013, 2012, 2011; Fontani et al. 2010; Val’tts et al. 2000); all of them are compiled in the catalog presented by Yang et al. (2017). We detected emission toward 23 of the 32 common sources. The sources 18507+0121, 18264–1152 and 18018–2426 have the most intense lines reported, with integrated flux densities of 65, 59 and 33 Jy km s^{-1} , respectively (Chen et al. 2011, 2012; Gan et al. 2013). This is consistent with our results since we detected the brightest 95 GHz lines toward these three sources as well, with integrated flux densities of 18, 26 and 19 Jy km s^{-1} , respectively.

Most of these 23 detected sources showed multiple velocity components. We show in Table 5.5 the integrated flux density of each component and also the total integrated flux density which is the sum of the integrated flux densities of each component toward each source. Since we are not able to resolve the maser components of each source, we compare the total integrated flux densities reported in the literature with our results. We show an histogram in Figure 5.3 of this ratio and note that our results are within a factor of 2 to 5 from the measurements obtained by higher spectral resolution observations. Although this factor may seem rather large, it is reasonable considering the large errors in our flux density measurements due to the spectral dilution. Nine sources were reported as non-detections at a 1 Jy level in the catalog of Yang et al. (2017). However, we detect weak emission toward 2 of these non-detections, which are sources 18162–1612 and 18532+0047. These 2 sources, together with 18517+0437, 18527+0301, 18396–0431, 18530+0215, 18553+0414 and 18566+0408, should be considered as tentative new detections since they were detected at the 5σ noise level. Two of these tentative detections (18396–0431 and 18566+0408) have information in the literature and can be clearly identified on Figure 5.3 since they show the larger ratios. We will comment on this in Section 5.4.2.

Table 5.4: Parameters measured for the class I methanol lines at 84.5 and 95.1 GHz.

Source IRAS Name	84.5 GHz			95.1 GHz		
	rms (mJy)	S_p Jy	S_{int} Jy km s $^{-1}$	rms (mJy)	S_p Jy	S_{int} Jy km s $^{-1}$
05274+3345	7.6	0.16	34.3	3.2	0.06	10.0
05358+3543	3.7	0.07	17.0	2.6	0.07	10.3
18018–2426	5.7	0.44	83.0	7.4	0.11	19.0
18024–2119	4.3	0.18	34.2	3.6	0.05	8.8
18089–1732	4.4	0.07	11.8	3.3	0.03	6.2
18102–1800	3.4	0.17	33.2	4.1	0.03	4.7
18144–1723	4.0	0.19	37.8	7.3	0.09	15.1
18151–1208	4.1	0.03	5.6	2.5	0.02	3.6
18162–1612	2.6	0.06	12.3	2.1	0.02	2.3
18182–1433	4.5	0.14	30.4	5.0	0.08	11.1
18247–1147	2.5	–	–	2.6	–	–
18264–1152	3.5	0.16	31.2	7.6	0.16	26.3
18290–0924	2.1	0.05	9.7	2.3	0.08	12.3
18306–0835	3.5	0.14	30.0	3.1	0.10	16.3
18308–0841	3.3	0.07	16.5	2.5	0.05	7.4
18310–0825	2.0	–	–	2.0	–	–
18337–0743	2.6	0.02	5.3	2.2	0.02	3.5

Table 5.4 – continued

Source IRAS Name	84.5 GHz			95.1 GHz		
	rms (mJy)	S_p Jy	S_{int} Jy km s ⁻¹	rms (mJy)	S_p Jy	S_{int} Jy km s ⁻¹
18345–0641	3.4	0.05	9.5	3.0	0.03	4.5
18396–0431	2.5	0.02	4.0	3.0	0.02	3.0
18488+0000	3.7	0.07	14.0	2.7	0.03	4.8
18507+0121	4.1	0.27	58.0	9.3	0.12	18.6
18511+0146	3.5	0.02	3.5	2.4	–	–
18517+0437	3.6	0.08	15.5	3.8	0.02	3.4
18521+0134	2.0	0.01	1.1	2.7	–	–
18527+0301	2.0	–	–	2.0	0.01	1.1
18530+0215	2.7	0.02	3.7	2.0	0.01	1.2
18532+0047	2.3	–	–	2.0	0.01	0.9
18551+0302	2.7	0.03	7.2	4.2	–	–
18553+0414	3.1	0.02	2.0	3.0	0.01	1.4
18565+0349	3.3	0.04	8.6	3.0	–	–
18566+0408	4.2	0.04	8.0	2.8	0.01	1.5
19043+0726	2.2	0.02	4.9	2.3	0.01	1.3
19088+0902	2.2	0.05	11.5	4.0	0.08	11.6
19092+0841	3.1	0.05	10.5	3.0	0.02	2.2
19094+0944	2.2	–	–	2.0	–	–
19198+1423	1.7	–	–	1.6	–	–
20050+2720	2.5	0.05	8.4	3.2	0.02	3.0
20056+3350	2.5	0.02	1.6	2.7	–	–
Mean	3.2	0.09	17.6	3.4	0.05	7.6
Median	3.2	0.05	11.0	2.9	0.03	4.8
Additional pointings toward IRAS positions						
05274+3345*	2.8	–	–	2.0	–	–
05358+3543*	3.3	0.03	0.03	2.7	–	–
18144–1723*	2.8	0.18	0.18	4.8	0.06	0.06
18264–1152*	3.6	0.10	0.10	7.4	0.04	0.04
18345–0641*	3.7	0.05	0.05	2.8	0.02	0.02
18507+0121*	3.6	0.21	0.21	6.8	0.11	0.11

Notes. To differentiate the pointings made toward the IRAS source position from the other pointings, we add an asterisk to the source name.

– Emission below the 5σ detection limit.

Table 5.5: List of parameters for the 95 GHz maser lines reported in the literature.

Source IRAS Name	J2000 Position		V_{LSR}	ΔV	S_{peak}	S_{int}^\dagger	S_{tot}^\ddagger	References
	α (h m s)	δ ($^\circ$ ' ")	km/s	km/s	Jy	Jy km/s	Jy km/s	
05274+3345	05 30 46.00	+33 47 52.00	–0.38	1.00		3.56	23.73	<i>f</i>
05274+3345	05 30 46.00	+33 47 52.00	–3.15	0.88		7.38	23.73	<i>f</i>
05274+3345	05 30 46.00	+33 47 52.00	–4.62	2.18		6.05	23.73	<i>f</i>
05274+3345	05 30 46.00	+33 47 52.00	–1.90	1.27		6.75	23.73	<i>f</i>
05358+3543	05 39 10.60	+35 45 19.00	–16.05	1.26		2.94	13.84	<i>f</i>
05358+3543	05 39 10.60	+35 45 19.00	–18.84	5.58		10.90	13.84	<i>f</i>
18018–2426	18 04 53.90	–24 26 41.00	+10.80	0.62	50.0	33.50	33.50	<i>b</i>
18024–2119	18 05 25.60	–21 19 25.00	–0.46	0.26	5.4	1.50	20.90	<i>d</i>
18024–2119	18 05 25.60	–21 19 25.00	–0.39	0.73	10.7	8.20	20.90	<i>d</i>
18024–2119	18 05 25.60	–21 19 25.00	–1.58	0.78	3.0	2.50	20.90	<i>d</i>

Table 5.5 – continued

Source IRAS Name	J2000 Position		V_{LSR} km/s	ΔV km/s	S_{peak} Jy	S_{int}^\dagger Jy km/s	S_{tot}^\ddagger Jy km/s	References
	α (h m s)	δ ($^\circ$ ' ")						
18024–2119	18 05 25.60	–21 19 25.00	–1.80	5.71	1.4	8.70	20.90	<i>d</i>
18089–1732	18 11 51.33	–17 31 26.40	+31.66	0.47	8.7	4.40	27.60	<i>d</i>
18089–1732	18 11 51.33	–17 31 26.40	+32.71	0.57	2.3	21.8	27.60	<i>d</i>
18089–1732	18 11 51.33	–17 31 26.40	+32.94	3.87	5.3	4.40	27.60	<i>d</i>
18102–1800	18 13 11.47	–17 59 48.60	+19.83	0.88	8.8	8.20	24.20	<i>d</i>
18102–1800	18 13 11.47	–17 59 48.60	+21.17	0.90	3.8	3.60	24.20	<i>d</i>
18102–1800	18 13 11.47	–17 59 48.60	+22.76	2.20	5.3	12.4	24.20	<i>d</i>
18144–1723	18 17 24.40	–17 22 13.00	+47.91	2.07	12.0	26.40	26.40	<i>b</i>
18151–1208	18 17 57.10	–12 07 22.00	+32.20	1.30	3.3	4.60	7.10	<i>a</i>
18151–1208	18 17 57.10	–12 07 22.00	+33.90	0.60	3.9	4.60	7.10	<i>a</i>
18182–1433	18 21 09.20	–14 31 45.00	+61.37	0.84	19.0	17.10	29.90	<i>d</i>
18182–1433	18 21 09.20	–14 31 45.00	+60.36	0.72	8.3	6.40	29.90	<i>d</i>
18182–1433	18 21 09.20	–14 31 45.00	+58.68	1.84	3.3	6.40	29.90	<i>d</i>
18264–1152	18 29 14.70	–11 50 25.00	+44.37	0.82		7.75	59.19	<i>f</i>
18264–1152	18 29 14.70	–11 50 25.00	+43.42	4.53		21.27	59.19	<i>f</i>
18264–1152	18 29 14.70	–11 50 25.00	+43.32	1.14		29.22	59.19	<i>f</i>
18264–1152	18 29 14.70	–11 50 25.00	+40.98	0.26		0.95	59.19	<i>f</i>
18290–0924	18 31 43.60	–09 22 20.00	+84.00	0.82	21.4	18.60	18.60	<i>c</i>
18306–0835	18 33 23.90	–08 33 24.00	+77.96	1.50	14.0	22.30	22.30	<i>c</i>
18308–0841	18 33 33.30	–08 39 04.00	+76.53	1.75	6.0	11.20	11.20	<i>c</i>
18337–0743	18 36 28.00	–07 40 24.00	+58.71	0.68	2.4	1.70	5.40	<i>c</i>
18345–0641	18 37 17.50	–06 38 31.00	+95.46	1.36	6.3	9.20	9.20	<i>c</i>
18396–0431	18 42 18.80	–04 28 37.00	+50.37	1.24	2.9	3.80	31.40	<i>b</i>
18396–0431	18 42 18.80	–04 28 37.00	+57.40	7.00	1.9	14.0	31.40	<i>b</i>
18396–0431	18 42 18.80	–04 28 37.00	+61.50	1.30	2.5	4.00	31.40	<i>b</i>
18396–0431	18 42 18.80	–04 28 37.00	+71.30	3.40	2.2	8.00	31.40	<i>b</i>
18396–0431	18 42 18.80	–04 28 37.00	+130.5	0.70	2.1	1.60	31.40	<i>b</i>
18488+0000	18 51 24.97	+00 04 11.10	+83.22	1.55	3.8	6.30	6.30	<i>d</i>
18507+0121	18 53 18.60	+01 25 17.00	+58.08	5.01	11.5	61.40	64.90	<i>d</i>
18507+0121	18 53 18.60	+01 25 17.00	+60.25	0.99	3.4	3.60	64.90	<i>d</i>
18566+0408	18 59 10.40	+04 12 18.00	+79.03	0.63	5.4	3.60	17.80	<i>g</i>
19043+0726	19 06 48.50	+07 31 42.00	+58.35	0.88	3.9	3.60	4.90	<i>g</i>
19088+0902	19 11 17.60	+09 07 29.00	+58.47	1.28	11.4	15.60	15.60	<i>g</i>
19092+0841	19 11 39.57	+08 46 30.40	+58.10	3.49	2.7	10.00	11.10	<i>d</i>
19092+0841	19 11 39.57	+08 46 30.40	+58.19	0.27	3.6	1.00	11.10	<i>d</i>
20050+2720	20 07 06.20	+27 28 53.00	+6.32	2.76		3.29	3.29	<i>f</i>
Sources not detected								
18162-1612	18 19 07.40	–16 11 34.00	–	–	–	–	–	<i>g</i>
18247-1147	18 27 32.00	–11 45 53.00	–	–	–	–	–	<i>g</i>
18310-0825	18 33 47.90	–08 23 47.00	–	–	–	–	–	<i>g</i>
18511+0146	18 53 38.30	+01 50 24.00	–	–	–	–	–	<i>g</i>
18521+0134	18 54 40.90	+01 38 04.00	–	–	–	–	–	<i>g</i>
18532+0047	18 55 51.00	–00 50 56.00	–	–	–	–	–	<i>g</i>
18551+0302	18 57 42.60	+03 06 03.00	–	–	–	–	–	<i>g</i>
19094+0944	19 11 51.20	+09 49 35.00	–	–	–	–	–	<i>g</i>
19198+1423	19 22 07.90	+14 29 19.00	–	–	–	–	–	<i>g</i>

Notes. To differentiate the pointings made toward the IRAS source position from the other pointings, we add an asterisk to the source name.

† Integrated intensity of each maser component.

‡ Total integrated intensity of all maser components.

^aVal'ts et al. (2000), ^bFontani et al. (2010), ^cChen et al. (2011), ^dChen et al. (2012),

^eChen et al. (2013), ^fGan et al. (2013), ^gYang et al. (2017).

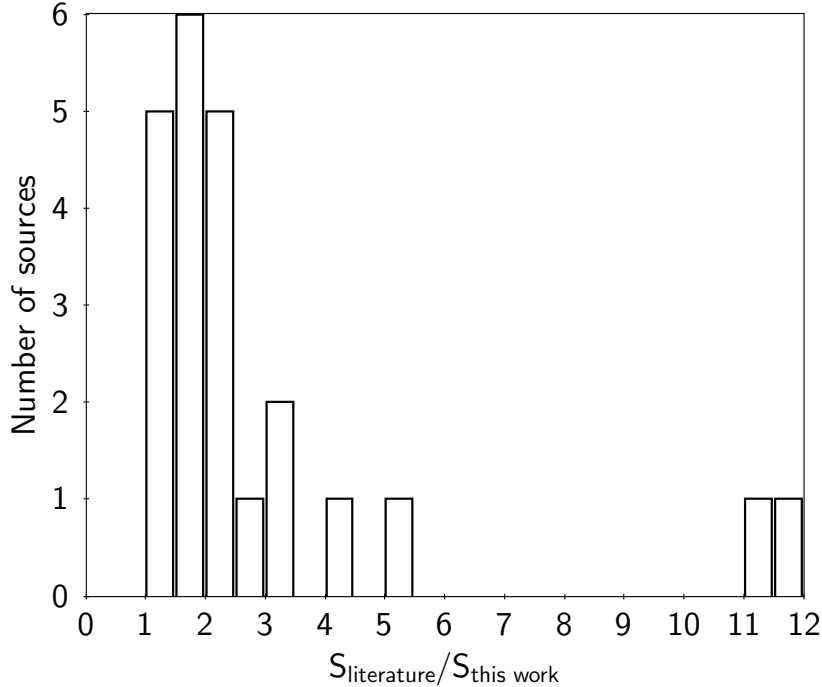


Figure 5.3: Histogram of the ratio between the total integrated flux densities reported in the literature for the class I methanol masers at 95.1 GHz (see Table 5.5) and the integrated intensities measured in this work (see Table 5.4).

5.3.2 Class II methanol masers detections

We found a moderate detection rate in the class II methanol transition at 108.8 GHz and a very low detection rate in the 107.0 GHz line. We do not detect emission in the class II methanol transitions at 85.5, 86.6 and 86.9 GHz but this is not surprising since these are rare transitions that usually show low detection rates (Cragg et al. 2001; Minier and Booth 2002; Ellingsen et al. 2003). Additionally, the few tens of detections reported in the literature showed weak emission that could be easily missed in our low resolution channels. The properties of class II methanol maser detections are shown in Table 5.6.

We detected the 107.0 GHz line toward 2 of the 38 targets observed (5% detection rate); both of them are new detections. Source 18024–2116 has a peak flux density of 0.07 Jy and an integrated flux density of 6.3 Jy km s⁻¹, and for source 18182–1433, we detect a peak flux density of 0.05 Jy, close to the detection limit, and an integrated flux density of 8.8 Jy km s⁻¹. Our low detection rate contrasts with the higher rates found in previous surveys of this transition (Val'tts et al. 1995, 1999; Caswell et al. 2000; Minier and Booth 2002). This could be explained since the few systematic searches made to date have been targeted toward the peak position of the strongest class II 6.6 GHz masers while we used the peak position of the brightest class I 44 GHz masers as the pointing centers. The authors justify their pointing selection mentioning that the 107.0 GHz emission appears to coincide within a few arcseconds (5'') with the position of 6.6 GHz masers. If this assumption applies in our sample as well, there could be cases where the emission would not be well covered by the LMT primary beam, since the 44 GHz masers were often offset by several arcseconds from the location of 6.6 GHz masers. Additionally, this transition is placed in a complicated part of the spectrum affected by the strong oscillations of the ¹³CO line that increase the rms noise level.

We report new detections of the 108.8 GHz line which was detected toward 15 of 38 regions observed (39% detection rate). This result is similar to the surveys made by Val'tts et al. (1999) and Minier and Booth (2002) where they found detection rates of 39% (16 of 41 sources) and 43% (10 of 23 sources), respectively. We found peak flux densities ranging from 0.03 to 0.16 Jy (similar mean and median values of 0.07 Jy) and integrated flux densities in the range from 4.8 to 23.4 Jy km s⁻¹ (similar mean and median values of 10.8 Jy).

Table 5.6: Parameters measured for the thermal transition at 96.7 GHz and the class II methanol masers at 107.0 and 108.8 GHz.

Source IRAS Name	96.7 GHz			107.0 GHz			108.8 GHz		
	rms (mJy)	S_p (Jy)	S_{int} (Jy km s ⁻¹)	rms (mJy)	S_p (Jy)	S_{int} (Jy km s ⁻¹)	rms (mJy)	S_p (Jy)	S_{int} (Jy km s ⁻¹)
05274+3345	5.3	0.16	28.6	10.2	—	—	12.5	0.08*	12.0
05358+3543	4.5	0.19	35.6	4.4	—	—	6.7	0.03*	5.5
18018–2426	1.4	0.05	8.4	12.3	—	—	12.4	—	—
18024–2119	5.4	0.30	48.5	6.3	0.07	6.3	7.4	0.09	11.5
18089–1732	5.3	0.19	30.7	11.0	—	—	8.0	—	—
18102–1800	3.9	0.30	48.2	7.2	—	—	6.8	0.09	10.9
18144–1723	5.3	0.32	55.5	9.4	—	—	11.5	0.16	23.4
18151–1208	1.8	0.06	9.3	8.1	—	—	6.4	—	—
18162–1612	3.5	0.14	24.6	8.0	—	—	10.0	—	—
18182–1433	5.1	0.18	33.5	10.0	0.05 [†]	8.8	20.9	—	—
18247–1147	2.5	0.05	9.0	7.3	—	—	10.0	—	—
18264–1152	4.8	0.26	45.5	10.5	—	—	10.5	0.07	9.9
18290–0924	4.7	0.09	15.3	9.1	—	—	12.0	—	—
18306–0835	7.5	0.28	48.2	7.7	—	—	11.0	0.09	12.3
18308–0841	5.0	0.22	39.4	7.7	—	—	11.0	0.06*	7.4
18310–0825	2.5	0.06	10.9	5.2	—	—	6.2	—	—
18337–0743	2.7	0.05	9.6	4.4	—	—	6.1	—	—
18345–0641	5.2	0.21	33.9	7.7	—	—	9.5	0.05	6.5
18396–0431	3.6	0.10	17.6	7.0	—	—	9.0	—	—
18488+0000	5.2	0.21	37.3	8.7	—	—	12.2	0.11	13.8
18507+0121	7.3	0.50	90.1	8.9	—	—	11.4	0.12	19.0
18511+0146	3.2	0.08	15.4	6.6	—	—	9.3	—	—
18517+0437	3.6	0.15	24.7	13.4	—	—	11.5	0.07	10.2
18521+0134	2.9	0.03	6.0	9.2	—	—	9.4	—	—
18527+0301	2.7	0.04	7.1	6.8	—	—	8.3	—	—
18530+0215	2.7	0.05	9.2	7.3	—	—	8.8	—	—
18532+0047	2.1	0.05	10.5	5.8	—	—	9.7	—	—
18551+0302	2.0	0.06	11.1	4.7	—	—	5.5	0.03	4.8
18553+0414	2.7	0.06	9.4	6.0	—	—	9.5	—	—
18565+0349	3.4	0.14	23.1	8.8	—	—	14.1	—	—
18566+0408	4.0	0.16	27.2	6.1	—	—	8.1	0.07	8.9
19043+0726	2.2	0.04	6.9	6.4	—	—	7.5	—	—
19088+0902	4.4	0.20	39.7	6.1	—	—	7.1	0.03	5.6
19092+0841	2.6	0.08	15.5	6.3	—	—	7.7	—	—
19094+0944	2.0	0.17	3.1	5.5	—	—	5.0	—	—
19198+1423	1.4	0.02	3.9	6.1	—	—	11.5	—	—
20050+2720	3.4	0.15	24.3	5.5	—	—	9.2	—	—
20056+3350	1.6	0.04	7.2	7.0	—	—	14.1	—	—
Average	3.7	0.14	24.3	7.6	0.06	7.5	9.7	0.08	10.8
Median	3.4	0.14	20.3	7.2	0.06	7.5	9.5	0.07	10.2

Additional pointings toward IRAS positions

Table 5.6 – continued

Source IRAS Name	96.7 GHz			107.0 GHz			108.8 GHz		
	rms (mJy)	S_p (Jy)	S_{int} (Jy km s ⁻¹)	rms (mJy)	S_p (Jy)	S_{int} (Jy km s ⁻¹)	rms (mJy)	S_p (Jy)	S_{int} (Jy km s ⁻¹)
05274+3345*	2.0	0.03 ^a	4.2 ^a	5.1	–	–	5.4	–	–
05358+3543*	2.6	0.05	9.3	5.1	–	–	5.6	–	–
18144–1723*	4.0	0.25	44.1	5.9	–	–	9.7	0.1	15.3
18264–1152*	3.3	0.19	32.5	9.1	–	–	11.0	–	–
18345–0641*	4.6	0.20	32.5	6.7	–	–	8.4	–	–
18507+0121*	6.1	0.42	77.3	7.3	–	–	10.2	0.07	12.1

Notes. To differentiate the pointings made toward the IRAS source position from the other pointings, we add an asterisk to the source name.

† Emission at the 5σ detection limit.

– Emission below the 5σ detection limit.

^a Emission was detected in absorption (see Figure 5.9).

5.3.3 Thermal methanol detections

We found a detection rate of 100 % for the thermal methanol line at 96.7 GHz. The parameters of these detections are reported in the first column of Table 5.6. The peak flux densities range from 0.02 to 0.50 Jy (same mean and median value of 0.14 Jy) and the integrated flux densities from 3.1 to 90.1 Jy (mean and median values of 24.3 and 20.3 Jy). Our result is similar to the 96% detection rate (22 of 23 sources detected) reported by Minier and Booth (2002) for this line, made with the Onsala 20-m telescope.

The 96.7 GHz line consists of four methanol transitions in the family $2_k \rightarrow 1_k$ of *A* and *E* type (see Table 5.2). We can not resolve them in frequency space due to our low spectral resolution, but in most cases, we detect their emission in 2 RSR channels (see Figure 5.2). Our detections are interesting since this is the first detection of this thermal line toward the majority of these sources except for 05358+3543, 18089–1732, 18151–1208, 18182–1433, 18264–1152 and 18310–0825, that were previously detected by Leurini et al. (2007a,b). These results motivate us to conduct LMT follow up observations with higher spectral resolution to obtain physical parameters such as column density and estimate lower limits for the gas temperature of each source through the rotational diagram method that will be discussed in Chapter 6.

5.3.4 Molecular line detections

We detected several thermal molecular lines that are high density gas tracers, commonly found in star-forming regions. The brightest, with 100% detection rates are from HCN, HCO⁺, HNC, N₂H⁺, CS, SO and ¹³CO; all these lines show a single transition within the RSR passband. Emission from the SiO molecule — a known shocked gas tracer — was also detected but with a slightly lower detection rate of 76%. There are other molecular lines with several transitions within the passband that were also detected with moderate detection rates, for example, CH₃CN and HC₃N. For comparison with similar studies, here we will present the results of the HC₃N transition at 90.9 GHz. The remaining transitions of HC₃N, CH₃CN among other molecules detected will be discussed as future work in Chapter 6. The parameters measured for these lines are presented in Tables 5.7, 5.8 and 5.9.

Such high detection rates ($\sim 77 - 89\%$) were also found for the $(1 - 0)$ transitions of HCN, HCO⁺, HNC and N₂H⁺ in the Millimetre Astronomy Legacy Team 90 GHz survey (MALT90; Rathborne et al. 2016). They observed 3,247 high-mass clumps selected from the ATLASGAL 870 μ m Galactic plane survey. Four of our sources (18024–2119, 18089–1732, 18102–1800 and 18144–1723) correspond in position within $10''$ with the MALT90 sample, thus confirming our detections.

Table 5.7: Parameters measured for the molecular lines SiO, HCN and HCO⁺.

Source IRAS Name	SiO (86.8 GHz)			HCN (88.6 GHz)			HCO ⁺ (89.1 GHz)		
	rms (mJy)	S_p (Jy)	S_{int} (Jy km s ⁻¹)	rms (mJy)	S_p (Jy)	S_{int} (Jy km s ⁻¹)	rms (mJy)	S_p (Jy)	S_{int} (Jy km s ⁻¹)
05274+3345	22.7	0.24	32.7	61.8	1.7	238.9	95.2	1.2	203.3
05358+3543	8.7	0.11	11.2	13.0	0.9	129.4	37.8	1.0	144.1
18018-2426	11.4	—	—	348.1	1.6	267.0	26.4	1.1	169.0
18024-2119	7.5	0.17	31.6	44.0	0.5	82.7	2.1	0.2	36.1
18089-1732	9.4	0.06	6.4	9.3	0.3	38.8	6.2	0.3	31.9
18102-1800	7.2	0.16	24.4	2.2	0.6	99.2	8	0.4	63.0
18144-1723	8.2	0.31	41.5	4.8	1.7	250.5	4.6	0.9	133.1
18151-1208	14.6	0.07	6.7	126.5	1.4	204.6	18.6	1.2	158.7
18162-1612	11.0	0.06	7.5	7.5	0.9	124.4	2.9	0.5	78.6
18182-1433	5.2	0.14	15.2	22.3	1.3	182.8	40	0.8	111.6
18247-1147	4.0	—	—	49.7	0.2	40.7	20.5	0.2	29.3
18264-1152	17.3	0.22	28.0	48.4	2.3	335.1	12.6	2.0	286.6
18290-0924	8.9	0.03	2.9	33.3	0.7	96.7	84	0.4	62.5
18306-0835	13.8	0.15	21.3	53.7	1.3	184.2	98.5	0.6	89.3
18308-0841	9.7	0.09	14.2	32.5	0.7	100.9	70.6	0.4	63.7
18310-0825	5.3	—	—	5.4	0.2	32.1	18.2	0.1	18.7
18337-0743	3.8	—	—	2.6	0.1	9.4	0.1	0.1	6.1
18345-0641	9.5	0.06	7.4	86.7	0.6	97.1	69.2	0.4	85.9
18396-0431	5.0	0.04	6.1	1.5	0.2	40.3	24.2	0.1	25.7
18488+0000	9.6	0.12	17.6	11.3	0.3	38.3	29.2	0.2	30.4
18507+0121	9.1	0.34	50.5	4.9	1.1	153.4	26.8	0.4	54.8
18511+0146	7.8	0.06	6.5	6.8	0.2	33.5	7.6	0.3	44.7
18517+0437	15.3	0.09	10.7	19.7	1.4	193.6	6.2	1.4	193.0
18521+0134	4.0	—	—	6.2	0.2	26.4	10.3	0.1	15.3
18527+0301	4.6	0.02	2.1	8.0	0.2	28.7	16.4	0.1	16.6
18530+0215	9.0	—	—	22.6	0.6	84.8	2.7	0.4	69.7
18532+0047	4.8	—	—	6.1	0.2	21.5	5	0.1	8.9
18551+0302	8.7	0.04	3.4	7.1	0.5	66.6	11.9	0.2	18.7
18553+0414	4.1	0.02	2.7	34.6	0.2	31.4	14.9	0.1	18.6
18565+0349	4.5	0.04	8.2	1.6	0.3	48.9	48.2	0.2	34.2
18566+0408	9.6	0.09	12.2	18.2	0.3	38.2	38.6	0.2	33.0
19043+0726	4.2	0.02	3.2	5.0	0.3	43.5	10.4	0.2	25.8
19088+0902	7.6	0.05	6.0	4.3	0.3	39.1	11.2	0.2	26.6
19092+0841	8.0	0.05	5.3	8.3	0.5	69.7	20.3	0.4	64.6
19094+0944	5.2	0.06	7.8	5.6	0.5	70.5	23.1	0.3	43.3
19198+1423	4.1	—	—	6.1	0.3	34.2	5.3	0.2	31.1
20050+2720	6.9	0.06	8.1	39.2	0.5	76.1	25.7	0.6	85.5
20056+3350	6.3	—	—	69.3	0.4	62.1	14.1	0.3	43.1
Mean	8.3	0.1	13.8	32.6	0.7	97.8	25.5	0.5	69.9
Median	7.9	0.1	8.1	10.3	0.5	70.1	17.3	0.3	44.0
Pointings toward IRAS positions									
05274+3345*	3.7	—	—	2.4	0.1	16.1	19.9	0.1	17.9
05358+3543*	6.30	0.04	4.2	4.2	0.4	61.9	24.2	0.5	62.1
18144-1723*	10.30	0.22	30.5	10.8	1.2	165.3	18.7	0.6	80.7
18264-1152*	13.45	0.17	19.0	83.5	1.5	222.9	26.8	1.3	182.6
18345-0641*	7.90	0.07	10.7	22.9	0.6	90.7	118.3	0.5	76.6
18507+0121*	9.24	0.26	38.7	11.1	0.7	94.6	1.9	0.4	52.8

Notes. To differentiate the pointings made toward the IRAS source position from the other pointings, we add an asterisk to the source name.

—Emission below the 5σ detection limit.

Table 5.8: Parameters measured for the molecular lines HNC, HC₃N and N₂H⁺.

Source IRAS Name	HNC (90.6 GHz)			HC ₃ N (90.9 GHz)			N ₂ H ⁺ (93.1 GHz)		
	rms (mJy)	S_p (Jy)	S_{int} (Jy km s ⁻¹)	rms (mJy)	S_p (Jy)	S_{int} (Jy km s ⁻¹)	rms (mJy)	S_p (Jy)	S_{int} (Jy km s ⁻¹)
05274+3345	36.6	0.6	88.7	6.53	0.19	22.5	32.1	0.6	88.8
05358+3543	4.1	0.5	67.9	5.58	0.20	25.5	43.0	0.8	138.8
18018–2426	93.0	0.5	89.2	30.49	0.16	26.8	11.6	0.5	73.6
18024–2119	39.6	0.2	34.1	17.62	0.12	16.6	9.8	0.7	103.3
18089–1732	17.4	0.3	37.1	25.24	0.21	32.7	11.3	0.8	129.5
18102–1800	28.9	0.5	70.4	13.34	0.12	20.5	5.8	0.6	106.7
18144–1723	11.5	0.9	120.5	0.78	0.29	41.0	3.0	0.8	163.6
18151–1208	67.7	0.6	85.4	23.83	0.12	11.3	12.1	0.5	82.1
18162–1612	7.4	0.4	52.8	2.10	0.08	9.5	5.2	0.5	93.9
18182–1433	5.2	0.6	81.9	7.75	0.24	29.4	4.3	0.7	122.6
18247–1147	33.8	0.2	33.1	4.71	0.03	3.6	7.1	0.3	50.3
18264–1152	54.5	0.9	113.3	24.13	0.21	23.0	115.6	0.9	170.8
18290–0924	21.4	0.3	45.2	0.07	0.06	7.4	23.5	0.6	85.9
18306–0835	20.9	0.6	82.1	5.37	0.21	26.0	41.3	0.9	139.8
18308–0841	15.6	0.4	59.1	3.29	0.14	16.5	46.4	0.8	127.2
18310–0825	1.1	0.2	27.0	2.08	0.06	6.9	6.3	0.4	59.7
18337–0743	2.3	0.1	11.3	1.20	0.06	9.0	12.4	0.3	49.8
18345–0641	1.6	0.4	61.2	0.56	0.10	13.8	5.4	0.5	81.8
18396–0431	6.5	0.2	27.1	4.77	0.04	4.7	4.9	0.4	57.7
18488+0000	8.7	0.4	53.7	5.35	0.17	23.3	5.6	0.6	105.0
18507+0121	4.0	0.7	92.1	9.31	0.38	48.2	57.3	1.4	257.0
18511+0146	6.6	0.3	41.9	5.91	0.10	14.1	28.9	0.5	91.7
18517+0437	19.1	0.6	84.8	12.49	0.14	17.5	75.3	0.5	95.1
18521+0134	5.7	0.2	21.6	1.18	0.05	7.5	14.9	0.3	40.7
18527+0301	5.8	0.1	11.9	1.85	0.04	4.9	10.0	0.2	26.7
18530+0215	5.3	0.4	55.1	2.57	0.08	9.5	23.2	0.4	62.5
18532+0047	5.3	0.2	20.7	1.63	0.05	7.4	18.8	0.3	44.1
18551+0302	6.5	0.3	42.9	5.82	0.11	14.8	8.2	0.3	57.6
18553+0414	24.2	0.1	15.7	6.21	0.04	6.0	4.2	0.2	31.0
18565+0349	6.1	0.2	29.9	3.31	0.06	8.0	13.2	0.4	58.2
18566+0408	13.7	0.2	34.3	5.91	0.12	13.5	12.8	0.4	57.1
19043+0726	5.7	0.1	17.2	1.81	0.04	4.2	10.7	0.1	22.0
19088+0902	4.1	0.2	33.0	6.05	0.16	20.8	39.5	0.8	140.7
19092+0841	6.8	0.3	35.2	5.57	0.09	11.0	21.6	0.3	54.2
19094+0944	3.8	0.2	26.6	1.46	0.04	3.8	6.3	0.2	32.7
19198+1423	5.7	0.1	19.3	0.91	0.02	2.2	9.9	0.1	23.4
20050+2720	28.8	0.3	42.1	17.86	0.10	16.2	12.6	0.7	111.7
20056+3350	37.0	0.2	28.2	11.48	0.06	9.1	6.6	0.2	35.9
Mean	17.7	0.4	49.8	7.5	0.1	15.5	20.5	0.5	86.1
Median	7.1	0.3	42.0	5.5	0.1	13.6	11.9	0.5	81.9
Pointings toward IRAS positions									
05274+3345*	2.2	0.1	11.6	3.00	–	–	3.7	0.1	11.2
05358+3543*	4.2	0.2	27.3	1.49	0.03	3.2	15.1	0.2	42.4
18144–1723*	12.2	0.6	81.9	15.17	0.19	22.3	30.1	0.6	115.9
18264–1152*	28.3	0.6	82.6	13.97	0.09	9.5	28.0	0.6	112.9
18345–0641*	8.1	0.3	56.7	2.37	0.08	11.3	7.6	0.4	67.4
18507+0121*	6.1	0.5	61.5	8.78	0.25	31.1	60.9	1.1	208.4

Notes. To differentiate the pointings made toward the IRAS source position from the other pointings, we add an asterisk to the source name.

–Emission below the 5 σ detection limit.

Table 5.9: Parameters measured for the molecular lines CS, SO and ^{13}CO .

Source IRAS Name	CS (97.9 GHz)			SO (99.2 GHz)			^{13}CO (110.2 GHz)		
	rms (mJy)	S_p (Jy)	S_{int} (Jy km s $^{-1}$)	rms (mJy)	S_p (Jy)	S_{int} (Jy km s $^{-1}$)	rms (mJy)	S_p (Jy)	S_{int} (Jy km s $^{-1}$)
05274+3345	9.71	0.24	35.2	6.70	0.65	90.2	68.0	1.6	183.0
05358+3543	15.46	0.28	40.0	12.32	0.24	35.6	10.8	0.5	72.1
18018-2426	9.97	0.18	29.3	24.15	0.41	57.7	35.8	2.8	316.8
18024-2119	15.50	0.17	22.7	4.76	0.15	22.1	6.8	0.9	99.7
18089-1732	12.50	0.20	40.4	15.31	0.16	27.3	243.3	1.6	199.8
18102-1800	20.37	0.15	25.3	15.01	0.15	23.7	100.0	1.1	134.9
18144-1723	23.05	0.32	46.7	16.71	0.24	40.1	222.6	1.3	188.4
18151-1208	35.38	0.23	40.8	11.83	0.09	15.1	112.5	1.4	186.8
18162-1612	10.76	0.17	25.2	4.78	0.08	11.0	57.8	1.3	139.2
18182-1433	18.44	0.30	43.0	10.70	0.24	37.4	278.7	2.3	298.1
18247-1147	7.46	0.11	18.9	2.13	0.03	4.5	19.6	1.3	191.2
18264-1152	4.74	0.46	78.5	43.40	0.26	43.8	202.0	1.4	209.0
18290-0924	7.37	0.17	23.3	3.18	0.07	9.8	22.8	1.9	224.4
18306-0835	16.32	0.31	42.8	5.41	0.18	24.9	30.9	1.4	183.0
18308-0841	13.20	0.22	30.9	7.40	0.12	17.9	5.1	1.6	195.2
18310-0825	6.21	0.11	17.7	1.93	0.05	6.6	35.0	0.3	31.6
18337-0743	3.86	0.06	11.3	2.49	0.04	5.7	1.1	0.3	42.9
18345-0641	8.21	0.16	26.2	4.00	0.08	11.3	12.1	1.1	132.7
18396-0431	5.12	0.10	15.9	5.62	0.05	6.8	21.7	1.2	139.6
18488+0000	10.99	0.24	33.1	4.76	0.22	31.6	4.8	1.7	196.8
18507+0121	37.41	0.55	80.1	16.89	0.42	65.3	60.3	1.4	186.1
18511+0146	11.71	0.19	28.9	6.16	0.08	11.7	83.2	1.0	119.7
18517+0437	17.29	0.23	34.0	48.48	0.25	42.7	2.0	1.8	302.2
18521+0134	4.18	0.12	17.4	3.09	0.06	7.9	62.6	1.5	186.2
18527+0301	3.89	0.09	14.4	3.25	0.08	11.7	42.6	1.1	115.3
18530+0215	4.25	0.19	29.0	2.38	0.06	8.3	18.8	1.2	151.4
18532+0047	8.05	0.12	17.3	4.88	0.06	8.7	40.4	0.8	101.2
18551+0302	4.10	0.19	31.0	7.84	0.12	20.3	63.3	0.5	51.8
18553+0414	9.38	0.10	15.2	5.41	0.08	12.1	6.5	0.9	105.6
18565+0349	5.34	0.12	19.6	6.39	0.10	14.2	8.3	1.4	158.0
18566+0408	5.69	0.12	16.5	5.15	0.13	18.6	16.3	0.9	101.8
19043+0726	2.43	0.09	14.5	2.78	0.05	7.8	106.0	0.8	99.4
19088+0902	6.42	0.19	31.1	8.18	0.11	16.5	35.1	0.5	58.0
19092+0841	10.74	0.14	21.0	9.76	0.13	20.5	176.3	1.2	155.6
19094+0944	6.47	0.08	12.0	5.40	0.05	8.1	32.8	0.7	86.3
19198+1423	6.24	0.08	12.2	3.30	0.03	4.8	153.4	1.2	152.2
20050+2720	8.10	0.29	45.2	7.46	0.09	13.0	11.1	0.8	95.6
20056+3350	2.96	0.13	21.6	8.88	0.10	15.2	102.0	1.3	154.4
Mean	10.8	0.2	29.2	9.4	0.1	21.9	66.1	1.2	151.2
Median	8.2	0.2	25.7	5.9	0.1	15.1	35.4	1.2	151.8
Additional pointings toward IRAS positions									
05274+3345*	1.89	0.04	6.6	4.80	—	—	16.0	0.5	60.8
05358+3543*	6.21	0.11	19.2	7.12	0.10	15.4	32.1	0.6	79.5
18144-1723*	17.65	0.21	31.4	13.24	0.14	23.2	184.7	0.9	120.5
18264-1152*	4.65	0.30	50.1	23.62	0.22	37.2	304.5	1.4	206.1
18345-0641*	8.68	0.16	23.9	3.96	0.08	13.1	12.5	1.1	124.1
18507+0121*	27.33	0.37	50.6	4.91	0.29	46.2	60.8	1.3	171.5

Notes. To differentiate the pointings made toward the IRAS source position from the other pointings, we add an asterisk to the source name.

—Emission below the 5σ detection limit.

5.4 Discussion

5.4.1 Line Identification

The main problem we had with the spectra was to unambiguously identify the molecular lines detected. Since the spectral resolution is 100 km s^{-1} (31 MHz), many molecular lines fall within a single RSR channel. The identification was made according to the probability of the molecule being present based on its upper energy level, the associated Einstein spontaneous emission coefficient, and the molecular complexity and abundance.

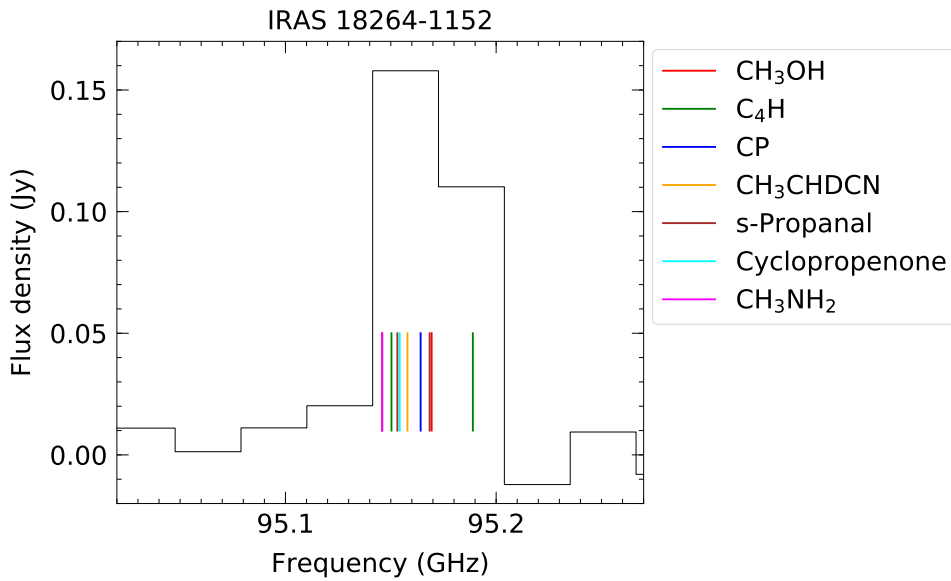


Figure 5.4: Molecular emission near 95 GHz. The color lines indicate seven different molecular species within two channels of 100 km s^{-1} each.

To search for the most likely molecules, we restrict the upper energy level to 160 K and the minimum Einstein spontaneous emission coefficient to $1 \times 10^{-6} \text{ s}^{-1}$. These reduced the number of molecules within one channel to at least five different molecular species. For example, Figure 5.4 shows emission near 95 GHz within two RSR channels of 100 km s^{-1} . Seven different molecular species were identified, C_4H , CP, CH_3OH , CH_3OCHO , CH_3CHDCN , CH_3HN_2 , s-Propanal and Cyclopropanone. We can not provide a definitive identification but in terms of abundance in star-forming regions, methanol is likely to dominate the other molecules.

5.4.2 Spectral Dilution

As mentioned in Section 5.3.1, the 95.1 GHz methanol line was previously observed at high spectral resolution by several authors toward 32 of the 38 sources and emission was detected in 23 of the 32 sources. The parameters reported in the literature for the 23 regions are given in Table 5.5. From this table and also from Figure 5.5, we can note multiple velocity components with narrow line widths and peak flux densities larger than 1 Jy. The integrated flux density of each component is also given as well as the total integrated flux density which is the sum of all velocity components.

In principle the integrated flux density should be conserved, i.e., the total integrated flux density reported in the literature should be the same as the integrated flux density reported in this work. We considered the total integrated flux density given in the literature (column 8 of Table 5.5) since RSR can not distinguish each velocity component separately. The histogram presented in Figure 5.3 shows the ratio between the total integrated flux density from the literature and the integrated flux density obtained in this work. The majority of the sources have ratios ≤ 2.5 . There are two extreme cases where the ratios were 11 and 12 for sources 18566+0408 and 18396-0431. These high values may be due to the low signal to noise ratio since both sources were detected close to the 5σ noise level. The mean and median ratios are 3 and 2, respectively. Although one might hope for ratios closer to 1, given the uncertainties of beam size, pointing position, spectral dilution, calibration errors, etc, we consider ratios ≤ 2.5 to be reasonable.

Another way to examine the spectral dilution is by considering the peak flux density and the line widths. For example, we show in Figure 5.5 the spectra obtained from the single-dish observations made by Chen et al. (2012) with a spectral resolution of 0.19 km s^{-1} along with the corresponding RSR spectra. For 18182-1433, they fitted three different maser components but for our purposes we will consider the component with the largest peak flux density. They reported a peak flux density of 19.0 Jy and a line width of 0.84 km s^{-1} (see Table 5.5). Such a line observed in a channel of 100 km s^{-1} would show a peak flux density of about 0.16 Jy. However, we found a channel peak flux density of 0.08 Jy, a factor of 2 lower (see right panel of Figure 5.5). The difference is even greater for 18507+0121 which has the largest peak flux density and line width of all sources reported in Table 5.5. In this case, the peak flux density is 11.5 Jy and line width of 5.0 km s^{-1} . Therefore, the diluted peak flux density would be 0.6 Jy, but we detected 0.1 Jy, a factor of 6 lower.

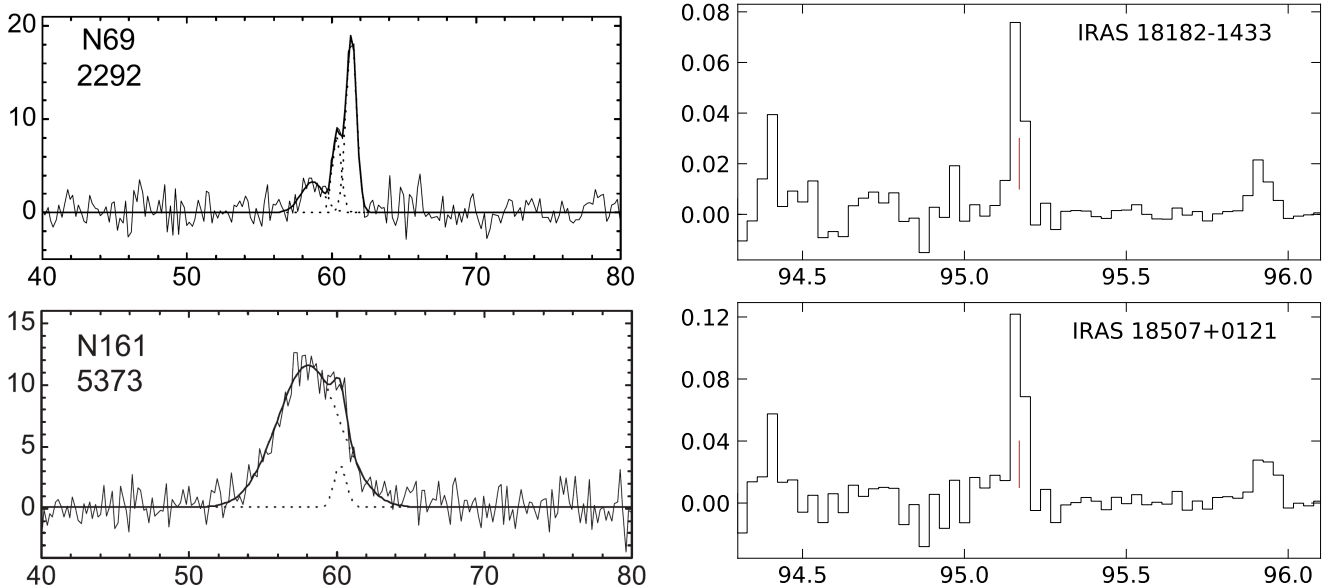


Figure 5.5: Spectra of 95 GHz class I methanol maser lines. Left: spectra obtained by Chen et al. (2012) with a spectral resolution of 0.19 km s^{-1} . The horizontal axis represents velocity in units of km s^{-1} . Right: spectra from this work with channel width of 100 km s^{-1} . The horizontal axis represents frequency in units of GHz. The red line indicates the rest frequency of the 95169.46 MHz maser line. In both the left and right images, the vertical axis represents flux density in units of Jansky.

5.4.3 Double pointing observations

There are six regions where we made two different pointings; these regions are 05274+3345, 05358+3543, 18144–1723, 18264–1152, 18345–0641 and 18507+0121. We made a single pointing at the position of the brightest 44 GHz methanol maser reported in previous VLA Surveys III and IV (hereafter maser pointing). Another pointing was made toward the IRAS source position reported by the catalogs of Molinari and Sridharan et al. (hereafter IRAS pointing). In general, we do not note a substantial difference in the two resulting spectra, except for 05274+3345 and 05358+3543 (hereafter 05274 and 05358, respectively).

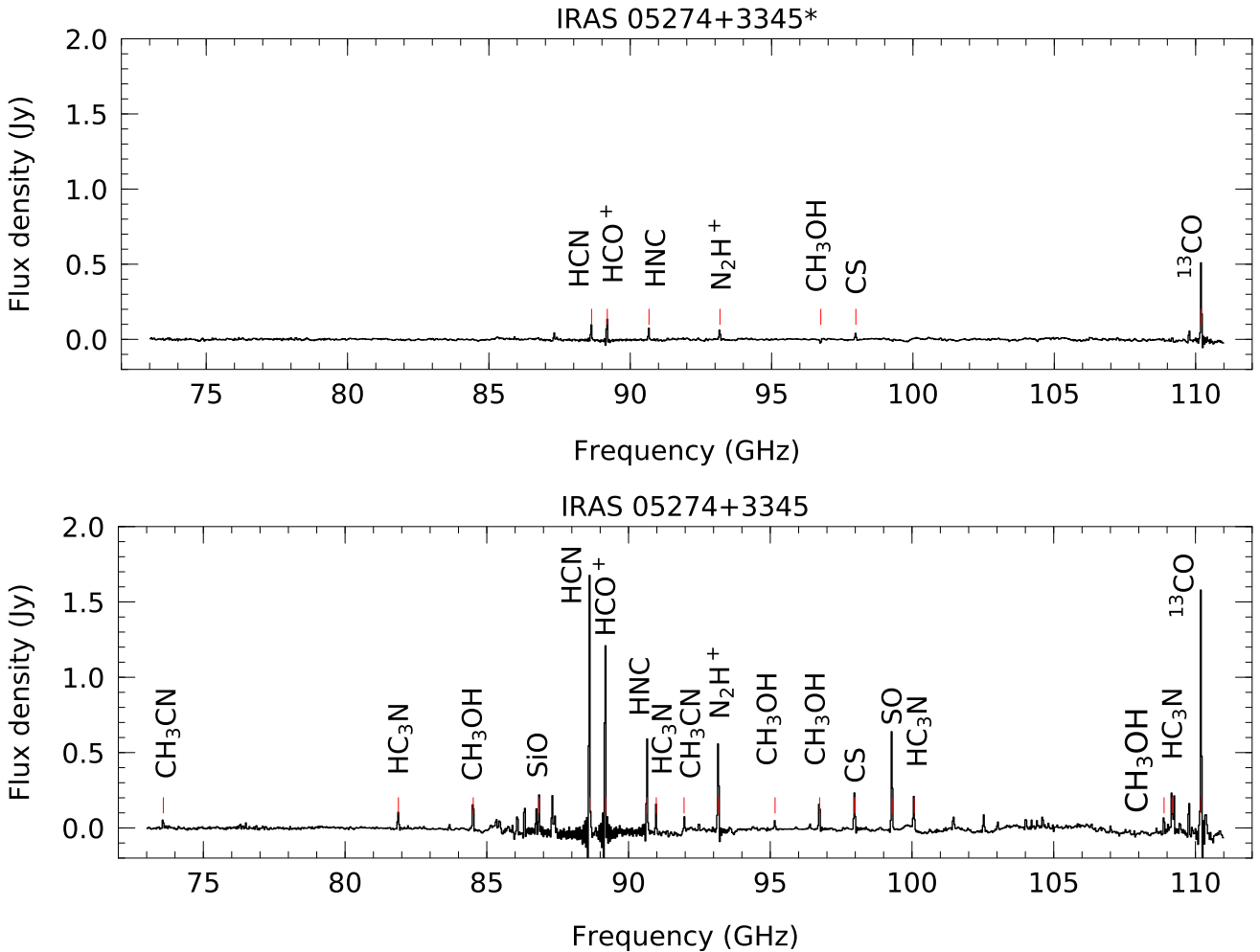


Figure 5.6: Molecular lines detected within the RSR bandpass (73 – 111 GHz). Upper: Spectrum obtained for the pointing at the IRAS source position. Bottom: Spectrum obtained toward the position of the brightest class I 44 GHz methanol maser reported by Survey III.

The area covered by each dual pointing toward 05274 and 05358 is shown in Figure 5.1. We can clearly see that each region hosts two clusters, separated by about 30'' which corresponds to ~ 0.3 pc for 05274 and 05358 at a distance of 1.8 kpc. In the case of 05274 the LMT beams are slightly overlapped while in source 05358 the beams are well separated. The clusters show different characteristics, for example, in the Spitzer images one is seen in green —consistent with an EGO— and the other is redder. Moreover,

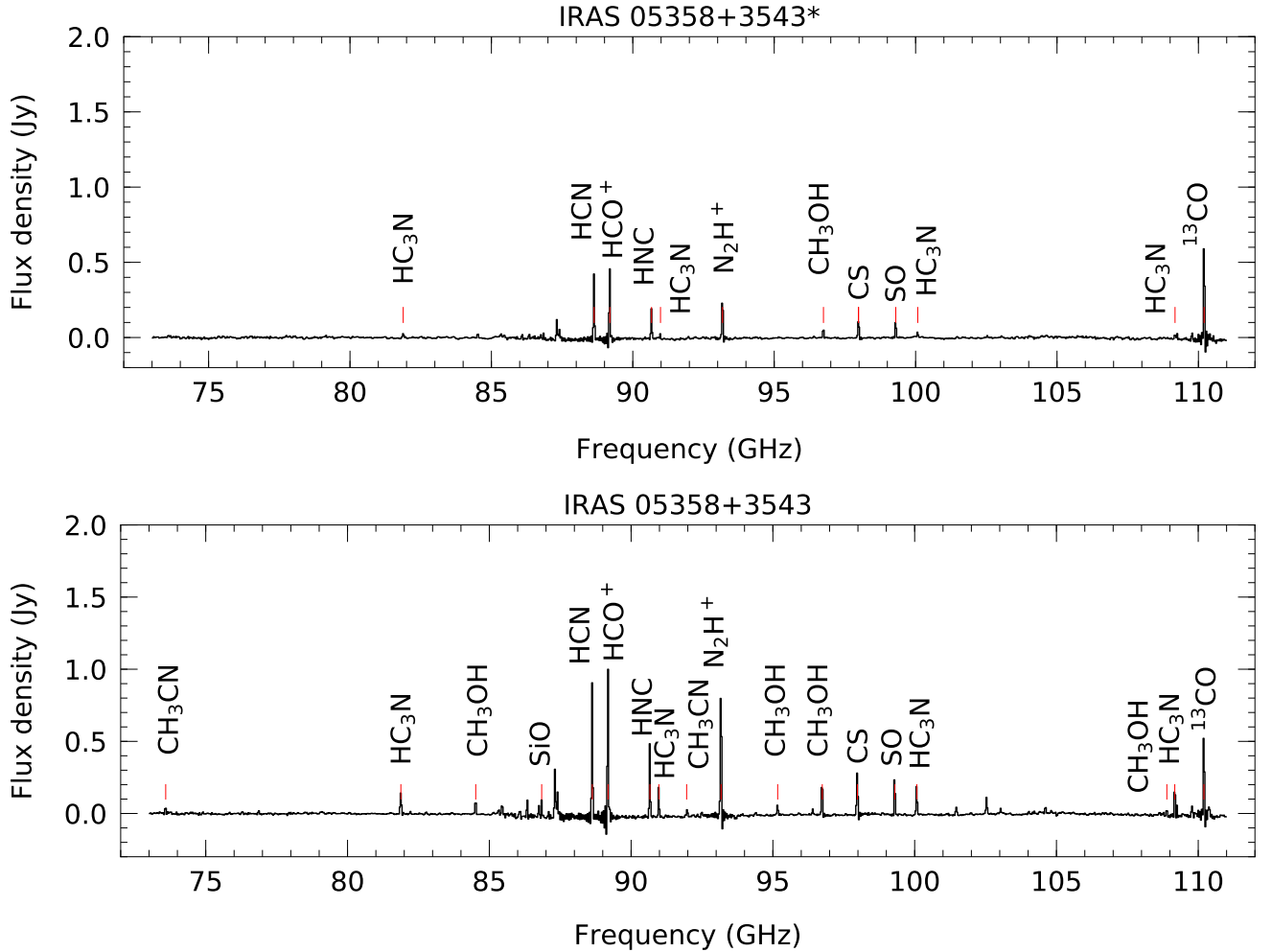


Figure 5.7: Molecular lines detected within the RSR bandpass (73 – 111 GHz). Upper: Spectrum obtained for the pointing at the IRAS source position. Bottom: Spectrum obtained toward the position of the brightest class I 44 GHz methanol maser reported by Survey IV.

many star formation indicators such as water and methanol masers, molecular outflows and millimeter and centimeter continuum emission are associated with the EGO clusters. In contrast, the red clusters—which harbor the IRAS source—lack star formation tracers and age estimates suggest a later evolutionary stage. For example, for the region 05358, Porras et al. (2000) made an age estimation of $\lesssim 2$ Myr for the EGO cluster and 3 Myr for the red cluster. For a detailed discussion on the nature of these clusters, we refer the reader to Section 3.4.2 of Chapter 3 and Section 5.2.1 of Gómez-Ruiz et al. (2016).

The important point to note here is that the 44 GHz masers favor the clusters associated with an EGO (see Figure 5.1) which apparently are the younger clusters with active star formation activity. The LMT spectra toward the maser pointings revealed many more molecular lines and flux densities at least two times larger than in the IRAS pointing. The comparison between each pointing spectra for both sources are shown in Figures 5.6 and 5.7. All methanol maser lines—except the rare transitions—were detected in the maser pointings but none of them were detected toward the IRAS pointing. The thermal methanol was detected

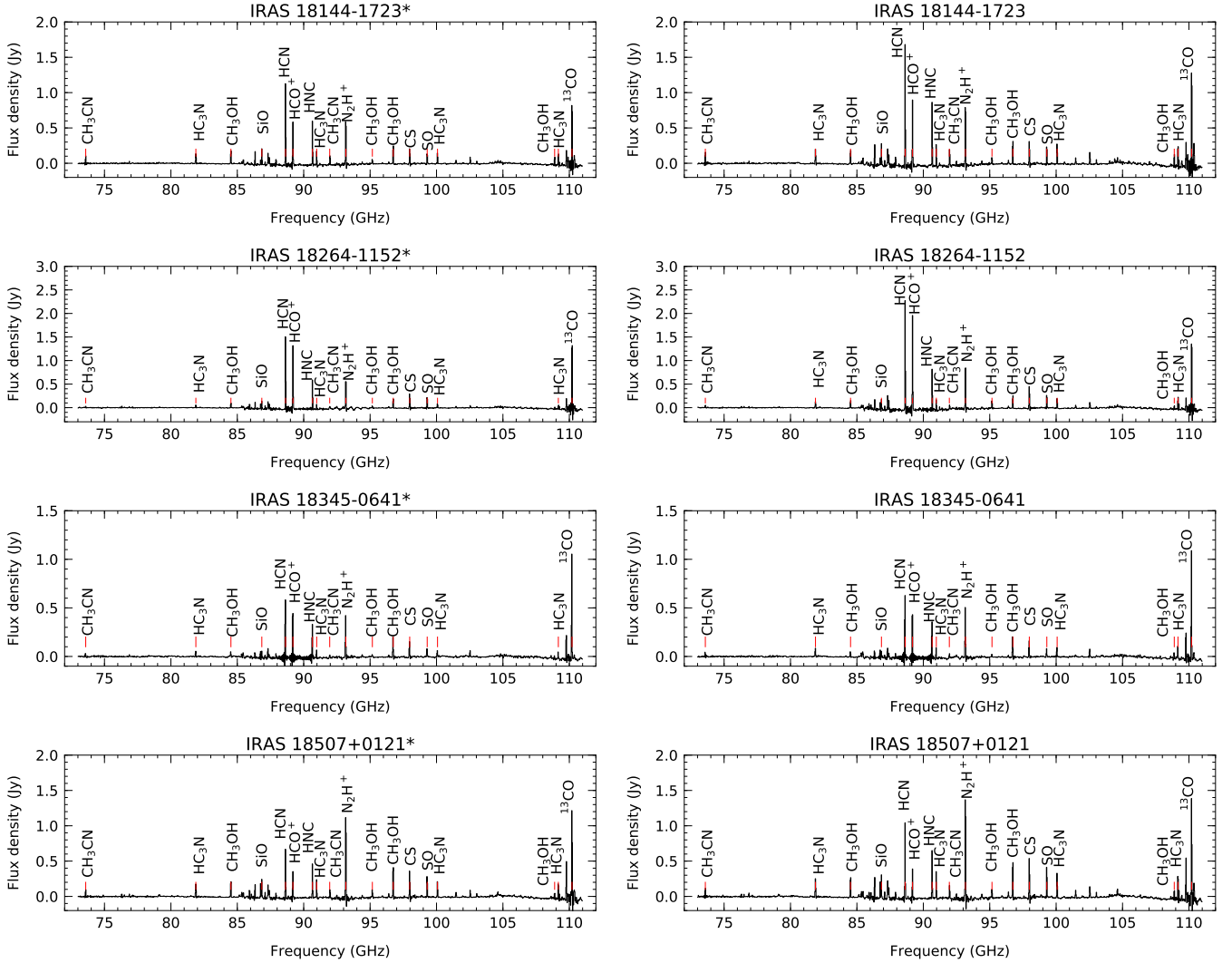


Figure 5.8: Molecular lines detected within the RSR passband (73 – 111 GHz). Left: Spectra obtained for the pointings at the IRAS source position (marked with a star in the title). Right: Spectra obtained toward the position of the brightest 44 GHz methanol maser detected by VLA observations in Surveys III and IV. The pointing centers toward both positions are reported in Table 5.3.

in all observations. The results of the maser pointings suggest a spatial coincidence between the class I and class II methanol masers, but certainly, we need higher angular and spectral resolution observations for confirmation. The comparison between the two spectra of each region support the idea that the clusters are in different evolutionary stages since their molecular richness is quite different.

The other four regions do not show considerable difference between pointings. The main difference is that maser pointings show more intense molecular lines than IRAS pointings. This can be noted in the spectra shown in Figure 5.8 and also can be seen quantified in the integrated flux densities of various molecules given in Tables 5.4, 5.6, 5.7, 5.8 and 5.9.

Another interesting result was found for source 05274. Thermal methanol emission at 96.7 GHz was

detected toward all targets observed except in the IRAS position of source 05274+3345. In this case, the line was detected in absorption, as shown in Figure 5.9.

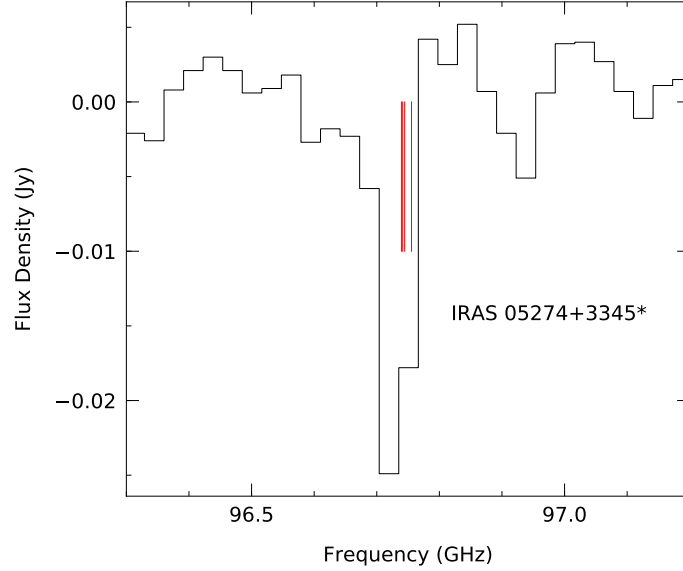


Figure 5.9: The LMT pointing toward the IRAS position of source 05274+3345 revealed a thermal methanol line profile with a behaviour that is unique in our sample. This is the only line in all spectra seen in absorption. The single line detected at 96.7 GHz actually consists of four methanol lines spaced very closely in frequency (indicated by the red lines) that we were not able to resolve (see Table 5.2).

5.4.4 Comparison between 44, 84, and 95 GHz flux densities

A close association exists between the class I methanol maser transitions $7_0 \rightarrow 6_1A^+$ and $8_0 \rightarrow 7_1A^+$ at 44 and 95 GHz, since they are consecutive transitions in the same transition series ($J_0 \rightarrow (J-1)_1A^+$). The difference between them is that the upper energy level of the 95 GHz transition (8_0) is 18.5 K higher than the upper level of the 44 GHz transition (7_0). Therefore the level population of the former is expected to be lower than the population of the latter, resulting in a lower intensity of the 95 GHz emission compared with the intensity of the 44 GHz transition as suggested by modelling of Cragg et al. (1992).

To investigate the relationship between these transitions, several authors have performed comparisons between the intensities of these maser lines. Val'tts et al. (2000) reported a linear dependence with a slope of 0.32 and a correlation coefficient of 0.73 between the peak flux densities of the 44 and 95 GHz masers. They also found a similarity in the spectra of the two transitions, and that on average, the peak flux density of the 95 GHz methanol masers is a factor of 3 weaker than the 44 GHz masers. More recently, McCarthy et al. (2018) found similar results for these two transitions: they found a linear behaviour with a slope of 0.35 and a correlation factor of 0.78 between the observed peak flux densities. They also found a similar 3:1 ratio between the 44 and 95 GHz flux density as reported by Val'tts et al. In the case of the 84 and 95 GHz methanol masers, Kalenskii et al. (2001) made comparisons between their integrated flux densities instead of peak flux densities. They found a linear relationship with a slope of 0.4 and similarities in the spectra of the 84 and 95 GHz lines. The observed relationship between frequency and flux density reported by these authors are consistent with the expectations based on the models of Cragg et al. (1992) and Leurini et al.

(2016).

We made comparisons between the class I methanol maser transitions at 44, 84 and 95 GHz. Due to the low spectral resolution of our LMT observations and the double-channel effect seen in the lines, we do not have reliable information on the actual peak flux densities, therefore, our comparisons were made using the integrated flux densities given in Table 5.4. The flux densities of the 44 GHz masers were taken from the VLA Surveys III and IV. For some sources, the VLA observations detected several velocity components, for example, 18532+0047 showed three 44 GHz masers with integrated flux densities of 0.20, 0.66 and 0.24 Jy km s⁻¹. For such cases, we considered the sum of all integrated flux densities (1.1 Jy km s⁻¹ for 18532+0047) since they could not be resolved by the LMT observations.

In Figure 5.10 we show the comparison between the integrated flux densities of the 44 and 95 GHz methanol lines. We made a linear fit of the form: $\log S_{95} = 0.42 \log S_{44} + 0.39$, and found a correlation coefficient of 0.46. Although these two transitions belong to the same transition series and are two of the strongest transitions reported by models of Cragg et al., we found a weak correlation between them. This could be explained because their intensities have distinct uncertainties since they were obtained by different telescopes. The LMT uncertainties are quite large compared to the VLA flux density uncertainty.

For the integrated flux densities of the 84 and 95 GHz methanol masers, we found a correlation coefficient of 0.70 and a linear dependence of the form: $\log S_{95} = 0.80 \log S_{84} - 0.14$ (see Figure 5.10). In this case, the intensities were obtained by the same telescope (LMT). We detected a steeper relationship between these two transitions compared to the slope of 0.4 found by Kalenskii et al. (2001).

Our results are in agreement with the expected relationship between the 44, 84 and 95 GHz transitions (Cragg et al. 1992). The most intense transition is the 44 GHz, followed by the 84 GHz line and then the 95 GHz transition.

5.4.5 Comparison between methanol lines and other molecular emission

We searched for correlations between the integrated flux densities of the methanol transitions at 84.5, 95.1 and 96.7 GHz with the thermal molecular transitions of SiO, HCN, HCO⁺, HNC, HC₃N, N₂H⁺, CS, SO and ¹³CO. These correlations are shown in Figures 5.11, 5.12 and 5.13.

Figure 5.11 shows comparisons between the integrated flux densities of the class I methanol maser transition at 84.5 GHz with the 9 thermal molecules mentioned above. We noted positive trends and correlation coefficients of 0.94, 0.63, 0.45, 0.64, 0.71, 0.53, 0.50, 0.75 and 0.43. We found a close correlation with the SiO emission which is a good tracer of shocked gas and molecular outflows (Martin-Pintado et al. 1992). As class I CH₃OH masers are collisionally excited by shocks, they may be excited in regions also containing SiO emission. There is also a significant correlation with SO and HC₃N.

Figure 5.12 shows comparisons between the integrated flux densities of the class I methanol transition at 95.1 GHz with the same 9 molecules. The plots show positive trends and moderate correlation coefficients of 0.66, 0.72, 0.56, 0.68, 0.68, 0.71, 0.73, 0.61 and 0.40. Although the 95.1 GHz line is also a class I methanol maser transition, the correlation with SiO appears to be weaker than that found with the 84.5 GHz line. The most notable correlations with less degree of scatter are with N₂H⁺ and CS.

Figure 5.13 shows comparisons between the integrated flux densities of the thermal methanol lines near 96.7 GHz and the 9 thermal molecules. We noted positive trends and correlation coefficients of 0.86, 0.42, 0.28, 0.61, 0.82, 0.91, 0.73, 0.55 and 0.17. We found a tight correlation with N₂H⁺, SiO and HC₃N.

Comparisons between the integrated flux densities of class I CH₃OH masers and thermal emission of SiO (1–0), CS (1–0) and CH₃OH (1₀–0_{0A}⁺) in the 7 mm band were made by Jordan et al. (2015, 2017). They also found positive trends with moderate correlation coefficients of 0.41, 0.57 and 0.40, respectively. They noted a closer relationship between the integrated intensity of the 44 GHz CH₃OH masers with the

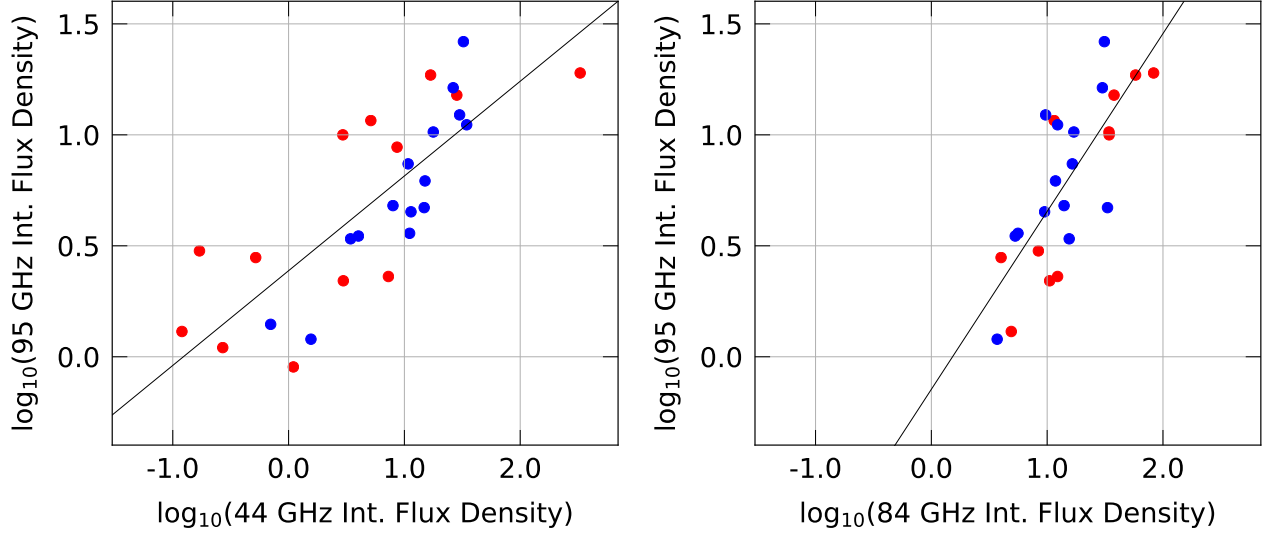


Figure 5.10: Left: Correlation between the integrated flux densities (Jy km s^{-1}) of class I methanol maser transitions at 44 and 95 GHz, the correlation coefficient is 0.46. The black line shows the best linear fit of the form: $\log S_{95} = 0.42 \log S_{44} + 0.39$. The 44 GHz data were taken from the VLA Surveys III and IV. Right: Correlation between the integrated flux densities of class I methanol maser transitions at 84 and 95 GHz. The correlation coefficient is 0.70. The 84 and 95 GHz integrated flux densities are listed in Table 5.4. The black line shows the linear fit of the form: $\log S_{95} = 0.80 \log S_{84} - 0.14$. The red dots indicate sources of Survey III (Molinari sample) and the blue ones are sources of Survey IV (Sridharan sample).

integrated intensity of SiO emission. Our results indicate an even closer relationship between the SiO and the 84.5 and 95.1 GHz integrated intensities than that of the 44 GHz masers. For the comparisons between the integrated intensities of thermal emission of CS and CH_3OH with the integrated intensities of 44 GHz methanol masers, Jordan et al. (2017) found moderate correlation coefficients and positive slopes indicating that brighter class I 44 GHz CH_3OH masers are more likely to be associated with brighter thermal lines. Their expectation was that higher-mass regions of star formation contain more molecular gas, and thus the thermal line emission would be brighter. Therefore, they conclude suggesting that the brighter class I 44 GHz methanol masers may be associated with the more massive star-forming regions. They reinforced this suggestion with the significant correlation (0.84) found between the integrated intensity of CS and the integrated intensity of the 870 μm dust continuum emission; since the brightness of dust continuum emission is directly proportional to the mass.

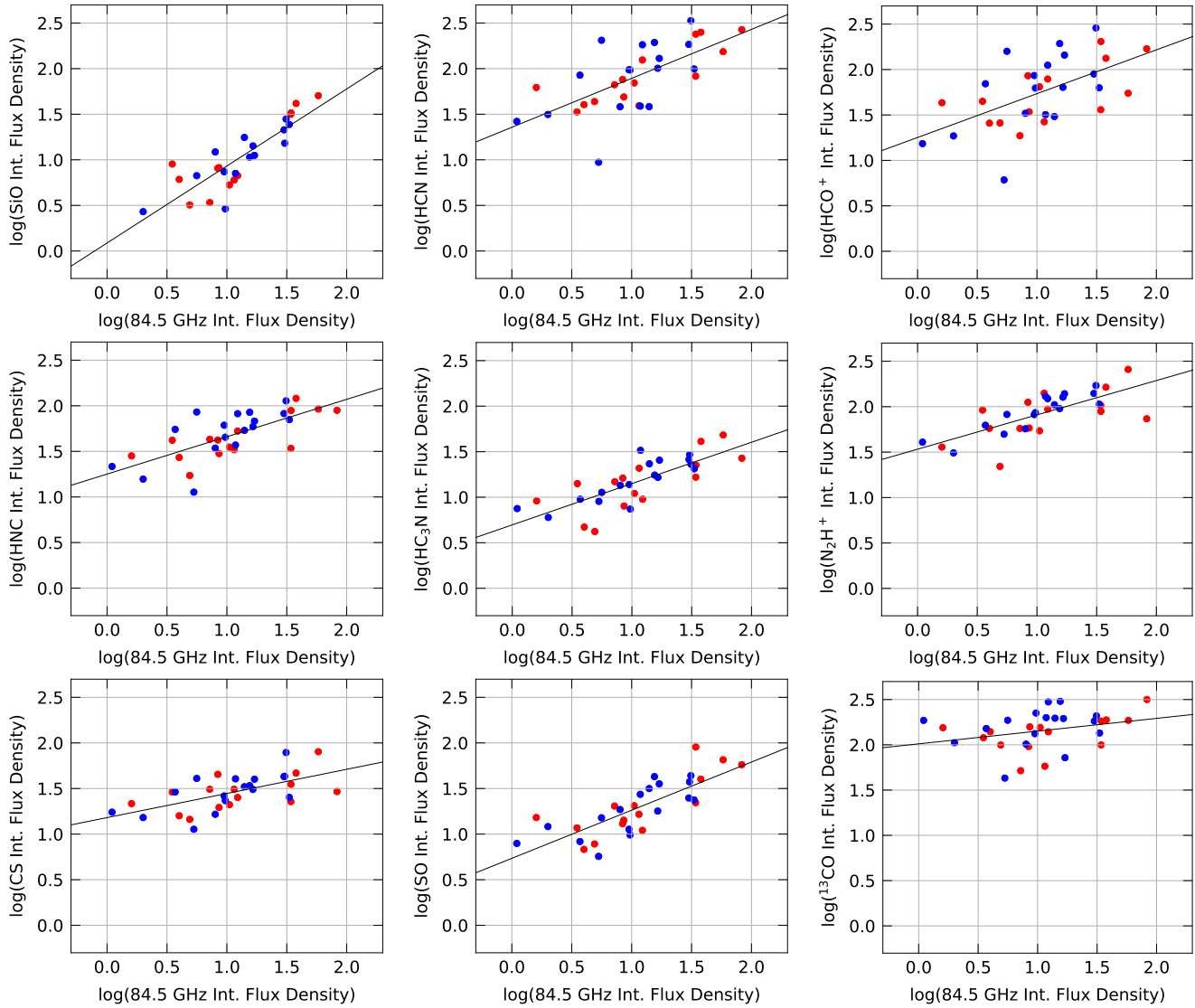


Figure 5.11: Correlation between the integrated flux densities (Jy km s^{-1}) of class I 84.5 GHz methanol maser detections with some of the strongest molecular lines in the passband. The correlation coefficients between the 84.5 GHz masers and the SiO, HCN, HCO^+ , HNC, HC_3N , N_2H^+ , CS, SO and ^{13}CO are 0.94, 0.63, 0.45, 0.64, 0.71, 0.53, 0.50, 0.75 and 0.43, respectively. The black line represents the best linear polynomial fit. The slopes are: 0.84, 0.53, 0.48, 0.40, 0.45, 0.37, 0.26, 0.52 and 0.14. The red and blue markers indicate sources from Surveys III and IV, respectively.

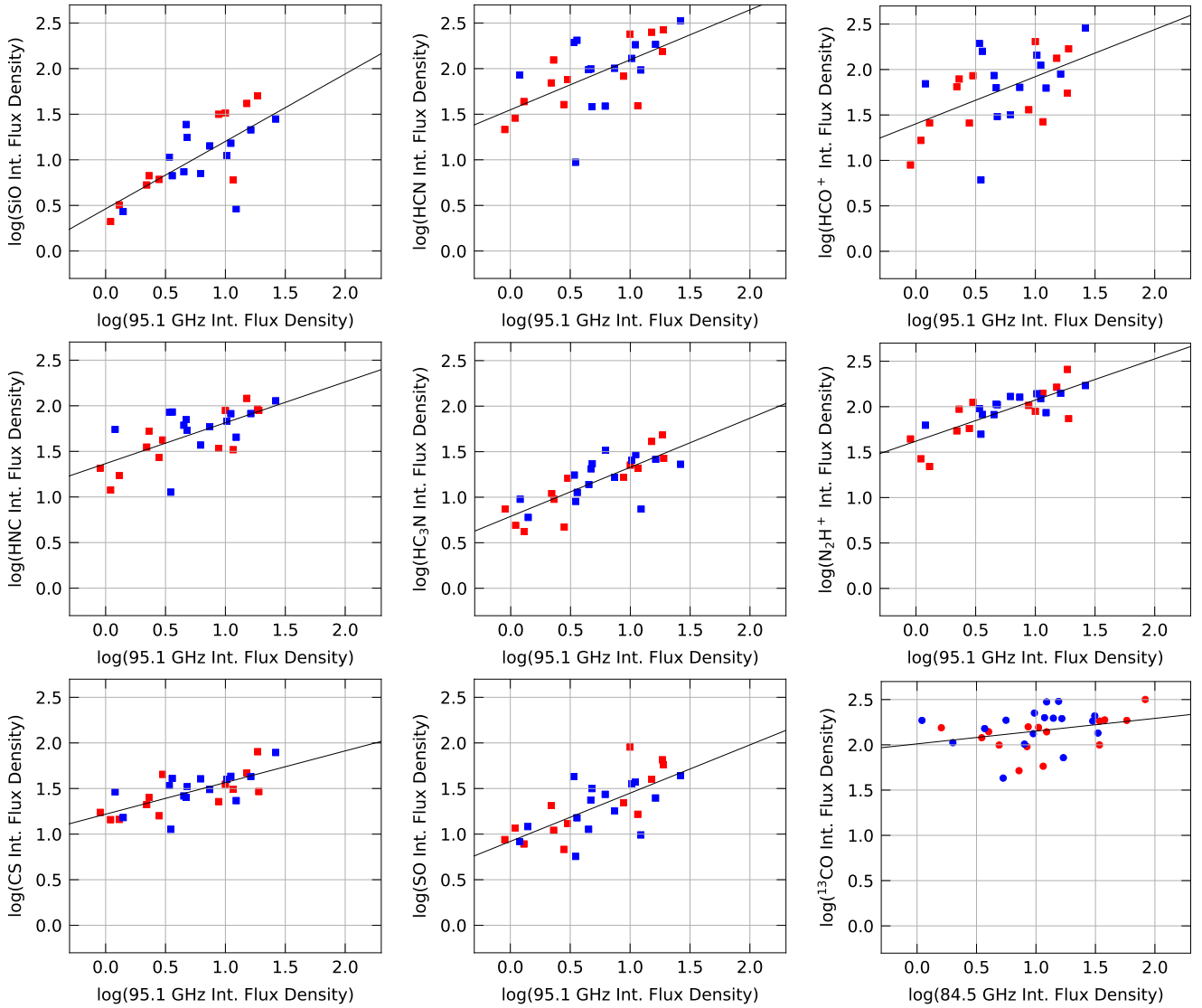


Figure 5.12: Correlation between the integrated flux densities (Jy km s^{-1}) of class I 95.1 GHz methanol maser detections with some of the strongest molecular lines in the passband. The correlation coefficients between the 95.1 GHz masers and the SiO, HCN, HCO^+ , HNC, HC_3N , N_2H^+ , CS, SO and ^{13}CO are 0.66, 0.72, 0.56, 0.68, 0.68, 0.71, 0.73, 0.61 and 0.40, respectively. The black line represents the best linear polynomial fit. The slopes are: 0.74, 0.54, 0.51, 0.44, 0.53, 0.45, 0.34, 0.52 and 0.16. The red and blue markers indicate sources from Surveys III and IV, respectively.

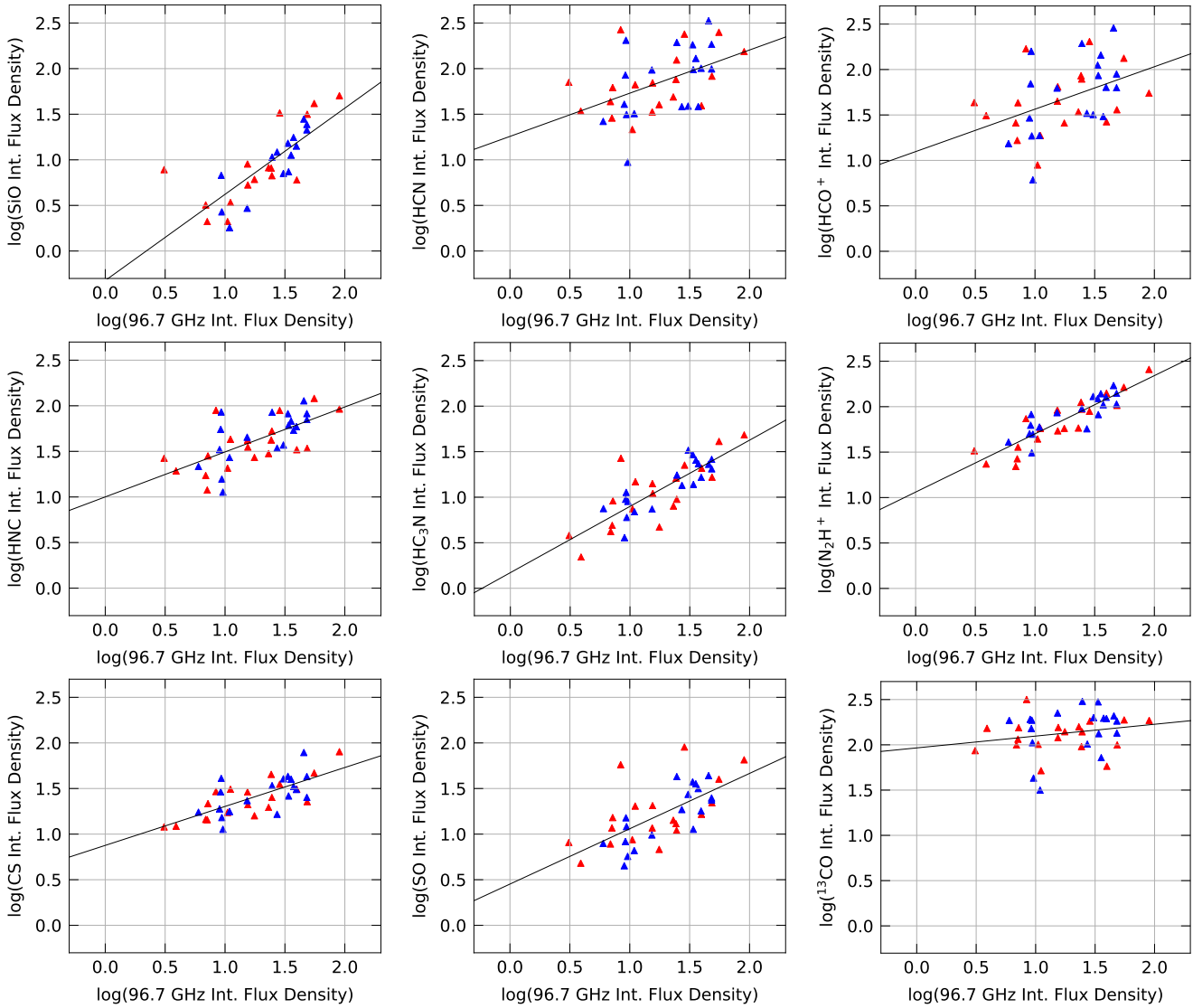


Figure 5.13: Correlation between the integrated flux densities (Jy km s^{-1}) of thermal 96.7 GHz methanol maser detections with some of the strongest molecular lines in the passband. The correlation coefficients between the 96.7 GHz masers and the SiO, HCN, HCO^+ , HNC, HC_3N , N_2H^+ , CS, SO and ^{13}CO are 0.86, 0.42, 0.28, 0.61, 0.82, 0.91, 0.73, 0.55 and 0.17, respectively. The black line represents the best linear polynomial fit. The slopes are: 0.94, 0.47, 0.49, 0.72, 0.64, 0.42, 0.60 and 0.13. The red and blue markers indicate sources from Surveys III and IV, respectively.

5.5 Summary

We observed a sample of 38 high-mass protostars to search for methanol maser and thermal emission in the 73–111 GHz frequency range covered by the Redshift Search Receiver on the Large Millimeter Telescope. The targets were selected from the VLA surveys of 44 GHz methanol masers made by Gómez-Ruiz et al. (2016, Survey III) and Rodríguez-Garza et al. (2017, Survey IV). In spite of the low spectral resolution of RSR (100 km s^{-1}), we were able to identify the methanol lines alongside many other molecular lines in the spectra. For simplicity we will refer to several methanol transitions as class I and class II methanol masers, although we caution that our low spectral resolution observations prevents a definitive interpretation of their maser or thermal nature.

We summarize our results as follows:

- We detect emission in the class I methanol transition $5_{-1} \rightarrow 4_0E$ at 84.5 GHz toward 32 of the 38 targets observed (84% detection rate), all of them are new detections. We find a lower detection rate for the class I methanol transition $8_0 \rightarrow 7_1A^+$ at 95.1 GHz where we detect emission toward 29 of the 38 targets observed (76% detection rate). Emission at 95.1 GHz was previously reported for 21 of our 29 detections with high spectral resolution, therefore, we report only 8 sources as new tentative detections. On average, the integrated intensities of the 84.5 GHz masers are about two times larger than the 95.1 GHz emission which is in agreement with the prediction made by the models of Cragg et al. (1992). The rare transition $11_{-1} \rightarrow 10_{-2}E$ at 104.3 GHz was not detected.
- We detect emission in the class II methanol transition $3_1 \rightarrow 4_0A^+$ at 107.0 GHz toward 2 of the 38 targets observed (5% detection rate). We find a higher detection rate in the class II transition $0_0 \rightarrow 1_{-1}E$ at 108.8 GHz; we detect emission toward 15 of the 38 targets (39% detection rate). All of them are new detections. None of the rare transitions at 85.5, 86.6 and 86.9 GHz were detected.
- We report a 100% detection rate for the thermal methanol transitions near 96.7 GHz; 32 of the 38 are new detections.
- We detect with a 100% detection rate many other molecular lines commonly found in star-forming region which are known to be high density gas tracers. We detect the $(1-0)$ transitions of HCN, HCO^+ , HNC, N_2H^+ and ^{13}CO ; HC_3N ($10-9$), CS ($2-1$) and SO ($2-1$). We also detect emission from SiO ($2-1$)—a good shock tracer—with a detection rate of 76 % (29 of 38 sources).
- We searched for correlations between the integrated flux densities of the class I methanol masers at 44, 84 and 95 GHz. The correlation coefficient between integrated intensities of the 44 and 95 GHz transitions is 0.46. We obtain a linear fit of the form: $\log S_{95} = 0.42 \log S_{44} + 0.39$ which combined with the correlation coefficient indicate a moderate and positive correlation. We find a closer relationship between the integrated intensities of the 84 and 95 GHz transitions. We obtain a linear fit of the form $\log S_{95} = 0.80 \log S_{84} - 0.14$ and a correlation coefficient of 0.70, indicating moderate and positive correlation as well.
- We searched for correlations between the integrated flux densities of the thermal lines SiO, HCN, HCO^+ , HNC, HC_3N , N_2H^+ , CS, SO and ^{13}CO with the integrated flux densities of the class I methanol masers at 84.5 and 95.1 GHz and the thermal methanol emission at 96.7 GHz. We find positive slopes and correlation coefficients in the range between 0.17 to 0.94. The strongest correlation was between the integrated intensities of SiO and the integrated intensities of 84.5 GHz masers. This supports the idea that class I methanol masers are good tracers of shocked gas since this correlation suggest that SiO and 84.5 GHz masers arise from the same regions.

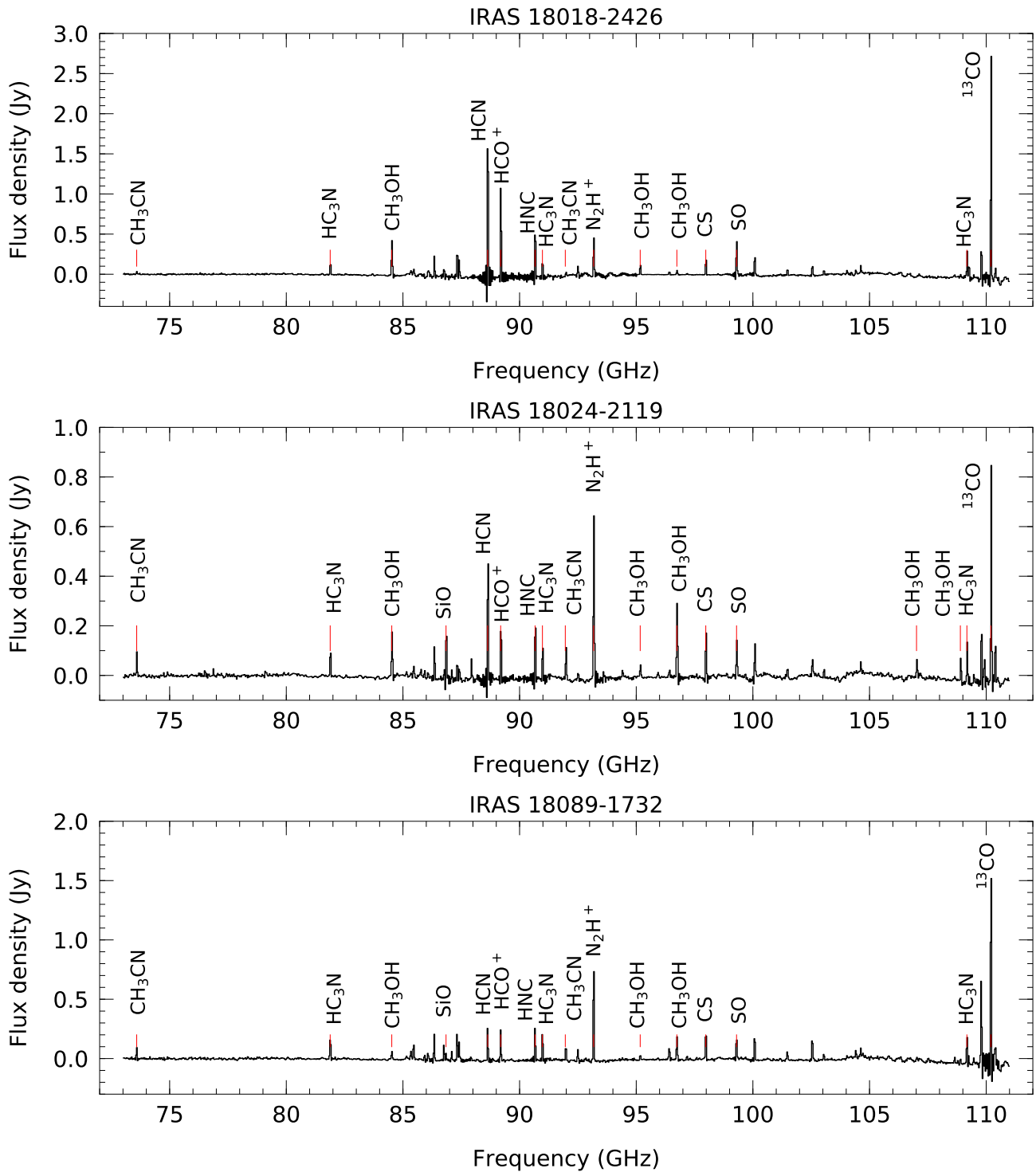


Figure 5.14: Molecular lines detected within the RSR bandpass (73 – 111 GHz). We labeled some of the brightest lines identified. The rest frequencies are indicated with the red lines.

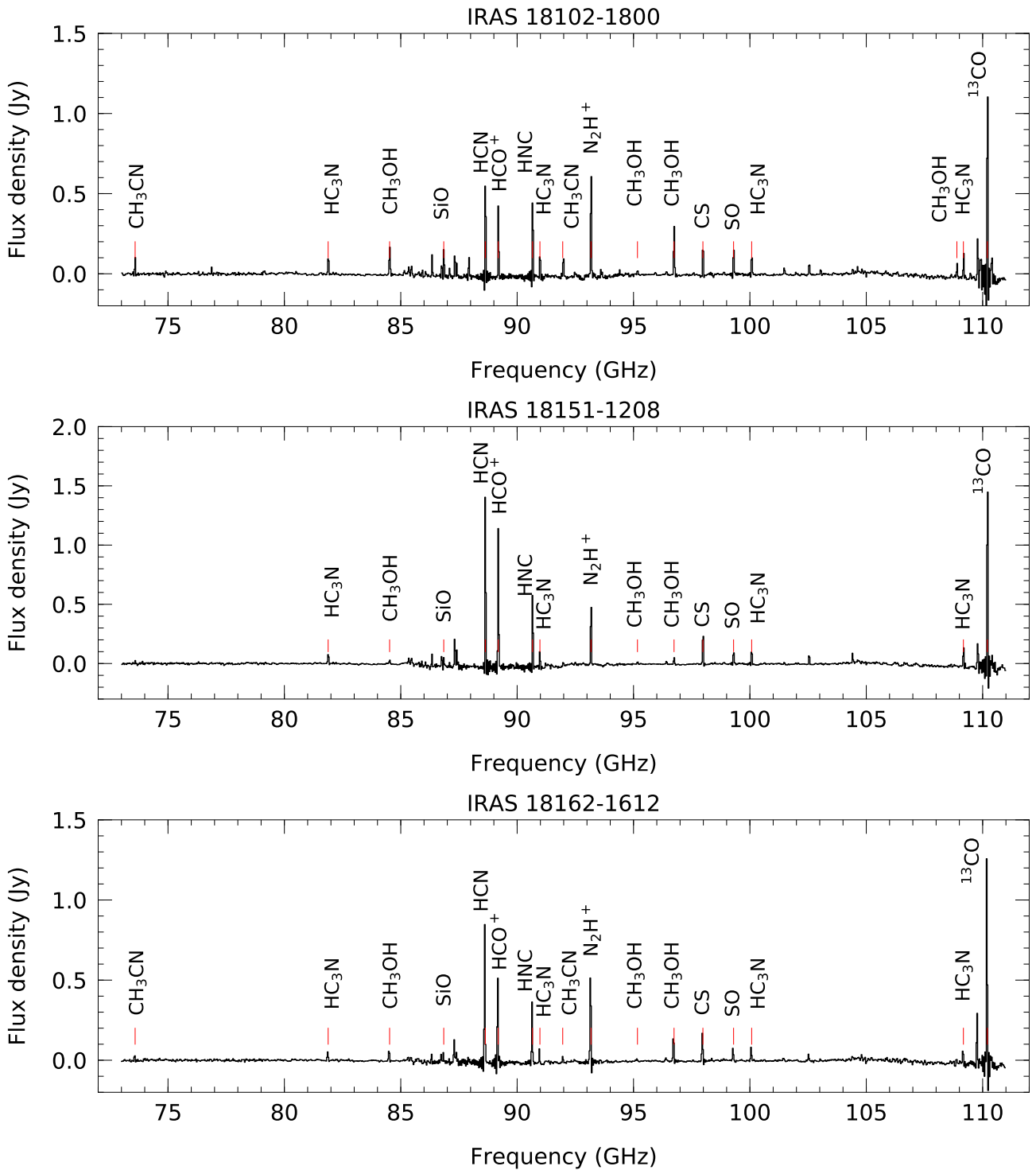


Figure 5.14: Continued.

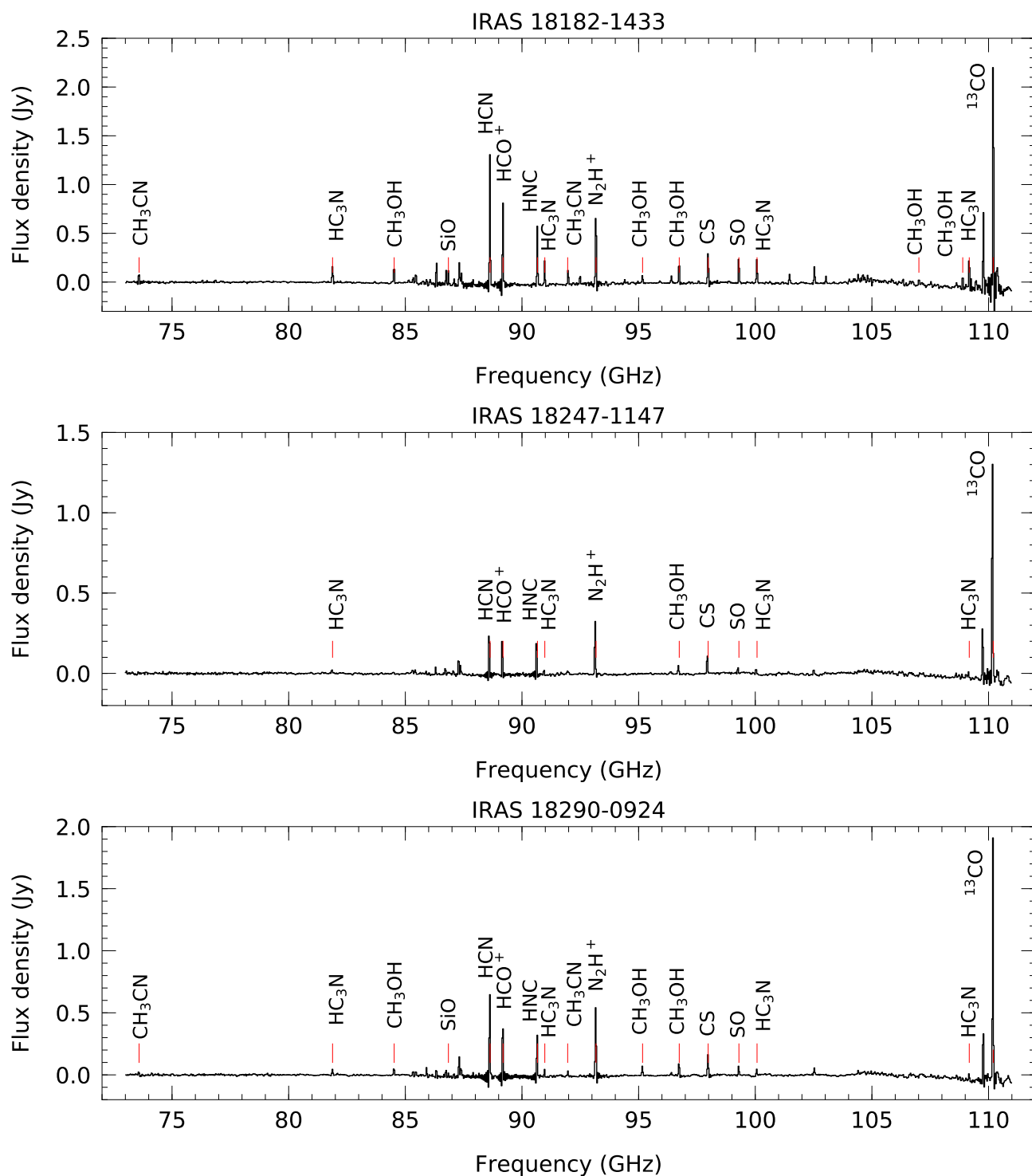


Figure 5.14: Continued.

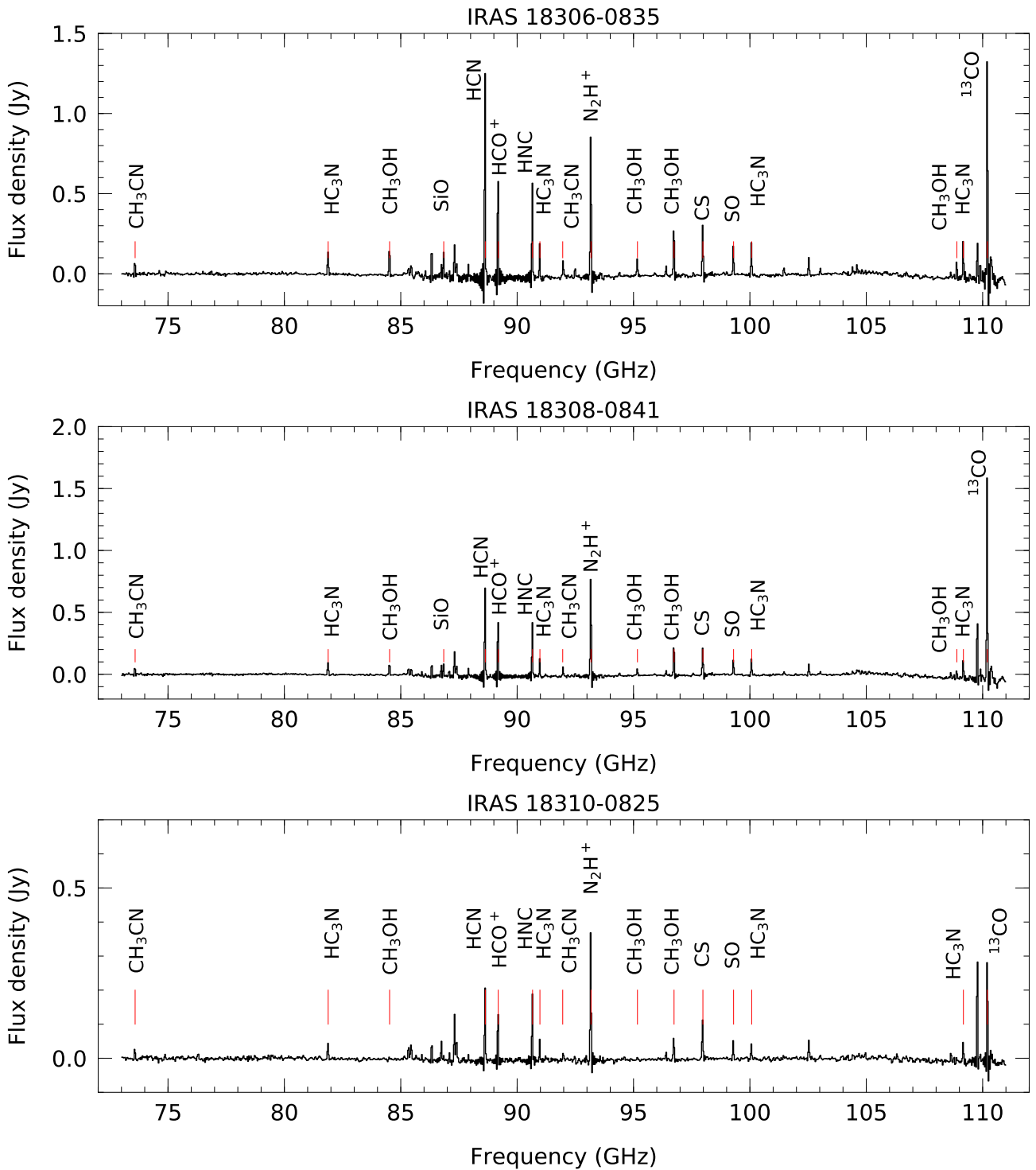


Figure 5.14: Continued.

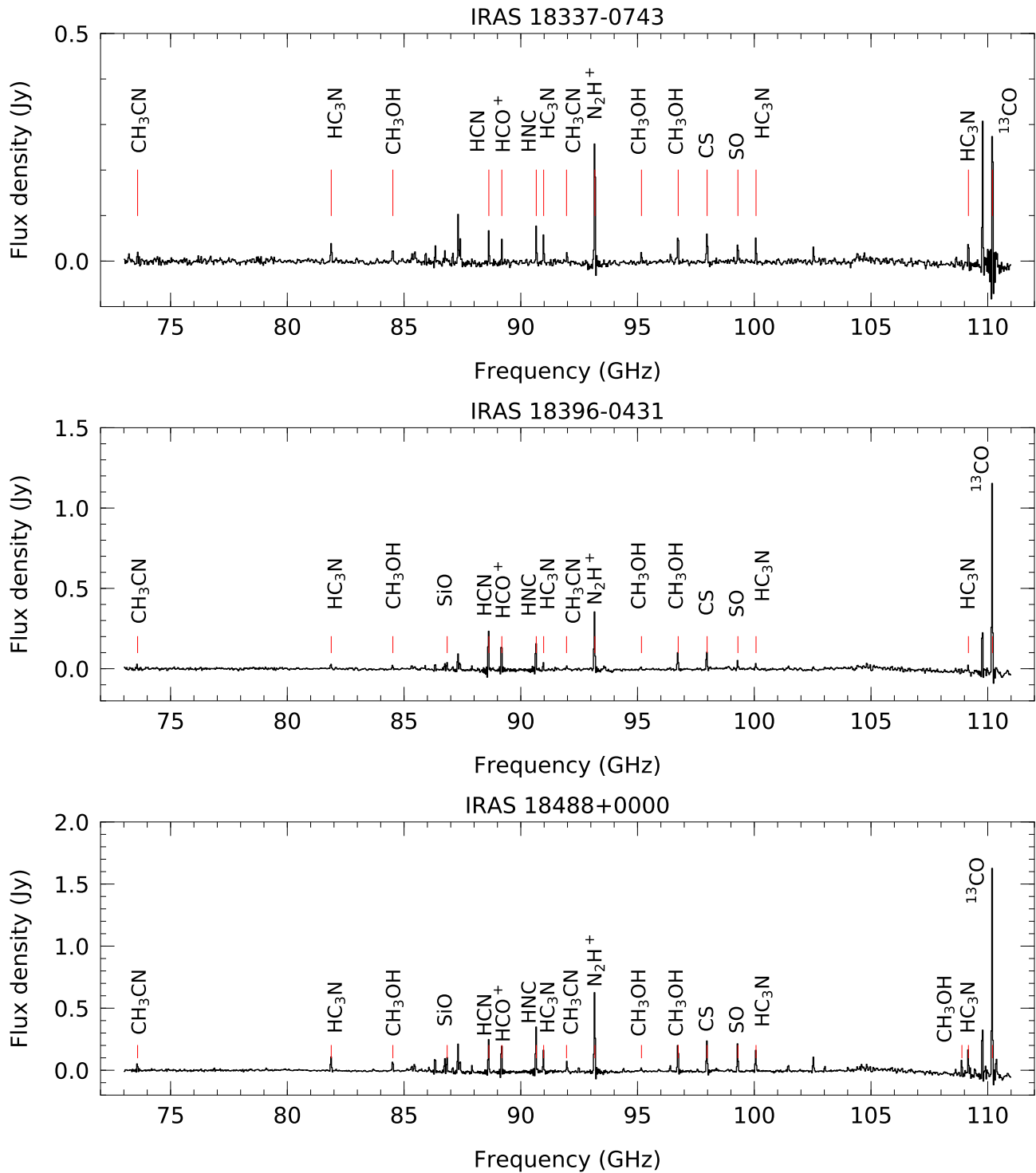


Figure 5.14: Continued.

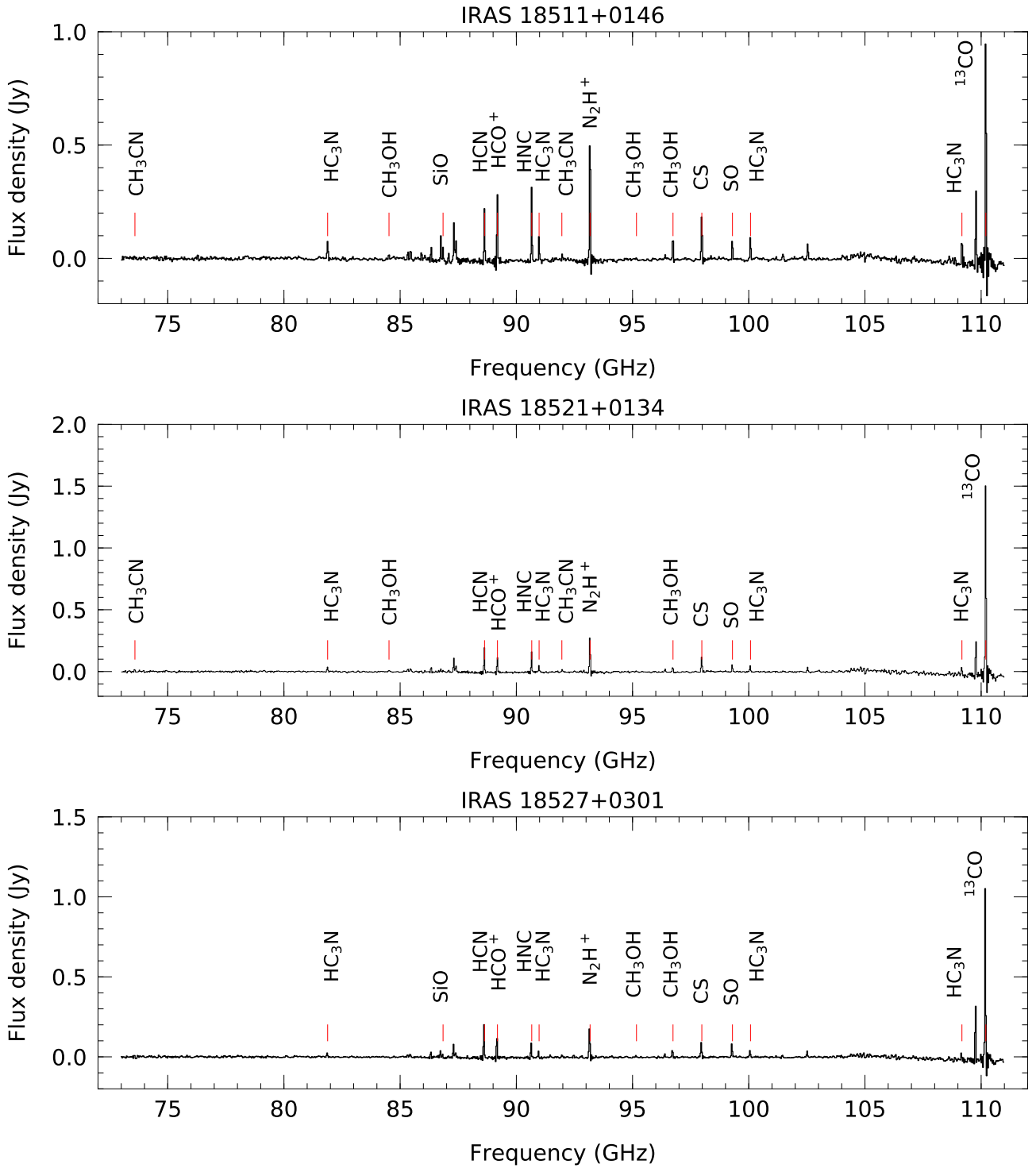


Figure 5.14: Continued.

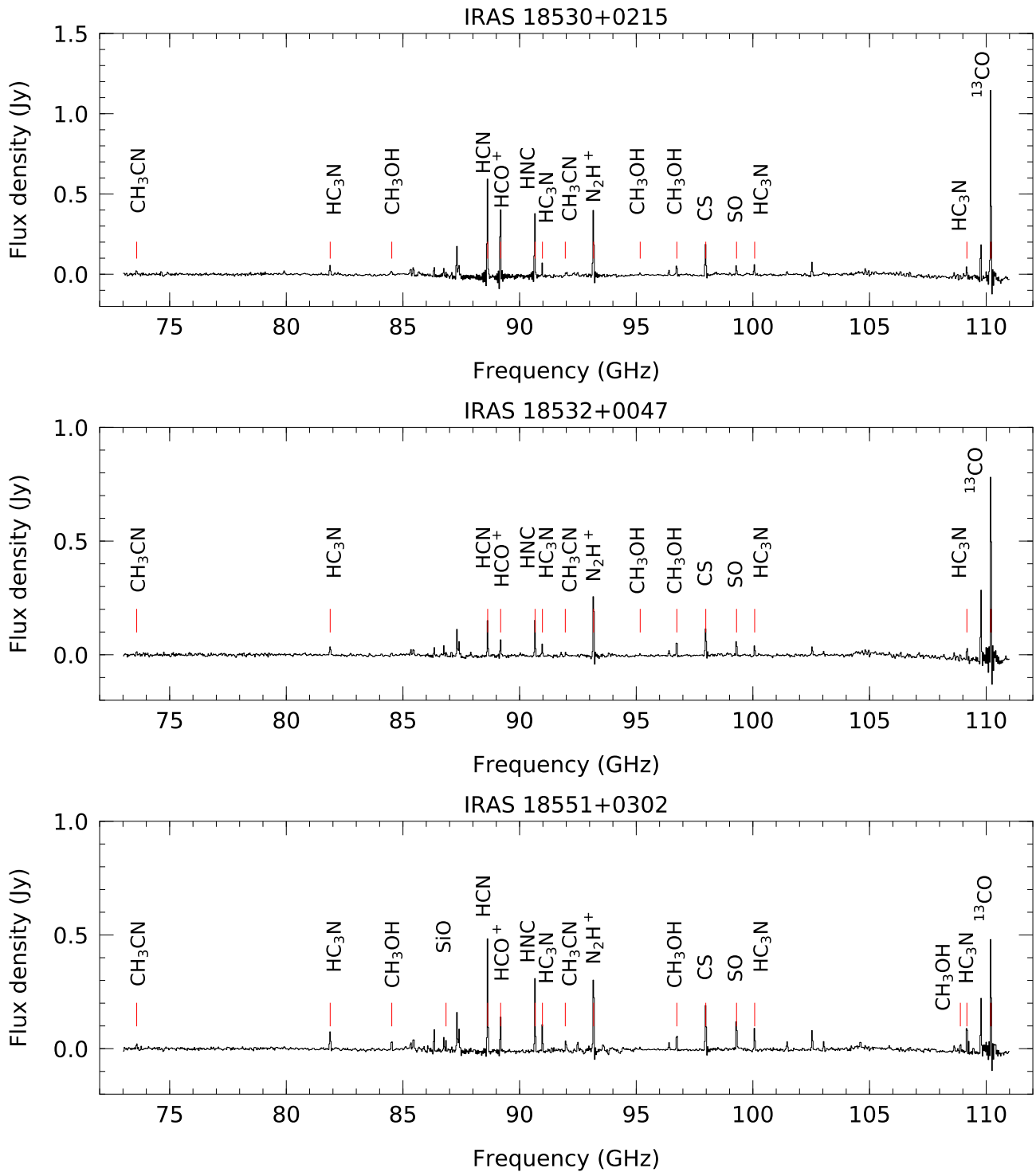


Figure 5.14: Continued.

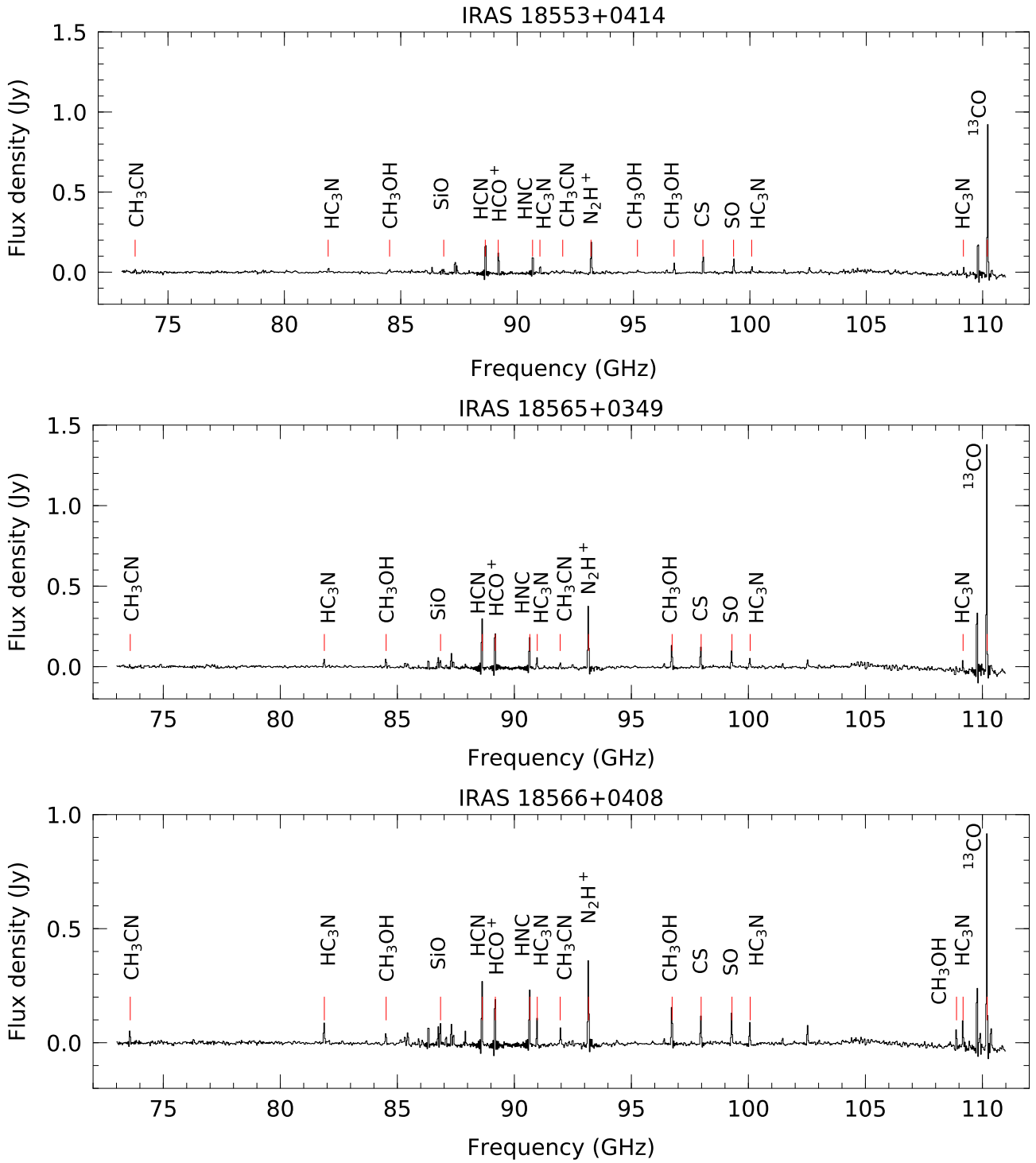


Figure 5.14: Continued.

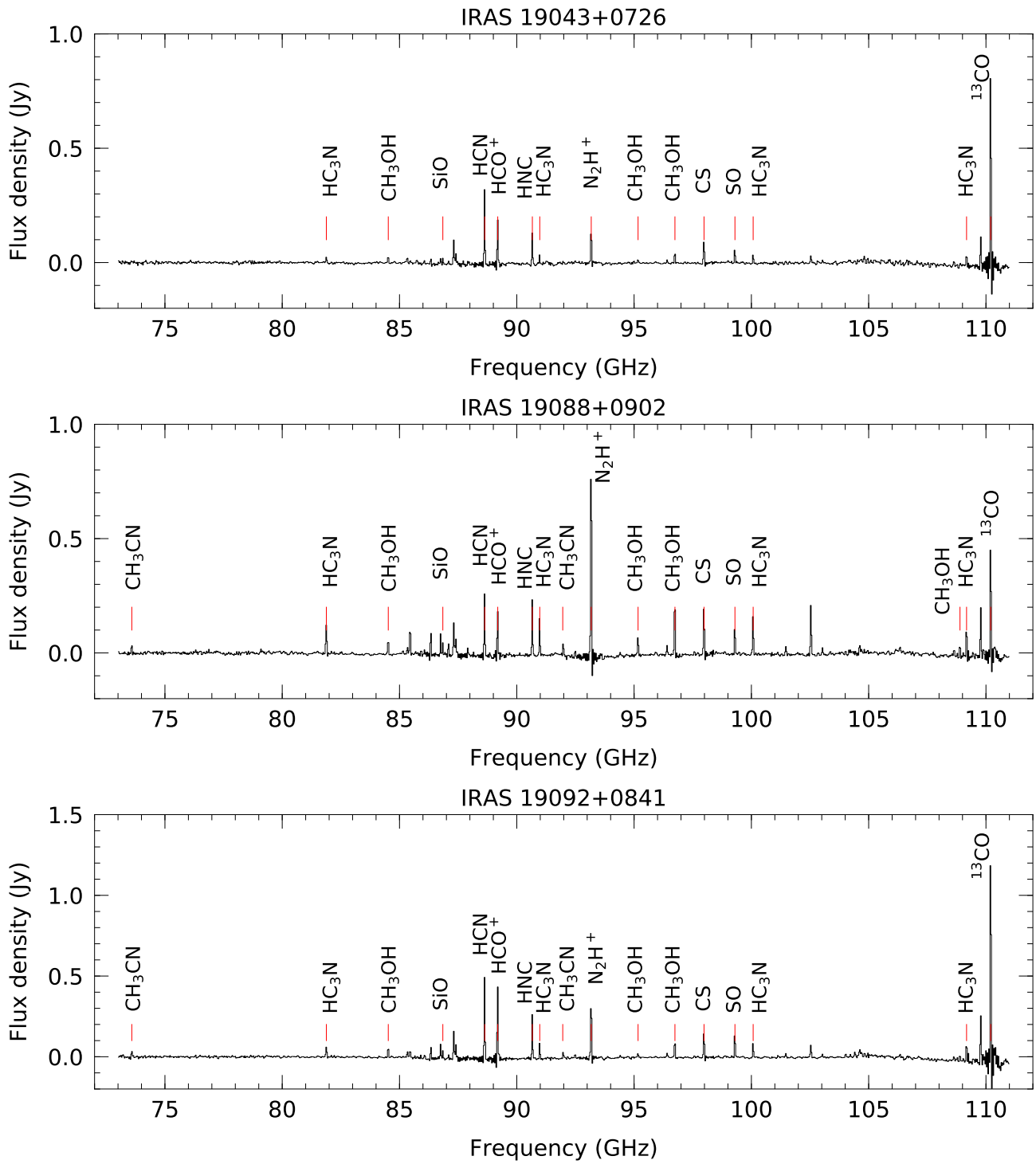


Figure 5.14: Continued.

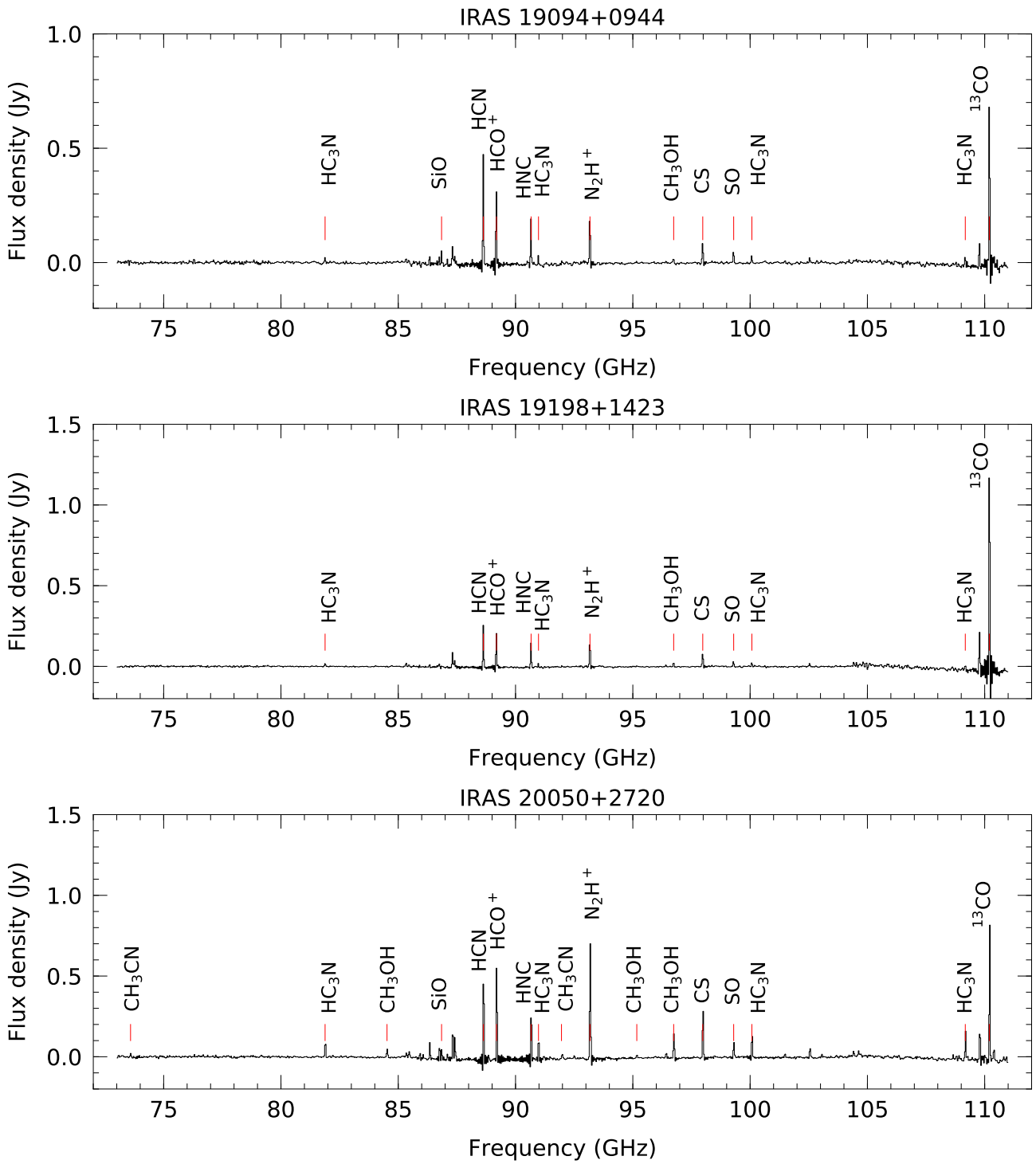


Figure 5.14: Continued.

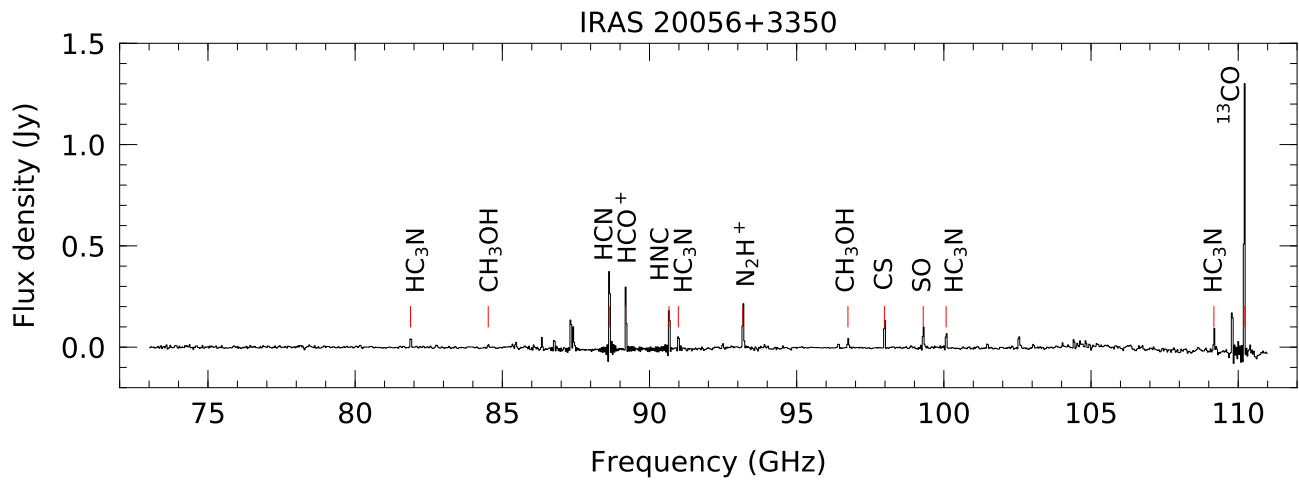


Figure 5.14: Continued.

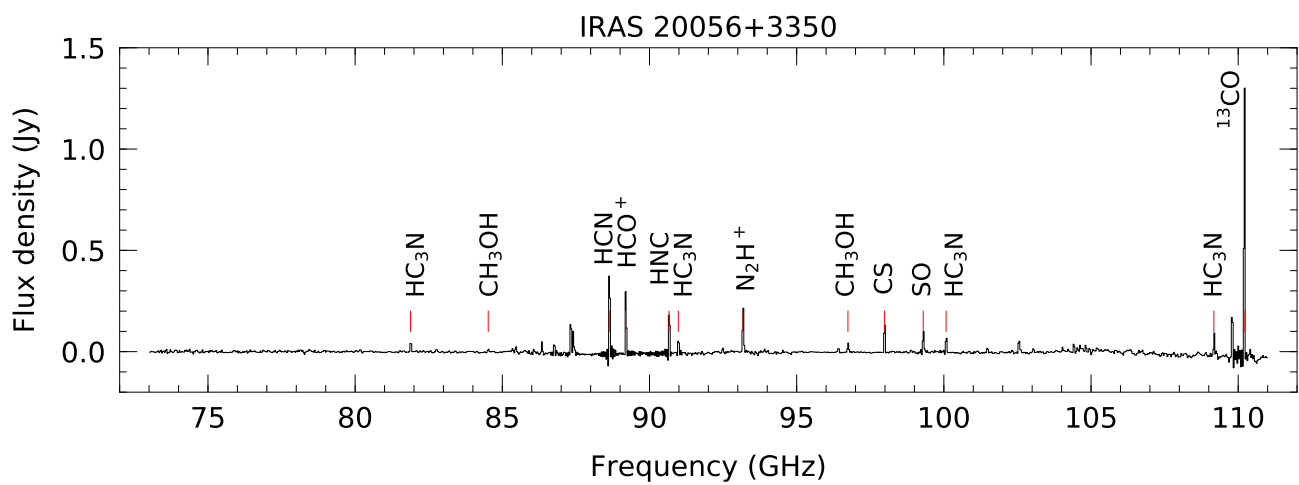
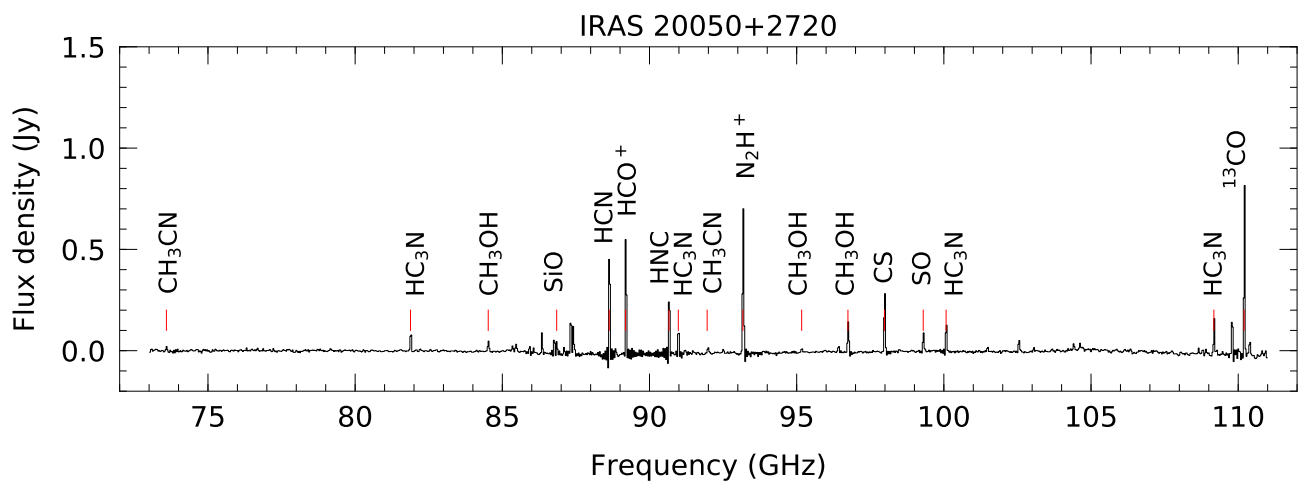


Figure 5.14: Continued.

Chapter 6

Conclusions and Future Work

This Thesis has focused in the study of the millimeter transitions of Class I methanol masers in a total of 88 high-mass star-forming regions. The work is mainly divided in two parts. The first part is dedicated to the study of Class I 44 GHz methanol masers based on observations made with the Karl G. Jansky Very Large Array (VLA) towards a homogeneous sample of 69 well-known high-mass protostellar objects reported in the catalog of Sridharan et al. (2002). We observed 56 out of the 69 regions with the VLA in D-configuration with an angular resolution of $\sim 1''.5$ and a spectral resolution of 0.17 km s^{-1} . The remaining 13 regions were observed in C-configuration which corresponds to an angular resolution of $\sim 0''.5$ and a spectral resolution of 13.6 km s^{-1} . The second part consists of a single-dish multi-transition observation of methanol masers and thermal emission toward a sample of 38 Class I 44 GHz methanol maser sites. The observations were made in the 3 mm band (from 73 to 111 GHz) with the Redshift Search Receiver (RSR), during the early science phase of the Large Millimeter Telescope (LMT) Alfonso Serrano. We selected 19 of the 38 sites from the VLA 44 GHz methanol maser observations mentioned above and the other 19 were taken from a similar VLA survey presented by Gómez-Ruiz et al. (2016) toward the sample of Molinari et al. (1996). In spite of the low spectral resolution of RSR (100 km s^{-1}), we were able to identify the methanol lines. For simplicity, we refer to some of them as methanol masers although we caution that the low spectral resolution prevents a definitive interpretation of their maser or thermal nature.

For the interferometric part the conclusions are as follows:

- We detected Class I 44 GHz methanol masers in 24 out of 56 observed regions. We found 5 other regions with presumably maser emission at 44 GHz but we could not confirm their nature since they were observed with lower spectral resolution (13.6 km s^{-1}). There are only a few systematic observations of Class I 44 GHz methanol masers made with high precision reported in the literature. Hence, our observations contribute to the identification of a number of new Class I 44 GHz maser sites with sub-arcsecond accuracy.
- We found a total of 83 maser components with line width median values of 1.1 km s^{-1} . The maser lines showed velocities close to the LSR velocity of their host molecular clouds. This is a behaviour commonly reported in the literature although somewhat unexpected since Class I methanol masers are believed to trace molecular outflows and therefore they should have high velocity components. This type of masers have been associated with EGOs (Extended Green Objects) which have been proposed to be also good tracers of molecular outflows. We searched for correlations in the projected positions of the Class I masers against the infrared sources seen in three-color coded images of the Spitzer Space Telescope. We found a number of regions with spatial coincidence between the masers

and emission excess in the 4.5 μm IRAC band (seen in color green). This may support the idea that Class I methanol masers are tracers of molecular outflows.

- Interestingly, we found a Class I maser component projected toward a protostar that has been proposed to be a low-mass object. If its nature is corroborated, this protostar would be the fifth low-mass protostar associated with Class I methanol masers.
- We found evidence of variability of the masers flux densities in one of the studied regions.
- We detected radio continuum emission in 5 of 13 regions observed, 4 of them are new detections at 7 mm. We found compact sources with spectral indices between -0.1 to 0.9, indicating emission from either optically thin/thick HII regions or ionized jets.

For the single-dish part the conclusions are:

- We detected Class I methanol masers at 84.5 GHz in 32 of the 38 regions observed (84% detection rate), all of them are new detections. These are the third systematic observations of the 84.5 GHz masers reported to date which yielded a considerable number of new maser sources. We also detected Class I methanol masers at 95.1 GHz toward 29 of the 38 targets (76% detection rate) but only 8 sources are reported as tentative new detections. We did not detect emission of the rare Class I methanol masers at 104.3 GHz. On average, the integrated flux densities of the 84.5 GHz masers are about 2 times larger than that of the 95.1 GHz masers which is in agreement with the prediction made by the model of Cragg et al. (1992).
- We detected Class II methanol masers at 107.0 GHz in 2 of the 38 regions observed (5% detection rate). We found a higher detection rate for the Class II methanol masers at 108.8 GHz where emission was detected in 15 of the 38 targets (39% detection rate), all of them are new detections. None of the rare transitions at 85.5, 86.6 and 86.9 GHz were detected.
- We found a 100% detection rate of the thermal methanol line series near 96.7 GHz and many other thermal molecular lines such as HCN, HCO⁺, HNC, HC₃N, N₂H⁺, CS, SO and ¹³CO which are indicators of high density gas. We also detected emission from SiO(2 – 1) —a good shock tracer— in 29 of the 38 regions (76% detection rate).
- We searched for correlations between the integrated flux densities of the thermal lines SiO, HCN, HCO⁺, HNC, HC₃N, N₂H⁺, CS, SO and ¹³CO with the integrated flux densities of the Class I methanol masers at 84.5 and 95.1 GHz and the thermal methanol emission at 96.7 GHz. We found positive slopes and correlation coefficients from 0.17 to 0.94. The strongest correlation was between the integrated flux densities of SiO and the integrated intensities of 84.5 GHz masers. This supports the idea that Class I methanol masers are good tracers of shocked gas since this correlation suggests that SiO and 84.5 GHz masers arise from the same regions.

6.1 Future Work

To determine the maser nature of the methanol lines detected with the LMT and their relationship with molecular outflows, additional high resolution observations are necessary to derive the actual line parameters such as line width, peak and integrated flux densities and the precise position of the masers. It is of particular interest the study of the thermal methanol line series near 96.7 GHz which consists of four different lines of

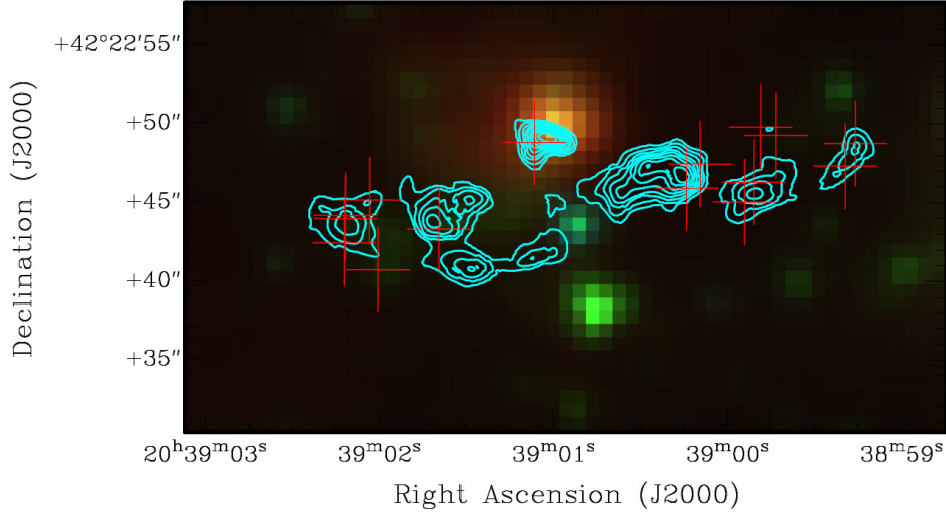


Figure 6.1: Spitzer IRAC image of the DR21(OH) region (IRAC bands: 3.6 μm = blue; 4.5 μm = green and 8.0 μm = red). The red crosses mark the positions of Class I 36 GHz masers from Fish et al. (2011). Cyan contours represent the integrated intensity of the thermal $4_2 \rightarrow 3_1$ E methanol line (Zapata et al. 2012) which traces the EW outflow seen in the Class I masers (see Figure 6.2).

low excitation energies, spaced very close in frequency: $2_{-1} \rightarrow 1_{-1}$ E (96739.39 MHz), $2_0 \rightarrow 1_0$ A⁺ (96741.42 MHz), $2_0 \rightarrow 1_0$ E (96744.58 MHz), $2_1 \rightarrow 1_1$ E (96755.51 MHz). Emission in this frequency was detected with the RSR toward all the observed sources. This result is very interesting because thermal methanol emission is an important tool to trace molecular outflows in high-mass protostars (Zapata et al. 2012), and therefore, could be useful to investigate their relationship with Class I methanol masers (see Figure 6.1).

Now that the LMT surface of 50 m has been completed and equipped with SEQUOIA, a receiver array that operates in the frequency range between 85–115 GHz with a spectral resolution up to 24 KHz, we can map simultaneously the emission. Recently, we proposed SEQUOIA observations of the four thermal methanol lines at 96739.39 MHz, 96741.42 MHz, 96744.58 MHz and 96755.51 MHz toward a sub-sample of 23 high-mass protostars previously detected with RSR. These new observations will provide useful information in the following aspects:

Mapping the relation between molecular outflows and Class I methanol masers

We are interested in mapping the 96.7 GHz methanol emission to trace the molecular outflows in all sources. Although half of the sources in our sample show evidence of large scale $^{12}\text{CO}(2-1)$ bipolar outflows (Beuther et al. 2002b), it is important to map the CH_3OH 96.7 GHz series since they are an excellent tracer of the outflowing gas closer to the central heating source. These new observations of thermal methanol together with our VLA detections of Class I 44 GHz methanol masers (Rodríguez-Garza et al. 2017) will complement and provide useful new information for modeling the maser properties and their excitation mechanisms.

In Figure 6.1 we show an image of the DR21(OH) region with an east-west (EW) molecular outflow traced by thermal methanol emission (Leurini et al. 2016). This outflow is also well traced by the Class I maser emission at 36 and 44 GHz (Araya et al. 2009) shown in Figure 6.1 and 6.2. We are interested in making similar comparisons to probe that Class I masers are a unique tool to investigate outflow activity specially in high extinction regions where other standard shock tracers (such as H_2 emission) are too weak

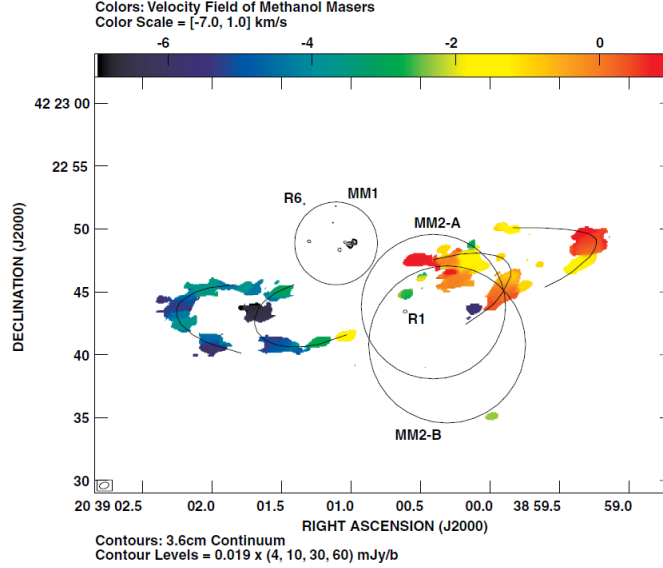


Figure 6.2: Velocity field of the Class I 44 GHz methanol masers in the DR21(OH) region. The EW methanol outflow shown in Figure 6.1 is also traced by the Class I methanol masers. The 3.6 cm continuum is shown in contours. The location of the NH₃ molecular cores from Mangum et al. (1992) are shown with circles; the diameter of the circles equals the major axis of the cores.

to be detected.

Line parameter estimates through rotational diagrams

The four methanol lines at 96739.39 MHz, 96741.42 MHz, 96744.58 MHz and 96755.51 MHz are well covered and resolved by SEQUOIA. To have an idea how the lines might look like when observed, we have computed a synthetic spectrum for these lines using the radiative transfer code CASSIS (Vastel et al. 2015). This software allows us to compute the synthetic spectrum assuming specific values for the temperature and column density under local thermodynamic equilibrium (LTE) conditions¹. For example, to compute the synthetic spectrum for source IRAS 20126+4104, we used a rotational temperature of 17 K and column density of $2 \times 10^{14} \text{ cm}^{-2}$ as reported by Liechti and Walmsley (1997). Figure 6.3 shows the resulting synthetic spectrum of the four methanol lines as should be observed by the LMT assuming a spectral resolution of 0.3 km s^{-1} .

From an observed spectrum with the LMT (the simulated synthetic spectrum for IRAS 20126+4104 in this case), we can estimate the rotational temperature and column density using the rotational diagram method (e.g. see Goldsmith and Langer 1999). This physical method takes into account that the measured integrated intensity of the lines $\int I_\nu dv$ ($\text{Jy beam}^{-1} \text{ km s}^{-1}$) is related to the column density of a given molecule in the upper level N_u through the equation

$$\frac{N_u}{g_u} = \frac{N_{tot}}{Q(T_{rot})} e^{-E_u/T_{rot}} = \frac{1.7 \times 10^{14}}{\nu \mu^2 S} \int I_\nu dv, \quad (6.1)$$

¹See for more details: <http://cassis.irap.omp.eu/docs/RadiativeTransfer.pdf>

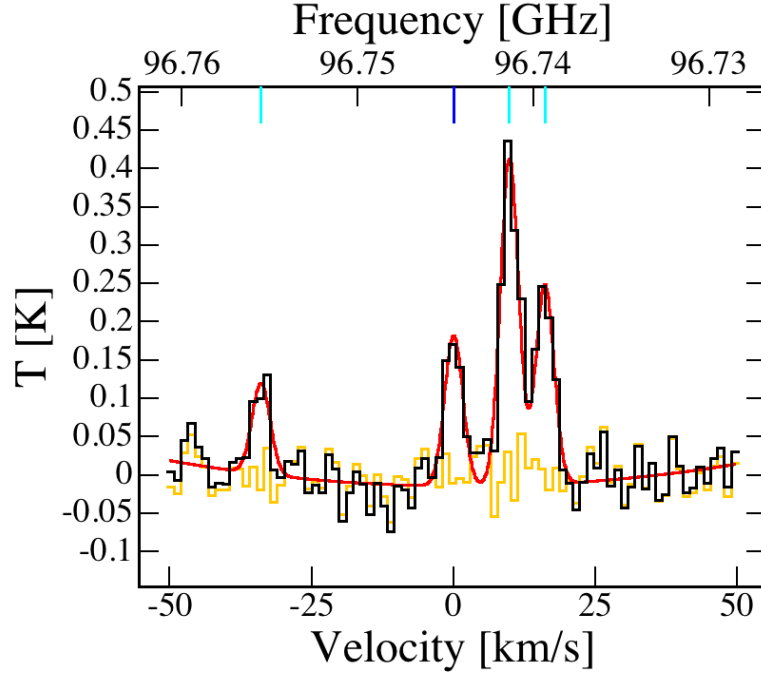


Figure 6.3: Synthetic spectrum of the four thermal methanol lines near 96.7 GHz for IRAS 20126+4104. The black line represent the spectrum as should be observed by the LMT-50m assuming a spectral resolution of 0.3 km s^{-1} . The spectrum was computed in CASSIS using a rotational temperature of 17 K and column density of $2 \times 10^{14} \text{ cm}^{-2}$ as reported by the observations of Liechti and Walmsley (1997). The red line indicates the Gaussian fit of the four lines and the yellow line represent the residual. The blue lines at the top indicate the line rest frequencies of each transition.

where g_u is the statistical weight of level u ; N_{tot} is the total column density in cm^{-2} ; $Q(T_{rot})$ is the partition function for the rotational temperature T_{rot} ; E_u is the energy of the upper level in Kelvin; μ is the permanent dipole moment in Debye and S is the strength value. Therefore, a logarithmic plot of the quantity on the right-hand side of the equation 6.1 as a function of E_u provides a straight line with the slope $1/T_{rot}$ and intercepts in $N_{tot}/Q(T_{rot})$. This gives the rotational temperature and the column density. This method assumes that all level populations can be characterized by a single rotational temperature T_{rot} and the lines are optically thin.

From the synthetic spectrum, we have made a gaussian fit to all lines at the same time to obtain the integrated intensity and produce a rotational diagram inside CASSIS. By fitting a straight line in the rotational diagram, we obtain directly the values for the temperature and density. In Figure 6.4 we show the rotational diagram and we verify that the obtained parameters are consistent with the initial values from Liechti and Walmsley (1997) that we used to produce the synthetic spectrum (note that we do not recover exactly the same values since the gaussian line fitting introduces statistical errors).

Thus, the rotational diagram method is a very useful tool that will allow us to obtain information on the physical conditions of the studied regions from the analysis of the observed spectra with the LMT.

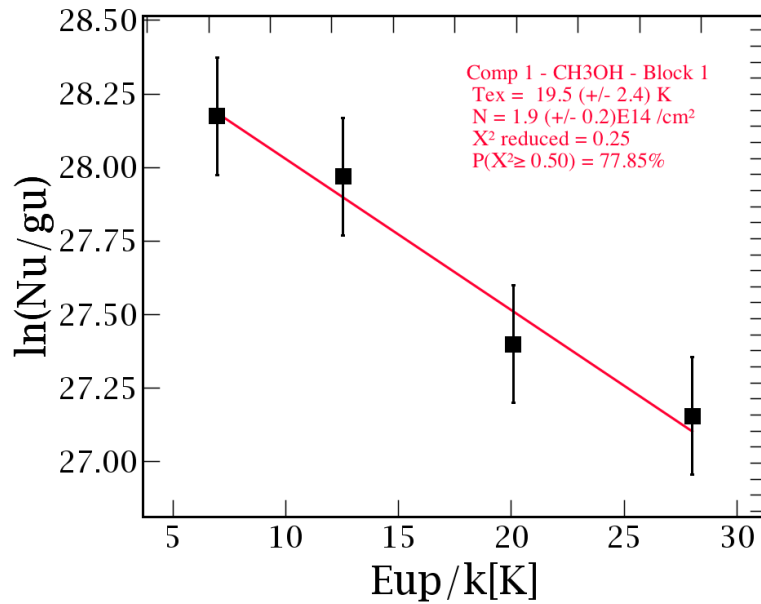


Figure 6.4: Rotational diagram obtained for the four methanol lines shown in Figure 6.3. Each transition is represented by a black square and the error bars indicate the uncertainty arising from the Gaussian fit when obtaining the integrated intensity. The x-axis indicates the energy of the upper level, and the y-axis, its corresponding value of $\ln(N_u/g_u)$. The red line indicates the best linear fit from which CASSIS estimates the total column density (the value where the red line intercepts the y-axis) and the rotational temperature (the slope of the red line is $1/T_{\text{rot}}$) of the gas (see Equation 6.1).

Bibliography

- L. D. Anderson and T. M. Bania. Resolution of the Distance Ambiguity for Galactic H II Regions. *ApJ*, 690:706–719, January 2009. doi: 10.1088/0004-637X/690/1/706.
- E. Araya, P. Hofner, S. Kurtz, L. Olmi, and H. Linz. Thermal Methanol Observations of the Outflow from the G31.41+0.31 Hot Molecular Core. *ApJ*, 675:420–426, March 2008. doi: 10.1086/527284.
- E. D. Araya, S. Kurtz, P. Hofner, and H. Linz. Radio Continuum and Methanol Observations of DR21(OH). *ApJ*, 698:1321–1329, June 2009. doi: 10.1088/0004-637X/698/2/1321.
- A. L. Argon, M. J. Reid, and K. M. Menten. Interstellar Hydroxyl Masers in the Galaxy. I. The VLA Survey. *ApJS*, 129:159–227, July 2000. doi: 10.1086/313406.
- R. Bachiller, J. Gomez-Gonzalez, A. Barcia, and K. M. Menten. The 44 GHz methanol masers - Results of an extensive survey in the 7(0)-6(1)A(+) line. *A&A*, 240:116–122, December 1990.
- J. A. Ball, C. A. Gottlieb, A. E. Lilley, and H. E. Radford. Detection of Methyl Alcohol in Sagittarius. *ApJL*, 162:L203, December 1970. doi: 10.1086/180654.
- A. H. Barrett, P. R. Schwartz, and J. W. Waters. Detection of Methyl Alcohol in Orion at a Wavelength of ~ 1 Centimeter. *ApJL*, 168:L101, September 1971. doi: 10.1086/180793.
- A. H. Barrett, P. Ho, and R. N. Martin. Time variations and spectral structure of the methanol maser in Orion A. *ApJL*, 198:L119–L122, June 1975. doi: 10.1086/181826.
- W. Batrla and K. M. Menten. Detection of a strong new maser line of methanol toward DR 21(OH). *ApJL*, 329:L117–L120, June 1988. doi: 10.1086/185189.
- W. Batrla, H. E. Matthews, K. M. Menten, and C. M. Walmsley. Detection of strong methanol masers towards galactic H II regions. *Nature*, 326:49–51, March 1987. doi: 10.1038/326049a0.
- H. Beuther and T. Henning. Multiple low-turbulence starless cores associated with intermediate- to high-mass star formation. *A&A*, 503:859–867, September 2009. doi: 10.1051/0004-6361/200912036.
- H. Beuther, P. Schilke, K. M. Menten, F. Motte, T. K. Sridharan, and F. Wyrowski. High-Mass Protostellar Candidates. II. Density Structure from Dust Continuum and CS Emission. *ApJ*, 566:945–965, February 2002a. doi: 10.1086/338334.
- H. Beuther, P. Schilke, T. K. Sridharan, K. M. Menten, C. M. Walmsley, and F. Wyrowski. Massive molecular outflows. *A&A*, 383:892–904, March 2002b. doi: 10.1051/0004-6361:20011808.
- H. Beuther, A. Walsh, P. Schilke, T. K. Sridharan, K. M. Menten, and F. Wyrowski. CH₃OH and H₂O masers in high-mass star-forming regions. *A&A*, 390:289–298, July 2002c. doi: 10.1051/0004-6361:20020710.

- H. Beuther, P. Schilke, and T. Stanke. Multiple outflows in IRAS 19410+2336. *A&A*, 408:601–610, September 2003. doi: 10.1051/0004-6361:20030795.
- H. Beuther, P. Schilke, and F. Gueth. Massive Molecular Outflows at High Spatial Resolution. *ApJ*, 608:330–340, June 2004. doi: 10.1086/386543.
- S. L. Breen, S. P. Ellingsen, J. L. Caswell, and B. E. Lewis. 12.2-GHz methanol masers towards 1.2-mm dust clumps: quantifying high-mass star formation evolutionary schemes. *MNRAS*, 401:2219–2244, February 2010. doi: 10.1111/j.1365-2966.2009.15831.x.
- R. B. Buxton, A. H. Barrett, P. T. P. Ho, and M. H. Schneps. Search for methanol masers. *AJ*, 82:985–988, December 1977. doi: 10.1086/112160.
- J. L. Caswell and R. F. Haynes. Atlas of main-line OH masers in the galactic longitude range 3 to 60 deg. *Australian Journal of Physics*, 36:417–442, 1983. doi: 10.1071/PH830417b.
- J. L. Caswell, J. Yi, R. S. Booth, and D. M. Cragg. Methanol masers at 107.0 and 156.6GHz. *MNRAS*, 313:599–616, April 2000. doi: 10.1046/j.1365-8711.2000.03277.x.
- X. Chen, S. P. Ellingsen, Z.-Q. Shen, A. Titmarsh, and C.-G. Gan. A 95 GHz Class I Methanol Maser Survey Toward Glimpse Extended Green Objects (EGOs). *ApJS*, 196:9, September 2011. doi: 10.1088/0067-0049/196/1/9.
- X. Chen, S. P. Ellingsen, J.-H. He, Y. Xu, C.-G. Gan, Z.-Q. Shen, T. An, Y. Sun, and B.-G. Ju. A 95 GHz Class I Methanol Maser Survey toward a Sample of GLIMPSE Point Sources Associated with BGPS Clumps. *ApJS*, 200:5, May 2012. doi: 10.1088/0067-0049/200/1/5.
- X. Chen, C.-G. Gan, S. P. Ellingsen, J.-H. He, Z.-Q. Shen, and A. Titmarsh. Newly Identified Extended Green Objects (EGOs) from the Spitzer GLIMPSE II Survey. I. Catalog. *ApJS*, 206:9, May 2013. doi: 10.1088/0067-0049/206/1/9.
- A. C. Cheung, D. M. Rank, C. H. Townes, D. D. Thornton, and W. J. Welch. Detection of Water in Interstellar Regions by its Microwave Radiation. *Nature*, 221:626–628, February 1969. doi: 10.1038/221626a0.
- E. Churchwell, M. S. Povich, D. Allen, M. G. Taylor, M. R. Meade, B. L. Babler, R. Indebetouw, C. Watson, B. A. Whitney, M. G. Wolfire, T. M. Bania, R. A. Benjamin, D. P. Clemens, M. Cohen, C. J. Cyganowski, J. M. Jackson, H. A. Kobulnicky, J. S. Mathis, E. P. Mercer, S. R. Stolovy, B. Uzpen, D. F. Watson, and M. J. Wolff. The Bubbling Galactic Disk. *ApJ*, 649:759–778, October 2006. doi: 10.1086/507015.
- W. D. Cotton and F. Yusef-Zadeh. A Large-scale Spectroscopic Survey of Methanol and OH Line Emission from the Galactic Center: Observations and Data. *ApJS*, 227:10, November 2016. doi: 10.3847/0067-0049/227/1/10.
- D. M. Cragg, K. P. Johns, P. D. Godfrey, and R. D. Brown. Pumping the interstellar methanol masers. *MNRAS*, 259:203–208, November 1992. doi: 10.1093/mnras/259.1.203.
- D. M. Cragg, A. M. Sobolev, S. P. Ellingsen, J. L. Caswell, P. D. Godfrey, S. V. Salii, and R. G. Dodson. Multitransition study and new detections of class II methanol masers. *MNRAS*, 323:939–951, May 2001. doi: 10.1046/j.1365-8711.2001.04294.x.
- D. M. Cragg, A. M. Sobolev, and P. D. Godfrey. Models of class II methanol masers based on improved molecular data. *MNRAS*, 360:533–545, June 2005. doi: 10.1111/j.1365-2966.2005.09077.x.

- C. J. Cyganowski, B. A. Whitney, E. Holden, E. Braden, C. L. Brogan, E. Churchwell, R. Indebetouw, D. F. Watson, B. L. Babler, R. Benjamin, M. Gomez, M. R. Meade, M. S. Povich, T. P. Robitaille, and C. Watson. A Catalog of Extended Green Objects in the GLIMPSE Survey: A New Sample of Massive Young Stellar Object Outflow Candidates. *AJ*, 136:2391–2412, December 2008. doi: 10.1088/0004-6256/136/6/2391.
- C. J. Cyganowski, C. L. Brogan, T. R. Hunter, and E. Churchwell. A Class I and Class II CH₃OH Maser Survey of EGOs from the GLIMPSE Survey. *ApJ*, 702:1615–1647, September 2009. doi: 10.1088/0004-637X/702/2/1615.
- K. A. Edris, G. A. Fuller, and R. J. Cohen. A survey of OH masers towards high mass protostellar objects. *A&A*, 465:865–877, April 2007. doi: 10.1051/0004-6361:20066280.
- M. Elitzur, editor. *Astronomical masers*, volume 170 of *Astrophysics and Space Science Library*, 1992. doi: 10.1007/978-94-011-2394-5.
- M. Elitzur and T. de Jong. A model for the maser sources associated with H II regions. *A&A*, 67:323–332, July 1978.
- S. P. Ellingsen. Methanol Masers: Reliable Tracers of the Early Stages of High-Mass Star Formation. *ApJ*, 638:241–261, February 2006. doi: 10.1086/498673.
- S. P. Ellingsen, D. M. Cragg, V. Minier, E. Muller, and P. D. Godfrey. A search for 85.5- and 86.6-GHz methanol maser emission. *MNRAS*, 344:73–82, September 2003. doi: 10.1046/j.1365-8711.2003.06788.x.
- S. P. Ellingsen, M. A. Voronkov, D. M. Cragg, A. M. Sobolev, S. L. Breen, and P. D. Godfrey. Investigating high-mass star formation through maser surveys. In J. M. Chapman and W. A. Baan, editors, *Astrophysical Masers and their Environments*, volume 242 of *IAU Symposium*, pages 213–217, March 2007. doi: 10.1017/S1743921307012999.
- F. Fontani, R. Cesaroni, and R. S. Furuya. Class I and Class II methanol masers in high-mass star-forming regions. *A&A*, 517:A56, July 2010. doi: 10.1051/0004-6361/200913679.
- J. R. Forster and J. L. Caswell. OH and H₂O masers in 74 star-forming regions. The FC89 database. *A&AS*, 137:43–49, May 1999. doi: 10.1051/aas:1999479.
- C.-G. Gan, X. Chen, Z.-Q. Shen, Y. Xu, and B.-G. Ju. A Search for 95 GHz Class I Methanol Masers in Molecular Outflows. *ApJ*, 763:2, January 2013. doi: 10.1088/0004-637X/763/1/2.
- G. Garay, L. F. Rodríguez, and I. de Gregorio-Monsalvo. Very Large Array Observations of Candidate High-Mass Protostellar Objects at 7 Millimeters. *AJ*, 134:906–911, September 2007. doi: 10.1086/520334.
- R. Genzel and D. Downes. H₂O in the Galaxy: sites of newly formed OB stars. *A&AS*, 30:145–168, October 1977.
- P. F. Goldsmith and W. D. Langer. Population Diagram Analysis of Molecular Line Emission. *ApJ*, 517:209–225, May 1999. doi: 10.1086/307195.
- A. I. Gómez-Ruiz, S. E. Kurtz, E. D. Araya, P. Hofner, and L. Loinard. A Catalog of Methanol Masers in Massive Star-forming Regions. III. The Molecular Outflow Sample. *ApJS*, 222:18, February 2016. doi: 10.3847/0067-0049/222/2/18.
- M. Gray. *Maser Sources in Astrophysics*. April 2012.
- A. D. Haschick, W. A. Baan, and K. M. Menten. Detection of three new methanol maser transitions toward star-forming regions. *ApJ*, 346:330–335, November 1989. doi: 10.1086/168013.

- V. A. Hughes and G. C. MacLeod. A comparison of the infrared luminosity and ionizing luminosity of selected star forming regions. *AJ*, 105:1495–1504, April 1993. doi: 10.1086/116528.
- T. R. Hunter, C. L. Brogan, C. J. Cyganowski, and K. H. Young. Subarcsecond Imaging of the NGC 6334 I(N) Protocluster: Two Dozen Compact Sources and a Massive Disk Candidate. *ApJ*, 788:187, June 2014. doi: 10.1088/0004-637X/788/2/187.
- C. H. Jordan, A. J. Walsh, V. Lowe, M. A. Voronkov, S. P. Ellingsen, S. L. Breen, C. R. Purcell, P. J. Barnes, M. G. Burton, M. R. Cunningham, T. Hill, J. M. Jackson, S. N. Longmore, N. Peretto, and J. S. Urquhart. MALT-45: a 7 mm survey of the southern Galaxy - I. Techniques and spectral line data. *MNRAS*, 448:2344–2361, April 2015. doi: 10.1093/mnras/stv178.
- C. H. Jordan, A. J. Walsh, S. L. Breen, S. P. Ellingsen, M. A. Voronkov, and L. J. Hyland. MALT-45: A 7 mm survey of the southern Galaxy - II. ATCA follow-up observations of 44 GHz class I methanol masers. *MNRAS*, 471:3915–3954, November 2017. doi: 10.1093/mnras/stx1776.
- S. V. Kalenskii and S. Kurtz. Analytical methods for measuring the parameters of interstellar gas using methanol observations. *Astronomy Reports*, 60:702–717, August 2016. doi: 10.1134/S1063772916080047.
- S. V. Kalenskii, V. I. Slysh, I. E. Val'tts, A. Winnberg, and L. E. Johansson. The Detection of New Methanol Masers in the $5_{-1}-4_0E$ Line. *Astronomy Reports*, 45:26–33, January 2001. doi: 10.1134/1.1336598.
- S. V. Kalenskii, V. G. Promyslov, V. I. Slysh, P. Bergman, and A. Winnberg. The detection of class I methanol masers towards regions of low-mass star formation. *Astronomy Reports*, 50:289–297, April 2006. doi: 10.1134/S1063772906040032.
- K. I. Kellermann and G. L. Verschuur. *Galactic and extragalactic radio astronomy (2nd edition)*. 1988.
- S. Kurtz. Hypercompact HII regions. In R. Cesaroni, M. Felli, E. Churchwell, and M. Walmsley, editors, *Massive Star Birth: A Crossroads of Astrophysics*, volume 227 of *IAU Symposium*, pages 111–119, 2005. doi: 10.1017/S1743921305004424.
- N. D. Kylafis. Masers and Star Formation. In C. J. Lada and N. D. Kylafis, editors, *NATO Advanced Science Institutes (ASI) Series C*, volume 342 of *NATO Advanced Science Institutes (ASI) Series C*, page 269, 1991.
- H.-T. Lee, W.-T. Liao, D. Froebrich, J. Karr, G. Ioannidis, Y.-H. Lee, Y.-N. Su, S.-Y. Liu, H.-Y. Duan, and M. Takami. Near-infrared H_2 and Continuum Survey of Extended Green Objects. II. Complete Census for the Northern Galactic Plane. *ApJS*, 208:23, October 2013. doi: 10.1088/0067-0049/208/2/23.
- R. M. Lees. On the E1-E2 Labeling of Energy Levels and the Anomalous Excitation of Interstellar Methanol. *ApJ*, 184:763–772, September 1973. doi: 10.1086/152368.
- R. M. Lees and J. G. Baker. Torsion-Vibration-Rotation Interactions in Methanol. I. Millimeter Wave Spectrum. *JChPh*, 48:5299–5318, June 1968. doi: 10.1063/1.1668221.
- S. Leurini, H. Beuther, P. Schilke, F. Wyrowski, Q. Zhang, and K. M. Menten. Multi-line (sub)millimetre observations of the high-mass proto cluster IRAS 05358+3543. *A&A*, 475:925–939, December 2007a. doi: 10.1051/0004-6361:20077977.
- S. Leurini, P. Schilke, F. Wyrowski, and K. M. Menten. Methanol as a diagnostic tool of interstellar clouds. II. Modelling high-mass protostellar objects. *A&A*, 466:215–228, April 2007b. doi: 10.1051/0004-6361:20054245.
- S. Leurini, K. M. Menten, and C. M. Walmsley. Physical characteristics of bright Class I methanol masers. *A&A*, 592:A31, July 2016. doi: 10.1051/0004-6361/201527974.

- S. Liechti and C. M. Walmsley. Thermal methanol emission in the DR21 complex. Interferometric maps: a comparison with maser emission. *A&A*, 321:625–633, May 1997.
- C. C. Lin and J. D. Swalen. Internal Rotation and Microwave Spectroscopy. *Reviews of Modern Physics*, 31:841–891, October 1959. doi: 10.1103/RevModPhys.31.841.
- I. D. Litovchenko, A. V. Alakoz, I. E. Val’Tts, and G. M. Larionov. Search for class I methanol maser emission in various types of objects in the interstellar medium. *ARep*, 55:1086–1095, December 2011. doi: 10.1134/S1063772911120080.
- X. Lu, Q. Zhang, H. B. Liu, P. Sanhueza, K. Tatematsu, S. Feng, H. A. Smith, P. C. Myers, T. K. Sridharan, and Q. Gu. Filamentary Fragmentation and Accretion in High-mass Star-forming Molecular Clouds. *ApJ*, 855:9, March 2018. doi: 10.3847/1538-4357/aaad11.
- J. G. Mangum, A. Wootten, and L. G. Mundy. Synthesis imaging of the DR 21 (OH) cluster. II - Thermal ammonia and water maser emission. *ApJ*, 388:467–488, April 1992. doi: 10.1086/171167.
- J. Martin-Pintado, R. Bachiller, and A. Fuente. SIO Emission as a Tracer of Shocked Gas in Molecular Outflows. *A&A*, 254:315, February 1992.
- T. P. McCarthy, S. P. Ellingsen, M. A. Voronkov, and G. Cimò. The relationship between Class I and Class II methanol masers at high angular resolution. *MNRAS*, 477:507–524, June 2018. doi: 10.1093/mnras/sty694.
- D. M. Mehringer and K. M. Menten. 44 GHz Methanol Masers and Quasi-Thermal Emission in Sagittarius B2. *ApJ*, 474:346–361, January 1997. doi: 10.1086/303454.
- K. M. Menten. Methanol Masers and Submillimeter Wavelength Water Masers in Star-Forming Regions. In A. D. Haschick and P. T. P. Ho, editors, *Atoms, Ions and Molecules: New Results in Spectral Line Astrophysics*, volume 16 of *Astronomical Society of the Pacific Conference Series*, pages 119–136, 1991a.
- K. M. Menten. The discovery of a new, very strong, and widespread interstellar methanol maser line. *ApJL*, 380:L75–L78, October 1991b. doi: 10.1086/186177.
- K. M. Menten and W. Batrla. Observations of various methanol maser transitions toward the NGC 6334 region. *ApJ*, 341:839–846, June 1989. doi: 10.1086/167542.
- K. M. Menten, C. M. Walmsley, C. Henkel, and T. L. Wilson. The centimeter transitions of E-type methanol. *A&A*, 157:318–328, March 1986.
- V. Minier and R. S. Booth. A methanol line survey toward high-mass star-forming regions. *A&A*, 387:179–186, May 2002. doi: 10.1051/0004-6361:20020290.
- V. Minier, S. P. Ellingsen, R. P. Norris, and R. S. Booth. The protostellar mass limit for 6.7 GHz methanol masers. I. A low-mass YSO survey. *A&A*, 403:1095–1100, June 2003. doi: 10.1051/0004-6361:20030465.
- S. Molinari, J. Brand, R. Cesaroni, and F. Palla. A search for precursors of ultracompact HII regions in a sample of luminous IRAS sources. I. Association with ammonia cores. *A&A*, 308:573–587, April 1996.
- M. Morimoto, M. Ohishi, and T. Kanzawa. New maser lines of methanol. *ApJL*, 288:L11–L15, January 1985. doi: 10.1086/184411.
- M. Nakano and S. Yoshida. Molecular line observations of the S235B region. *PASJ*, 38:531–545, 1986.
- N. Panagia. Some Physical parameters of early-type stars. *AJ*, 78:929–934, November 1973. doi: 10.1086/111498.

- R. L. Plambeck and K. M. Menten. 95 GHz methanol masers near DR 21 and DR 21(OH). *ApJ*, 364: 555–560, December 1990. doi: 10.1086/169437.
- R. L. Plambeck and M. C. H. Wright. A 95 GHz methanol maser in Orion-KL. *ApJL*, 330:L61–L65, July 1988. doi: 10.1086/185205.
- A. Porras, I. Cruz-González, and L. Salas. Young stellar clusters and H₂ nebulosities in S233IR. *A&A*, 361:660–670, September 2000.
- C. R. Purcell, S. N. Longmore, M. G. Burton, A. J. Walsh, V. Minier, M. R. Cunningham, and R. Balasubramanyam. Physical and chemical conditions in methanol maser selected hot cores and UCHII regions. *MNRAS*, 394:323–339, March 2009. doi: 10.1111/j.1365-2966.2008.14283.x.
- C. R. Purcell, M. G. Hoare, W. D. Cotton, S. L. Lumsden, J. S. Urquhart, C. Chandler, E. B. Churchwell, P. Diamond, S. M. Dougherty, R. P. Fender, G. Fuller, S. T. Garrington, T. M. Gledhill, P. F. Goldsmith, L. Hindson, J. M. Jackson, S. E. Kurtz, J. Martí, T. J. T. Moore, L. G. Mundy, T. W. B. Muxlow, R. D. Oudmaijer, J. D. Pandian, J. M. Paredes, D. S. Shepherd, S. Smethurst, R. E. Spencer, M. A. Thompson, G. Umana, and A. A. Zijlstra. The Coordinated Radio and Infrared Survey for High-mass Star Formation. II. Source Catalog. *ApJS*, 205:1, March 2013. doi: 10.1088/0067-0049/205/1/1.
- J. M. Rathborne, J. S. Whitaker, J. M. Jackson, J. B. Foster, Y. Contreras, I. W. Stephens, A. E. Guzmán, S. N. Longmore, P. Sanhueza, F. Schuller, F. Wyrowski, and J. S. Urquhart. Molecular Line Emission Towards High-Mass Clumps: The MALT90 Catalogue. *PASA*, 33:e030, July 2016. doi: 10.1017/pasa.2016.23.
- M. J. Reid and J. M. Moran. Masers. *ARA&A*, 19:231–276, 1981. doi: 10.1146/annurev.aa.19.090181.001311.
- M. J. Reid, K. M. Menten, A. Brunthaler, X. W. Zheng, T. M. Dame, Y. Xu, Y. Wu, B. Zhang, A. Sanna, M. Sato, K. Hachisuka, Y. K. Choi, K. Immer, L. Moscadelli, K. L. J. Rygl, and A. Bartkiewicz. Trigonometric Parallaxes of High Mass Star Forming Regions: The Structure and Kinematics of the Milky Way. *ApJ*, 783:130, March 2014. doi: 10.1088/0004-637X/783/2/130.
- T. Rodríguez-Esnard, M. A. Trinidad, and V. Migenes. Observational Study of the Continuum and Water Maser Emission in the IRAS 19217+1651 Region. *ApJ*, 761:158, December 2012. doi: 10.1088/0004-637X/761/2/158.
- C. B. Rodríguez-Garza, S. E. Kurtz, A. I. Gómez-Ruiz, P. Hofner, E. D. Araya, and S. V. Kalenskii. A Catalog of 44 GHz Methanol Masers in Massive Star-forming Regions. IV. The High-mass Protostellar Object Sample. *ApJS*, 233:4, November 2017. doi: 10.3847/1538-4365/aa8f4e.
- V. Rosero, P. Hofner, M. Claussen, S. Kurtz, R. Cesaroni, E. D. Araya, C. Carrasco-González, L. F. Rodríguez, K. M. Menten, F. Wyrowski, L. Loinard, and S. P. Ellingsen. Weak and Compact Radio Emission in Early High-mass Star-forming Regions. I. VLA Observations. *ApJS*, 227:25, December 2016. doi: 10.3847/1538-4365/227/2/25.
- S. V. Salii and A. M. Sobolev. Methanol and other molecular tracers of outflows and dense gas in the molecular cloud G345.01+1.79. *Astronomy Reports*, 50:965–982, December 2006. doi: 10.1134/S1063772906120031.
- Á. Sánchez-Monge, M. T. Beltrán, R. Cesaroni, F. Fontani, J. Brand, S. Molinari, L. Testi, and M. Burton. Different evolutionary stages in massive star formation. Centimeter continuum and H₂O maser emission with ATCA. *A&A*, 550:A21, February 2013. doi: 10.1051/0004-6361/201219890.

- A. Sanna, M. J. Reid, T. M. Dame, K. M. Menten, and A. Brunthaler. Mapping spiral structure on the far side of the Milky Way. *Science*, 358:227–230, October 2017. doi: 10.1126/science.aan5452.
- A. P. Sarma and E. Momjian. Detection of the Zeeman Effect in the 36 GHz Class I CH₃OH Maser Line with the EVLA. *ApJL*, 705:L176–L179, November 2009. doi: 10.1088/0004-637X/705/2/L176.
- A. P. Sarma and E. Momjian. Discovery of the Zeeman Effect in the 44 GHz Class I Methanol (CH₃OH) Maser Line. *ApJL*, 730:L5, March 2011. doi: 10.1088/2041-8205/730/1/L5.
- V. I. Slysh, S. V. Kalenskii, and I. E. Val'tts. The detection of a new methanol maser transition at 9.9 GHz. *ApJL*, 413:L133–L135, August 1993. doi: 10.1086/186977.
- V. I. Slysh, S. V. Kalenskii, and I. E. Val'tts. Detection of a series of methanol maser lines at 1.9 millimeter wavelength. *ApJ*, 442:668–673, April 1995. doi: 10.1086/175471.
- V. I. Slysh, S. V. Kalenskii, I. E. Val'tts, and V. V. Golubev. Detection of a New Methanol Maser Line with the Kitt Peak 12 Meter Telescope by Remote Observing from Moscow. *ApJL*, 478:L37–L40, March 1997. doi: 10.1086/310548.
- V. I. Slysh, I. E. Val'tts, S. V. Kalenskii, M. A. Voronkov, F. Palagi, G. Tofani, and M. Catarzi. The Medicina survey of methanol masers at 6.7 GHz. *A&AS*, 134:115–128, January 1999. doi: 10.1051/aas:1999127.
- V. I. Slysh, S. V. Kalenskii, and I. E. Val'tts. Methanol Radio Emission at Millimeter Wavelengths: New Masers at 1.3 and 2.8 Millimeters. *Astronomy Reports*, 46:49–56, January 2002. doi: 10.1134/1.1436204.
- V. V. Sobolev. *Moving envelopes of stars*. 1960.
- T. K. Sridharan, H. Beuther, P. Schilke, K. M. Menten, and F. Wyrowski. High-Mass Protostellar Candidates. I. The Sample and Initial Results. *ApJ*, 566:931–944, February 2002. doi: 10.1086/338332.
- T. K. Sridharan, H. Beuther, M. Saito, F. Wyrowski, and P. Schilke. High-Mass Starless Cores. *ApJL*, 634:L57–L60, November 2005. doi: 10.1086/498644.
- V. S. Strel'nitskii and R. A. Sunyaev. Nature of the High Velocities of H₂O Sources in W49. *Soviet Astron.*, 16:579, February 1973.
- M. Szymczak, G. Hrynek, and A. J. Kus. A survey of the 6.7 GHz methanol maser emission from IRAS sources. I. Data. *A&AS*, 143:269–301, April 2000. doi: 10.1051/aas:2000334.
- I. E. Val'tts, A. M. Dzura, S. V. Kalenskii, V. I. Slysh, R. S. Booth, and A. Winnberg. The discovery of methanol masers at 107 GHz. *A&A*, 294:825–830, February 1995.
- I. E. Val'tts, S. P. Ellingsen, V. I. Slysh, S. V. Kalenskii, R. Otrupcek, and M. A. Voronkov. Detection of new sources of methanol emission at 107 and 108GHz with the Mopra telescope. *MNRAS*, 310:1077–1086, December 1999. doi: 10.1046/j.1365-8711.1999.03009.x.
- I. E. Val'tts, S. P. Ellingsen, V. I. Slysh, S. V. Kalenskii, R. Otrupcek, and G. M. Larionov. Detection of new sources of methanol emission at 95GHz with the Mopra telescope. *MNRAS*, 317:315–332, September 2000. doi: 10.1046/j.1365-8711.2000.03518.x.
- C. Vastel, S. Bottinelli, E. Caux, J.-M. Glorian, and M. Boiziot. CASSIS: a tool to visualize and analyse instrumental and synthetic spectra. In F. Martins, S. Boissier, V. Buat, L. Cambr esy, and P. Petit, editors, *SF2A-2015: Proceedings of the Annual meeting of the French Society of Astronomy and Astrophysics*, pages 313–316, December 2015.

- M. A. Voronkov, K. J. Brooks, A. M. Sobolev, S. P. Ellingsen, A. B. Ostrovskii, and J. L. Caswell. Class I methanol masers in the outflow of IRAS16547-4247. *MNRAS*, 373:411–424, November 2006. doi: 10.1111/j.1365-2966.2006.11047.x.
- M. A. Voronkov, K. J. Brooks, A. M. Sobolev, S. P. Ellingsen, A. B. Ostrovskii, and J. L. Caswell. The Australia Telescope campaign to study southern class I methanol masers. In J. M. Chapman and W. A. Baan, editors, *Astrophysical Masers and their Environments*, volume 242 of *IAU Symposium*, pages 182–183, March 2007. doi: 10.1017/S1743921307012902.
- M. A. Voronkov, A. J. Walsh, J. L. Caswell, S. P. Ellingsen, S. L. Breen, S. N. Longmore, C. R. Purcell, and J. S. Urquhart. Discovery of the new class I methanol maser transition at 23.4 GHz. *MNRAS*, 413: 2339–2344, June 2011. doi: 10.1111/j.1365-2966.2011.18297.x.
- C. Watson, E. Araya, M. Sewilo, E. Churchwell, P. Hofner, and S. Kurtz. Resolution of Distance Ambiguities of Inner Galaxy Massive Star Formation Regions. I. *ApJ*, 587:714–726, April 2003. doi: 10.1086/368286.
- H. Weaver, D. R. W. Williams, N. H. Dieter, and W. T. Lum. Observations of a Strong Unidentified Microwave Line and of Emission from the OH Molecule. *Nature*, 208:29–31, October 1965. doi: 10.1038/208029a0.
- S. Weinreb, A. H. Barrett, M. L. Meeks, and J. C. Henry. Radio Observations of OH in the Interstellar Medium. *Nature*, 200:829–831, November 1963. doi: 10.1038/200829a0.
- S. Weinreb, M. L. Meeks, and J. C. Carter. Observations of Polarized OH Emission. *Nature*, 208:440–441, October 1965. doi: 10.1038/208440a0.
- T. L. Wilson, C. M. Walmsley, L. E. Snyder, and P. R. Jewell. Detection of a new type of methanol maser. *A&A*, 134:L7–L10, May 1984.
- T. L. Wilson, C. M. Walmsley, K. M. Menten, and W. Hermsen. The discovery of a new masering transition of interstellar methanol. *A&A*, 147:L19–L22, June 1985.
- T. L. Wilson, S. Huettemeister, G. Dahmen, and C. Henkel. Three transitions of methanol at 1 CM wavelength. *A&A*, 268:249–254, February 1993.
- T. L. Wilson, Q. Zeng, S. Huettemeister, and G. Dahmen. The $J_2 - J_1$ E methanol transitions for $J \geq 12$ in Orion KL. *A&A*, 307:209, March 1996.
- Y. Xu, J. J. Li, K. Hachisuka, J. D. Pandian, K. M. Menten, and C. Henkel. A high-sensitivity 6.7 GHz methanol maser survey toward H₂O sources. *A&A*, 485:729–734, July 2008. doi: 10.1051/0004-6361:200809472.
- Y. Xu, M. J. Reid, K. M. Menten, A. Brunthaler, X. W. Zheng, and L. Moscadelli. Trigonometric Parallaxes of Massive Star-Forming Regions: III. G59.7+0.1 and W 51 IRS2. *ApJ*, 693:413–418, March 2009. doi: 10.1088/0004-637X/693/1/413.
- T. Yanagida, T. Sakai, T. Hirota, N. Sakai, J. B. Foster, P. Sanhueza, J. M. Jackson, K. Furuya, Y. Aikawa, and S. Yamamoto. ALMA Observations of the IRDC Clump G34.43+00.24 MM3: 278 GHz Class I Methanol Masers. *ApJL*, 794:L10, October 2014. doi: 10.1088/2041-8205/794/1/L10.
- W. Yang, Y. Xu, X. Chen, S. P. Ellingsen, D. Lu, B. Ju, and Y. Li. A New 95 GHz Methanol Maser Catalog. I. Data. *ApJS*, 231:20, August 2017. doi: 10.3847/1538-4365/aa6ff3.
- F. Yusef-Zadeh, W. Cotton, S. Viti, M. Wardle, and M. Royster. Widespread Methanol Emission from the Galactic Center: The Role of Cosmic Rays. *ApJL*, 764:L19, February 2013. doi: 10.1088/2041-8205/764/2/L19.

-
- L. A. Zapata, L. Loinard, Y.-N. Su, L. F. Rodríguez, K. M. Menten, N. Patel, and R. Galván-Madrid. Millimeter Multiplicity in DR21(OH): Outflows, Molecular Cores, and Envelopes. *ApJ*, 744:86, January 2012. doi: 10.1088/0004-637X/744/2/86.

Appendices

Appendix A

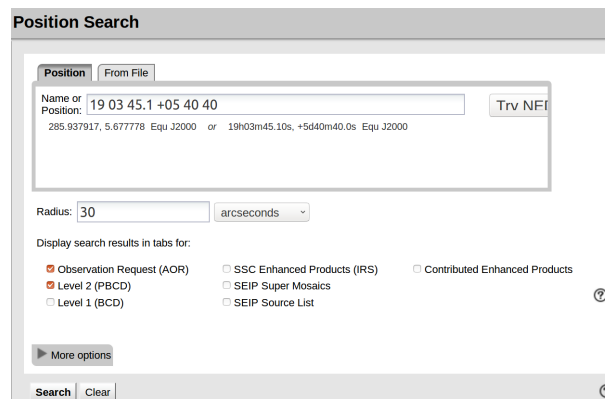
Three-color images with DS9

SAOImage DS9¹ is a software designed for the management of astronomical images in FITS (Flexible Image Transport System) format. It was developed in 1990 at the Smithsonian Astrophysical Observatory (SAO) of the Center for Astrophysics at Harvard University. It is commonly known as DS9, whose name was inspired by the television series *Star Trek: Deep Space Nine* (ST:DS9). Many of the three-color images shown in this Thesis were made with DS9, thus we present here the general procedure to build them.

A.1 Download Spitzer images

We search for images of each region in the *Spitzer Heritage Archive*². We download the images corresponding to the IRAC bands at 3.6, 4.5 and 8 μm whose color codes are blue, green and red, respectively.

Search: it is necessary to specify the source position and search radius. In this example, we searched for images of IRAS 19012+0536 whose central position is at R.A. = $19^{\text{h}}03^{\text{m}}45.1^{\text{s}}$ and Decl. = $+05^{\circ}40'40''$. We defined a search radius of 30'' (see Figure A.1).



The screenshot shows a web-based search interface titled "Position Search". It has two tabs: "Position" (selected) and "From File". The "Position" tab contains a text input field with the coordinates "19 03 45.1 +05 40 40" and a "Trv NFI" button. Below the input field, there is a list of alternative coordinate formats: "285.937917, 5.677778 Equ J2000 or 19h03m45.10s, +5d40m40.0s Equ J2000". Below this, there is a "Radius:" field with the value "30" and a dropdown menu set to "arcseconds". Underneath, there is a section "Display search results in tabs for:" with several radio button options: "Observation Request (AOR)" (checked), "Level 2 (PBCD)", "Level 1 (BCD)", "SSC Enhanced Products (IRS)", "SEIP Super Mosaics", "SEIP Source List", and "Contributed Enhanced Products". At the bottom left, there is a "More options" button with a right-pointing arrow. At the bottom right, there is a "Search" button and a "Clear" button. A help icon is visible in the bottom right corner.

Figure A.1: Searching for images of IRAS 19012+0536 at the specified position.

¹For more information and download: <http://ds9.si.edu/>

²<http://sha.ipac.caltech.edu/applications/Spitzer/SHA/>

Crop: once the search is done, a list of images that matched the input position are displayed. We select one of the images in the IRAC band at 4.5 μm and visualize it in the tab *Data*. The central position is automatically marked with a blue circle of radius equivalent to the radius of search (30") given by the user. We select a rectangular area of the desired size to crop the image using the *Crop* tool (see Figure A.2).

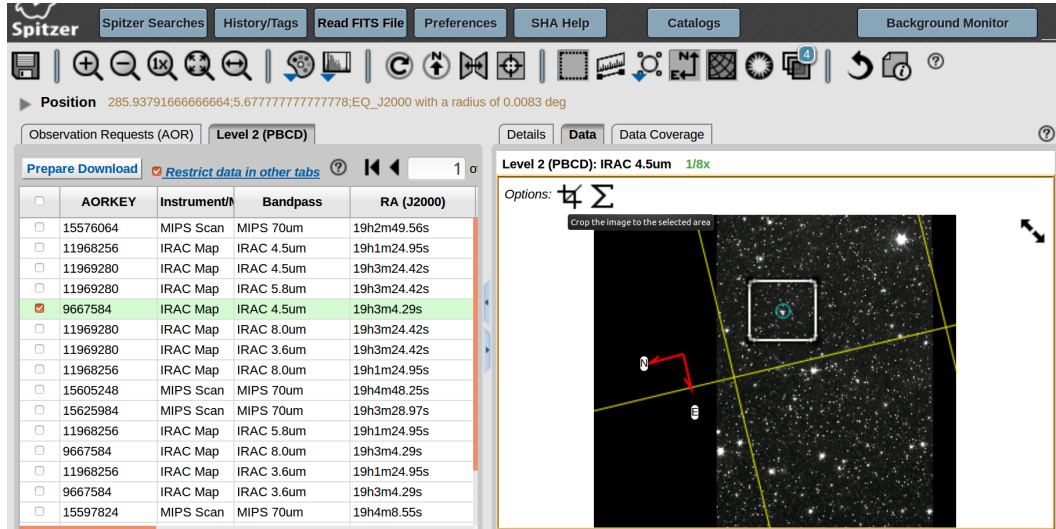


Figure A.2: Select the desired area around the blue circle and then crop it with the *Crop* tool.

Rotate: before downloading the image, is very important to *rotate* it so that north is up.

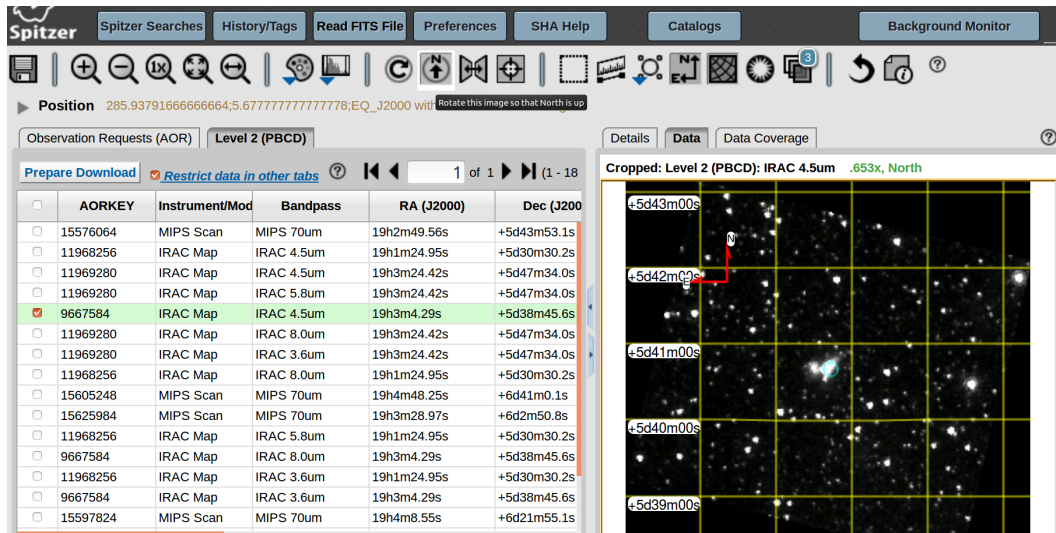


Figure A.3: Use the *rotate* tool to orient the north up.

Save: the user has the option of saving the original or the cropped version of the FITS file. In our case, the

cropped image is the preferred option to download.

A detailed description of the visualization tools can be found in the *Help* section of the Spitzer Heritage Archive web page³.

A.2 Managing images with DS9

The DS9 web page has a user manual⁴ describing briefly the basic steps to create three-color images but many important —and not obvious— steps are omitted. For that reason we present here a complete step by step recipe to build RGB images.

1. **Frame RGB:** Choose *New Frame RGB* from the *Frame* menu (see Figure A.4). When the frame is created, the RGB window (see Figure A.5) will be automatically displayed.
2. **Load:** To load the correspondig image of the 8 μm band, make sure that the *Red* band is selected in the *Current* column of the RGB window (see Figure A.5; left panel). Then load the green (4.5 μm) and blue (3.6 μm) files following the same steps. Once the three images are loaded, go to the *Lock* menu and lock the ten options displayed (see Figure A.5; right panel): WCS, Crop, Slice, Bin, Axes Order, Scale, Scale and Limits, Colorbar, Block and Smooth. This will ensure that any modification you make, will be applied to the three frames at once. For example, in Figure A.6 we selected the *Red* band to load the corresponding 8 μm image, SPITZER_I4_19012.fits.
3. **Scale:** once the three RGB images are loaded, DS9 applies the linear color scale automatically. Figure A.7 shows the composed image with the logarithmic scale, which was preferred in this Thesis. The minimum and maximum scale values can be adjusted using the right button of the mouse or with the *Scale Parameters* dialog box through the *Scale* menu.
4. **Crop:** as shown in Figure A.7, each of the three RGB images may have different sizes. This can be changed with the *Crop* option in the button bar or using the *Crop Parameters* dialog box within the *Zoom* menu. Both of them allow to crop the three images simultaneously if the *Crop* option is checked in the RGB window. The *Crop Parameters* dialog box permits to set manually the center position and size of the composed image to be cropped. Figure A.8 shows the RGB image cropped at a desired size.
5. **Coordinate Parameters:** Figure A.8 shows a coordinate grid in the image. This can be added with the *Coordinate Grid Parameters* option (see Figure A.9) from the *Analysis* menu. This tool allows to change the color, size, line style, and line tickness for all elements in the grid such as: labels, numerics and title.
6. **Regions:** the three-color images presented in this Thesis show circles to indicate to the reader the covered area in each region by a single antenna (the VLA primary beam). We also show ellipses as indicators of the IRAS positional error and crosses to mark the peak position of the maser emission (see Figure A.10). This can be done through the *Region* menu, which has other markers such as squares, diamonds, etc. We saved each of the markers used in separate files, which should be in *.reg* extension in order to be read by DS9. In Figure A.11 we show the file format of the VLA primary beam represented by a circle. We specified the center of the circle, its radius (30"), as well as the line width and color.

³<http://irsa.ipac.caltech.edu/onlinehelp/irsaviewer/visualization.html>

⁴<http://ds9.si.edu/doc/user/rgb/index.html>

- 7. Contours: it is possible to overlap contour maps on the RGB image using the *Contour Parameters* option from the *Analysis* menu. Figure A.12 shows 7 mm continuum emission overlapped as contours on the RGB image of IRAS 19012+0536. To do this, it is necessary to create first a new frame and load the 7 mm image as shown in Figure A.13. Then, open the *Contour Parameters* dialog box and check the *User* option from the *Limits* menu to enter manually the contour levels. Figure A.14 shows the four contour levels that were set ($8e-4$, $1e-3$, $1.2e-3$ and $1.4e-3$). Go to the *File* menu and choose *Save Contour Levels* to save them with the file extension *.lev*. Finally, select *Save Contours* whose extension is *.ctr*. The *.ctr* file is the one that should be selected when overlapping the contour map on the RGB image. Keep the *.lev* file for further reference of the contour level values.
- 8. Save Image: the image could be saved in different file formats. The *File* menu has the option *Save Image*, which allows you to save the RGB image in different extensions such as *.eps*, *.gif*, *.tiff*, *.jpeg* and *.png*.

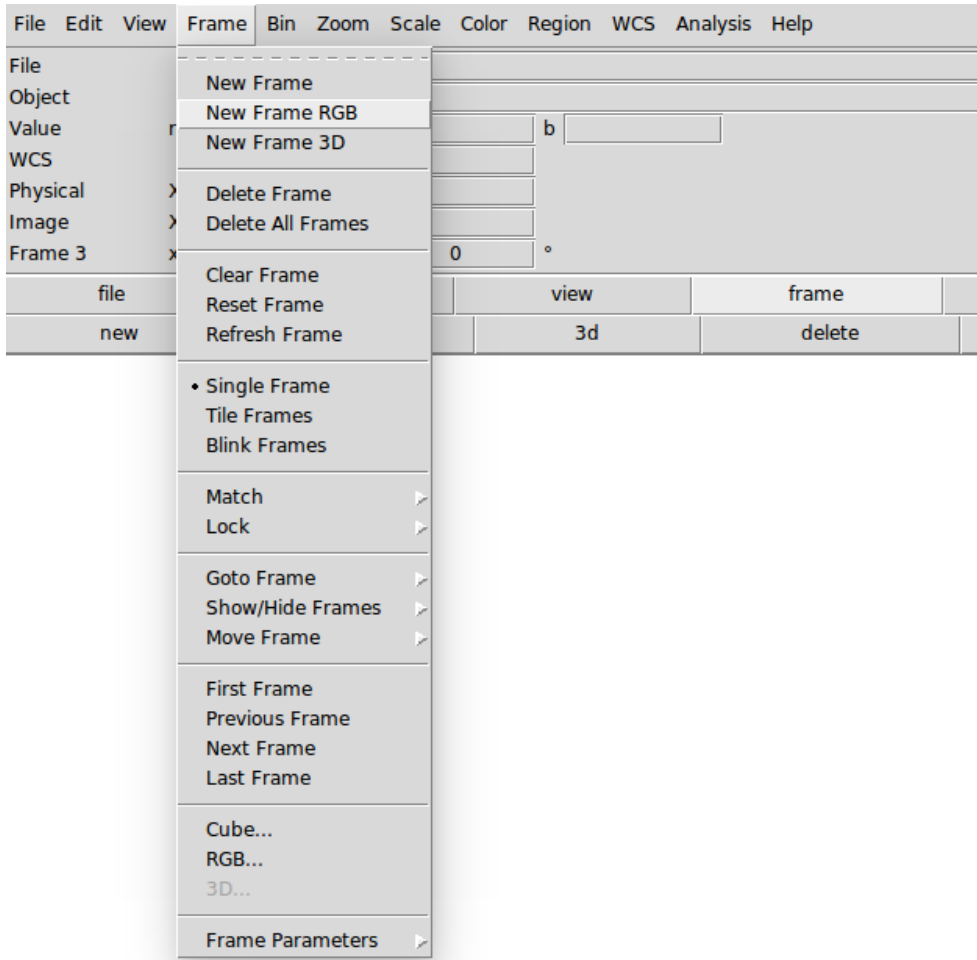


Figure A.4: The *Frame* options can be selected from the menu at the top of the windows or from the button bar displayed below.

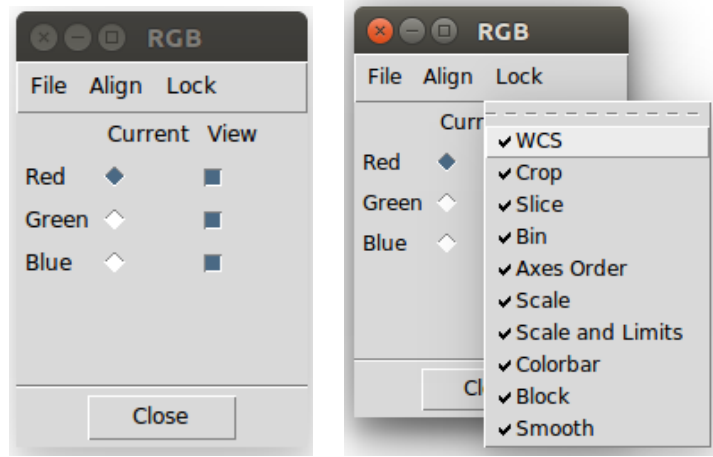


Figure A.5: The RGB window indicates which RGB frame will be uploaded or modified. Each RGB frame may have different crop sizes, color scales, etc. We can *lock* the frames together, so that the setting is applied to all three frames at once. This is done with the *Lock* menu in the RGB window by checking all the options displayed.

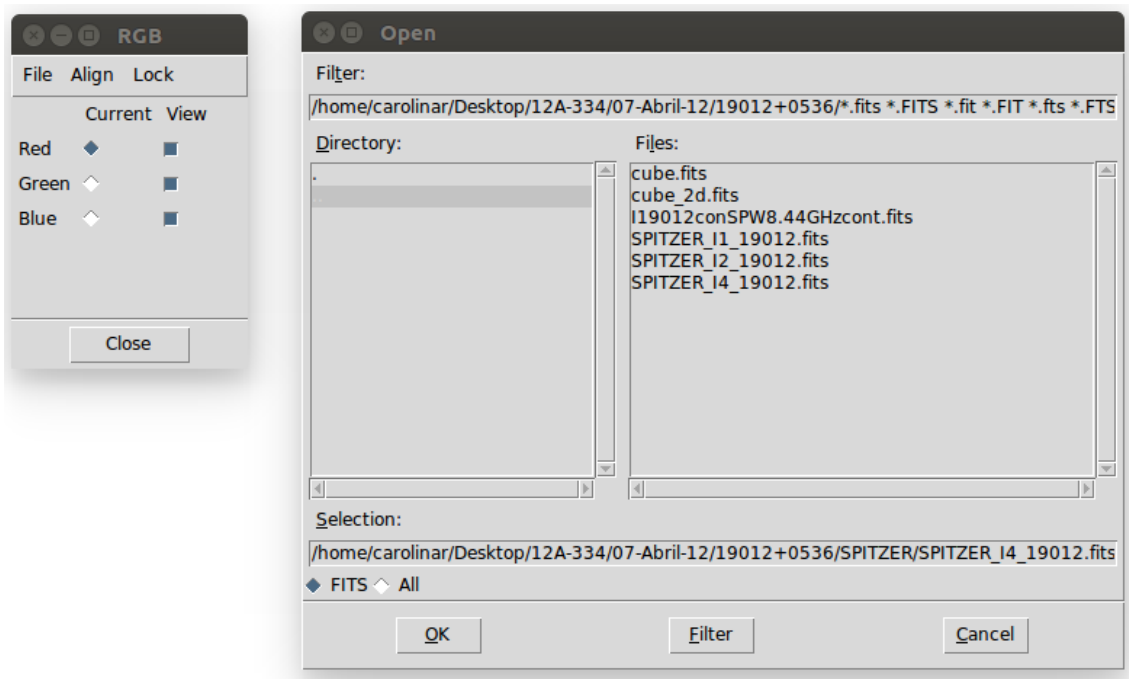


Figure A.6: We load the image “SPITZER_I4_19012.fits”, which was taken in the band 4 ($8\ \mu\text{m}$) of the IRAC camera on the Spitzer telescope. This band is usually represented with the color *Red*, note that this color is selected in the *RGB window*.

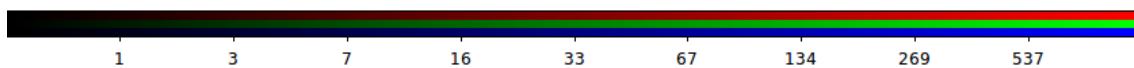
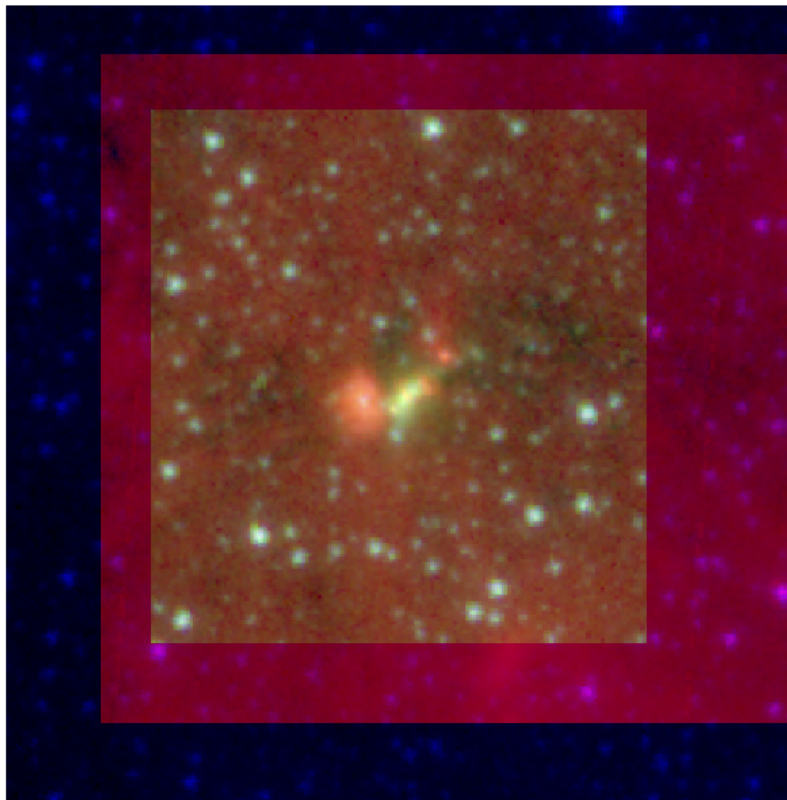
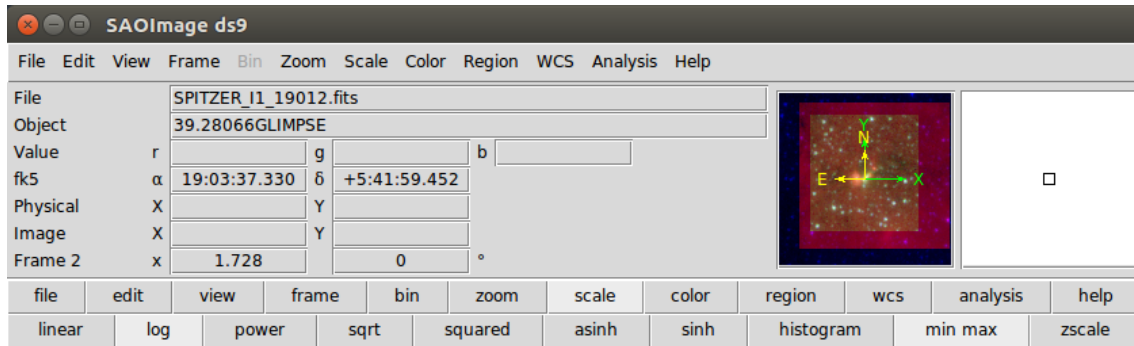


Figure A.7: The three images corresponding to each color were loaded. DS9 applies them automatically the linear color scale but we preferred the logarithmic scale. Note that each frame has different sizes.

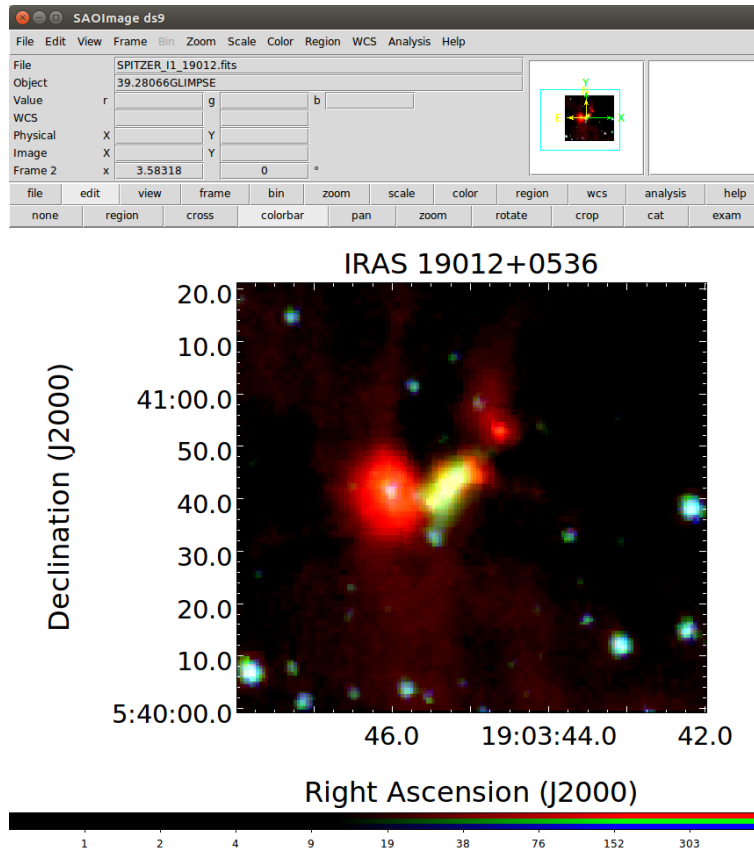


Figure A.8: We show a smaller portion of the region with different minimum and maximum color scale values. The composed image was trimmed using the *Crop* option from the *Edit* menu. The color scale was adjusted to certain values that permit to highlight interesting details. Note that the colorbar shown at the bottom of the image is different compared to that in Figure A.7.

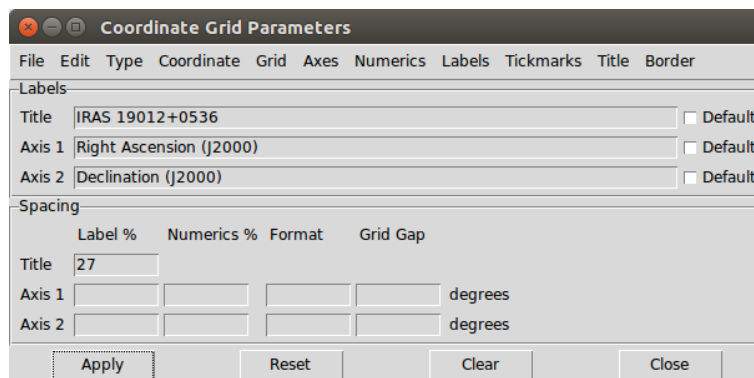


Figure A.9: This window allows to add a coordinate grid to the image and to change the color, size, line style, and line tickness for all elements in the grid such as: labels, numerics and title.

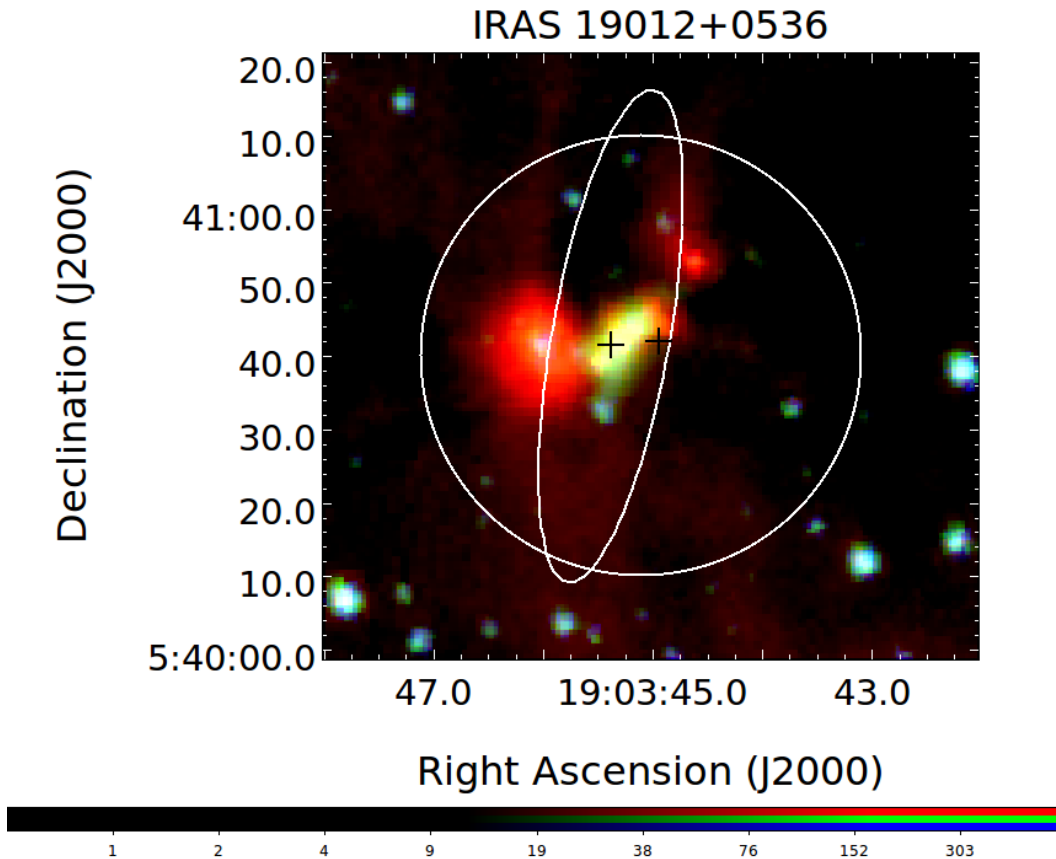
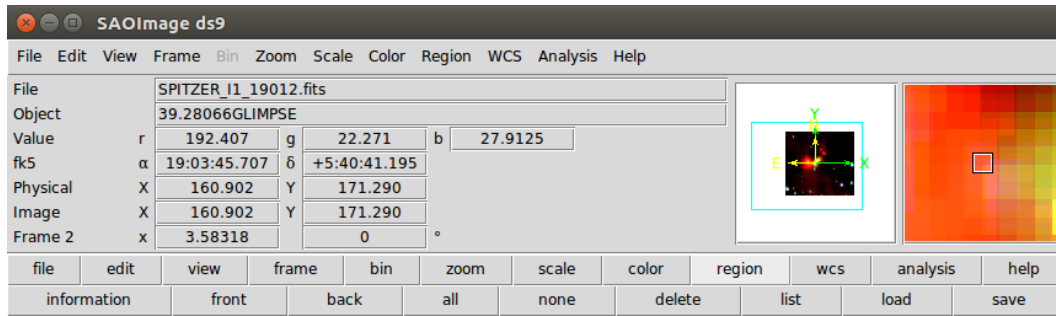


Figure A.10: The *Region* menu allows to add markers such as circles, ellipses and crosses. We used circles to indicate the covered area by the VLA antennas, ellipses to show the IRAS positional error and crosses to mark the peak position of the maser emission.



```
# Region file format: DS9 version 4.1
global color=white dashlist=8 3 width=2 font="helvetica 10 normal roman" select=1
highlite=1 dash=0 fixed=0 edit=1 move=1 delete=1 include=1 source=1
fk5
circle(19:03:45.1,+05:40:40,30)
```

Figure A.11: The DS9 *regions* can be saved in files with extension *.reg*. This is an example of the file format that should be followed to add a circle. We indicate the center position of the circle and its radius (30"), as well as line width and color.

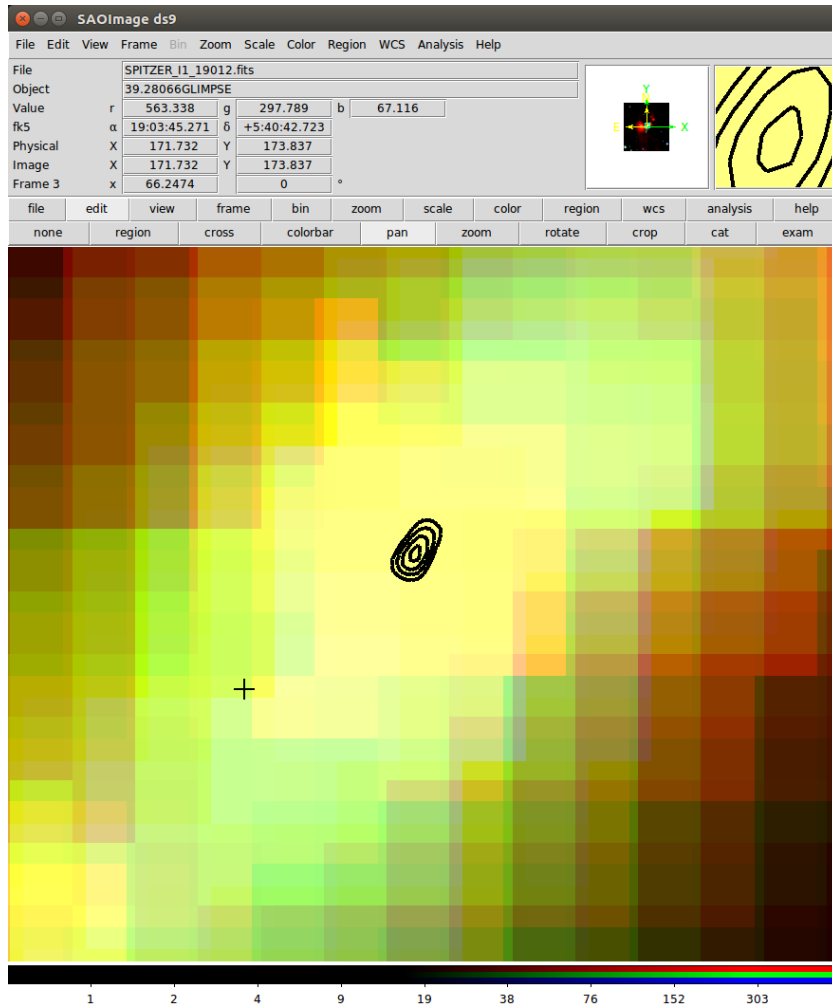


Figure A.12: It is possible to overlap contour maps on the RGB image using the *Contour Parameters* option from the *Analysis* menu. We overlap a contour map of the 7 mm continuum emission to the three-color image of IRAS 19012+0536.

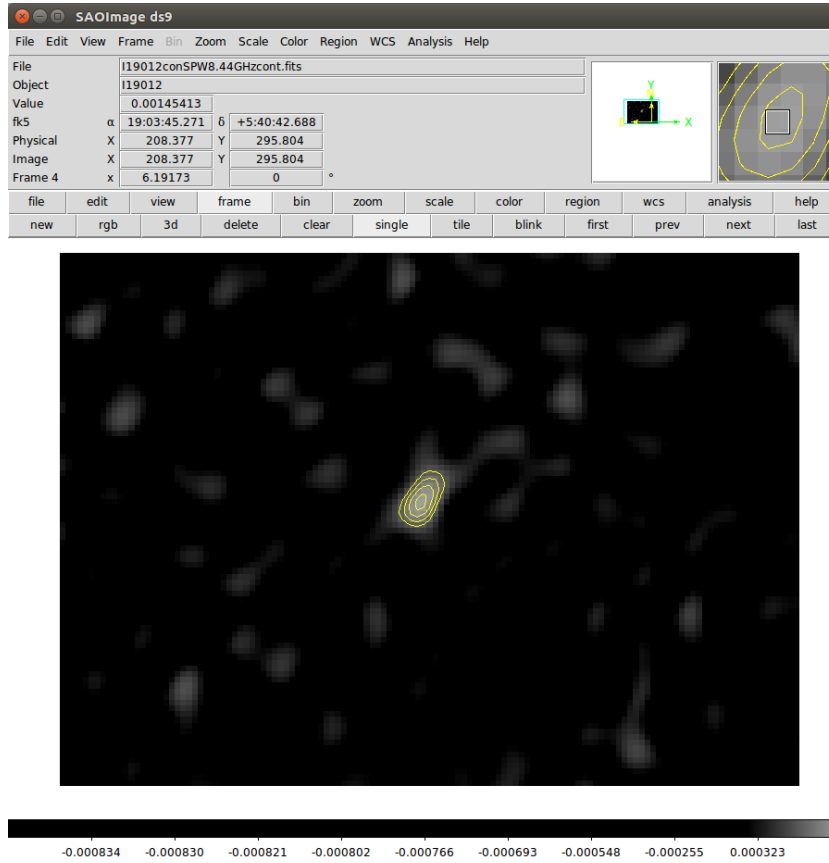


Figure A.13: It is necessary to create a new frame for loading the 7 mm continuum map.

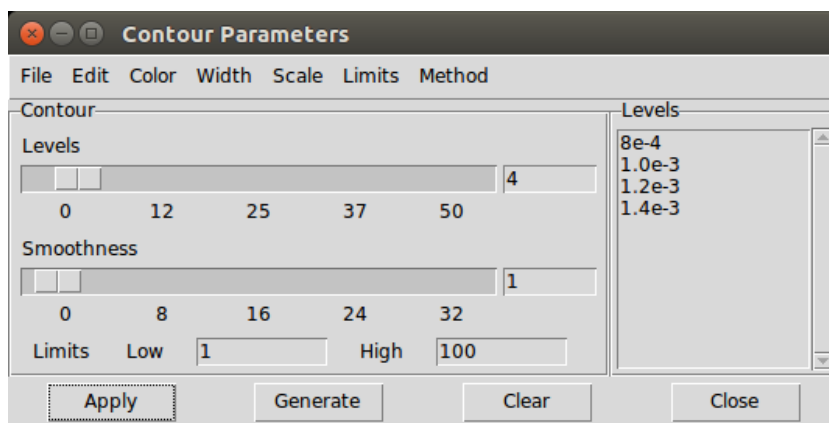


Figure A.14: Open the *Contour Parameters* dialog box from the *Analysis* menu. Then check the *User* option in the *Limits* menu to enter manually the contour levels. We set four contour levels: 8e-4, 1e-3, 1.2e-3 and 1.4e-3. Go to the *File* menu and choose *Save Contour Levels* to save the contour levels in a file with extension *.lev*. Finally, select *Save Contours* to save the contours with a file extension *.ctr*. The *.ctr* file is the one that should be selected when overlapping the contour map to the RGB image.